Segmentation and cycles of crustal accretion at mid-ocean ridges: a study of the Reykjanes Ridge

Alexander B. Gardiner

Segmentation and cycles of crustal accretion at mid-ocean ridges: a study of the Reykjanes Ridge

Alexander B. Gardiner

A thesis submitted for the degree of Doctor of Philosophy at the University of Durham

Department of Geological Sciences
August 2003

Declaration

This dissertation describes my own work, except where acknowledgement is made in the text, and is not substantially the same as any work that has been, or is being, submitted to any other university for any degree, diploma or other qualification.

Alexander B. Gardiner

August 2003

Segmentation and cycles of crustal accretion at mid-ocean ridges: a study of the Reykjanes Ridge

Alexander B. Gardiner

Abstract

Early studies of mid-ocean ridges suggest a fundamental difference between crustal accretionary processes at slow- and fast-spreading ridges. Accretion, and the supply of melt to the crust itself, is thought to be highly episodic at slow-spreading ridges but steady-state at fast-spreading ridges. However, recent studies are beginning to question this model, with evidence for the temporal variation in crustal accretionary processes at all spreading rates emerging.

This study provides evidence from bathymetry, TOBI sidescan, gravity and magnetic data, collected during different cruises to the Reykjanes Ridge, for the temporal nature of crustal accretion and its relationship to segmentation.

Interpretation of TOBI images indicates that individual adjacent axial volcanic ridges (AVRs) vary in relative age, suggesting that they are at various stages of an evolutionary lifecycle, with episodic cycles of magmatic and tectonic activity. However, prior to investigating the possible effects of tectonomagmatic cycles on the crustal structure of AVRs, the effect of the Iceland hotspot on the ridge is examined. The along-axis free-air gravity anomaly is forward modelled in 2-D, revealing an along-axis increase in crustal thickness towards Iceland from 7.5 km to 10.5 km and a decrease in mantle densities from 3.30 to 3.23 g cm^{-3} between 57°30'N and 62°N. Calculation of the residual mantle Bouguer Anomaly (RMBA) and inversion of magnetic anomaly data, reveal intermediate-wavelength fluctuations in RMBA amplitude and magnetization intensity respectively that are attributed to hotspot pulses, with 59°N marking the southern most extent of the most recent pulse.

Removal of the hotspot effect on the gravity data reveals short-wavelength RMBA lows, associated with individual AVRs, superimposed on a broad ridge-trending low. Along-AVR-axis gravity modelling shows that a number of these RMBA lows can be explained by a 200-800 m thickening of the crust and/or by the presence of 5-20% partial melt in the mid-crust. A correlation between relative AVR age and crustal structure is established, with longer, more mature AVRs having a thicker crust and shorter, younger AVRs having more partial melt in the mid-crust.

Short-wavelength magnetization intensity highs, associated with younger AVRs, corroborate the TOBI age interpretations. Local spreading rate calculations reveal that total spreading rates for younger AVRs are up to 20% faster than for older AVRs over the last 1.42 Ma.

On the basis of these results a model for the cyclicity of crustal accretion is presented, whereby far-field tectonic stresses result in spreading-orthogonal brittle deformation of the crust in the neovolcanic zone, and 3-D mantle upwelling, with a wavelength of ~70 km, follows the ridge trend and results in second order segments that comprise ~5 AVRs. It is proposed that along-axis migration of melt within such a segment results in the observed variations in AVR age, length, RMBA amplitude, magnetization intensity and local spreading rate.

The proposed model has implications for the temporal variability of crustal accretion at all spreading rates.

Acknowledgements

I would like to thank my primary supervisor Christine Peirce for helping me through these last three (and a bit) years, reading (and correcting!) numerous drafts of this thesis and providing funding for two conferences in San Francisco. Thanks must also go to Roger Searle who provided the code for the magnetic data inversion and helped me with the magnetic part of this thesis. I would also like to thank my third supervisor, Martin Sinha, for providing useful ideas during discussions in both Durham and Southampton.

All of the data presented here was collected thanks to the officers, crew and scientific staff on board the RRS Charles Darwin, R/V Maurice Ewing and RRS Discovery during cruises CD81/93 and CD87/94, EW9008/90 and D235c/98 respectively.

I am indebted to my office mates, Anthony and Kostas for showing me the ropes in the early years and Chris Gill for helping me with IT related matters and for letting me bounce ideas off him. Thanks also to Mrs. Grant and my housemates at The Wing: Jules for... well...being Jules and Jens and Wibke for making it easier for me to get up in the morning by fixing the shower and making bread.

Thanks to my parents for the constant encouragement and support.

Heather has been a great source of help and encouragement, especially in the latter stages of my PhD, by helping me cross-check references and formulate ideas. Thank you also H. for feeding and generally looking after me.

My three years at Durham were funded through a research studentship provided by the University of Durham and the Department of Geological Sciences.

Table of contents

List of figures

List of tables

Glossary of terms and abbreviations

The following terms and abbreviations are used throughout this dissertation.

2-D	Two-dimensional
3-D	Three-dimensional
4-D	Four-dimensional
AVR	Axial Volcanic Ridge
CAMH	Central Anomaly Magnetic High
CSEM	Controlled Source Electromagnetic
DEVAL	DEViation in Axial Linearity
DLVZ	Depleted Low Velocity Zone
EPR	East Pacific Rise
FAA	Free-Air Anomaly
FFT	Fast Fourier Transform
GMT	Generic Mapping Tool (version 3.3, see Wessel & Smith 1995)
GPS	Global Positioning System
GRS80	Geodetic Reference System 1980
IGRF	International Geomagnetic Reference Field
MAR	Mid-Atlantic Ridge
MARNOK	Mid-Atlantic Ridge North of Kane
MBA	Mantle Bouguer Anomaly
MCS	Mutli-Channel Seismic
MT	Magnetotelluric
NRM	Natural Remnant Magnetization
OSC	Overlapping Spreading Centre
RAMESSES	Reykjanes Axial Melt Experiment: Structural Synthesis from Electromagnetics and Seismics
RMBA	Residual Mantle Bouguer Anomaly
r.m.s.	root-mean-square
T_c	Curie temperature
TOBI	Towed Ocean Bottom Instrument

Chapter 1

Introduction

1.1 Mid-ocean ridges

The mid-ocean ridge system extends ~60 000 km in length beneath the world's oceans and is generally characterised by a shallowing of the seabed of 1000-3000 m relative to the surrounding seafloor that extends in width from a few hundreds to a few thousands of kilometres (Fig. 1.1). Mid-ocean ridges account for 70% of the Earth's volcanic output and are where new oceanic lithosphere is created as the plates move apart from each other according to the seafloor spreading hypothesis of Hess (1962).

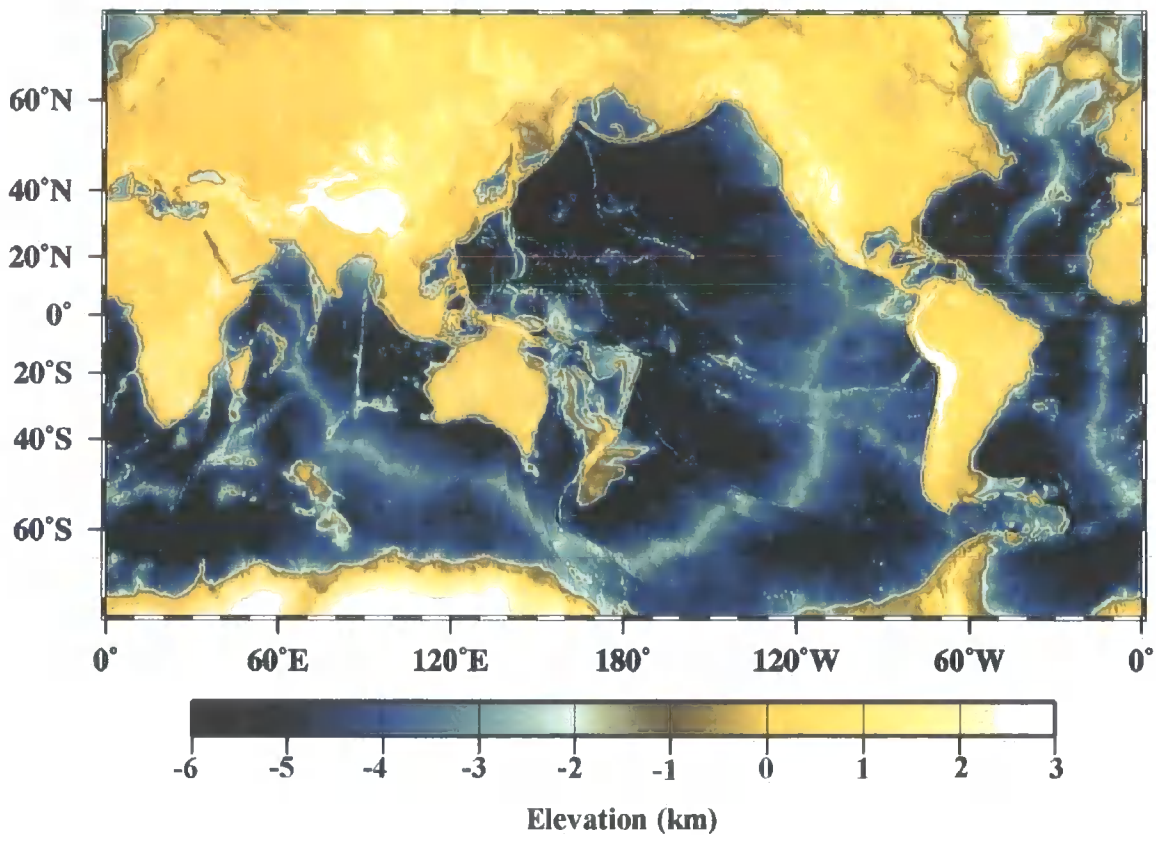

Figure 1.1: Elevation map of the world, highlighting the mid-ocean ridge system in oceanic areas (Sandwell & Smith 1997).

Observations of bilaterally symmetric magnetic anomalies over mid-ocean ridges (Vine & Matthews 1963) confirm the theory of seafloor spreading and when combined with a reversal timescale (e.g. Cande & Kent 1995), allow spreading rate calculations to

be made. The gross morphology of mid-ocean ridges appears to be influenced by spreading rate (Figs. 1.2 and 1.3). Fast-spreading ridges, such as the East Pacific Rise (EPR), spread at a total rate greater than 90 mm yr^{-1} and are characterised by a smooth axial high that is broken by an axial trough that may be up to ~100 m wide and 10 m deep. These fast-spreading ridges are associated with a high thermal regime and, consequently, have relatively smooth flanks with inward-facing faults developing 1-4 km from the ridge axis with fault throws of less than 50 m. Intermediate-spreading ridges, such as the Juan de Fuca Ridge, spread at a total rate of between 50 mm yr^{-1} and 90 mm yr^{-1} and have a 50-200 m deep axial trough superimposed on a broad axial high. The neovolcanic zone, present within the median valley, is 1-2 km wide and contains overlapping spreading centres (OSCs). Faulting at intermediate-spreading ridges is similar to that observed at faster-spreading ridges but the seafloor topography is slightly rougher due to the lower thermal regime. Slow-spreading ridges, such as the Mid-Atlantic Ridge (MAR), have total spreading rates of less than 50 mm yr^{-1} and are distinguished by a 1-3 km deep median valley that is 5-15 km wide and contains a series of en echelon axial volcanic ridges (AVRs). The low thermal regime at slow-spreading ridges results in inward-facing faults with throws of up to 1-2 km and rough seafloor topography. Although the morphology of ridges varies significantly with spreading rate, the actual structure of the crust (in terms of its layering) is very similar for all ridges, regardless of spreading rate.

1.2 Oceanic crust

Our current understanding of the composition and structure of the oceanic crust comes from a variety of sources. The combined analyses of dredge samples, drill cores, submersible dives over rock exposures and the study of ophiolites have been used to build a pseudostratigraphy of the oceanic crust. The composition of the crust is found to be remarkably similar for all spreading rates and comprises basaltic pillow lavas superimposed on a sheeted diabase dyke complex which, in turn, overlies isotropic to layered gabbroic rocks (Nicolas & Boudier 1995). These rock units constitute the oceanic crust and lie above melt-depleted peridotites, which are interpreted as residual upper mantle. Marine seismic refraction investigations (Raitt 1963; Houtz & Ewing 1976) suggest that the oceanic crust has a simple horizontally layered structure, with each seismically derived layer equating to a layer of the pseudostratigraphy described above (Fig. 1.4). However, detailed investigations of fault escarpments on the seafloor

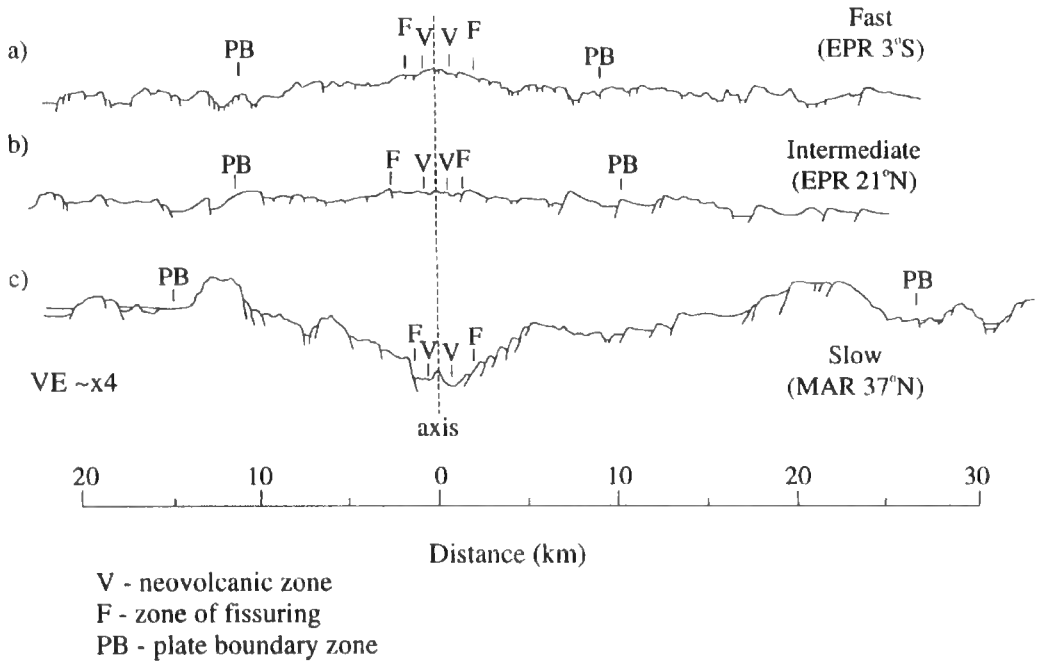

Figure 1.2: Across-axis seabed topographic characteristics of mid-ocean ridges. (a) Fast-spreading ridges have a broad, smooth axial high. (b) Intermediate-spreading ridges comprise a broad axial high with a small graben on-axis. (c) Slow-spreading ridges display a pronounced median valley. After Macdonald (1982).

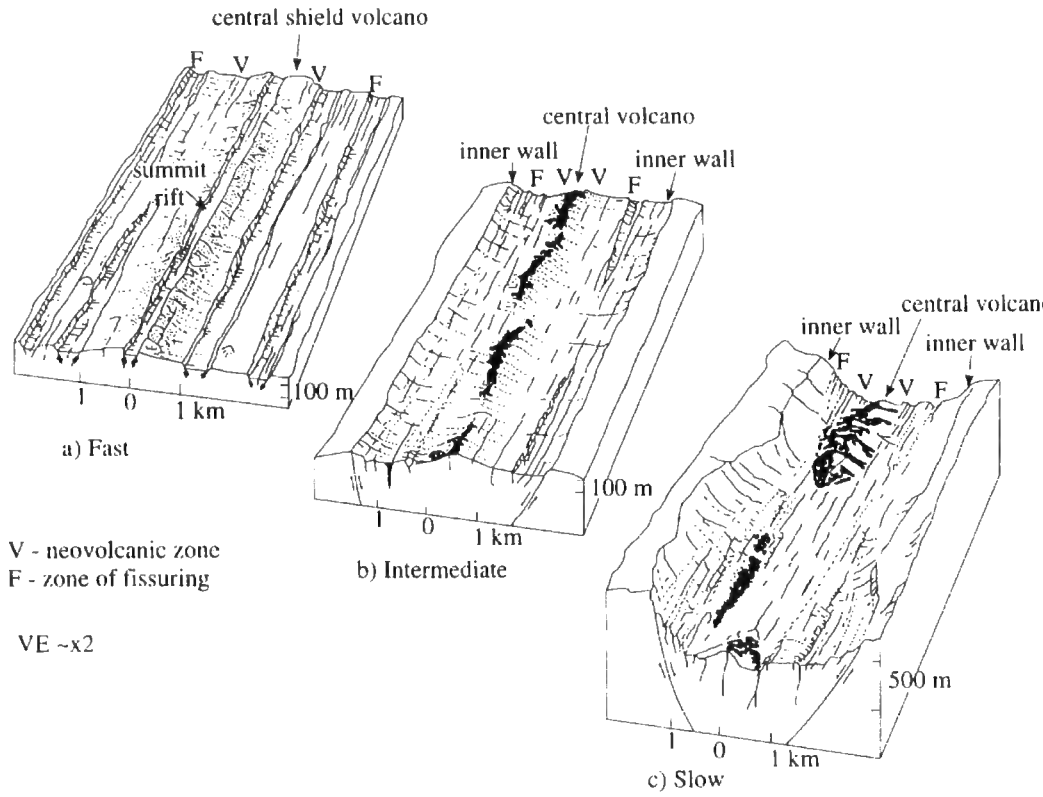

Figure 1.3: Mid-ocean ridge morphological characteristics associated with the main ridge types. (a) Fast-spreading ridges consist of a small summit rift within a broad axial high. (b) Intermediate-spreading ridges have a more pronounced graben with a less continuous central volcano. (c) Slow-spreading ridges have a deep median valley and discontinuous central volcano along-axis. After Macdonald (1982).

(Stewart *et al.* 2002; Karson *et al.* 2002) are starting to show that the structure of the oceanic crust is far more complicated than previously thought.

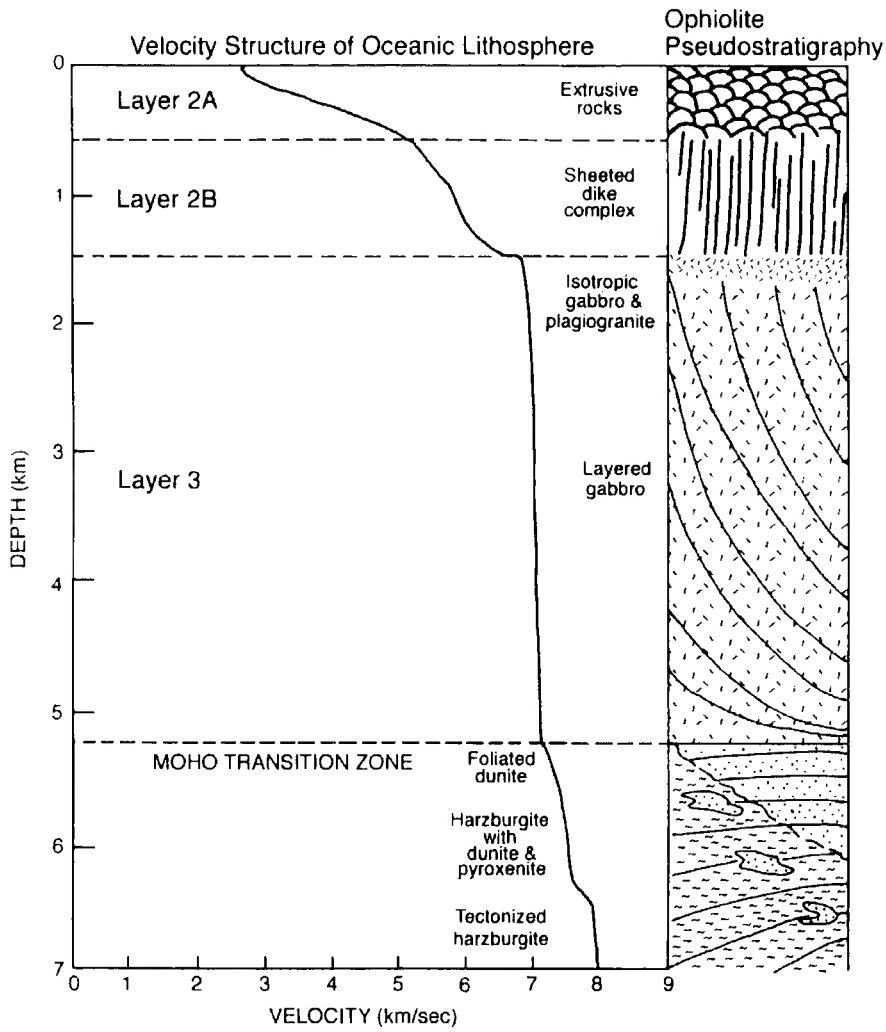

Figure 1.4: Velocity structure of the oceanic lithosphere correlated with ophiolite pseudostratigraphy (adapted from Dilek *et al.* 1998).

Layer 2A, corresponding to the extrusive layer, is defined by compressional wave velocities of 2.5 km s^{-1} to 4.5 km s^{-1}. The extrusive layer grades into a sheeted dyke complex, described as layer 2B, with velocities of 4.5 km s^{-1} to 6.5 km s^{-1}. The majority of the oceanic crust is made up of layer 3, defined by velocities of 6.5 km s^{-1} to 7.0 km s^{-1}, and comprises isotropic to layered gabbro. A jump in velocities to ~8.0 km s^{-1} defines the seismic Moho and the transition into the upper mantle.

These geological and seismic observations, which suggest that the oceanic crust is a layered igneous complex, require the presence of a magma chamber where fractionation of melt contained in a magma reservoir can account for the observed petrological

grading of the lower crust. Focussing of melt released from decompression melting of the mantle eventually establishes a shallow magma chamber. Melt from the magma chamber erupts, via sheeted dykes, on to the seafloor forming the extrusive layer. As the magma chamber cools the sides of the chamber solidify forming the gabbros of layer 3.

Evidence for the presence of magma chambers at intermediate- to fast-spreading ridges from seismic refraction and reflection data (Orcutt *et al.* 1975; Detrick *et al.* 1987; Vera *et al.*1990; Kent *et al.* 1993; Toomey *et al.* 1994; Mutter *et al.* 1995; Collier & Sinha 1992; Christenson *et al.* 1993) indicates that a typical magma chamber consists of an ~10 km wide zone of partial melt extending to the base of the crust overlain by a thin (10-100 m) melt lens that extends only 1-2 km across-axis and is located ~1 km beneath the seafloor (Fig. 1.5). The along-axis continuity of this melt body, along most of the ridge length between 15°30'N and 17°N on the EPR for example (Carbotte *et al.* 2000), suggests that magma bodies are steady-state features at faster-spreading rates.

Early seismic refraction experiments, however, failed to find evidence for a magma body beneath slow-spreading ridges. To date, only one multidisciplinary geophysical experiment (Navin *et al.* 1998) has found extensive evidence for the presence of an isolated magma chamber beneath a slow-spreading ridge, suggesting that magma chambers are transient, ephemeral, features at slow-spreading rates in contrast to the long-lived magma chambers observed at faster-spreading rates. Mid-ocean ridges are, therefore, not simple stable 2-D structures but complicated 3-D systems with a great variety of active processes. The along-axis variation in morphology and geometry of mid-ocean ridges is the most readily observable example of this complexity.

1.3 Segmentation

The development of swath bathymetry technology in the 1980s (Sempere & Macdonald 1987) allowed for greater coverage and higher resolution surveys of the mid-ocean ridge system to be made and revealed that mid-ocean ridges are not simple, continuous 2-D features occasionally disrupted by transform faults, but complex 3-D systems with as much variety along-axis as across-axis (Macdonald *et al.* 1988).

Significant along-axis variations in seafloor depth and the occurrence of non-transform ridge axis discontinuities (e.g. propagating rifts and OSCs) reveal that ridge systems are partitioned, or segmented, on a variety of length scales (Fig. 1.6) which may migrate with time.

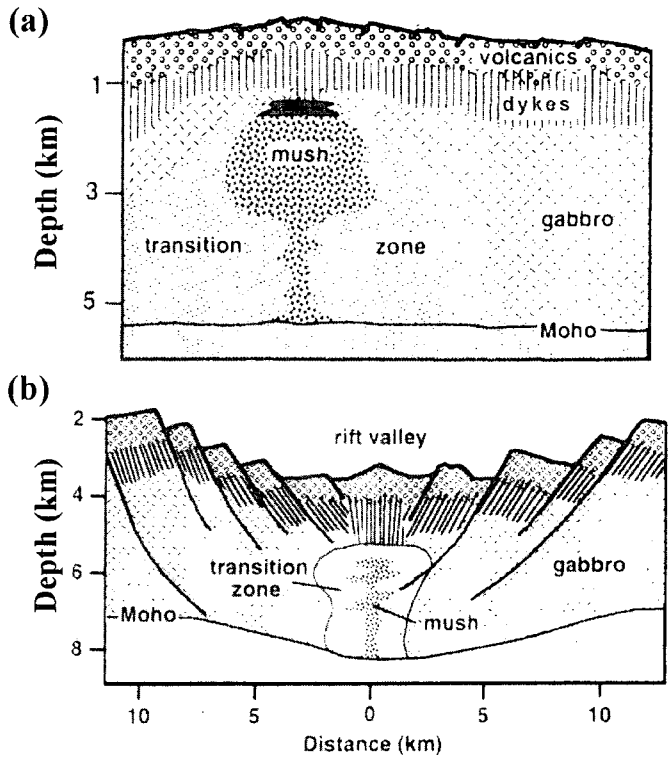

Figure 1.5: Interpretative models of magma chamber morphology. (a) Magma chambers at fast-spreading ridges consist of a melt lens overlying a crystal mush zone that extends to the Moho and is surrounded by a transition zone to the surrounding gabbro. Magma chambers at fast-spreading rates are relatively continuous along-axis. (b) Magma chambers at slow-spreading ridges are unlikely to be steady-state features or have a melt lens due to the low magma supply at slow-spreading rates. Most of the magma chamber, therefore, consists of an isolated dyke-like mush zone with a small transition zone to the surrounding gabbro. Adapted from Sinton & Detrick (1992).

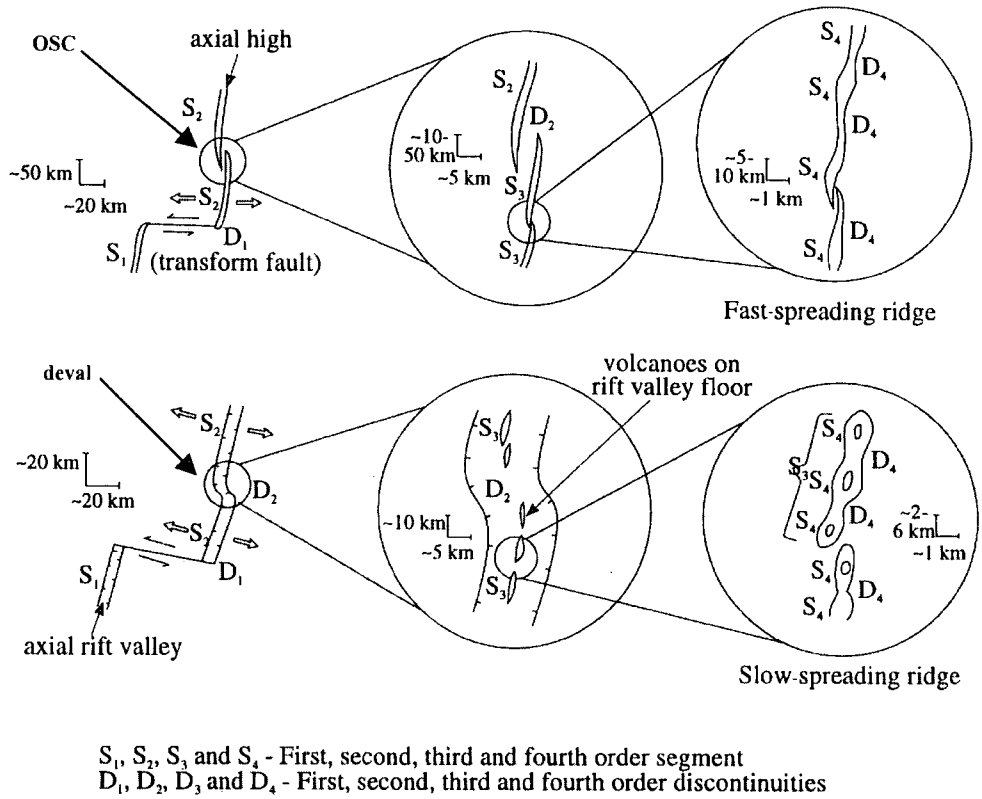

Figure 1.6: Orders of segmentation with their defining discontinuities for both fast- and slow-spreading ridges (after Macdonald *et al.* 1991). See text for details.

First order discontinuities are defined by transform faults that offset the ridge axis by 50 km or more and are associated with large axial depth anomalies. These discontinuities occur at intervals of 300-500 km along the ridge and disrupt magnetic anomalies showing that they have been stable features for the last 10 My or so (Batiza 1996). Segments also often show geochemical anomalies, with more fractionated basalts observed at segment centres, suggesting that melt delivery is focussed towards segment centres.

Second order discontinuities correspond to non-rigid features (i.e. that may migrate along the ridge axis on a timescale of 0.5 My) that offset the continuity of the ridge axis by 2 to 50 km and cause axial depth anomalies of hundreds of metres. These discontinuities are observed at 50-300 km intervals along-axis and take the shape of OSCs at fast- to intermediate-spreading centres and large-offset non-transform discontinuities at slow-spreading centres. Third order discontinuities are defined by small-offset (0.5-3.0 km), non-transform discontinuities that occur at 30-100 km along-axis with depth anomalies of only a few tens of metres. Fourth order discontinuities are very small (<1 km) offsets of the axial graben or deviations in the axial linearity (devals)

of the axis at fast- to intermediate-spreading ridges that occur at intervals of 10-50 km. Fourth order segments are rarely identified through depth anomalies and are usually associated with geochemical anomalies.

Segments	1st Order	2nd Order	3rd Order	4th Order
Length (km)	600 ± 300	140 ± 90	50 ± 30	14 ± 8
	400 ± 200	50 ± 30	15 ± 10?	7 ± 5?
Longevity (My)	>5	0.5 –5	0.01-0.1	0.001-0.01
	>5	0.5-30	?	?

Discontinuities	1st Order	2nd Order	3rd Order	4th Order
Type	Transform	OSCs	OSCs	Devals
	Transform	Rift valley jogs	Inter-volcano gap	Intra-volcano gap
Offset (km)	>50	2-50	0.5-3.0	<1
Offset (My)	>0.5	<0.5	0	0
	>2	<2	0	0
Depth anomaly (m)	300-600	100-300	30-100	0-50
	500-2000	300-1000	50-300	0-100
Off-axis trace	Fracture zone	V-shape zone	Faint or none	None
High amplitude magnetization?	Yes	Yes	Rarely	No?
Break in axial magma chamber?	Always	Yes	Yes	Rarely
	Always	N.A.	N.A.	N.A.
Geochemical anomaly?	Yes	Yes	Usually	~50%

Table 1.1: Segmentation characteristics of fast- (light grey shading) and slow- (dark grey shading) spreading ridges (adapted from Macdonald 1998). Parameter fields that are not shaded indicate values applicable to both fast- and slow-spreading ridges. Note that this hierarchy of segmentation probably represents a continuum in segmentation.

Geophysical investigations near 9°N on the EPR (Macdonald *et al.* 1988) indicate that the segmentation of mid-ocean ridges may be linked to spatial and temporal variations in magmatic flow beneath the ridge axis (Fig. 1.7). The presence of an axial magma chamber, imaged by seismic data, appears to be correlated to a broad cross-sectional shape of the ridge axis and the presence of an axial graben. An increase in magma supply to the ridge axis gives rise to a large shallow magma chamber which results in a broad axial bulge on which an "elongate caldera" like feature is formed as the melt supply dwindles. Conversely, a low magma supply to the ridge axis gives rise

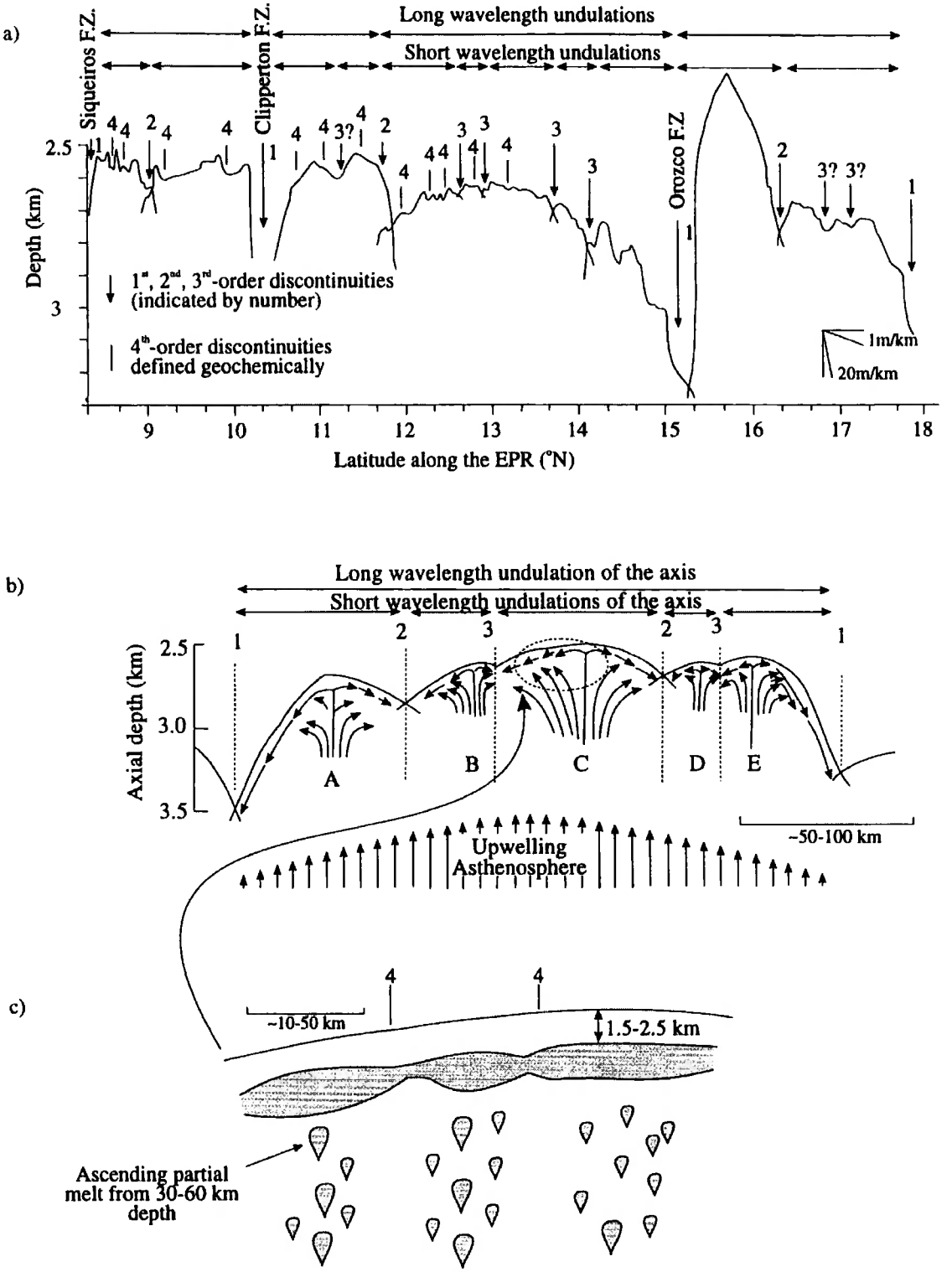

Figure 1.7: Varying scales of segmentation and its possible causes (after Navin 1996; Macdonald *et al.* 1988). (a) Along-axis bathymetry profile of the EPR, from ~9°N to 18°N, showing different degrees of segmentation. (b) Segmentation probably reflects variations in magma supply to the ridge axis, with upwelling melt focussed beneath the centre of first to third order segments. (c) Fourth order segmentation may reflect small-scale melt distribution within a magma chamber.

to only a small magma chamber, the absence of an axial bulge and a notable collapse structure.

The spatial variation in magma supply along the ridge axis is thought to be related to Rayleigh-Taylor instabilities in the lower-density layer of partial melt at the base of the melt-depleted mantle (Whitehead *et al.* 1984; Schouten *et al.* 1985; Crane 1985), which result in rising diapirs of melt concentrated at regular intervals (Figs. 1.8a-f). Schouten *et al.* (1985) showed that diapir spacing is dependent on spreading rate, among other less significant factors, and that the predicted spacing explains the observed variations in segment length at different spreading rates (Fig. 1.8g). The predicted shorter spacing of upwellings at slower-spreading ridges and a number of gravity studies and models of mantle flow patterns (Phipps Morgan & Forsyth 1988; Lin *et al.* 1990; Parmentier & Phipps Morgan 1990; Lin & Phipps Morgan 1992; Sparks & Parmentier 1993; Sparks *et al.* 1993; Jha *et al.* 1994) suggests that buoyant 3-D mantle flow occurs beneath slow-spreading ridges, whereas more 2-D flow occurs beneath faster-spreading ridges. Alternatively, the apparent difference in segmentation between fast- and slow-spreading ridges could be due to the higher thermal regime beneath faster-spreading ridges facilitating the along-axis redistribution of melt in the crust. This redistribution of crustal material gives the appearance of sheet-like mantle flow at fast-spreading ridges although 3-D mantle flow occurs at all spreading rates (Bell & Buck 1992; Wang & Cochran 1993; Stewart *et al.* 2002).

Gravity studies (Kuo & Forsyth 1988; Lin & Phipps Morgan 1992; Tolstoy *et al.* 1993; Cormier *et al.* 1995) have revealed mantle Bouguer anomaly (MBA) lows over segment centres at various ridges (Fig. 1.9). MBA variations are usually interpreted to reflect variations in crustal thickness and/or density (see Chapter 4). MBA lows, thus, indicate the presence of thicker and/or lower density crust beneath segment centres, suggesting that upper mantle upwelling is focussed. The decrease in MBA magnitude with increasing spreading rate suggests that 3-D mantle upwelling is more pronounced beneath slow-spreading ridges than at faster-spreading ridges. This, in turn, results in greater along-axis variation in crustal structure at slow-spreading ridges (Fig. 1.10).

The 3-D nature of crustal accretion is now well established and recent studies (Briais & Rabinowicz 2002; Stewart *et al.* 2002) are starting to reveal the 4-D nature of crustal accretion, describing how crustal production varies with time through the interplay of tectonic and magmatic forces.

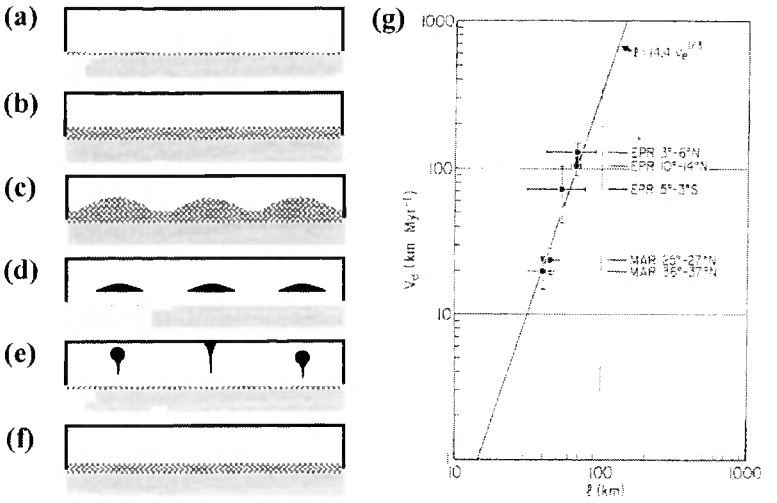

Figure 1.8: Possible mechanism for the observed segmentation of mid-ocean ridges. (a)-(c) Partial melt (stippled area) begins to collect in a region at the top of the undepleted mantle (light grey shading) in the asthenosphere. (d)-(e) As the volume of this region grows, a gravitational instability develops with regularly spaced disturbances rising diapirically (black areas). (f) Once the partially molten region is depleted of melt the process repeats itself, as more melt becomes available. (g) A model of upwelling spacing (l) dependence on spreading rate (v_e) appears to explain the spacing of segment centres from various ridges, inferred from bathymetry data. After Schouten *et al.* (1985).

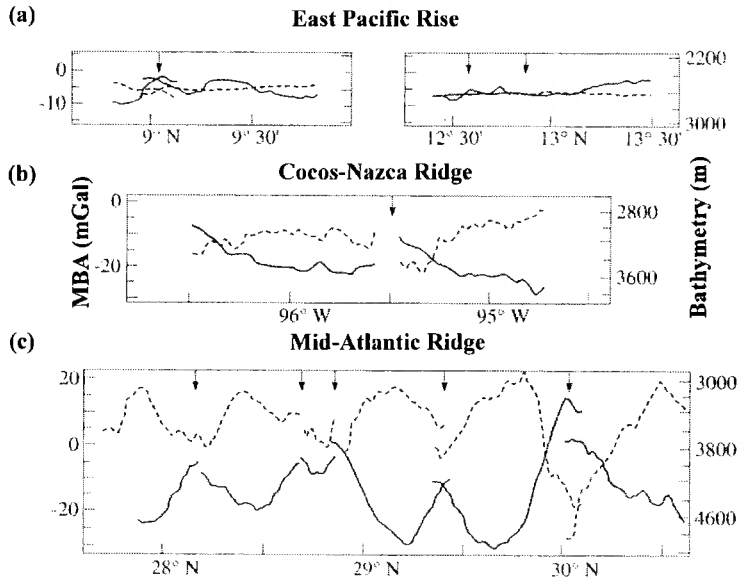

Figure 1.9: Along-axis profiles of seafloor depth (dashed lines) and MBA (solid lines) for fast-, intermediate- and slow-spreading ridge segments. (a) The fast-spreading East Pacific Rise is characterised by subdued along-axis variations in seafloor depth and MBA. (b) At intermediate-spreading ridges, e.g. the Cocos-Nazca Ridge, variations in both seafloor depth and MBA become more pronounced with relative MBA lows associated with elevated areas of the ridge. (c) The correlation between bathymetry highs and MBA lows is more pronounced at the slow-spreading Mid-Atlantic Ridge. Variations in MBA primarily reflect variations in crustal thickness and/or density, although mantle density variations may contribute to the anomalies. Note, arrows indicate the location of first to second order discontinuities and the zero level for the MBA is arbitrary (after Lin & Phipps Morgan 1992).

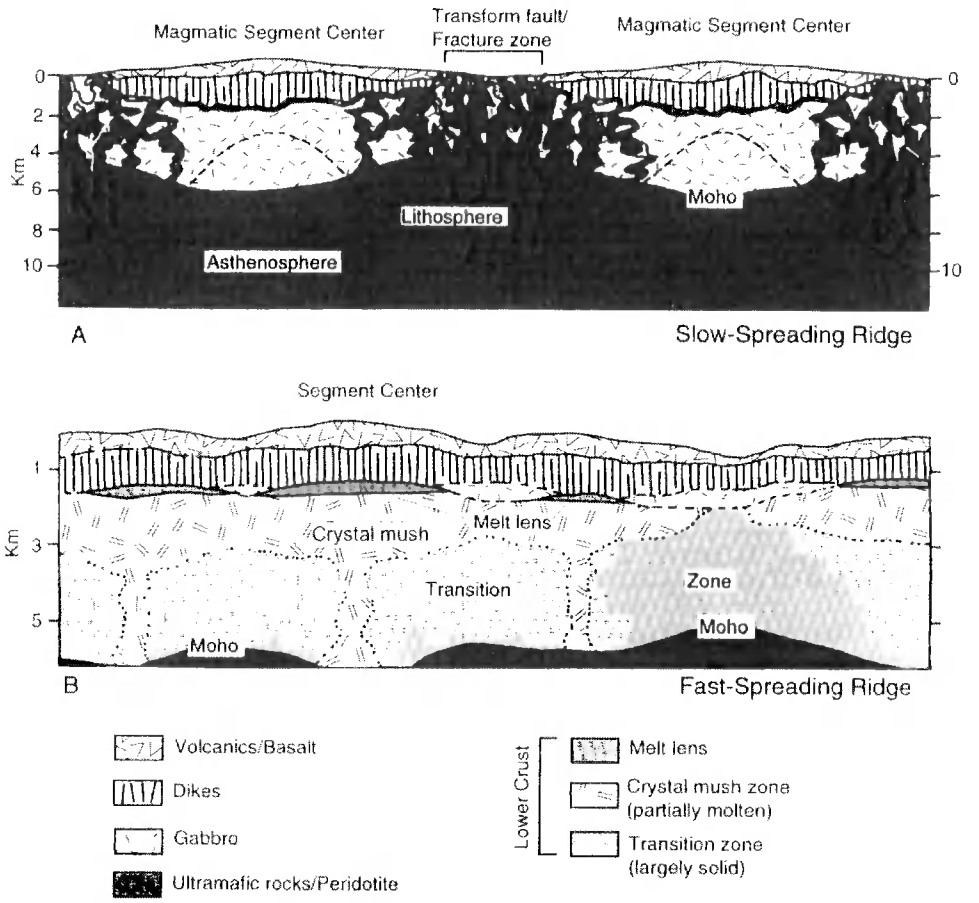

Figure 1.10: Along-axis models illustrating the differences in internal structure, stratigraphy and crustal thickness between slow- and fast-spreading ridges. (a) Segment centres of slow-spreading ridges are generally magma-rich and thick, whereas discontinuities are magma-poor, thin and faulted. Dashed line shows the boundary between the lithosphere and the asthenosphere. (b) Fast-spreading ridges show less along-axis variation in crustal thickness and structure (from Dilek *et al.* 1998, modified from Cannat *et al.* 1995 and Sinton & Detrick 1992).

1.4 Episodicity of crustal accretion

Segmentation studies of mid-ocean ridges have revealed a fundamental difference between crustal accretion at slow- and fast-spreading ridges. A basic division between a temporally variable accretionary pattern at slow-spreading ridges with cycles of magmatic injection and amagmatic, or tectonic, extension, and an essentially steady-state magma supply sustaining crustal accretion at fast-spreading ridges is inferred.

The episodicity of crustal accretion at slow-spreading rates has been highlighted by the most comprehensive multidisciplinary study of a magma chamber at a slow-spreading ridge to date (Navin *et al.* 1998; Sinha *et al.* 1997; Sinha *et al.* 1998; MacGregor *et al.* 1998; Heinson *et al.* 2000). The RAMESSES (Reykjanes Axial Melt

Experiment: Structural Synthesis from Electromagnetics and Seismics) experiment provided evidence from the combined interpretation of wide-angle seismic, normal incidence seismic, gravity, controlled source electromagnetic (CSEM) and magnetotelluric (MT) data for the existence of a magma chamber beneath an AVR at 57°45'N on the Reykjanes Ridge. A synthesis of the RAMESSES work is presented in Fig. 1.11. The conclusions drawn from the modelling and interpretation of all datasets are for the existence beneath the AVR of an ~18 km wide, low-velocity zone extending almost down to the Moho and for an ~4 km narrow, low-velocity ribbon extending down for ~100 m between layers 2B and 3. The magma chamber, thus, consists of a low-velocity zone and ribbon, interpreted as a region of sub-axis partial melt and a melt lens respectively.

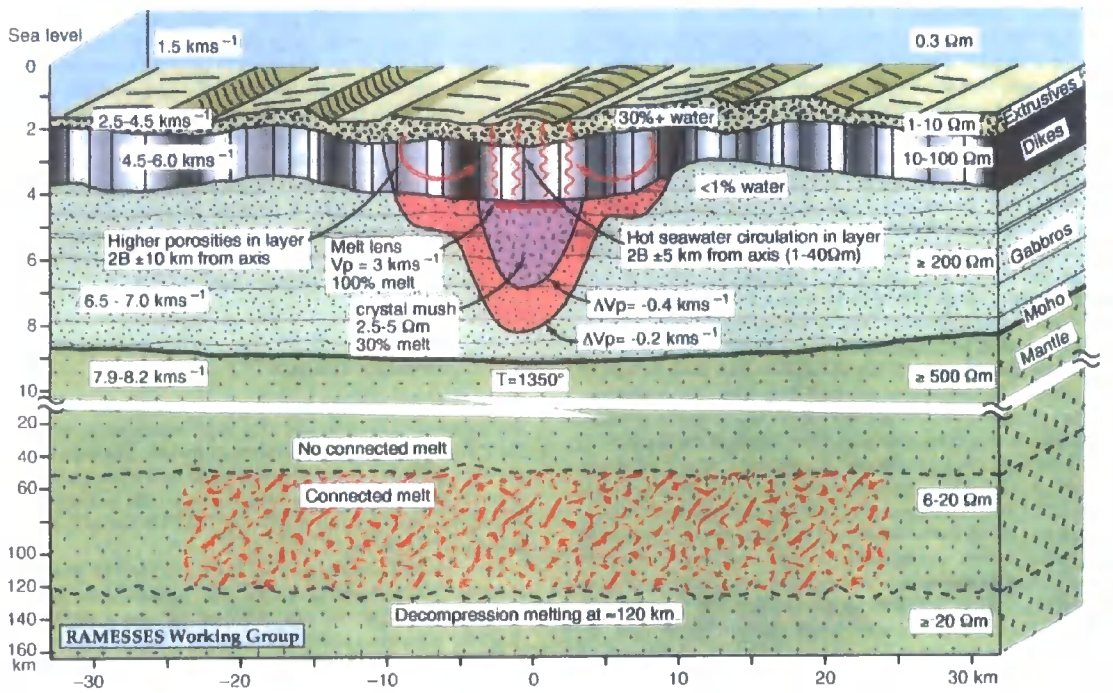

Figure 1.11: Cross-sectional model of the 57°45'N AVR based on a synthesis of the modelling and interpretation of RAMESSES (Reykjanes Axial Melt Experiment: Structural Synthesis from Electromagnetics and Seismics) datasets. The analyses of seismic, gravity, electromagnetic and magnetotelluric data suggest that a magma chamber underlies the 57°45'N AVR and that a zone of partial melt extends from ~50-100 km depth in the upper mantle. The position of seismic layer boundaries and estimates of velocity, electrical resistivity, porosity, melt content and temperature are based on the collected datasets and modelling. Note that a break in scale occurs a depth of 10 km beneath sea level. From Sinha *et al.* (1998).

To fit the CSEM data the resistivity model requires a low-resistivity region in the mid-crust, implying the presence of 20-40% partial melt (MacGregor *et al.* 1998) and,

thus, supporting the magma chamber model developed from the seismic and gravity data (Navin *et al.* 1998). The amount of partial melt in the mid-crust equates to ~20000 years worth of crustal accretion assuming that the spreading rate has remained constant. However, thermodynamic considerations suggest that this melt would cool to sub-solidus temperatures within ~1500 years (MacGregor *et al.* 1998). This fast cooling rate, therefore, implies that crustal accretion at slow-spreading rates is a cyclic process with periodic influxes of melt from the mantle to the crust. In addition, the lower resolution MT data show that the upper mantle, down to a depth of ~50 km beneath sea level, is highly resistive. However, beneath this region down to a depth below sea level of ~100 km, the upper mantle is characterised by a low resistivity, indicating the presence of partial melt.

The inferred presence of partial melt in the upper mantle at ~50-100 km depth below sea level has implications for the delivery of melt from the mantle to the crust (Sinha *et al.* 1998). The low-resistivity zone in the upper mantle may be where adiabatic decompression melting forms a layer of partial melt, with episodic influx of melt to the crust occurring either through conduits invisible to the MT method or through pervasive flow. Alternatively, the region between the crust and the layer of partial melt in the upper mantle could itself be the source of melt, with a recent flux of melt from this region to the crust explaining the high resistivities, indicative of a depleted mantle, observed here. In both cases, the absence of a clear conduit or connection between the melt in the mid-crust and the melt in the upper mantle suggests that it is the supply of melt from the mantle that is episodic and leads to cycles of crustal accretion. A recent study of the RAMESSES area (Peirce & Navin 2002), shows that a melt-free model for the top ~50 km of the mantle beneath the 57°45'N AVR is consistent with the gravity data. In addition, an along-axis gravity anomaly is observed suggesting that mantle upwelling follows the ridge trend, with episodic, diapiric magma influxes to the crust leading to cyclic accretion and the formation of AVRs (Peirce & Navin 2002).

The magma chamber model of the RAMESSES Working Group (Sinha *et al.* 1998) is similar, in terms of geometry and properties, to magma chambers imaged at faster-spreading ridges. This suggests that crustal accretion is similar at all spreading ridges with the temporal variability in melt transport from the upper mantle to the crust being the controlling factor in the differences between the crustal structure of slow- and fast-spreading ridges. The thermal considerations discussed above, together with evidence for the absence of magma bodies elsewhere along the ridge, indicate that crustal

accretion at the Reykjanes Ridge is an episodic process, with repeated influx of melt from the mantle required to generate the crust. Sidescan sonar studies (Parson *et al.* 1993) of the along-axis variation in morphology of AVRs suggests that AVRs undergo a cycle of accretion and dismemberment due to the episodic focusing of magmatic and tectonic forces along the ridge axis. Thus, it appears that the cyclicity of crustal accretion is imprinted into the seafloor morphology itself. One of the main aims of this study (see Section 1.6) is to investigate the apparent relationship between the seafloor expression of tectonomagmatic cycles, the underlying crustal structure and the melt supply and accumulation process.

The temporal dimension of crustal accretion is poorly understood, with recent studies (e.g. Stewart *et al.* 2002) suggesting that temporal variability in melt transport is a significant process even at fast-spreading ridges. Tectonomagmatic cycles may, therefore, reflect a fundamental process in crustal accretion that operates at all spreading rates.

The extensive and comprehensive datasets that exist at the Reykjanes Ridge, with existing detailed models of crustal structure, mean that this is an ideal site to investigate temporal patterns of accretion and their manifestation in seabed morphology and crustal structure.

1.5 The Reykjanes Ridge

Before outlining the aims of this study, the contextual setting of the Reykjanes Ridge will be discussed together with a synopsis of existing datasets and the results of previous studies.

1.5.1 Setting

The Reykjanes Ridge is a 900 km section of the slow-spreading (20 mm yr^{-1}, full rate) Mid-Atlantic Ridge running from the Bight fracture zone near 57°N to the Reykjanes Peninsula on Iceland at 63°N (Fig. 1.12). Iceland itself is the result of a hotspot, or mantle plume, influence on the ridge. However, a recent seismic tomography experiment over Iceland (Foulger *et al.* 2001) suggests that the plume does not extend into the lower mantle. Henceforth, in this study, the upwelling beneath Iceland will be referred to as a hotspot, without any inference as to its geometry or vertical dimension.

The proximity of the Reykjanes Ridge to the Iceland hotspot results in the ridge-trend of 036° being oblique to the spreading direction of 096° (DeMets *et al.* 1990), a

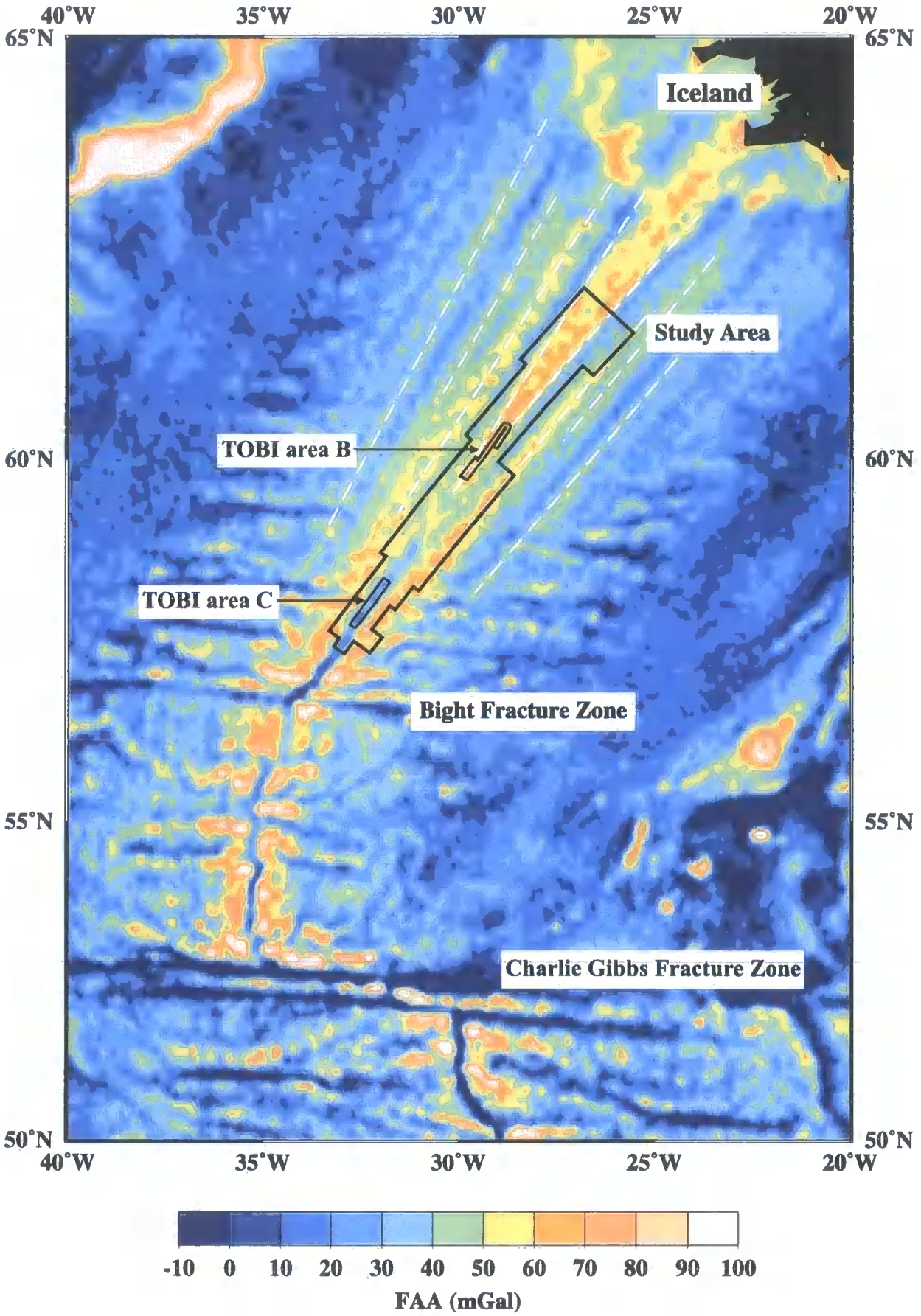

Figure 1.12: Satellite-derived free-air gravity anomaly (FAA) over the Reykjanes Ridge (Sandwell & Smith 1997). The ridge extends ~900 km from the Bight Fracture Zone to the Reykjanes Peninsula on Iceland. The black outline shows the study area and the smaller areas of TOBI data coverage. Dashed white lines show the position of the V-shaped ridges.

complete absence of transform faults, a change in axial morphology from median valley in the south to axial rise in the north, and a decreasing axial seafloor depth heading towards Iceland. Episodic increases in flux of melt and/or temperature beneath the Iceland hotspot result in pulses of thermal perturbations, with an associated increase in melting of the mantle, that propagate radially away from the hotspot (Ito 2001). Migration of the melt towards the ridge axis results in episodes of crustal thickening that give rise to the V-shaped ridges first observed by Vogt (1971) and clearly visible in Fig. 1.12.

1.5.2 Morphology and segmentation

The largest morphological feature of the Reykjanes Ridge is the shoaling of the ridge axis towards Iceland. On-axis depths decrease almost linearly from ~2500 m at 57°N to ~1000 m at 60°N and then decrease more gradually reaching ~500 m at 63°N (Fig 1.13). From 57°N to 58°50'N the ridge axis is characterised by a median valley morphology with ~700 m large topographic peak-to-trough amplitude variations. North of 58°50'N the median valley morphology gives way to an axial high with topographic variations of only ~400 m on average. The seafloor at the Reykjanes Ridge is smoother than found elsewhere on the MAR, which is characterised by topographic variations of 1000-1700 m on average (Searle & Laughton 1981; Lin & Phipps Morgan 1992).

Smaller-scale morphological features consist of 42 complete right-stepping en-echelon AVRs that occur between 57°30'N and 62°05'N which have an average separation of 11 km (Keeton *et al.* 1997). Maximum AVR heights vary along-axis (Searle *et al.* 1998) with 300-500 m high AVRs observed south of the median valley/axial high transition and smaller AVRs observed between ~59°N and 61°30'N. Larger AVRs re-appear north of 61°30'N. AVRs appear to be the most recent loci of volcanic activity on the ridge axis as they have the highest level of acoustic backscatter.

The smallest morphological features are circular seamounts that are principally observed on-axis, suggesting that they are either rapidly destroyed through faulting or buried by sediments as they move off-axis. There is no systematic increase in seamount height or abundance with latitude, although an abnormally high concentration of seamounts occurs between 59°30'N and 61°30'N (Magde & Smith 1995).

Normal faulting is predominantly ridge parallel with the distance between major faults decreasing from 13 ± 2 km near 58° (where they define the median valley) to 8 ± 2 km near 59° and then increasing again to about 14 ± 2 km up to 62°N.

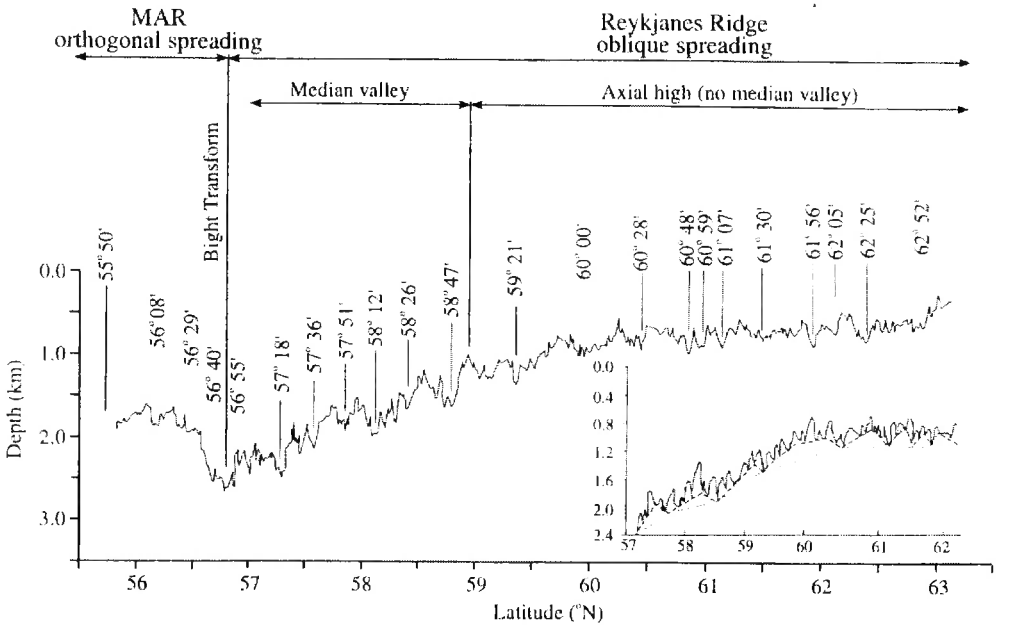

Figure 1.13: Along-axis bathymetric profile of the Reykjanes Ridge and MAR north of 55°50'N. The orthogonal spreading MAR gives way to the obliquely spreading Reykjanes Ridge at the Bight Transform. The axial seafloor depth decreases towards Iceland with 59°N marking the transition in ridge morphology from a median valley to the south to an axial high to the north. Second order discontinuities, associated with short-wavelength bathymetric deeps, are annotated (after Appelgate & Shor 1994). Inset shows the same profile with three different scales of segmentation superimposed: a long-wavelength swell towards Iceland (dotted line), intermediate-wavelength variations (dashed line) and short-wavelength variations associated with individual AVRs (solid line). From Navin (1996) after Murton & Parson (1993).

Fault throws also vary along-axis with throws of 1 km, less than 100 m and approximately 100 m observed near 58°N, 59°N and 62°N respectively (Searle *et al.* 1998). Volcanic fissures are observed on-axis and tend to be orientated normal to the spreading direction.

All of the above observations can be related to the proximity of the Iceland hotspot and its effect on the thermal structure of the Reykjanes Ridge (Searle *et al.* 1998). It is hypothesised that the lithosphere is stronger away from the hotspot and supports higher AVRs, bigger throw faults and the median valley topography. Whereas further north, as the influence of the hotspot becomes more pronounced with the elevated thermal regime supporting the axial high, the lithosphere is weaker and can only support smaller height AVRs and smaller throw faults. The V-shaped ridges intersect the ridge axis near 59°N and the high abundance of seamounts and the small throw faulting observed at this location have, therefore, been attributed to excess melt and high temperatures associated with the most recent hotspot pulse.

The influence of the Iceland hotspot on the Reykjanes Ridge was first recognized by Vogt (1971) using bathymetry data collected by Talwani *et al.* (1971). Vogt noticed symmetrical, time-transgressive, V-shaped basement ridges, elevated 300-600 m above the surrounding seafloor that intersect the ridge axis near ~59°N, implying a south-southwestward asthenospheric flow component from the hotspot of 20 cm yr^{-1}. Though the V-shaped ridges were first recognised in bathymetry data, sediment cover largely obscures their appearance and they are far more obvious in the free-air gravity field (Fig. 1.12) due to the high density contrast between the sediments and basement rocks (Jones *et al.* 2002). The flow pattern from the hotspot may consist of either circular or elliptical wave fronts, with the latter pattern deriving from preferentially channelled flow along the ridge-axis. White *et al.* (1995) suggest that, instead of melt being transported along the ridge axis, thermal pulses of up to 30°C travel along the ridge at 5-10 My intervals, increasing melting beneath the spreading axis itself, and generating crust thicker by up to ~2 km. This increase in crustal thickness provides sufficient isostatic uplift to account for the observed relief of the V-shaped ridges. Geodynamic models (Ito 2001) show that the V-shaped ridges can be formed by radial flow away from a pulsing hotspot stem and that dehydration of the upper mantle by partial melting increases the viscosity of the melting region and, in fact, inhibits preferential flow of hotspot material along the ridge axis.

Though no first order discontinuities occur along the entire length of the ridge, again possibly because of the hotspot influence (Searle *et al.* 1994a), higher order segmentation is observed. Initial studies (Murton & Parson 1993), based on incomplete bathymetric coverage of the ridge axis, identified three main trends in along-axis bathymetry (Fig 1.13). A long-wavelength swell associated with shoaling of the ridge axis towards Iceland. An intermediate-wavelength variation of 40-120 km and short-wavelength fluctuations of 5-30 km corresponding to axial depth variations associated with individual AVRs. A more detailed study (Appelgate & Shor 1994), combining acoustic imagery and bathymetry data, confirmed the broad results of the previous study and identified the intermediate-wavelength and the short-wavelength variations as second and/or third order to fourth order segmentation respectively. Appelgate & Shor (1994) defined one second and eleven third order segment boundaries structurally and bathymetrically by intermediate-wavelength axial depth maxima between 57°45'N and 62° (Fig. 1.13). The second order discontinuity near 57°50'N is characterised by a 600 m deep basin, a low magnetization and high gravity anomaly suggesting a reduced magma

supply and a thinning of the crust. Off-axis basins situated along the discontinuity flow line are also associated with gravity anomaly highs suggesting that the 57°50'N offset has existed for at least 2 My (Searle *et al.* 1994a). However, a study by Searle *et al.* (1998) only identified five segment boundaries between 57°45'N and 62°. These discontinuities, located at 57°52'N, 58°25'N, 58°50'N and 60°30'N, are characterised by small axial bathymetry and gravity anomaly highs.

1.5.3 Magnetic and gravity data

Lee & Searle (2000) inverted total magnetic field measurements between 57°N and 63°N for crustal magnetization intensity to investigate tectonic and magmatic processes over a range of length scales. They observed a long-wavelength, or regional, variation in the along-axis magnetization intensities, which they attributed to hotspot pulses. The along-axis magnetization intensities can be separated into three different regimes based on variations in magnitude. The axis south of 59°10'N has a high magnetization intensity and variability which Lee & Searle (2000) interpreted as a region unaffected by the hotspot pulse. Between 59°10'N and 60°50'N the ridge axis has the lowest average magnetization and this region is interpreted as being the position of the hotspot front. North of 60°50'N the average magnetization intensities show a slight increase suggesting that the crust is recovering from the passage of the most recent pulse. Superimposed on these regional observations are local-scale high magnetization intensity anomalies which, with a few exceptions, are associated with AVRs. Lee & Searle (2000) attribute these variations in magnetization intensity between AVRs to variations in the relative age of the extrusive layer 2A.

Searle *et al.* (1998) calculated the along-axis MBA for the whole length of the Reykjanes Ridge and interpreted the long-wavelength decrease in MBA towards Iceland as indicating crustal thickening of ~3 km. Searle *et al.* (1998) also noticed that the along-axis MBA does not show large amplitude variations as observed on the MAR.

1.5.4 Geochemistry and seismic data

The first comprehensive geophysical investigation of the Reykjanes Ridge, performed by Talwani *et al.* (1971), provided evidence from seismic refraction data for the existence of a low-velocity (< 3 km s^{-1}) layer 2A, a general off-axis increase in seismic velocities and confirmation of an unusually low-velocity upper mantle (~7.4 km s^{-1}) beneath the ridge axis that was first observed by Ewing & Ewing (1959). Since then a number of seismic refraction experiments (Bunch & Kennet 1980, Smallwood *et al.*

1995, Navin *et al.* 1998 and Weir *et al.* 2001) and geochemical analyses of samples dredged along the spreading-axis (Schilling 1973; Taylor *et al.* 1995; Murton *et al.* 2002) have helped to constrain the crustal structure of the ridge and to ascertain the extent of the hotspot influence.

Geochemical analysis of samples collected along-axis, from ~60°N to 65°N on the Reykjanes Peninsula (Schilling 1973) suggest that mixing occurs between melt derived from the deeper primordial mantle which feeds the Iceland hotspot, and melt released from the depleted low-velocity zone (DLVZ) associated with decompression melting at the ridge axis. The geochemical effect of the hotspot progressively attenuates with distance from Iceland and disappears near 61°N, 400 km from the tip of the Reykjanes Peninsula (Schilling 1973). Recently, however, Murton *et al.* (2002) proposed a more complicated mixing model than the binary model of Schilling (1973), suggesting that there are six different mantle components of melt, originating from within the deep upper and lower mantle, which are subsequently transported by hotspot outflow along the length of the ridge, with ~60°N marking the limit of direct hotspot influence. Taylor *et al.* (1995) found little geochemical variation within short-wavelength volcanic constructs, instead intermediate-wavelength bathymetry swells appear to correlate with indices indicating a greater degree of fractionation. Taylor *et al.* (1995) suggest that a longer residence time of melt in magma chambers or an increase in travel time for melt originating from the mantle and travelling through the thicker crust associated with intermediate-wavelength bathymetric swells are possible explanations for the inferred along-axis variations in fractionation

The geochemical studies discussed above provide information about the influence of the Iceland hotspot on the genesis and transport of melt from the mantle, through the crust and onto the seafloor along the ridge axis. However, the geochemical studies provide little information on how the hotspot affects the actual crustal structure of the ridge. In contrast, seismic refraction data can provide information on the effect of the hotspot proximity on crustal layering and thickness. The following sections describe a compilation (Fig. 1.14 and Table 1.2) of recent seismic refraction models of Navin *et al.* (1998), Bunch & Kennet (1980), Smallwood *et al.* (1995) and Weir *et al.* (2001) along the ridge axis at 57°45'N, 59°30'N, 61°40'N and 62°40'N respectively. This combination of different seismic experiments along the ridge axis is used to introduce the detailed crustal structure of the Reykjanes Ridge and to further illustrate the influence of the hotspot on the ridge.

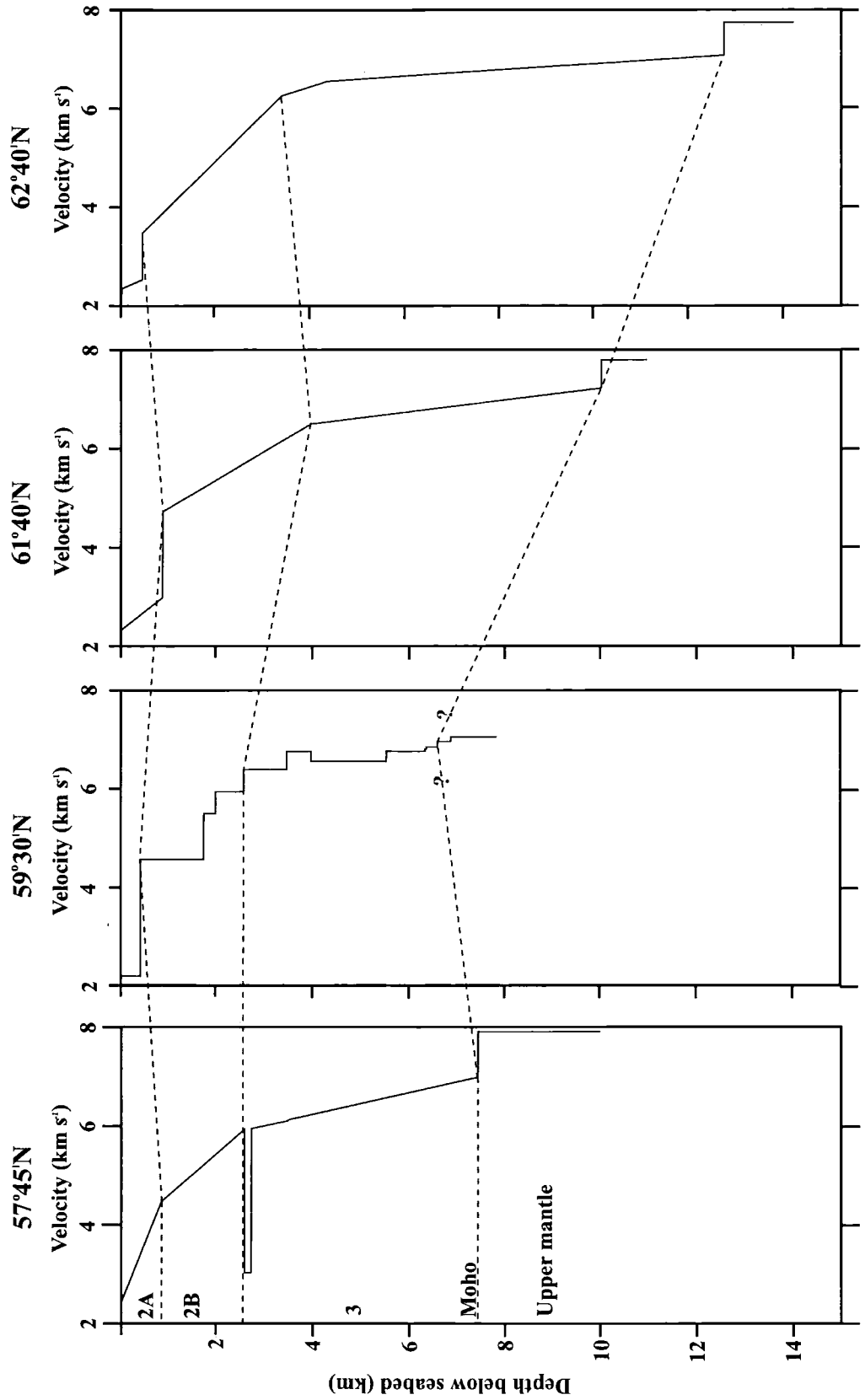

Figure 1.14: Compilation of seismic refraction models along the Reykjanes Ridge. Dashed lines show the location of layer interfaces as picked by the annotated authors and interpolated, in a long-wavelength sense, between the different models. Layer 2A thickness does not appear to vary systematically with the proximity of the plume, whereas layers 2B and 3 thicken significantly towards Iceland. Comparison of adjacent Moho depths and the more gradational change in velocity at ~7.5 km depth at 59°30'N suggest that the event picked by Bunch & Kennet (1980) at 59°30'N may not correspond to the crust/mantle interface as previously thought.

1.5.4.1 Layer 2

The layer 2A *P*-wave velocity (V_p) and thickness vary along the ridge axis, from V_p = 2.6 km s^{-1} and 0.8 km at 57°45'N to 2.2 km s^{-1} and 0.4 km at 59°30'N respectively. At 61°40'N a layer 2A velocity and thickness of 2.4 km s^{-1} and 1.0 km respectively are reported, with a slightly lower velocity of 2.5 km s^{-1} and thickness of 0.5 km, at 62°40'N. Layer 2A thickness variations do not appear to be systematic and are, therefore, probably related to the presence of AVRs with a thicker extrusive layer beneath their centres than beneath the non-transform discontinuities in between (Lee & Searle 2000 and see Section 5.3).

The layer 2B velocity appears to remain approximately constant, at 4.5-6.6 km s^{-1}, along-axis, whereas thickness increases gradually from 1.8 km at 57°45'N to 2.2 km at 59°30'N and 3.0 km at 61°40'N. At 62°40'N layer 2B is still approximately 3.0 km thick. Layer 2B, therefore, appears to increase in thickness towards Iceland more consistently than layer 2A, probably reflecting the increase in melting as the centre of the hotspot is approached. From approximately 61°40'N onwards, layer 2B thickness remains constant at ~3.0 km, possibly indicating that the layer has reached its maximum thickness with the overburden pressure exerted by the combined mass of layers 2A and B exceeding the driving pressure required for subsequent extrusions (Buck *et al.* 1997). Off-axis, layer 2A and 2B velocities generally increase with age due to pore infilling through hydrothermal circulation (Fryer *et al.* 1989; Shaw 1994; Collier & Singh 1998), whereas overall layer 2 thickness decreases, most likely through tectonic faulting of the brittle layer.

1.5.4.2 Layer 3

Layer 3 is characterised by a *P*-wave velocity of 6.5-7.2 km s^{-1}. At 57°45'N the layer is 4.8 km thick and V_p increases from 6.5 km s^{-1} at the top of the layer to 7.0 km s^{-1} at its base. An ~12 km wide low-velocity zone, with velocities reduced by 0.5 km s^{-1}, is observed beneath the midpoint of the AVR at 57°45'N (Fig 1.11), suggesting the presence of an axial magma chamber (see Section 1.4). At 59°30'N layer 3 is 4.1 km thick and V_p = 6.8-7.2 km s^{-1}. A 0.5 km thick, 6.6 km s^{-1} low-velocity zone is observed on-axis. A possible explanation for this low-velocity layer is the presence of a partially frozen magma chamber with an associated temperature anomaly of ~250°C. At 61°40'N, layer thickness reaches ~6.0 km with V_p = 6.9-7.1 km s^{-1} and, at 62°40'N, layer thickness increases to 8.1 km thick with V_p = 6.5-7.2 km s^{-1}.

1.5.4.3 Moho

In seismic terms the upper mantle is usually identified by a jump in *P*-wave velocity from ~7.0 km s^{-1} to ~8.0 km s^{-1}. Beneath a ridge axis, however, the jump in velocity is usually lower due to elevated temperatures and/or the presence of melt. At 57°45'N, an upper mantle velocity of 7.8 km s^{-1}, is reported on-axis (increasing slightly off-axis to 7.9 km s^{-1}) at a depth of ~7.5 km. The highest velocity observed on-axis at 59°30'N is 7.1 km s^{-1}, increasing to 8.2 km s^{-1} for 9 Ma crust, at a depth of 7.2 km. Bunch & Kennet (1980) recognised that this is an unusually low velocity for on-axis upper mantle and were uncertain about its origins. Comparing their velocity profile to ones at 57°45'N and 61°40'N (Fig. 1.14), it appears that they may have not recorded arrivals from the Moho and that total crustal thickness at 59°30'N is nearer 8.0 km (Searle *et al.* 1994a). At 61°40'N, the Moho, with V_p = 7.6 km s^{-1}, is imaged at 10.0 km depth on-axis and 8.4 km depth at 4 Ma. Zero-age crustal thickness increases further from 11 km at 62°40'N, V_p = 7.6 km s^{-1}, to 21 km in south-west Iceland. The crust thins to 9.8 km off-axis at 5 Ma near 63°N with an increase in *P*-wave velocity to 8.0 km s^{-1}.

	57°45'N (Navin *et al.* 1998)		**59°30'N** (Bunch & Kennet 1980)		**61°40'N** (Smallwood *et al.* 1995)		**62°40'N** (Weir *et al.* 2001)	
Layer	**V_p** (km s^{-1})	**T** (km)	**V_p** (km s^{-1})	**T** (km)	**V_p** (km s^{-1})	**T** (km)	**V_p** (km s^{-1})	**T** (km)
2A	2.6	0.8	2.2	0.4	2.4	1.0	2.5	0.5
2B	4.5-6.6	1.8	4.6-6.5	2.2	4.8-6.5	3.0	3.5-6.3	3.0
3	6.5-7.0	4.8	6.8-7.2	4.1	6.9-7.1	6.0	6.5-7.2	8.1
UM*	7.8	7.5*	7.1	7.2*	7.6	10.0*	7.6	11.0*

Table 1.2: Compilation of zero-age *P*-wave velocities (**V_p**) and layer thicknesses (**T**) for oceanic crustal layers 2A, 2B, 3 and upper mantle (**UM**) at locations along the ridge axis as annotated. Velocity ranges, where quoted, indicate on-axis velocities from the top to the base of the layer. *Note: values in the **T** columns, with superscript asterix, indicate total crustal thickness.

1.5.4.4 Summary of seismic data compilation

Layer 2A thickness does not vary systematically along-axis towards Iceland, instead thickness variations appear to be correlated with the position of AVRs, with an increase in thickness beneath AVR midpoints. In contrast, layer 2B and 3 thickness increases significantly towards Iceland reaching a maximum thickness of 3.0 km at 61°40'N and 8.1 km at 62°40'N respectively. Layer 2A, 2B and 3 velocities do not vary

systematically towards Iceland suggesting that there are no significant along-axis crustal density variations, though upper mantle density variations probably exist (see Section 5.2.2 and Weir *et al.* 2001). Most of the excess melt generated by the high temperatures associated with the proximity of the hotspot, therefore, appears to go into building layer 3 and 2B, as evidenced by the along-axis increase in total crustal thickness towards Iceland from 7.5 km at 57°45'N to 11.0 km at 62°40'N. Layer 2A thickness appears to be decoupled from layer 2B and 3 thickness. A possible explanation for this observation is that magmatic activity at the Reykjanes Ridge is slow and episodic enough for melt to freeze in layers 2B and 3 before it has time to significantly increase the thickness of layer 2A by eruption. In fact, thermal calculations suggest that melt in the mid-crust associated with the 57°45'N AVR (see Section 1.4) would freeze within 1500 years without replenishment from the mantle. As this timescale is at least a factor of magnitude smaller than the estimated lifetime of an AVR (Sinha *et al.* 1998) it appears that de-coupling of layer 2A from layers 2B and 3 might indeed occur. In addition, analyses of along-axis seamount characteristics (Magde & Smith 1995, Smith *et al.* 1995) show no systematic variation with latitude of seamount height or abundance. This observation also supports the hypothesis that the thickness of layer 2A and, therefore, the seafloor morphology is not directly related to the amount of available melt beneath the Reykjanes Ridge.

1.6 Aims of this study

The Reykjanes Ridge is an ideal site to investigate the relationship between segmentation and tectonomagmatic processes as oblique spreading results in two different trends in seabed features. Tectonic features are generally oriented parallel to the ridge axis, whereas magmatic features are aligned normal to the plate-spreading direction.

Previous work on the Reykjanes Ridge (see Section 1.5) has revealed three main scales of observations. All of the long-wavelength observations (decreasing axial depth, change in axial morphology, increasing crustal thickness and geochemical anomalies towards Iceland) can be attributed to the thermal effect of the Iceland hotspot, whereas intermediate-wavelength observations (V-shaped ridges, abundance of seamounts and magnetization intensity variations) are linked to pulsing of the hotspot. Short-wavelength observations (layer 2A thickness variation, short-wavelength magnetization intensity variation) are related to the position of individual AVRs. It is these short-

wavelength features, their interrelationships and possible link to segmentation that are poorly understood and which are investigated in detail in this study. Studies (Parson *et al.* 1993; Lee & Searle 2000) mainly based on seafloor morphology variations suggest that AVRs follow an evolutionary lifecycle, although the evidence presented for this is currently inconclusive.

Thus, the underlying hypothesis that this thesis aims to test is that crustal structure is intimately related to tectonomagmatic cycles through temporal variations in melt supply. Under this hypothesis, AVRs in the early stage of their magmatic phase should differ in their crustal thickness and/or density when compared to AVRs undergoing tectonic extension, or to ones at the very beginning of their lifecycle. Therefore there should, theoretically, be a direct correlation between crustal structure and an AVR's lifecycle stage. The purpose of this study is, thus, to provide further evidence for the theory of tectonomagmatic cycles by correlating AVR-associated variation in seabed morphology with crustal structure derived from gravity modelling in both 2- and 3-D. In addition, magnetic data will be used to help constrain temporal variations in crustal accretion and to make spreading rate determinations. Evidence for tectonomagmatic cycles will also be incorporated into the overall pattern of segmentation at the Reykjanes Ridge and compared to evidence for the temporal variability of crustal accretion at other ridges to develop a model of the cyclicity of crustal accretion that is relevant for all spreading rates.

1.7 Structure of thesis

This thesis is divided into chapters which outline the various stages and datasets required to test the above hypothesis. The bathymetry, sidescan sonar, gravity and magnetic data acquisition, processing and compilation are discussed in Chapter 2. Sidescan sonar images are interpreted in Chapter 3 to age, in a relative sense, AVRs according to the tectonomagmatic ageing scheme developed by Parson *et al.* (1993). In Chapter 3, gravity data are used, together with bathymetry data, to calculate the MBA. Thermal corrections are applied to remove the effect of passive upwelling at the ridge axis. Long-wavelength features are analysed for hotspot-associated effects and short-wavelength features, associated with individual AVRs, are investigated by modelling along-AVR-axis gravity profiles. These models are used to test the hypothesis of a link between stage in the tectonomagmatic cycle and broad-scale crustal structure of an AVR. The magnetic data are inverted in 3-D in Chapter 5 and the resultant

magnetization intensity map is used to test the relative age interpretations of Chapter 3. In addition, local spreading rates are calculated for selected AVRs to investigate any possible spreading rate variation associated with tectonomagmatic cycles. Chapter 6 integrates all of the observations and results of modelling the different datasets into long- and short-wavelength models of crustal accretion at the Reykjanes Ridge, outlining the temporal dependence of accretionary processes and the relationship of segmentation to the pattern of mantle upwelling at slow-spreading rates. These models are then compared to recent work on segmentation at other ridges and the importance of the temporal variability of crustal accretion at all spreading rates is discussed.

Chapter 2

Data acquisition, processing and compilation

2.1 Introduction

This chapter contains a description of the acquisition, processing and compilation of the bathymetry, gravity and magnetic data acquired during four different surveys of the Reykjanes Ridge (R/V Maurice Ewing EW9008/90, RRS Charles Darwin CD81/93, RRS Charles Darwin CD87/94 and RRS Discovery D235c/98 – syntax: cruise number/year) and of Towed Ocean-Bottom Instrument (TOBI) sidescan sonar data collected solely during EW9008/90, all of which form the basis of this study. The ship tracks of the aforementioned cruises are shown in Fig. 2.1(a).

Data acquisition details for all four cruises are presented in Section 2.2 and the compilation of the bathymetry data is discussed in Section 2.3. Section 2.4 describes the principles of TOBI acquisition, and the compilation and error analyses of the gravity and magnetic data are discussed in Sections 2.5 and 2.6 respectively.

2.2 Data acquisition cruises to the Reykjanes Ridge

The R/V Maurice Ewing cruise EW9008/90 (Parson *et al.* 1993), that took place between the 29th September and 26th October 1990, collected multibeam bathymetry data with a Krupp-Atlas Hydrosweep Centre Beam echo-sounder, gravity data with a Bell Aerospace BGM-3 gravimeter at one second intervals and total magnetic field data with a Varian V75 proton precession magnetometer every twenty seconds. Navigation relied primarily on the Global Positioning System (GPS), with ship positions recorded every twenty seconds and averaged over one minute intervals. Gravity and magnetic data were merged with the one minute averaged navigation data resulting, at an average ten knot ship's speed, in a 300 m along-track separation between readings. The free-air anomaly (FAA), including Eötvös correction, was calculated onboard using equation 2.1:

$$g_{faa} = g_{obs} - g_{\Phi} - g_{Eötv} \qquad (2.1)$$

where, g_{faa} is the free-air anomaly obtained by subtracting the predicted value of gravity at sea level, g_{Φ}, based on the Geodetic Reference System 1980 (GRS80) and the Eötvös

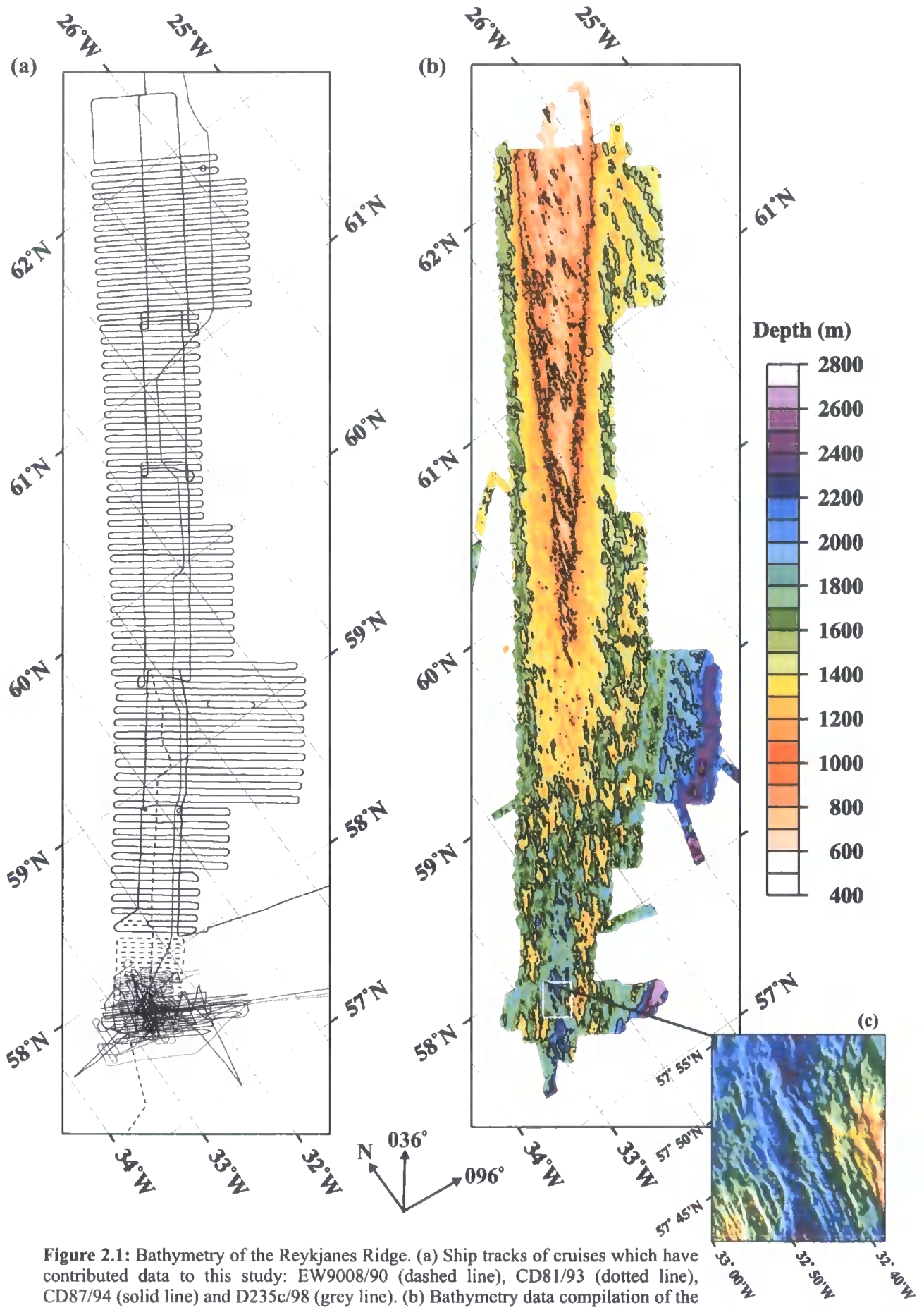

Figure 2.1: Bathymetry of the Reykjanes Ridge. (a) Ship tracks of cruises which have contributed data to this study: EW9008/90 (dashed line), CD81/93 (dotted line), CD87/94 (solid line) and D235c/98 (grey line). (b) Bathymetry data compilation of the study area with contours plotted at 500 m intervals. (c) A typical AVR, centred on 57°45'N, ~35 km in length with an elevation of ~400 m relative to the surrounding seafloor. Note: arrows indicating the average ridge trend of 036° and the spreading direction of 096° relative to north are shown at the bottom of the plot.

correction, $g_{Eötv}$, from the observed gravity, g_{obs}. The Eötvös correction removes the gravitational effect of a moving observation platform, in this case a ship, on a rotating Earth and was calculated using equation 2.2:

$$g_{Eötv} = 14.585v \cos\theta \sin\alpha + 0.01569v^2 \qquad (2.2)$$

where $g_{Eötv}$ is in mGal, and v, θ, and α are the ship's speed in ms^{-1}, heading and latitude respectively (Dehlinger 1978). See Section 2.5 for further details.

Total field magnetic measurements were reduced to the 1985 International Geomagnetic Reference field (IGRF). The IGRF is a spherical harmonic model of the Earth's main internal magnetic field with time varying coefficients to account for secular variation. Model coefficients are obtained from geomagnetic measurements from observatories, ships, aircrafts and satellites. For cruise EW9008/90 the reduced data were thus extrapolated to September 1990.

From the 3rd October to the 1st November 1993 and from the 16th June to the 20th July 1994 respectively the RRS Charles Darwin CD81/93 (Sinha *et al.* 1994) and CD87/94 (Searle *et al.* 1994b) cruises collected multibeam bathymetry data with a Simrad EM12-S echo-sounder, gravity data with a LaCoste-Romberg gravimeter and magnetic data with a Varian proton precession magnetometer. Gravity and magnetic readings were taken every thirty seconds during cruise CD81/93 and every ten seconds during cruise CD87/94. For both cruises initial measurements were averaged to produce "observations" every one minute, equivalent to a ~300 m along-track spacing. Gravity data were reduced to FAA as outlined above and total field magnetic measurements were reduced to magnetic anomalies using the IGRF90 model extrapolated to 1993 for cruise CD81/93 and 1994 for cruise CD87/94.

During RRS Discovery D235c/98 (Peirce & Sinha 1998), from the 15th July to the 4th August 1998, gravity and magnetic data were acquired every ten seconds (~25 m spacing) using a LaCoste-Romberg gravimeter and a Varian proton precession magnetometer respectively. Gravity data were reduced to FAA and total field magnetic measurements to magnetic anomalies with the IGRF95 extrapolated to 1998. No multibeam data were acquired. However, an echo-sounder was used to measure the seafloor depth along each ship track.

2.3 Bathymetry data compilation

For this study bathymetry data from D235c/98 were added to the compilation of Keeton *et al.* (1997), that comprises data from cruises EW9008/90, CD81/93 and CD87/94, and the whole dataset re-gridded with a sampling interval of 0.002° in longitude by 0.001° in latitude (approximately equal to a 100 m by 100 m node interval at the centre of the study area). Almost complete coverage (99.9%) of the Reykjanes Ridge is achieved from 57°30'N to 62°05'N, extending off-axis to between 30 and 100 km (3 – 10 Ma).

The resulting combined bathymetry grid is shown in Fig. 2.1(b). The overall ridge trend of 036°, with a 5° change in trend evident near 58°50'N (Fleischer 1974), is oblique to the 096° spreading direction. The axial depth decreases almost linearly from ~2000 m at 57°30'N to ~800 m at 60°30'N where it remains effectively constant to 62°N. The morphology of the ridge also varies along-axis with median valley topography, characteristic of slow-spreading ridges, prevalent from its southern end to 58°50'N and an axial rise, more characteristic of intermediate- and faster-spreading ridges, extending further north. These various changes in ridge characteristics are thought to relate to the influence of the nearby Iceland hotspot, with 58°50'N regarded as marking the maximum southerly extent of hotspot-ridge interaction. There are no transform offsets along the entire length of the ridge. However, high-order segmentation is particularly clear, with overlapping, right-stepping, en-echelon AVRs accommodating the oblique spreading of the ridge. AVRs, composed of ridges, flows and seamounts 0.5 km to 3.0 km in diameter (Murton & Parson 1993; Parson *et al.* 1993; Appelgate & Shor 1994; Magde & Smith 1995) are offset from each other by 11 km on average and overlap by up to 50% of their length (Searle *et al.* 1998). AVRs (e.g. Fig. 2.1c), on average, extend 10 km to 40 km in length, are 1.5 km to 4.5 km wide and display 200 m to 400 m of vertical relief above the surrounding seafloor (Keeton *et al.* 1997).

The bathymetry data compilation described above is used in Chapter 3 to help delineate AVRs in the interpretation of the TOBI data. In addition, the bathymetry data are required to remove the topographic effects of the ridge in the modelling of the gravity and magnetic data in Chapter 4 and 5 respectively.

2.4 TOBI data

TOBI is a deep-towed sidescan sonar vehicle developed by the Institute of Oceanographic Sciences (Rouse 1991, Flewellen *et al.* 1993) and presently operated out

of the Southampton Oceanography Centre. Seafloor pseudo-morphology images were acquired and processed throughout EW9008/90 over two areas, B and C, extending from 59°44'N to 60°28'N, 28°40'W to 29°59'W and 57°45'N to 58°27'N, 31°46'N to 32°23'W respectively (see Fig 1.12). Operational difficulties prevented data from being acquired over a third area, A, at the northern end of the ridge.

Sidescan sonar systems emit acoustic pulses that are reflected off the seafloor and subsequently recorded by sensors mounted on the tow vehicle. This backscatter is analysed and carefully processed to produce "acoustic photographs" of the seafloor, highlighting changes in seafloor texture. The resolution of these images is enhanced by towing the instrument close to the seafloor at a constant altitude (~400 m). Fig. 2.2 shows the construction of the TOBI vehicle, which is 4.25 m long, 1.1 m wide and 1.45 m high and is ballasted with syntactic foam for neutral buoyancy at operational depth (Le Bas *et al.* 1995). Two 3.0 m long and 0.12 m wide sidescan transducer arrays, operating at slightly different frequencies around 30 kHz to avoid cross-talk, are mounted on either side of the instrument. A 200 m long, neutrally buoyant cable connects the TOBI vehicle to a 600 kg depressor fish that, in turn, is connected to the main towing cable. A cable ~1.5 times the water depth in length is required for towing, with the depressor also ensuring that the TOBI vehicle is decoupled from sudden movements of the ship propagated through the tow cable. The array size and the 2.8 ms pulse length produce a 4 m along-track by 7 m across-track acoustic footprint at near-range, and approximately 40 m along-track by 2 m across-track at far-range. Data collected by TOBI is reduced to a manageable size for processing by averaging 8 across-track samples into 1 sample. A time varying gain is then applied to compensate for attenuation in signal strength with distance from the tow vehicle, together with a slant-range correction that converts the slant return of the acoustic signal to the horizontal distance from the instrument. High-frequency noise is filtered out using a median filter and data "dropouts", from which no reflected data was recorded most likely due to acquisition problems, are replaced by interpolated values. The final step in the processing sequence is to reduce the data range for grey-scale display purposes to 8 bits via simple division or logarithmic condensing and to assign geographic coordinates to the TOBI image prior to display. The reader is referred to Le Bas *et al.* (1995) and Blondel & Murton (1997) for examples of how TOBI data is processed. The TOBI data interpreted in this dissertation was processed during EW9008/90 by the scientific team (Parson 1993).

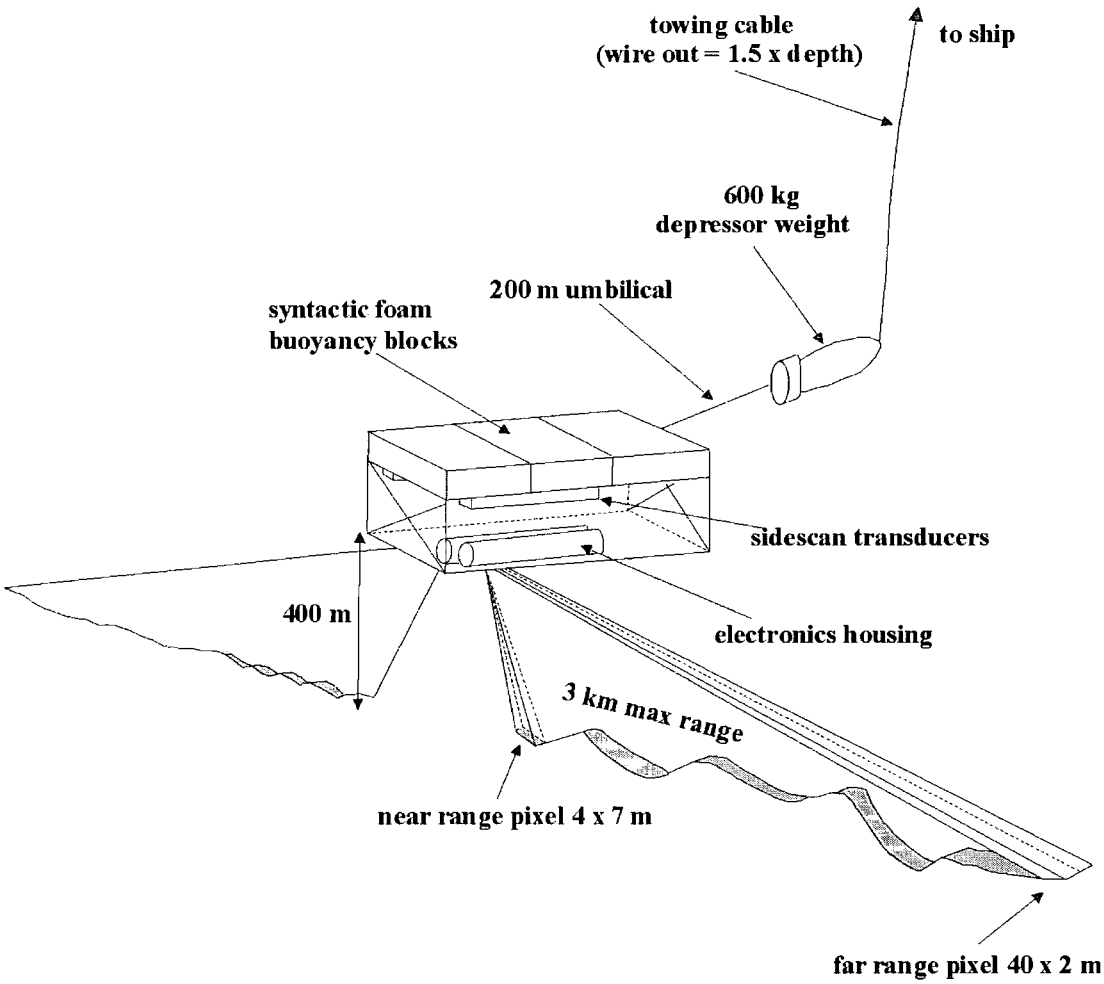

Figure 2.2: Schematic representation of the principal components and characteristics of the Towed Ocean Bottom Instrument (TOBI), adapted from Flewellen *et al.* (1993). See text for details.

The TOBI images described above are interpreted, in conjunction with the bathymetry data compilation (Section 2.3), to provide relative age constraints on the AVRs in TOBI areas B and C (see Chapter 3).

2.5 Gravity data

Gravity data may be acquired and modelled to investigate the three-dimensional (3-D) structure of the crust. However, before modelling to investigate the contribution to the observed anomalies of density and thickness variations within the crust (see Chapter 4), errors in the data itself must be quantified and reduced if possible. For this study FAA values from each cruise were first extracted from MGD-77 format 8 mm underway data tapes. Data acquired whilst turning were removed from the dataset as the rapid changes in ship's heading during turns can give rise to spurious readings due to the sensitivity of the gravimeter beam to centripetal forces.

A cross-over error analysis for each cruise was then performed separately to estimate the accuracy of the gravity measurements and attempts were made to minimise errors. A cross-over error (Fig. 2.3) is defined as the difference in the observed value of the gravity field, in this case the FAA field, at ship track intersections and is due to a combination of instrumental, navigational and systematic errors (Wessel & Watts 1988). Errors associated with the mechanical construction of the instrument include: cross-coupling and off-levelling errors, where the horizontal acceleration of the ship exerts a torque on the beam of the gravity meter when it is not quite level, and "tares" and non-linear drift, which are sudden offsets in readings due to mechanical problems with the meter itself. These errors are corrected automatically onboard by instrument-based software. Navigational errors result in an incorrect Eötvös correction, and uncertainties in positioning of the readings. Incorrect tie-ins to the base station and the use of different reference fields lead to systematic errors and DC shifts. The Generic Mapping Tools (GMT) supplementary package *x2sys_cross* (Wessel & Smith 1995) was used for the cross-over error analysis. *x2sys_cross* determines all intersections between tracks and outputs the time, position, discrepancies in FAA (linearly interpolated), the mean value of the FAA, heading along each track and the distance along-track at the cross-over point. Sections 2.5.1 to 2.5.4 describe the errors in the gravity field observations for each cruise and the approach adopted to achieve minimisation. The error for the combined data is quantified in Section 2.5.5 and a summary of the gravity data processing, modelling and gridding is presented in Section 2.5.6.

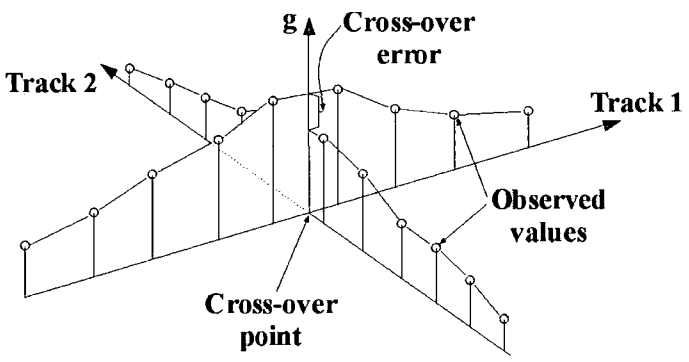

Figure 2.3: Cross-over error associated with two intersecting ship tracks. A cross-over error is calculated by subtracting the observed value (linearly interpolated between two points either side of the exact cross-over position) of Track 2 from that of Track 1 at the cross-over point (after Wessel & Watts 1988).

2.5.1 EW9008/90 cross-over errors

As a post-cruise gravity tie-in was not performed for EW9008/90, an estimate of the drift of the gravimeter was calculated using the pre-cruise tie-in in Bergen on the 24th September 1990 and the tie-in previous to that, performed on the 23rd August 1990. The estimated drift rate for EW9008/90 was, thus, taken to be 0.18 mGal day^{-1} (EW9008/90 – Lamont data reduction cruise summary). A plot of cross-over error against time (Fig. 2.4a) suggests a drift rate of approximately -1 mGal day^{-1} during the cruise period. However, this drift calculation is based on a linear trend through only 45 points. Wessel & Watts (1988) showed that more than approximately one hundred cross-over errors are required to accurately determine drift rates and consequently no drift correction was made to the EW9008/90 data since the most reliable estimate of systematic drift of 0.18 mGal day^{-1} is too small to be worth correcting for given the magnitude of the overall average individual data value error derived from the cross-over error analysis itself. Fig 2.4(b) shows the profiles from EW9008/90, with cross-over errors superimposed, that fill the gap in coverage between the CD87/94 and CD81/93 datasets. The root-mean-square (r.m.s.) of the cross-over errors is 0.2 mGal (Fig. 2.4c).

2.5.2 CD81/93 cross-over errors

No gravity tie-in information was available for CD81/93. Thus, an estimate of instrument drift was obtained by calculating the linear trend in cross-over error with time (Fig 2.5a), which shows negligible drift (-0.02 mGal day^{-1}) over the survey period. Careful inspection of the gravity data on a profile-by-profile basis showed that the source of the unusually large cross-over errors (Fig 2.5a) was outlier points on a number of short profiles, possibly due to the gravimeter beam still being unstable following a turn. Short profiles with large cross-over errors were, thus, classified as unreliable and were manually removed from the dataset reducing the r.m.s. cross-over error of 1.2 mGal to 0.5 mGal (Fig. 2.5c).

2.5.3 D235c/98 cross-over errors

A -0.06 mGal day^{-1} drift of the Lacoste-Romberg gravimeter was observed from a plot of cross-over errors against time (Fig. 2.6a) and the r.m.s. cross-over error was calculated to be 0.2 mGal (Fig. 2.6c).

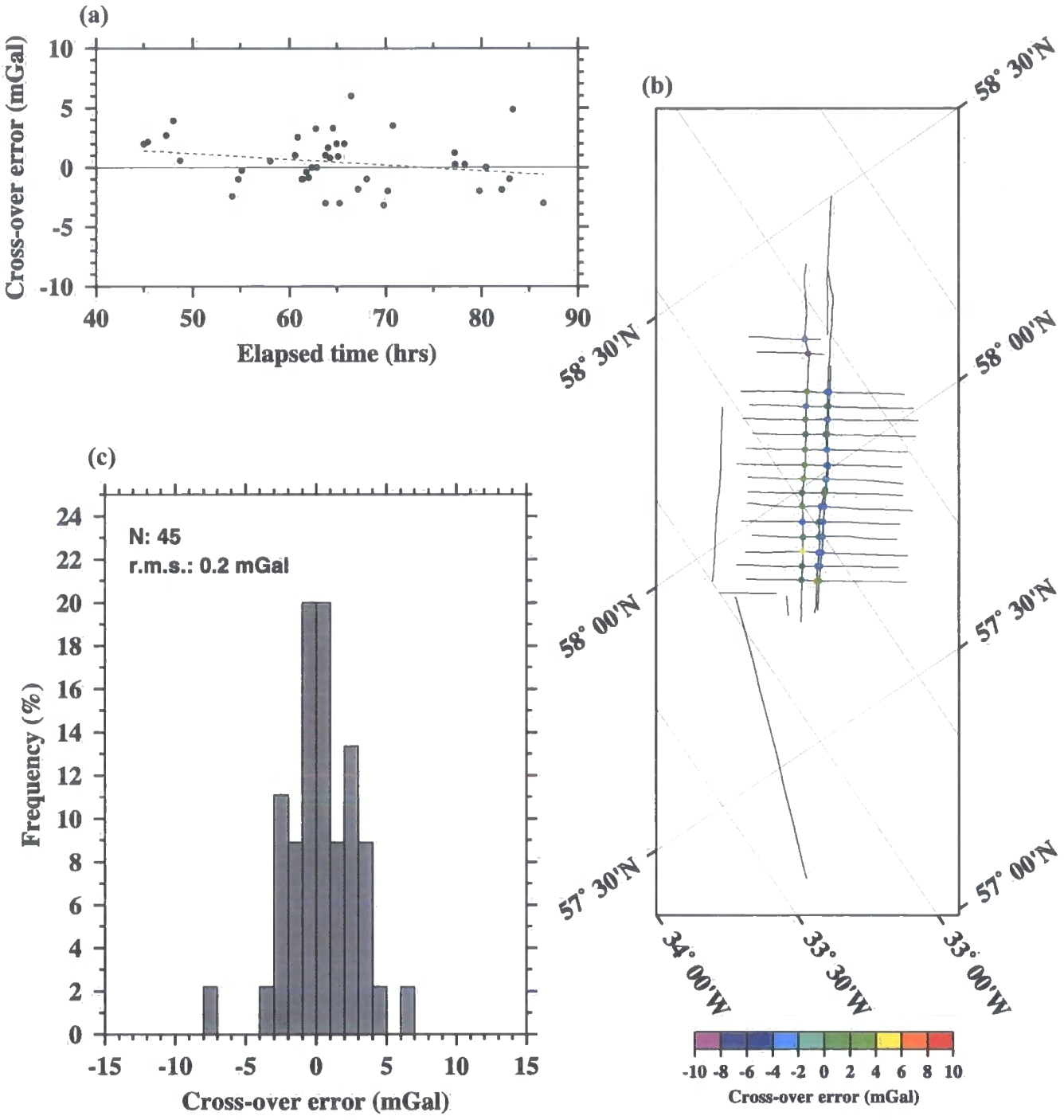

Figure 2.4: Cross-over error analysis for EW9008/90. (a) Drift estimate for the cruise. Plot of cross-over error magnitude (solid dot) against elapsed time. The dashed line shows the -1 mGal day^{-1} linear trend of the data as determined by a least-squares fit using the GMT program *trend1d*. (b) Straight line profiles extracted from the cruise dataset with cross-over error magnitudes superimposed as colour-coded dots. (c) Histogram of cross-over errors shown in (b). The number (N) of cross-over errors is 45 and the r.m.s. of these errors is 0.2 mGal.

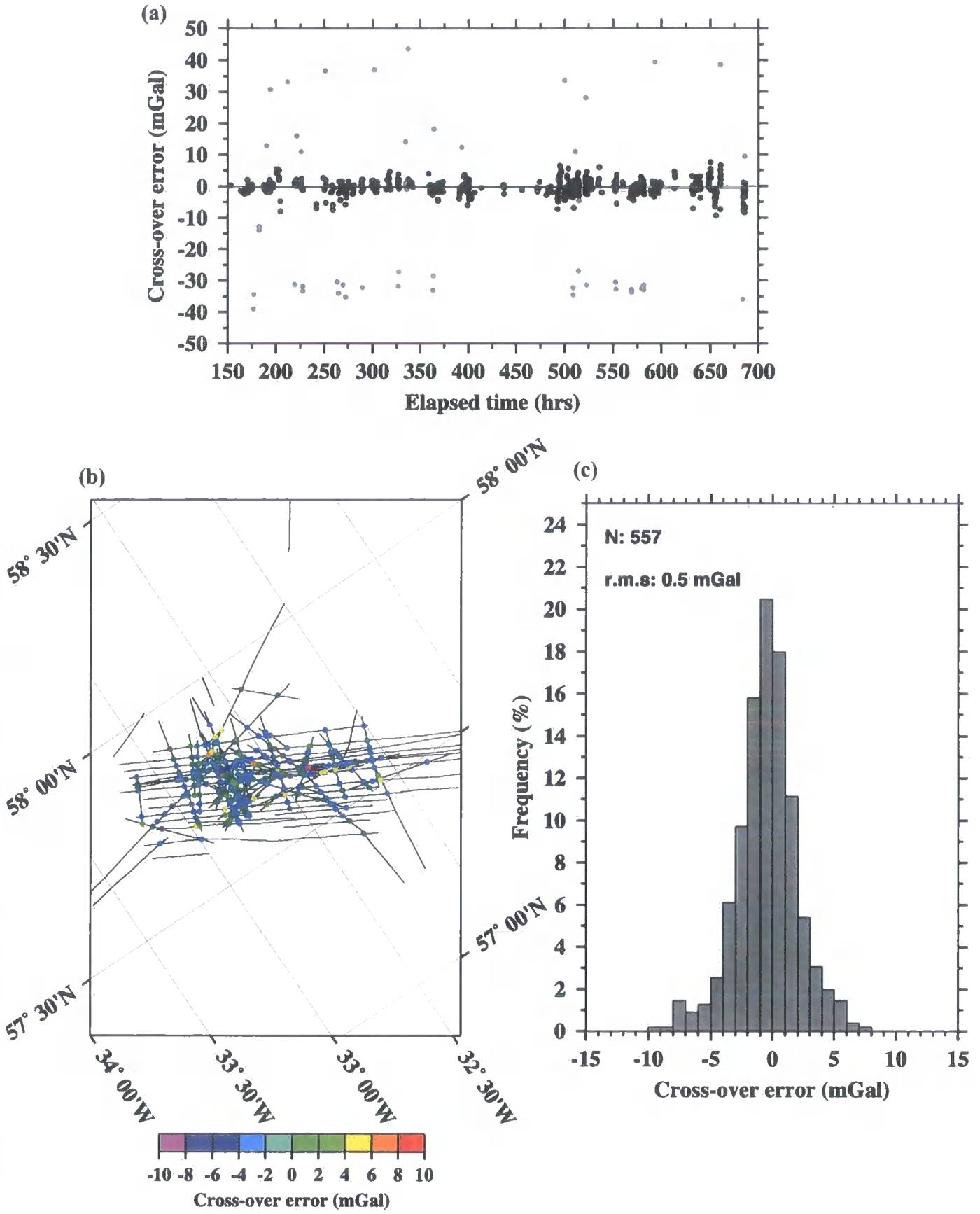

Figure 2.5: Cross-over error analysis for CD81/93. (a) Plot of cross-over error magnitude against elapsed time. Grey shaded dots show the high-cross-over errors associated with short profiles that were removed from the dataset leaving the cross-over errors shaded in black. The linear trend in the data is approximately -0.02 mGal day^{-1}, as calculated using *trend1d*. (b) Straight line profiles extracted from the entire cruise dataset with cross-over error magnitude superimposed as colour-coded dots. (c) Histogram of cross-over errors shown in (b). The number (N) of cross-over errors is 557 and the r.m.s. of these errors is 0.5 mGal.

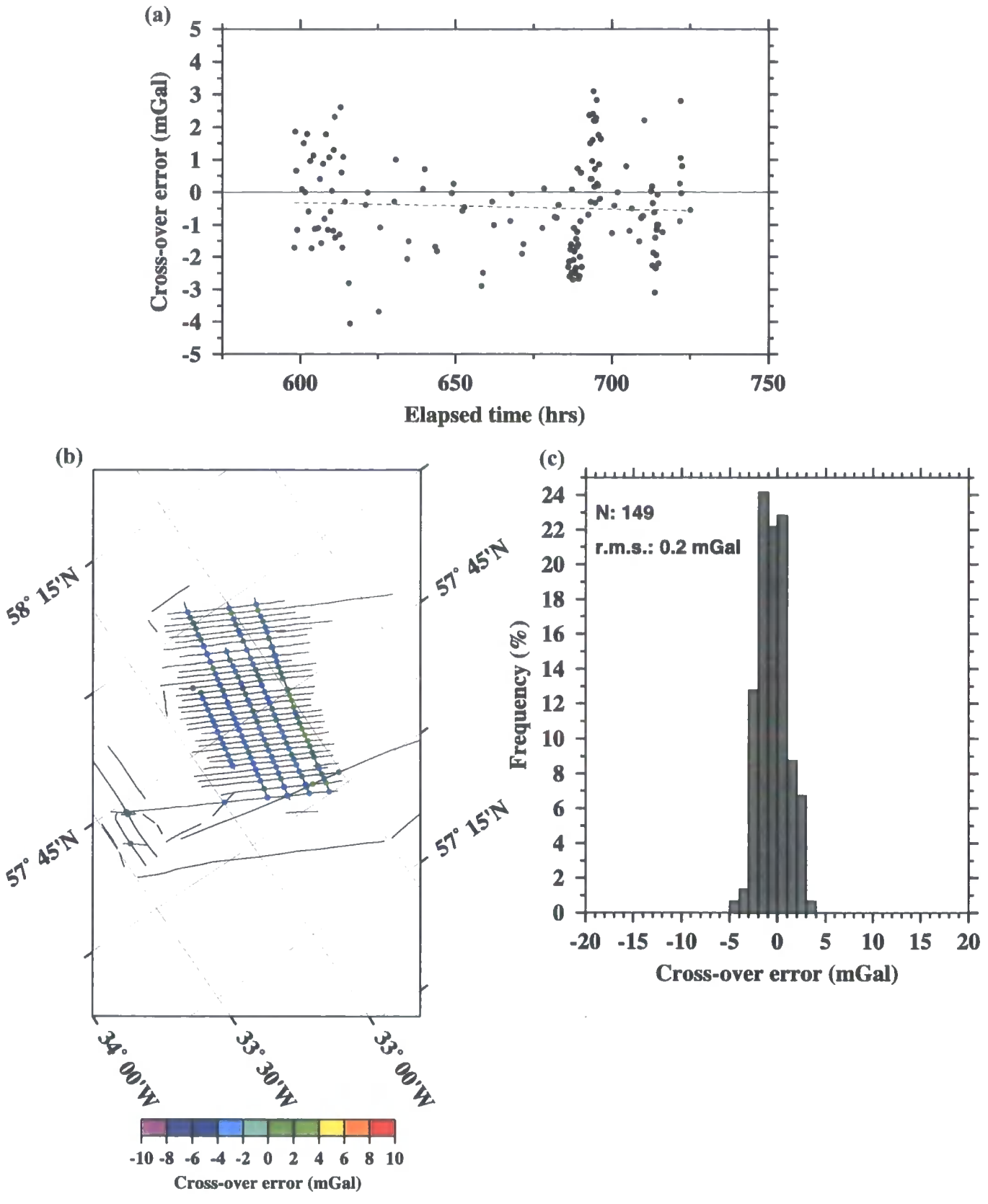

Figure 2.6: Cross-over error analysis for D235c/98. (a) Drift estimate for the cruise. Plot of cross-over error magnitude (solid dot) against elapsed time. The dashed line shows the -0.06 mGal day^{-1} linear trend of the data calculated using *trend1d*. (b) Straight line profiles extracted from the entire cruise dataset with cross-over error magnitude superimposed as colour-coded dots. (c) Histogram of cross-over errors shown in (b). The r.m.s. error of the 149 cross-over points (N) is 0.2 mGal.

2.5.4 CD87/94 cross-over errors

Cross-over error calculations were undertaken during CD87/94 (Searle *et al.* 1994b). A drift rate of 0.09 mGal day^{-1}, based on tie-ins in Barry and Reykjavik, was calculated for this cruise. Significant cross-coupling errors were observed onboard during rough weather and were corrected onboard using a Lacoste-Romberg supplied program, reducing the cross-over errors to an r.m.s. of 0.8 mGal (Fig. 2.7).

2.5.5 Combined cross-over error analysis

Having corrected each individual cruise for internal cross-over errors, a datum consistency check between all cruises was undertaken to identify any possible DC shift in the gravity readings between the different cruises. A cross-over error analysis, incorporating all four cruises, was subsequently performed. Fig. 2.8, shows that the r.m.s. error for the combined dataset is 1.0 mGal. This value is thus taken to be the error for the whole gravity dataset and will be used in the modelling described in Chapter 4.

2.5.6 Data merging and gridding

The dataset was then merged and padded with values from the 2' x 2' satellite data (Sandwell & Smith 1997) to fill gaps within the study area "footprint", although the padded areas are not areas on which subsequent interpretations are made. The combined FAA data were gridded with 601 nodes in both latitude and longitude at a node spacing of 1', approximately equal to 800 m by 1.6 km at the latitude of the study area (Fig. 2.9).

The FAA, as would be expected due to the large density contrast between seawater and the seafloor, primarily mirrors the seafloor bathymetry. As the seabed shoals heading northwards towards Iceland, the axial anomaly amplitude increases from ~10 mGal at 57°30'N to 65 mGal at 62°N. FAA amplitudes of less than 40 mGal occur over the median valley at the ridge axis, with local minima of 20 mGal associated with inter-AVR basins. Further north, the axial rise morphology of the ridge is characterised by a FAA mean amplitude of 50 mGal with local maxima of 70 mGal over larger AVRs. Larger-scale features of the FAA are the V-shaped anomaly highs (Vogt 1971; Ito 2001) thought to be caused by fluctuations in plume temperature and flow rate.

2.5.7 Summary of gravity data processing, merging and gridding

The gravity data collected during four separate cruises to the Reykjanes Ridge were analysed using cross-over error analysis and errors for a number of cruises were reduced. Prior to merging the data a datum consistency check between the cruises was

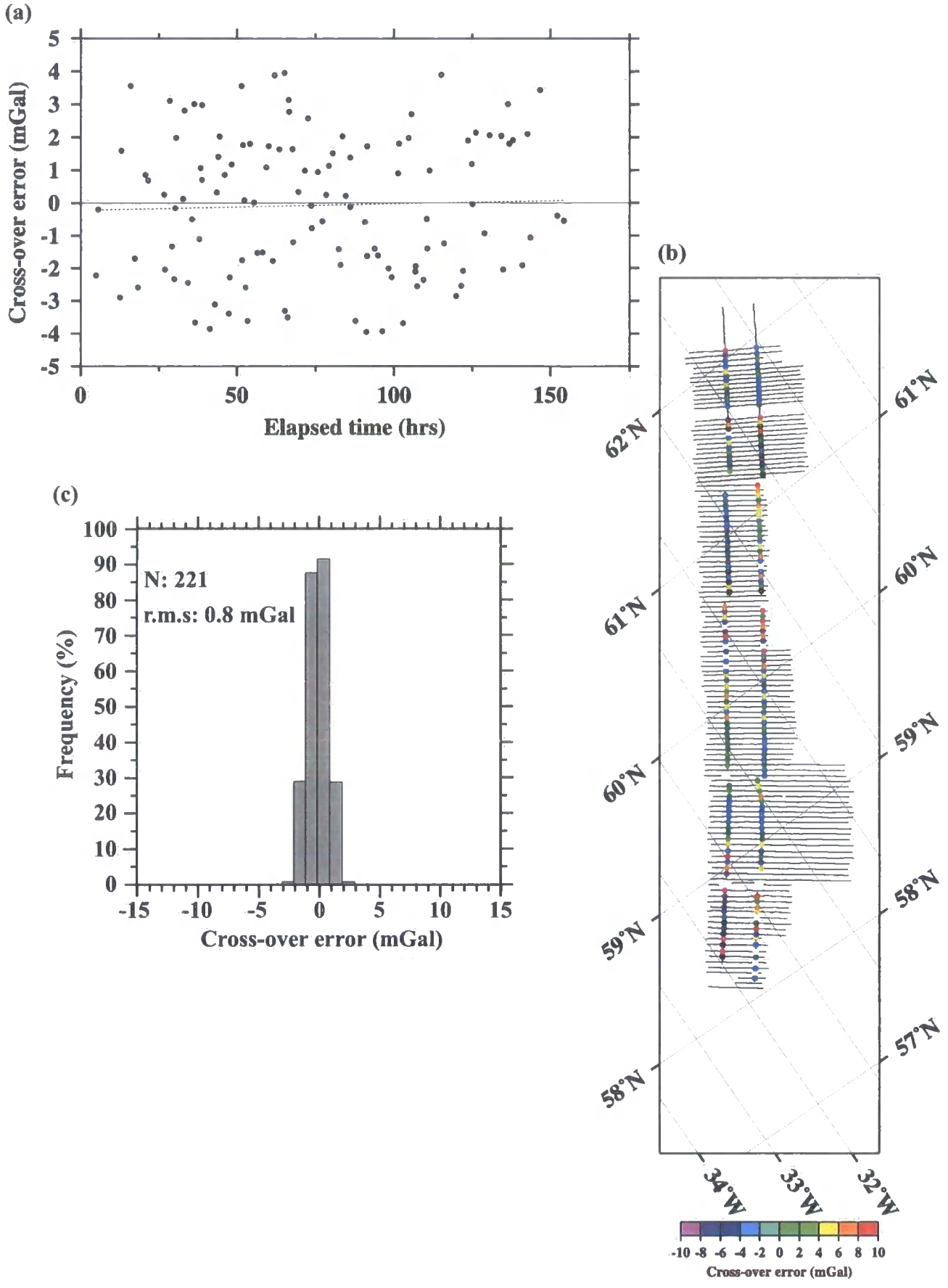

Figure 2.7: Cross-over analysis for CD87/93. (a) Drift estimate for the cruise. Plot of cross-over error magnitude (solid dot) against elapsed time. The dashed line shows the 0.05 mGal day^{-1} linear trend calculated using *trend1d*. (b) Straight line profiles extracted from the entire cruise dataset with cross-over error magnitude superimposed as colour-coded dots. (c) Histogram of cross-over errors after adjustment and cross-coupling correction (see text for details). The r.m.s. error of the 221 cross-over points (N) is 0.8 mGal.

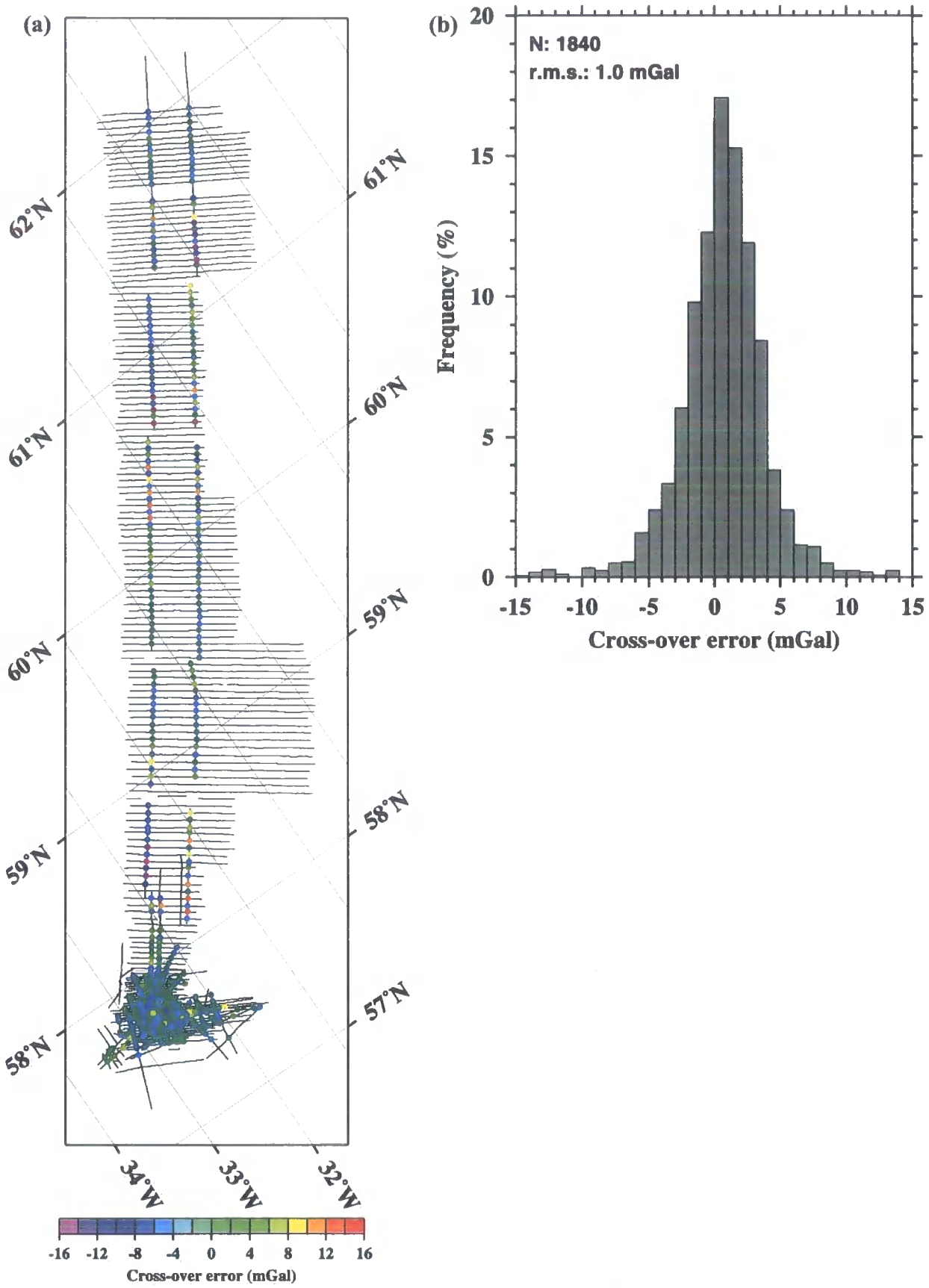

Figure 2.8: Cross-over error analysis of combined cruise gravity data. (a) Segment profiles of cruises EW9008/90, CD87/91, CD81/93 and D235c/98 with internal (within an individual cruise) and external (between different cruises) cross-over errors superimposed as colour-coded dots. (b) Histogram of all internal and external cross-over errors showing the average error for the combined gravity dataset. The r.m.s. error is 1.0 mGal from 1840 cross-over points.

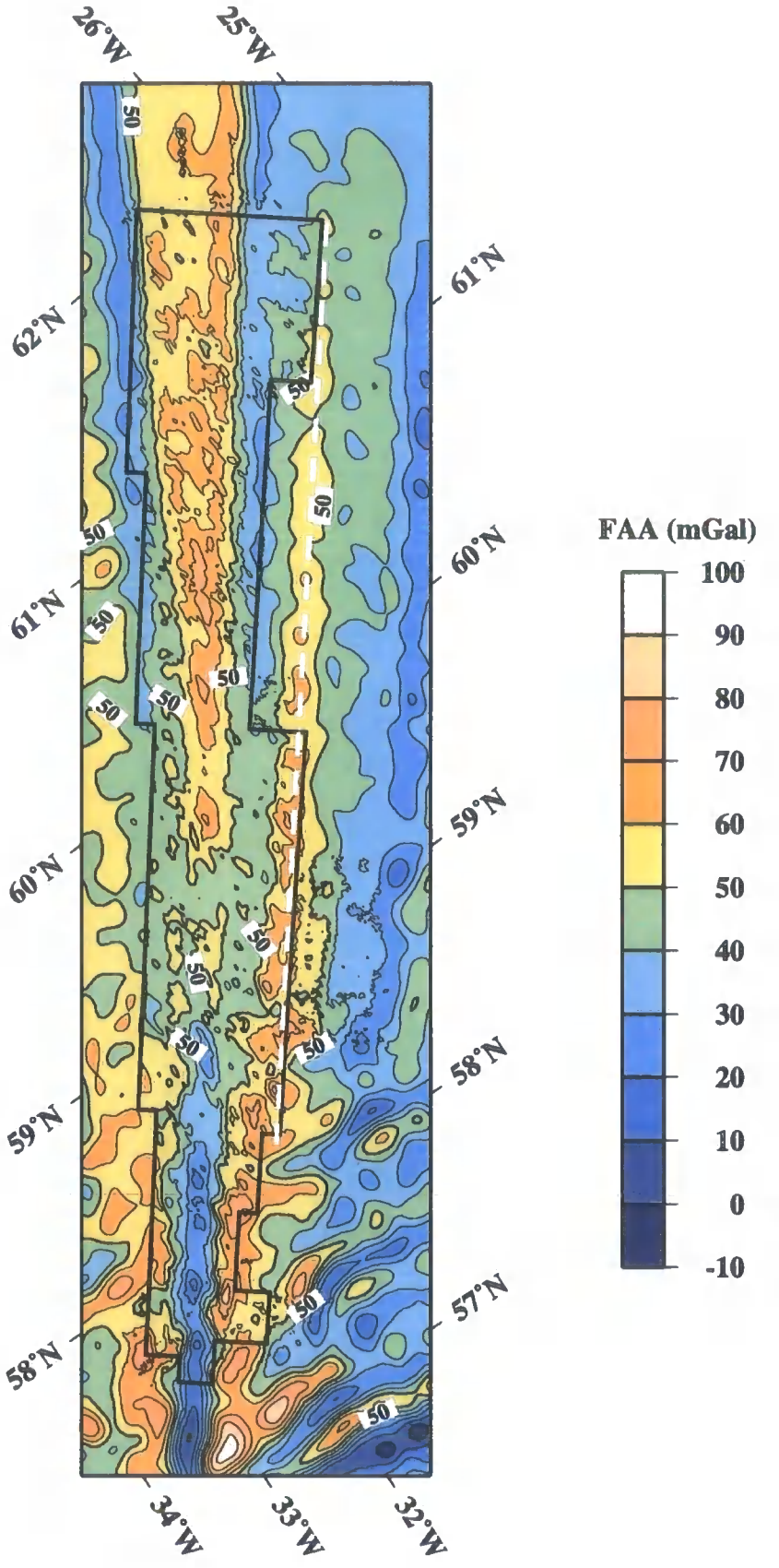

Figure 2.9: Free-air anomaly compilation of the Reykjanes Ridge padded with 2' x 2' satellite data (Sandwell & Smith 1997). The FAA mirrors the seafloor topography with the transition from median valley to axial rise morphology and the decreasing axial depth towards Iceland particularly prominent. The eastern limb of one of the V-shaped ridges is also visible (white dashed line). The black outline box highlights the study area. Contour interval is 10 mGal with only the 50 mGal contour annotated for clarity.

performed, with a subsequent cross-over error analysis revealing a 1.0 mGal error for the combined data. The data were then merged and gridded and are modelled in Chapter 4 to investigate crustal thickness and density and/or mantle density contributions to the observed gravity anomaly.

2.6 Magnetic Data

Total field magnetic data, collected with a proton precession magnetometer during cruise D235c/98 was added to the magnetic anomaly compilation of Lee & Searle (2000) that comprises data from cruises EW9008/90, CD81/93, and CD87/94, extending coverage over the entirety of the 57°45'N AVR. The magnetic data from D235c/98 were considered first, with short-wavelength spikes (Fig. 2.10), attributed to instrumentation spikes, filtered out using a 6 minute wide (in time) Gaussian filter. A cross-over error analysis was performed and removal of the spikes reduced r.m.s. error from 87 nT to 84 nT (Fig. 2.11). This compares favourably to the 60 nT r.m.s. error calculated by Lee & Searle (2000) for their compilation. Older cruises over the study area (V2303/66, SHACK877/77 & DI84LI-2/77) were not included in the compilation as their r.m.s. cross-over errors were around 300 nT, significantly higher than the later cruises. A datum consistency check between the D235c/98 data and the compilation of Lee & Searle (2000) was made prior to merging the datasets and gridding at a 1' node spacing (Fig 2.12).

Anomalies are linear and symmetrical about the ridge axis, which is defined by a central anomaly magnetic high (CAMH). The CAMH remains approximately constant along-axis, even though the seafloor depth decreases significantly towards Iceland. Lee & Searle (2000) attribute this lack of variability to the small difference in strike of the ridge axis and the declination of the Earth's field (022°) at this latitude, which results in amplification of the across-axis anomalies at the expense of the along-axis anomalies. Short-wavelength anomalies, however, do disrupt the along-axis continuity of the CAMH and generally correlate with the position of AVRs (see Chapter 5).

The magnetic data compilation described in this section is inverted in Chapter 5 to obtain a magnetization intensity solution, which is used to test the relative age interpretation of AVRs (see Chapter 3) and to make spreading rate determinations.

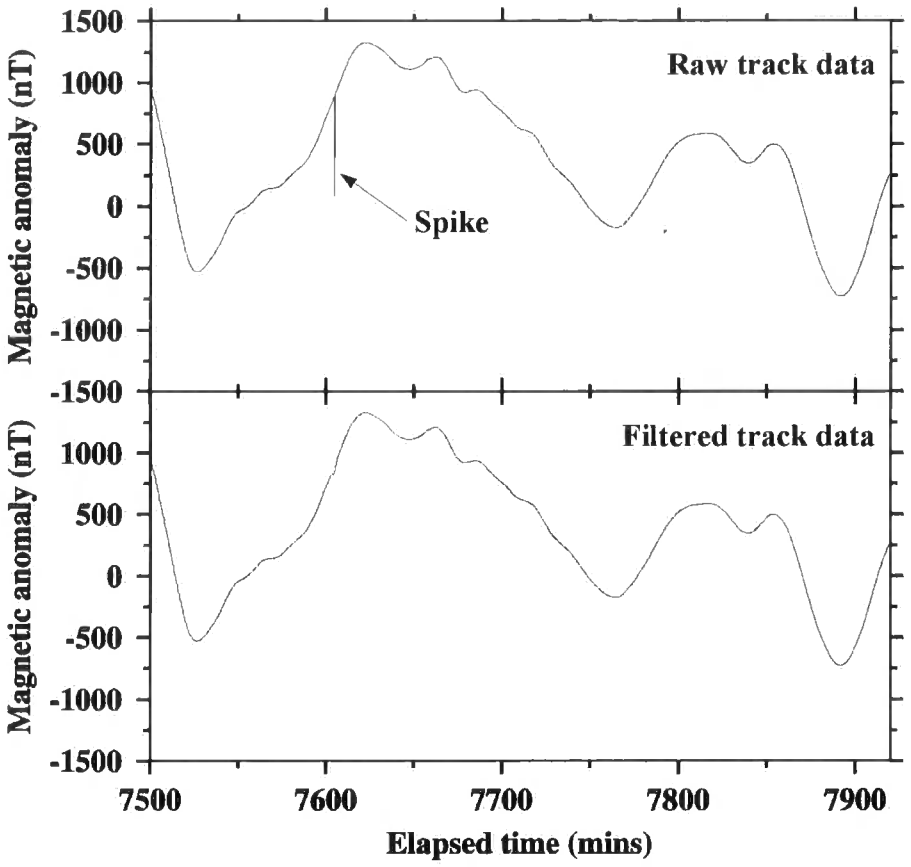

Figure 2.10: Example of the application of a de-spiking filter on magnetic data from D235c/98. A 6 minute wide (in time) Gaussian filter was used to eliminate spurious data spikes. Note how the spike at ~7600 minutes in the raw track data (top panel) has been removed in the filtered track data (bottom panel) without greatly effecting the rest of the data at the wavelength of interest.

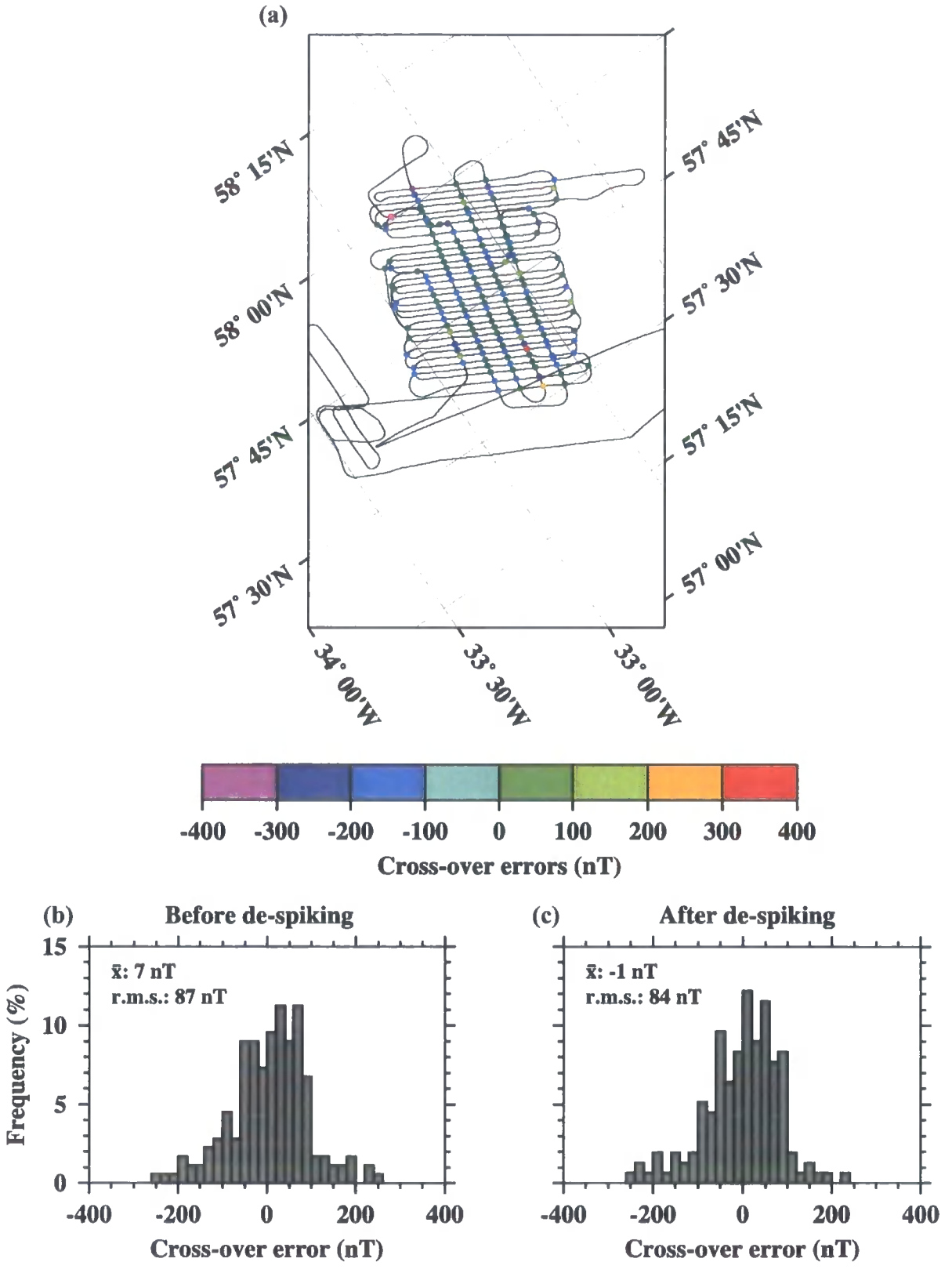

Figure 2.11: Cross-over error analysis following the de-spiking operation on the magnetic data of D235c/98. (a) Ship tracks with total magnetic field cross-over errors superimposed as colour-coded dots. (b) Histogram of cross-over errors before applying de-spiking filter (see Fig. 2.10). The average magnetic field is -7 nT and the r.m.s. cross-over error is 87 nT. (c) Histogram of cross-over errors after application of de-spiking filter. The average magnetic field and the r.m.s. cross-over error have been reduced to -1 nT and 84 nT respectively. The small effect of the de-spiking operation on the r.m.s. cross-over error is most likely due to only a few spikes actually occurring at cross-over points.

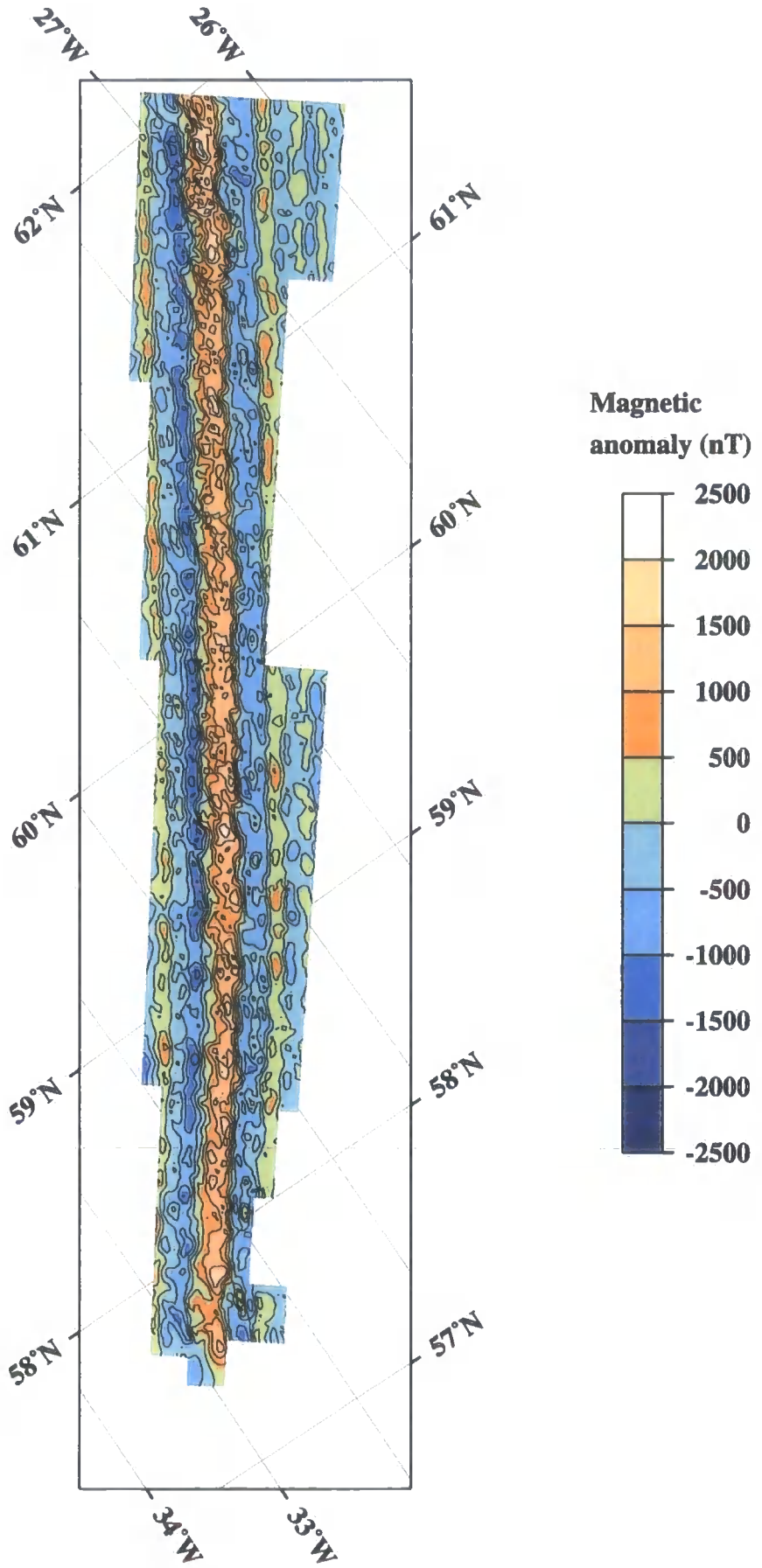

Figure 2.12: Magnetic data compilation for the study area. Note how the anomalies follow the general ridge trend and decrease in amplitude away from the ridge axis. The small difference in strike of the ridge axis and the declination of the Earth's field at this latitude result in subdued along-axis anomalies relative to across-axis anomalies. However, small-scale along-axis anomalies generally correlate with the position of AVRs. Contour interval is 500 nT.

2.7 Summary

In this chapter the collection, basic processing and compilation of bathymetry, TOBI, gravity and magnetic data acquired over the Reykjanes Ridge during four cruises which form the basis of this study were described. Analyses of cross-over errors for the gravity and magnetic data have quantified the error associated with each dataset. The TOBI data are interpreted in Chapter 3 and modelling and interpretation of the gravity and magnetic data are described in Chapters 4 and 5 respectively.

Chapter 3

TOBI data interpretation

3.1 Introduction

TOBI data are primarily used to reveal the detail of seafloor morphology by mapping the differences in the acoustic properties of the ensonified seabed terrain. For example, sediment significantly attenuates backscatter resulting in weak returns and a dark appearance on sidescan images, whereas sheet flows, which have a greater acoustic impedance contrast with water, result in brighter returns (Fig. 3.1).

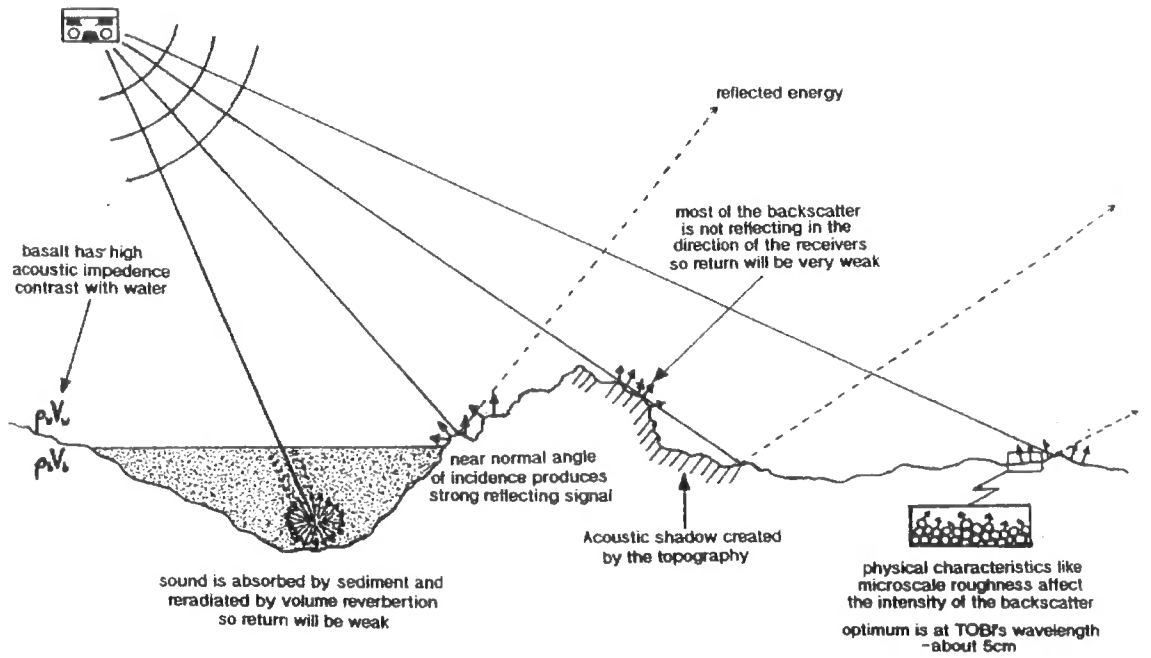

Figure 3.1: Interaction of acoustic energy with the seafloor in the generation of sidescan images (from Lawson 1996 as adapted from Johnson & Helferty 1990).

In the following sections the concept of tectonomagmatic cycles of crustal accretion is introduced. To test the hypothesis that tectonomagmatic cycles affect not only the seafloor morphology, but also the underlying crustal structure, a relative age scheme for AVRs is developed. The basic units of oceanic crustal construction at the Reykjanes Ridge are AVRs, which consist of sheet flows, hummocky terrain and ridges, point-source, conical, cratered and flat-topped volcanoes. These magmatic features, together

with features that modify the oceanic crust, such as fissures, faults and sediment cover appear at various stages in what is the apparent lifecycle of an AVR (see Section 3.1.1).

The aforementioned features are described in Section 3.1.2 and, by careful mapping, form the basis by which the relative ages of AVRs in TOBI areas C and B (Fig. 1.12) are determined in Sections 3.2 and 3.3 respectively. The TOBI interpretations for both areas are summarised in Section 3.4.

3.1.1 Tectonomagmatic cycles

AVRs are the fundamental building blocks of the crust at the ridge axis (Laughton *et al.* 1979; Searle & Laughton 1981). At most spreading ridges, where spreading occurs normal to the ridge trend, AVRs follow the ridge axis and are rafted off-axis by ridge-parallel normal faults. However, oblique spreading results in two trends in seabed features- one ridge-parallel and one perpendicular to the spreading direction (see Section 3.1.3). AVRs, separated by right-stepping en-echelon offsets, are oriented orthogonal to the spreading direction whereas normal faulting is predominantly ridge-parallel. Studies of AVR geomorphology based on high-resolution sonar data (e.g. Parson *et al.* 1993), suggest that each AVR has its own life span comprising a period of magmatic accretion followed by a period of amagmatic tectonic extension. These observations suggest that crustal construction at the Reykjanes Ridge occurs not as a steady-state process, but in a cyclic fashion. Parson *et al.* (1993) postulate that during the *magmatic phase* of a cycle, vigorous volcanism leads to the formation and rapid growth of a linear axial volcano, the so-called AVR, which typically extends up to ~30 km along-axis (the *young* stage) (Fig. 3.2).

Parson *et al.* (1993) also suggest that AVRs appear to reach full maturity as the rate of magmatic activity starts to decline (the end of the *adolescent* stage). With on-going seafloor spreading during the later stages of the magmatic phase and throughout the post-magmatic or *tectonic phase*, AVRs become dissected by many spreading-orthogonal normal faults (the *mature* stage). Eventually, the volcanic terrain of the magmatic phase becomes overprinted by younger tectonic features and, ultimately, extinct AVRs become completely dismembered by faulting (the *old* stage). Observations also indicate that after a further period of tectonic extension a new magmatic phase is initiated, leading at first to isolated fresh lava flows that overprint the tectonised seafloor, and then to the establishment and growth to maturity of a new AVR.

The duration of this cycle, a *tectonomagmatic cycle*, is believed to be of the order of 0.5 Ma years based on seafloor observation alone (Searle *et al.* 1998). Tectonomagmatic

cycles thus comprise the *young* and *adolescent* stages of the *magmatic* phase and the *mature* and *old* stages of the *tectonic* phase (after Parson *et al.* 1993).

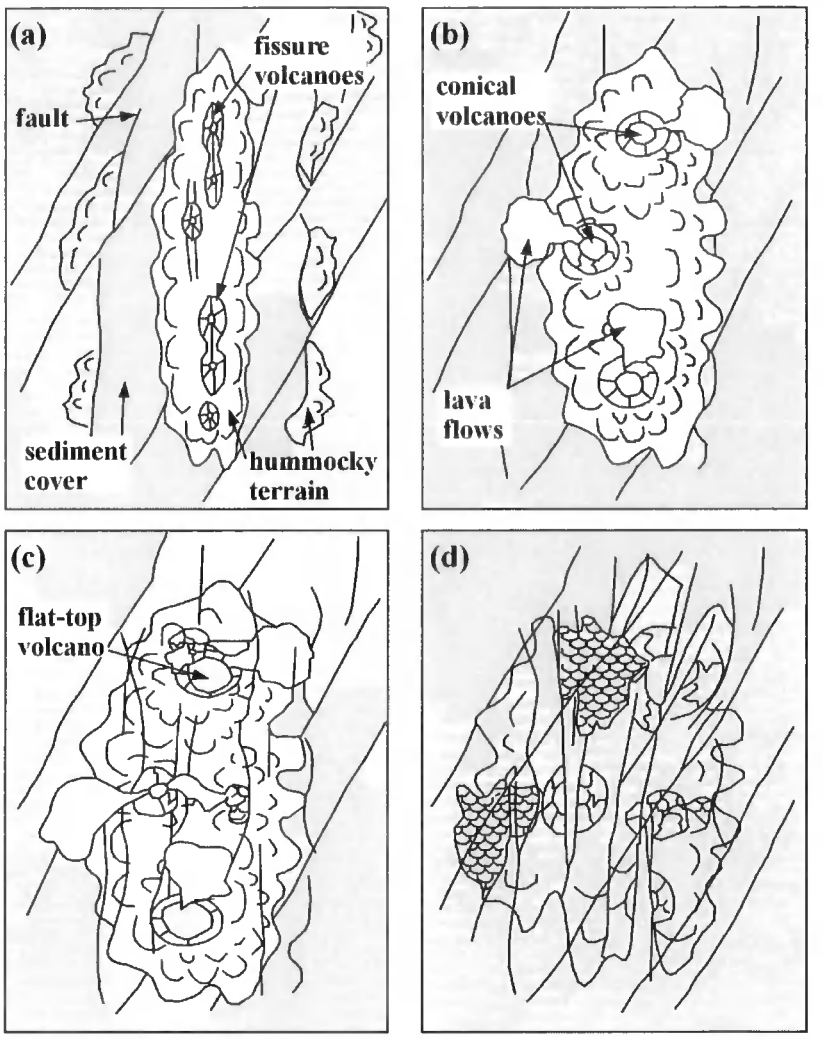

Figure 3.2: Tectonomagmatic cycle, showing an axial volcanic ridge at various stages in its lifecycle at an oblique spreading segment centre. The *magmatic* phase comprises the *young* (a) and *adolescent* (b) stages, while the *tectonic* phase includes the *mature* (c) and *old* (d) stages. Note that through the lifecycle there is a change from fissure to conical to flat-topped (shield) volcanoes, reflecting the mode of magma delivery to the seafloor. As AVRs age through their lifecycle the dominant direction of faulting changes from AVR-parallel to ridge-parallel as the AVR is dismembered during its later life. After Parson *et al.* (1993).

AVRs identified in the TOBI data were initially interpreted in terms of their relative age by adopting the morphology vs. age definition of Parson *et al.* (1993). However, this relative ageing scheme was later extended to allow a finer scale of relative age subdivision.

In this study, thin ridges associated with fissure-type volcanism are classified as *young* AVRs. Broader ridges with conical seamounts are interpreted to be slightly older

and are placed at the *adolescent* stage of the cycle. *Mature* AVRs have flat-topped seamounts and are generally periclinal in shape with a few AVR-parallel swarms, whereas *old* ridges are covered by a thin layer of sediment and are dissected by ridge-parallel faults. AVRs that fall into the same age group (i.e. *young*, *adolescent*, *mature* or *old*) are separated further by taking into account the abundance of sediment cover and the extent of faulting.

The following sections discuss the main volcanic and tectonic features observed at the Reykjanes Ridge. These features are then used in Sections 3.2 and 3.3 as a means of relative ageing AVRs in TOBI areas B and C (see Fig.1.12) respectively.

3.1.2 Volcanic morphology

AVRs are common on slow- to intermediate-spreading ridges and are, on average, 10 to 50 km long by 3 to 10 km wide and 50 to 200 m high. They are formed by a coalescence of individual volcanic units (e.g. conical and flat-topped), hummocky ridges and a variety of lava flow types. Volcanic edifices are usually the smallest resolvable features of TOBI data at mid-ocean ridges and are one of the fundamental expressions of crustal construction on the seafloor. Their type (point-source, composite, flat-topped or clustered) depends on the viscosity and effusion rate of the magma. However, as viscosity is proportional to silica content, which is approximately constant at 48% for basaltic lava, the type of volcano generated on the seafloor is largely a function of effusion rate (Smith & Cann 1990) which, in turn, can be related to the relative age of the surrounding seafloor (see Sections 3.1.2.1 to 3.1.2.5).

Each of the volcanic edifice types will now be considered in turn.

3.1.2.1 Point-source volcanoes

These conical-shaped volcanoes range in diameter from hundreds of metres to a few kilometres and rise up to a few hundred metres above the surrounding seafloor (see Fig. 3.3). Calderas are often observed at the top of these volcanoes, suggesting draining of melt in the feeding magma chamber and confirming that point-source volcanoes are monogenic edifices (Blondel & Murton 1997) that are usually observed on *adolescent* AVRs.

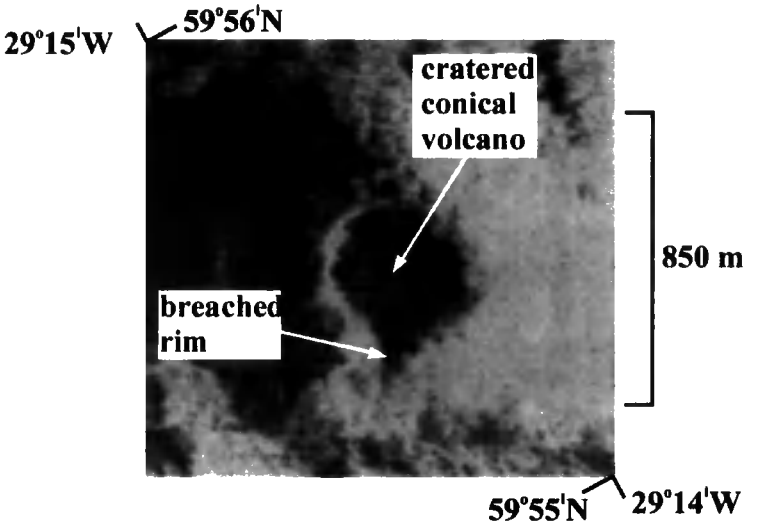

Figure 3.3: TOBI image of a cratered conical volcano on the Reykjanes Ridge.

3.1.2.2 Composite volcanoes

In contrast to point-source volcanoes, these features consist of one main point-source volcano surrounded by several smaller, parasitic cones that probably post-date the main edifice (see Fig. 3.4). These types of structures are commonly formed by slow and episodic lava eruptions and are usually found on *mature* AVRs.

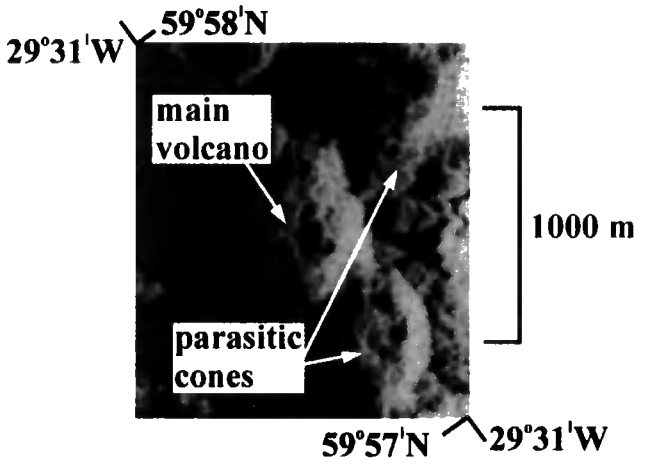

Figure 3.4: TOBI image of a composite volcano on the Reykjanes Ridge.

3.1.2.3 Flat-top volcanoes

Flat-top volcanoes are usually slightly bigger than point-source volcanoes and occur at high effusion rates or after a prolonged period of more subdued magmatic activity. When volcanoes reach their maximum height, a function of depth to the magma reservoir (Smith & Cann 1992), lava flows from the summit horizontally forming a smooth flat-top (see Fig. 3.5). The slow and episodic nature of crustal accretion at the Reykjanes Ridge (see Section 1.4) means that flat-top volcanoes are usually observed on *mature* AVRs.

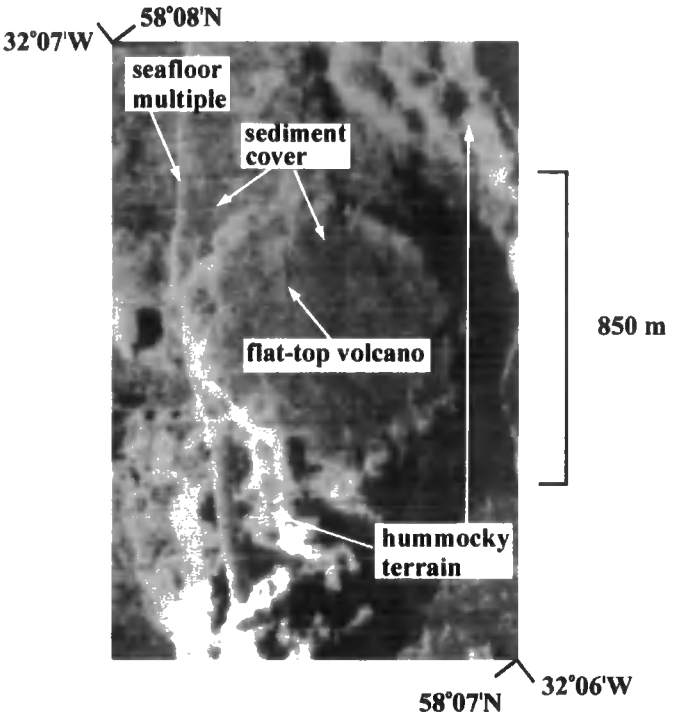

Figure 3.5: TOBI image of a flat-topped volcano from area C on the Reykjanes Ridge.

3.1.2.4 Clustered volcanoes

Observations of clusters of either point-source or a range of types of volcanoes (see Fig. 3.6) have led to the "plum pudding" model of the crust, in which a number of discreet magma bodies at different depths in the crust are postulated to feed individual volcanoes. The latter are often observed at intermediate-spreading ridges suggesting that they might represent a transitional mode of crustal formation between isolated, ephemeral, magma bodies at slow-spreading ridges and fissure type eruptions at faster-spreading ridges.

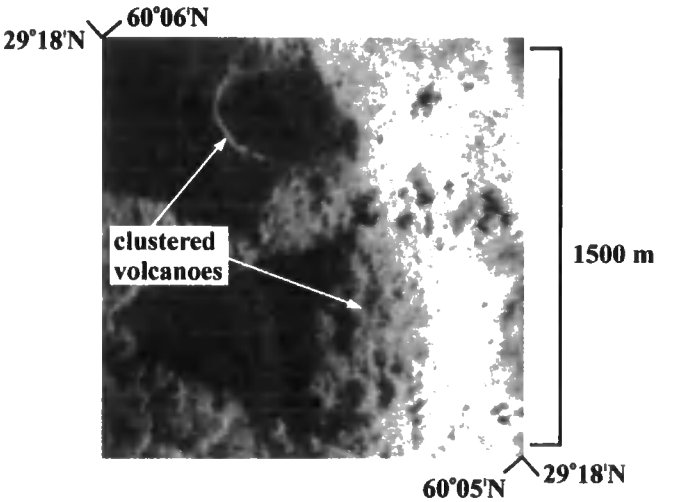

Figure 3.6: TOBI image of a cluster of flat-top and conical volcanoes on the Reykjanes Ridge.

3.1.2.5 Hummocky ridges

These ridges form when multiple monogenic eruptive centres coalesce and are usually a function of fissure-controlled eruption with the hummocky ridge aligned in the direction of minimum compressive stress (Blondel & Murton 1997). These ridges are often observed at slow-spreading ridges (Fig 3.7), as low effusion rates are required to generate hummocky terrain.

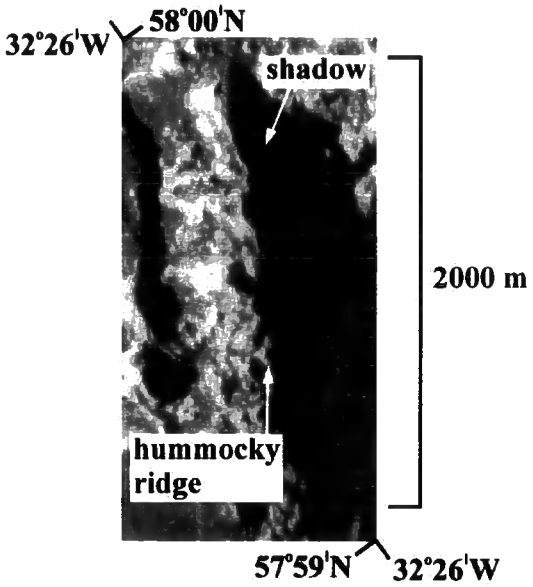

Figure 3.7: TOBI image of a hummocky ridge on the Reykjanes Ridge.

3.1.3 Tectonic features

Faulting at mid-ocean ridges follows two general trends: parallel to the plate boundary and perpendicular to the spreading direction. For most spreading ridges these trends are the same, but at ridges where spreading is in a direction oblique to the ridge axis, faulting follows two distinct trends. On-axis, faulting is predominantly normal to the spreading direction, whereas off-axis, ridge axis-parallel faulting is prevalent (Fig 3.8). A number of on-axis faults exhibit a sigmoidal, or curvilinear, appearance in plan view, with their extremities aligned with the ridge trend. These observations have been interpreted to represent deformation of the lithosphere by two different stress regimes (Searle & Laughton 1981).

The two main factors controlling faulting at the ridge axis are lithospheric strength and plate separation. Lithospheric strength is largely a function of temperature. Isothermal lines follow the ridge trend, and the gradient of increasing lithospheric strength is perpendicular to them. Off-axis faulting is, therefore, perpendicular to the

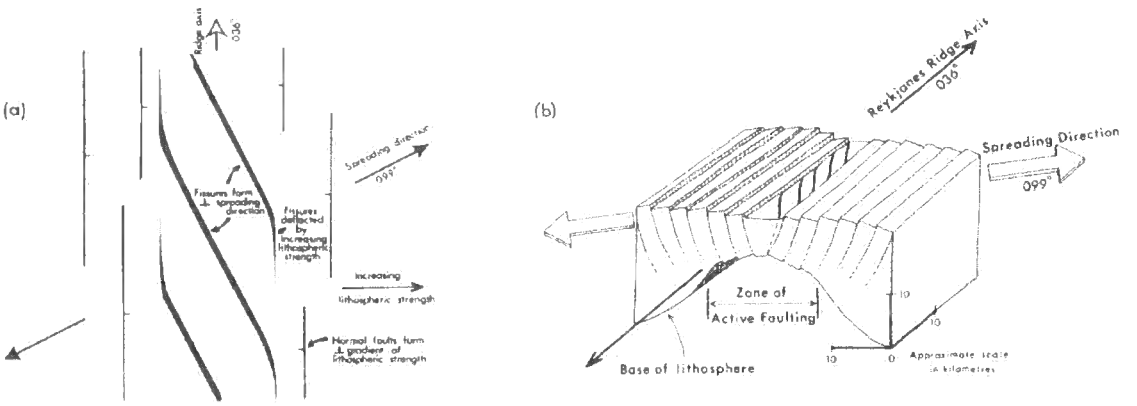

Figure 3.8: Predominant faulting patterns at the Reykjanes Ridge (from Searle & Laughton 1981). (a) Plan view of the axial region, showing development of axial fissures normal to the spreading direction. Fissures are deflected in the ridge-axis direction toward the edge of the axial zone, giving rise to their sigmoidal appearance. Normal faulting occurs parallel to the ridge axis at the edge of the axial zone. (b) Block diagram showing same process. AVRs form above the fissures but have been omitted from the figure for clarity.

gradient of lithospheric strength, i.e. parallel to the ridge trend. Whereas, on-axis the separation of the plates gives rise to minimum compressive stress, normal to the spreading direction. Fissure-type eruptions propagate in this direction into progressively older and stronger lithosphere. At a certain point lithospheric strength exceeds the local tensional stress and faulting will tend to be deflected towards the ridge trend, parallel to lines of equal lithospheric strength. Ridge-parallel faulting is rarely observed on-axis, suggesting that either: a) plate spreading distorts the thermal field on-axis, resulting in spreading-normal faulting; or b) that the lithospheric strength gradient is weak on-axis (Searle & Laughton 1981). For this study faults are defined as having variable vertical displacement, while fissures are defined as having constant vertical displacement. The actual magnitude of the displacement can be estimated, if the angle of ensonification is known, from the shadow projected by the faults or fissures. Both of these fracture types can have either a bright or dark appearance in TOBI data depending on the direction of ensonification (Fig. 3.9).

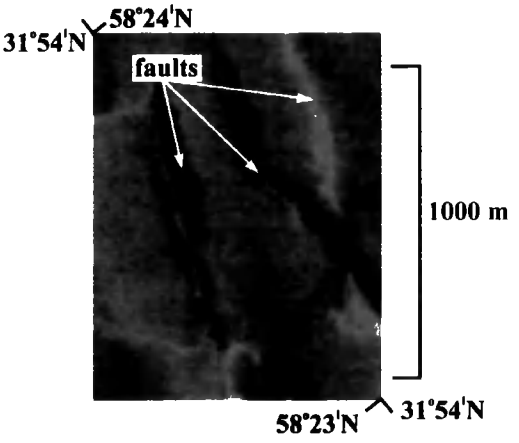

Figure 3.9: TOBI image of faults. Faults can have a bright or dark appearance depending on the direction of ensonification and the type of faulting (i.e. normal or reverse).

3.1.4 Sediment cover

Although pelagic sediment cover is relatively thin on-axis compared to off-axis at the Reykjanes Ridge (Talwani *et al.* 1971), topographic basins, usually associated on-axis with non-transform discontinuities, often contain small pockets of sediment. Sediments absorb the sidescan sonar signal and, therefore, give rise to weak returns and a dark appearance on TOBI images (Fig. 3.10). If a constant rate of sedimentation is assumed for the study area, then variations in the extent of sediment cover may provide a useful means of relative ageing AVRs.

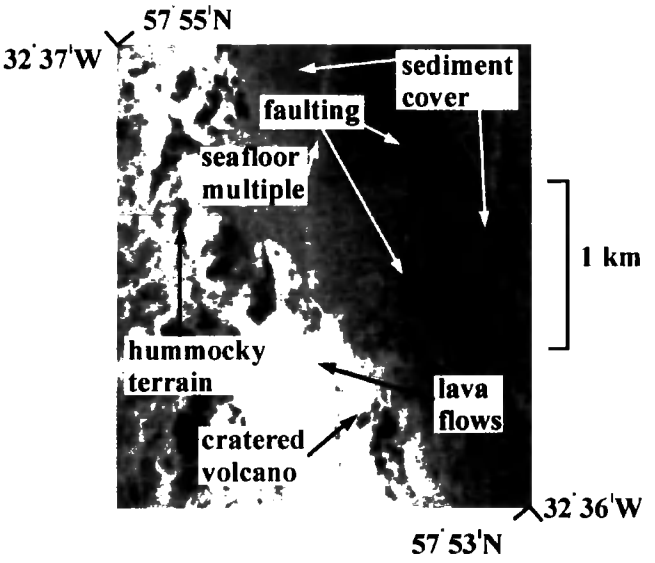

Figure 3.10: TOBI image showing the different reflection characteristics of sediment cover (dark grey area) and lava flows (bright area).

3.2 TOBI area C

TOBI area C extends from 31°46'W to 32°47'W and 57°45'N to 58°27'N (see Fig 1.12). The average seafloor depth in this region is ~1950 m and AVRs rise up to ~500 m above the surrounding terrain. Median valley faults, 10-12 km apart with throws of ~500 m, are prominent features that extend up to 30 km in length in a flip-flop fashion, i.e. alternating from one side of the ridge axis to the other, giving rise to asymmetric axial graben in cross-section. The AVRs chosen for interpretation in TOBI area C consist of: the RAMESSES AVR at 57°45'N, as it has been the subject of extensive geophysical study (Navin *et al.* 1998), and adjacent AVRs of different lengths with good TOBI coverage at 57°55'N, 58°05'N, 58°15'N, and 58°24'N.

Area C is south of 59°N, where the V-shaped ridges intersect the ridge and the axial morphology changes from a median valley to an axial high (see Section 1.5). It is therefore assumed in this section that area C is not within the hotspot influence, although further constraints on the extent of hotspot influence are discussed in Chapters 4 and 5. The AVR numbering scheme of Keeton *et al.* (1997) is adopted for the TOBI interpretation presented in the following sections and applies for the entire study. The RAMESSES AVR, at 57°45'N, is defined as AVR number one with AVRs further north defined incrementally.

3.2.1 AVR 1 (RAMESSES)

This ~30 km long AVR centred on 57°45'N consists of a hummocky ridge, with cratered conical and flat-topped volcanoes superimposed. Bright backscatter around the edges of this AVR indicates the presence of recent lava flows (Fig 3.11). There is no clear evidence of faulting on the AVR itself but large AVR-parallel normal faults occur to the east of this AVR with similar smaller throw faults cutting off-axis hummocky terrain to the west of it. Little to no sediment cover is observed on-axis. The long length of this AVR, its broad convex shape, and the presence of cratered conical and flat-topped volcanoes support the interpretation that it is in a more *mature* part of its lifecycle and that recent extrusives overprint faulting on the AVR itself giving it a younger appearance (Lee & Searle 2000).

3.2.2 AVR 2

This relatively short AVR (~10 km) near 57°55'N is composed mainly of hummocky terrain with some lava flows, that are sediment covered in places (Fig. 3.11). A large,

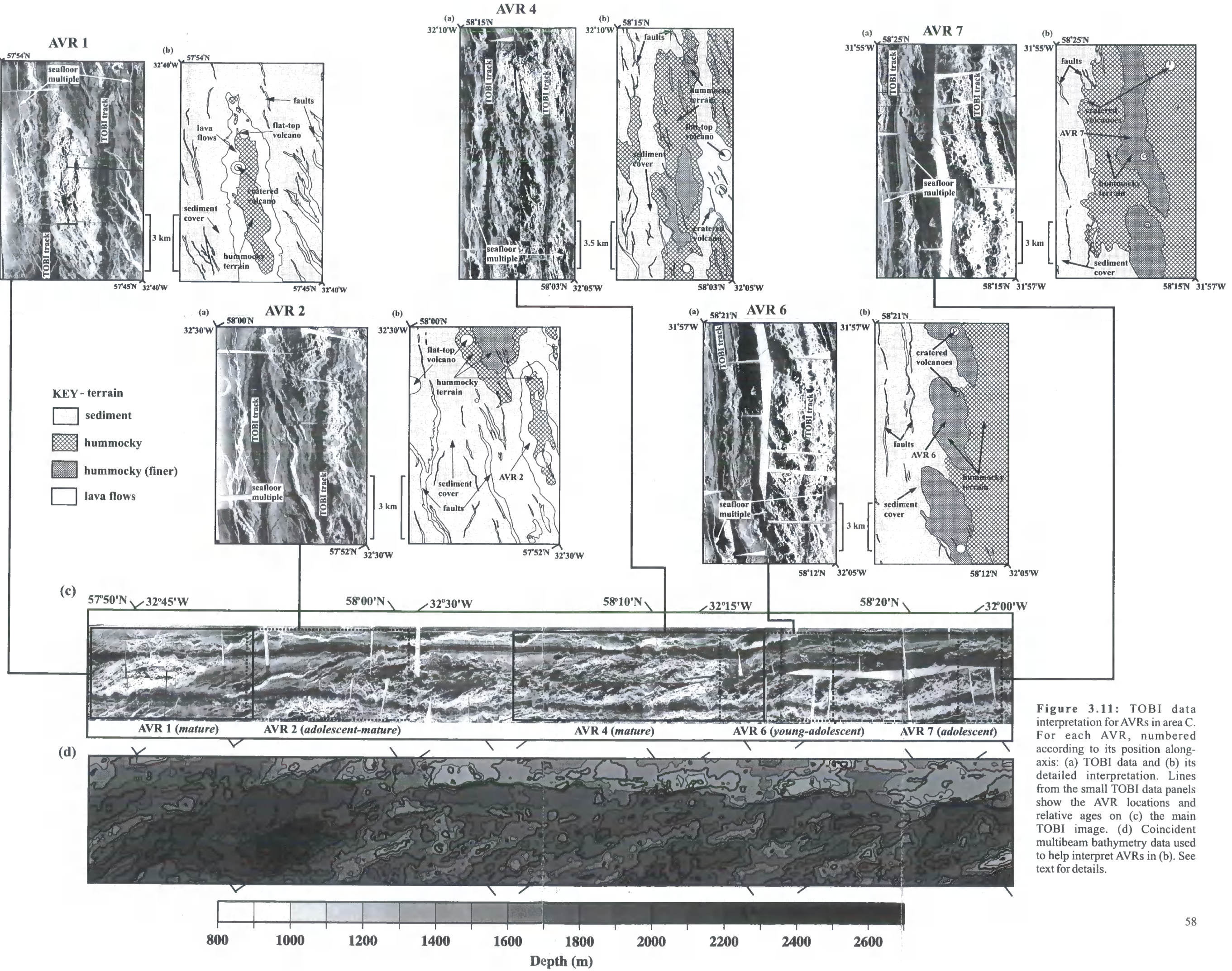

Figure 3.11: TOBI data interpretation for AVRs in area C. For each AVR, numbered according to its position along-axis: (a) TOBI data and (b) its detailed interpretation. Lines from the small TOBI data panels show the AVR locations and relative ages on (c) the main TOBI image. (d) Coincident multibeam bathymetry data used to help interpret AVRs in (b). See text for details.

faulted, flat-topped volcano can be seen at its southern end and an unfaulted, but heavily sedimented flat-topped volcano at the northern end. Two short AVR-trending hummocky ridges lie at the northern end of this AVR, while numerous small ridge-trending normal faults overprint it entirely. The patchy sediment cover, extensive small-throw faulting and flat-topped volcanoes suggest that this AVR is probably at the very end *adolescent*/earliest *mature* phase of the cycle.

3.2.3 AVR 4

The ~35 km long hummocky edifice at 58°05'N contains one sediment covered, flat-topped volcano to the southeast (Fig. 3.11). Normal faulting is more extensive than for AVR 2, and mainly follows the ridge trend. Patchy sediment cover is visible on the edges of the volcanic terrain. This AVR is the longest and appears to be the oldest of the five AVRs presented here and is probably at the early stages of the *mature* part of the cycle.

3.2.4 AVR 6

Incomplete TOBI coverage makes the interpretation of this 58°15'N-centred AVR difficult (Fig. 3.11). Some bright-backscatter is observed around the edges of this ~11 km long AVR, possibly indicating the presence of fresh lava flows. The volcanic terrain is mainly hummocky in appearance with no volcanoes observed. Ridge-parallel normal faulting is only observed off-axis to the west. This AVR is younger in appearance than AVR 4, and is possibly at the *young* to *adolescent* stage of the cycle.

3.2.5 AVR 7

Again, sparse TOBI coverage makes the interpretation of this AVR at 58°24'N difficult (Fig. 3.11). However, fresh lava flows can be observed around the edges of this ~20 km long hummocky ridge with no clear evidence for on-axis faulting, though normal faulting is prevalent off-axis to the north. Patchy sediment cover on the edges of this AVR suggests it is younger than AVR 4 but slightly older than AVR 6, probably at the *adolescent* part of its cycle.

3.2.6 Summary of TOBI area C

TOBI area C contains AVRs that are mainly *adolescent* to *mature* in age. The AVRs are generally well defined with a number of conical and flat-topped volcanoes observed.

Faulting is ubiquitous off-axis but less prevalent on-axis. Where faults do occur on-axis, they are generally parallel the AVR trend.

A correlation between relative AVR age and length can be made for TOBI area C. Shorter AVRs appear younger than longer AVRs. In addition, a spatial pattern with a wavelength of ~70 km is observed in the relative age of AVRs (Fig. 3.11), with progressively younger and shorter AVRs being found to the north and south of the oldest and longest AVR (AVR 4). This along-axis pattern in the relative ages of AVRs suggests that AVRs are not randomly distributed along-axis, but that some underlying process controls the emplacement of AVRs and the tectonomagmatic cycle itself.

3.3 TOBI area B

TOBI area B extends from 28°40'W to 29°58'W and 59°44'N to 60°28'N (see Fig. 1.12). It is assumed to be within a region affected by the latest hotspot pulse as suggested by the absence of a median valley and the greatest abundance of seamounts along the whole ridge (Magde & Smith 1995). As discussed for TOBI area C, further constraints for the extent of hotspot influence are presented in Chapters 4 and 5. The average water depth in this area is 1250 m and AVRs rise ~400 m above the seafloor. The AVRs chosen for interpretation were selected on the basis of available TOBI data coverage, their length and along-track spacing. The chosen AVRs are: AVR 20, centred on 59°50'N, AVR 21 at 59°55'N, AVR 23 at 60°02'N, AVR 25 at 60°15'N and AVR 26 near 60°25'N.

3.3.1 AVR 20

This ~28 km long AVR, centred on 59°50'N, is composed of sheet flows, hummocky terrain and a variety of volcanoes (Fig. 3.12). The southern half of the AVR is characterised by relatively bright backscatter, indicating the presence of lava lows. A number of circular features with weak backscatter at their centre, interpreted as flat-topped volcanoes, are observed to the east and west of the southern half of the AVR. Sedimented hummocky terrain is visible off-axis to the west of the AVR. Small, unsedimented, hummocky ridges are visible on the AVR further to the north, towards the middle of the AVR. These ridges, which follow the overall trend of the AVR, probably originate from fissure type eruptions. Two large flat-topped volcanoes occur to the west of the hummocky ridges. The northern half of the AVR contains one large,

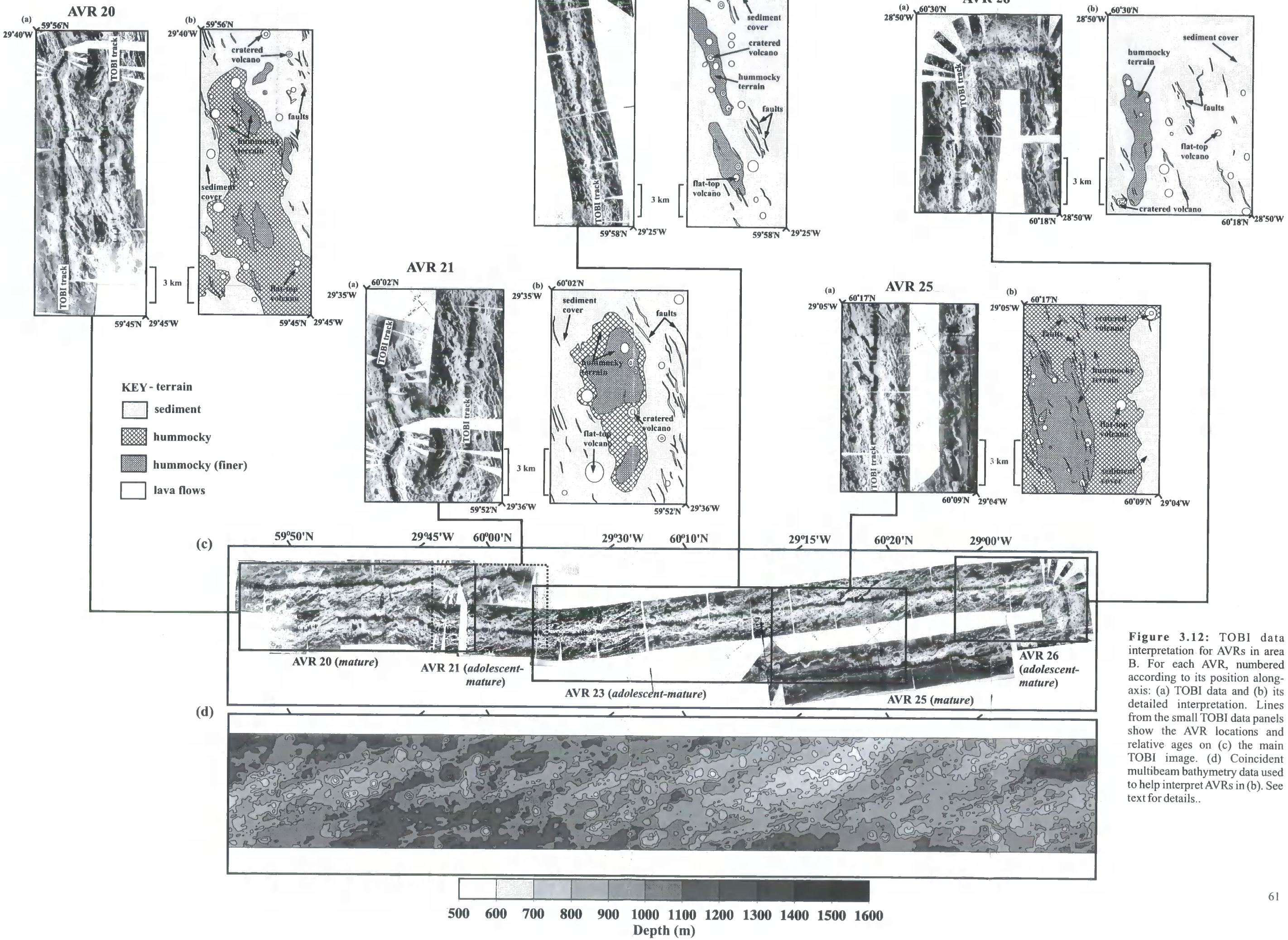

Figure 3.12: TOBI data interpretation for AVRs in area B. For each AVR, numbered according to its position along-axis: (a) TOBI data and (b) its detailed interpretation. Lines from the small TOBI data panels show the AVR locations and relative ages on (c) the main TOBI image. (d) Coincident multibeam bathymetry data used to help interpret AVRs in (b). See text for details..

prominent, normal fault that follows the AVR trend, four small, flat-topped volcanoes to the east and a hummocky ridge adjacent to a sigmoidal fault. The northern tip of the AVR contains one large flat-topped volcano and three cratered conical volcanoes can be observed in an offset basin to the north-east of the AVR. Normal faults principally appear off-axis and follow the AVR trend. The presence of flat-topped volcanoes, the AVR's broad shape and the presence on-axis of spreading-normal faults suggest that this AVR is at the *mature* part of its lifecycle.

3.3.2 AVR 21

The next AVR north, near 59°55'N, is 13 km long (Fig. 3.12). The southern end of the AVR comprises a large hummocky mound and a flat-topped and cratered conical volcano. The northern half is generally more hummocky, with one large, flat-topped volcano to the west and two smaller cratered conical, and one flat-topped volcanoes to the east. A number of volcanic edifices occur next to the AVR and faulting is pervasive off-axis, with a greater apparent number of faults to the east of the AVR, possibly indicating asymmetric spreading, which has been suggested for the ridge further south (Owen 1991; Searle *et al.* 1994a). This AVR appears to be slightly younger than the previous AVR and is probably *adolescent* to *mature* in age.

3.3.3 AVR 23

Further to the north, centred on 60°02'N, is the 12 km long AVR 23 (Fig. 3.12). This AVR is hummocky in appearance, with two cratered conical volcanoes at its southern end. The central portion of the AVR contains a large cratered conical volcano surrounded by two flat-topped volcanoes. Faulting is evident off-axis to the east, where a number of flat-topped volcanoes are also visible. The presence of cratered conical and flat-topped volcanoes suggest that this AVR is between the *adolescent* and *mature* stage of the cycle.

3.3.4 AVR 25

AVR 25, near 60°15'N, is 32 km long and consists of mainly hummocky terrain (Fig. 3.12). A number of flat-topped and a few conical volcanoes are visible over the whole AVR. Faulting is also visible on-axis with two prominent AVR-trending faults on the eastern and western sides of the AVR. The western fault is approximately 4 km long and bisects a flat-topped volcano at its southern end. The eastern fault, 3 km long, has a more sigmoidal appearance. A sediment patch is observed 6 km off-axis to the east. The

abundance of flat-topped and conical volcanoes, together with the extensive on-axis faulting suggests that this AVR is *mature* in age.

3.3.5 AVR 26

The most northerly AVR of TOBI area B, centred on 60°23'N, is 20 km long and hummocky in terrain (Fig. 3.12). Only three small flat-topped volcanoes are visible at its northern end. Faulting is less extensive than on the previous AVR, with a few small normal faults visible on-axis and larger faults off-axis to the east, suggesting that this AVR is *adolescent* to *mature* in age.

3.3.6 Summary of TOBI area B

AVRs in TOBI area B are mainly *adolescent* to *mature* in age and show less variability in morphology than AVRs in TOBI area C. In addition, the number of seamounts for each TOBI area is significantly different, with area B having twice the abundance of seamounts as area C and the ridge further to the north (Magde & Smith 1995). The seamounts in area B are also smoother than those in area C, where the proportion of hummocky seamounts is similar to that observed elsewhere on the MAR (e.g. Magde & Smith 1995).

These observations confirm the interpretation from gravity modelling (see Chapter 4) that TOBI area C is not, whereas TOBI area B is, directly effected by the Iceland hotspot. The lack of variability in AVR morphology may also be attributed to the proximity of the hotspot, with an increase in upper mantle temperature and corresponding melt production facilitating along-axis redistribution of melt (Bell & Buck 1992). Although no significant along-axis variation in AVR morphology is observed, a pattern similar to that described for area C, although perhaps more subdued, is apparent in the relative age of AVRs over ~70 km of the ridge axis. The oldest looking AVRs (20 and 25) are also the longest and AVRs appear to get progressively younger and shorter away from them (Fig. 3.12).

3.4 Summary of TOBI interpretation

In this chapter the morphological interpretation of the TOBI data confirms the existence of variations in the relative age of AVRs and reveals a correlation between relative AVR age and length, with shorter AVRs generally being younger than longer AVRs.

However, the four-stage cycle proposed by Parson *et al.* (1993) does not adequately explain all the morphological observations. AVRs are observed that have characteristics

of two stages, e.g. *adolescent* and *mature*. It is therefore proposed that a tectonomagmatic cycle can not be clearly defined by four stages alone, but that the *young-adolescent-mature-old* stages merely reflect snapshots of the continuous lifecycle of an AVR. An AVR does not jump from being *young* to *adolescent*, or *adolescent* to *mature*, instead it gradually evolves from one stage to the next, incorporating features characteristic of each stage in the transition process. In addition, AVRs of different age do not appear to be randomly distributed along-axis. Instead, a pattern, with a wavelength of ~70 km is observed, with progressively younger and shorter AVRs appearing to the north and south along-axis of an older and longer AVR.

In the next chapter, gravity modelling will be used to test the hypothesis outlined in Chapter 1, that the relative age of AVRs, as determined by the TOBI data interpretations presented in this chapter, should also be reflected in the crustal structure of individual AVRs.

Chapter 4

Gravity data reduction and modelling

4.1 Introduction

This chapter describes the theory and method of reducing gravity data by removing predictable effects from the observed anomaly. The resultant anomalies show different wavelengths, with long- (> 100 km), intermediate- (< 100 km) and short-wavelengths (< 10 km) modelled in terms of the steady-state influence of the Iceland hotspot, the pulsing of the hotspot and the effect of tectonomagmatic cycles respectively. The short-wavelength models are interpreted in conjunction with the TOBI data interpretation (see Chapter 3) to assess the effect of tectonomagmatic cycles on the crustal structure of individual AVRs.

The observed gravity field includes the gravitational effect of the whole Earth in addition to the contribution of anomalous mass distributions in the crust and upper mantle at all scales. To isolate the latter, the predictable parts of the Earth's gravitational field, which include the shape and rotation of the Earth as well as the latitude of the observation point together with its elevation above the chosen datum, must be removed. Thus, field measurements are corrected to obtain the FAA. The FAA observed over ocean covered areas primarily reflects the nature of the seafloor topography since the seawater-seafloor interface has a relatively large density contrast across it and it is the closest interface to the observation plane. The effect of this interface can be removed from the FAA with the Bouguer correction where the water layer is replaced with material of a density representative of basement rock, provided that accurate knowledge of the seafloor is known. This 1-D approach, however, is inadequate for areas of pronounced seafloor topography, such as the Reykjanes Ridge, and so the MBA, which involves a fully 3-D Bouguer correction, is applied in this case.

In the following section the theory and method of the MBA calculation is described. The gravitational effect of passive upwelling at the ridge axis is calculated and removed from the MBA in Section 4.3 and the results of modelling the resultant anomalies are presented according to their wavelength in Section 4.4. The main conclusions drawn from the models are summarised in Section 4.5.

4.2 Calculating the MBA

The MBA calculation, first applied in 3-D by Prince & Forsyth (1988) using a Fourier transform method developed by Parker (1973), extends the concept of the Bouguer correction by not only accounting for the variation in water column thickness in 3-D but also by calculating and removing the gravitational effect of the whole crust. For this process, a simple crustal model, often constrained by seismic refraction data, is draped beneath the seafloor topography and its 3-D gravitational effect is calculated and subtracted from the FAA. The remaining anomaly can then be attributed to crustal thickness and/or density variations from the model. In mid-ocean ridge environments, for example the Reykjanes Ridge, another possible source of anomaly is mantle density variations due to passive and/or buoyant upwelling at the ridge axis. Passive upwelling contributions to the gravity anomaly may also be predicted and subtracted from the MBA to create the residual mantle Bouguer anomaly (RMBA) (see Section 4.3).

4.2.1 Theory

The simplest way of calculating the gravitational effect of a 3-D body is to decompose it into smaller volumes (e.g. prisms or rectangular blocks) and to calculate and sum the gravitational effect of each small volume. However, this proves to be computationally demanding for complex bodies and the Fourier method developed by Parker (1973) provides a more efficient approach to the problem. In this method the gravitational field associated with a non-uniform and uneven layer is calculated on an observation plane that is everywhere above the layer (Fig. 4.1). The gravitational potential, U, at a position specified by $\mathbf{r}_o$ on the plane $z=z_o$, due to a layer of thickness $z=h(\mathbf{r})$ is given by equation 4.1, where G is the gravitational constant, ρ is the density of the layer material and $\mathbf{r}$ is the projection of $\mathbf{r}_o$ on the x-y plane.

$$U(\boldsymbol{r}_o) = G\rho \int_V \frac{dV}{|\boldsymbol{r}_o - \boldsymbol{r}|} = G\rho \int_D dS \int_0^{h(r)} \frac{dZ}{|\boldsymbol{r}_o - \boldsymbol{r}|} \qquad (4.1)$$

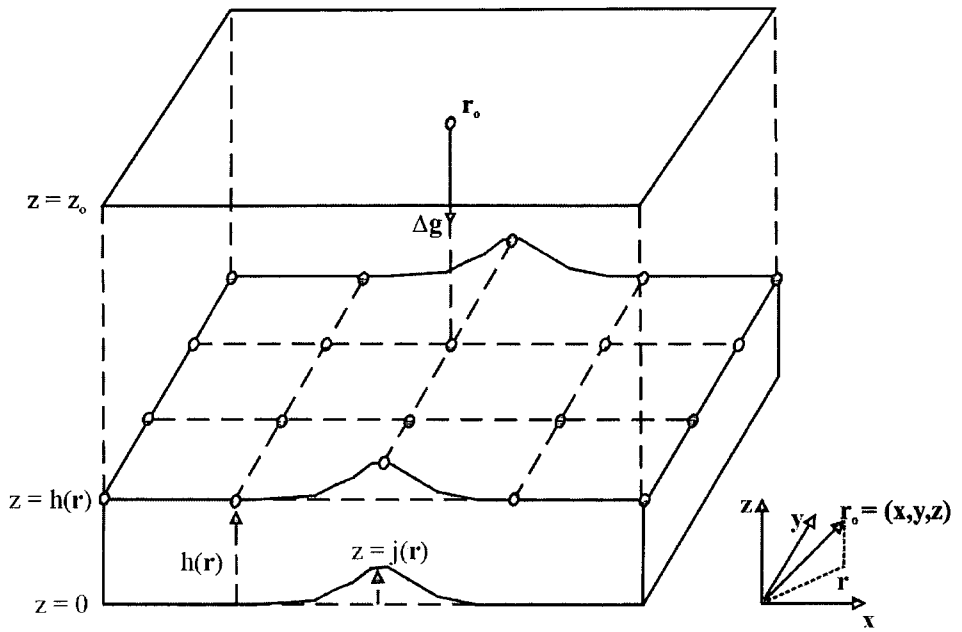

Figure 4.1: Parameters used in calculating the gravitational effect of an uneven layer. The gravitational attraction, $\Delta\mathbf{g}$, is calculated at a point specified by $\mathbf{r}_0$ on the observation plane $z=z_0$, for a layer whose density, $\rho(\mathbf{r})$, varies with position and with undulations of the top and bottom of the layer described by $h(\mathbf{r})$ and $j(\mathbf{r})$ respectively. $\mathbf{r}$ is the projection of $\mathbf{r}_0$ on the x-y plane.

Taking the Fourier transform of equation (4.1) and expressing one of the resulting exponential functions as a Taylor series leads to equation (4.2), and since the observation plane is everywhere above the layer, $\nabla \cdot g = 0$ and therefore $\nabla^2 U = 0$. The gravitational acceleration is $\Delta g = \frac{\partial U}{\partial z}$ and taking its Fourier transform gives the following expression $F[\Delta g] = -|k| F[U]$ which, when substituted into equation (4.2) leads to equation (4.3) where the lower boundary of the layer now varies as $g(\mathbf{r})$ and the density, ρ, now varies with $\mathbf{r}$. This equation can be readily extended for a multiple layer model.

$$F[U(\mathbf{r}_0)] = 2\pi G\rho \exp(-|k|z_o)\sum_{n=1}^{\infty}\frac{|k|^{n-2}}{n!}F[h^n(\mathbf{r})] \qquad (4.2)$$

$$F[\Delta g] = -2\pi G \exp(-|k|z_o)\sum_{n=1}^{\infty}\frac{|k|^{n-1}}{n!}F[\rho(\boldsymbol{r})\{h^n(\boldsymbol{r}) - j^n(\boldsymbol{r})\}] \qquad (4.3)$$

The gravitational attraction, Δg, is then obtained by taking the inverse transform of equation (4.3). These equations, numerically implemented using Fast Fourier Transforms (FFT), form the basis of a fortran computer program *grav2d* (Kuo & Forsyth 1988), that calculates the gravitational effect of a constant thickness and density crust draped beneath the seafloor bathymetry. The use of FFT requires the layer geometry to be specified on a regular grid of nodes with the node separation being less than the distance between the observation plane and the source layer to avoid aliasing problems. In addition, Fourier transforms assume a periodicity in the data that does not exist in seafloor bathymetry and possible edge effects must, therefore, be taken into consideration by either mirroring the dataset or by padding the edges of the dataset so that the study area is distanced from the edges.

4.2.2 Method

A simple crustal model (Fig. 4.2), based on the off-axis wide-angle seismic refraction model of Navin *et al.* (1998) near 57°45'N, together with the seafloor bathymetry compilation (see Section 2.3) was used to calculate the MBA as described above. Navin *et al.* (1998)'s off-axis model was chosen in preference to other available models (Bunch & Kennet 1980; Smallwood *et al.* 1995; Weir *et al.* 2001) as it is the only model constrained by a multidisciplinary geophysical dataset collected together with the seismic data. The off-axis model was chosen as the basis of this calculation as it is considered to be more representative of "normal" oceanic crust than the on-axis model. In this way, gravity anomalies associated with the on-axis AVRs will be highlighted relative to the gravity anomaly off-axis background.

The simple crustal model consists of constant thickness and density layers 2A, 2B and 3 draped beneath the seafloor. Average thicknesses of 0.5 km, 2.0 km and 4.5 km for layers 2A, 2B and 3 respectively were taken from Navin *et al.* (1998)'s off-axis wide-angle model. A sediment layer was not included in the model as there is insufficient data to construct a sediment isopach along the entire length of the ridge and the ridge axis is mainly devoid, except for isolated sediment pockets in basins, of sediment cover (Talwani *et al.* 1971).

The presence of these sediment pockets will, however, give rise to local MBA lows, as sediment density is lower than layer 2A density. It has been shown, however, (Prince & Forsyth 1988; Kuo & Forsyth 1988; Field 1994) that the gravitational attraction of a gradational crustal density structure does not significantly differ from the effect of a constant crustal density model. The stratified crustal model was nevertheless retained

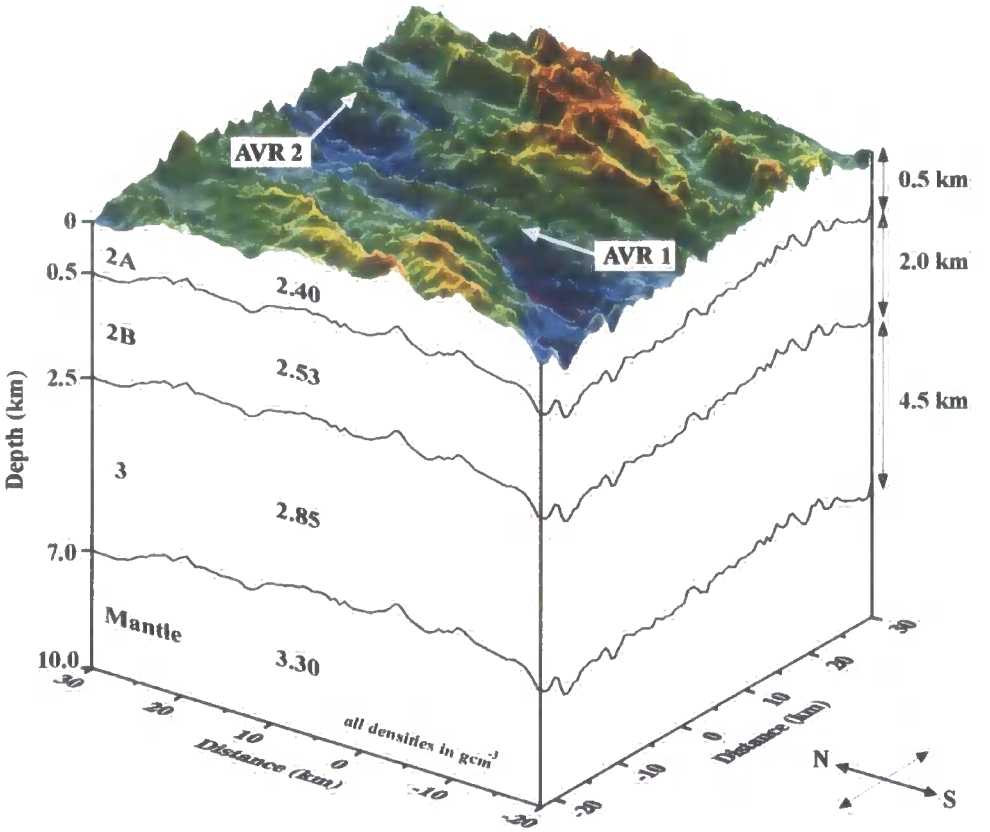

Figure 4.2: Simple crustal model shown here for the area surrounding the 57°45'N AVR (AVR 1) and the AVR centred on 58°05'N (AVR 2). Layers of constant density and thickness (derived from the off-axis wide-angle seismic model of Navin *et al.* 1998) are draped beneath the seafloor topography. Thickness and densities of each layer are annotated.

for reasons of completeness. Estimates of layer density, summarised in Table 4.1, were initially based upon *P*-wave velocity-density relationships (Nafe & Drake 1957, 1962; Carlson & Raskin 1984). Navin *et al.* (1998) adjusted these initial densities for their wide-angle models, keeping the seismically-derived layer geometries unchanged, until a best-fit to the observed gravity anomaly was obtained. Thus for this study Navin *et al.* (1998) densities and a mantle density of 3.30 g cm^{-3}, typical of many ridge axis gravity studies (e.g. Kuo & Forsyth 1988; Cormier *et al.* 1995), were used for the layers of the model in the MBA calculation. Throughout this thesis densities are quoted in g cm^{-3} for the purpose of brevity of annotation on figures – 1 g cm^{-3} is equivalent to 1000 kg m^{-3}.

		Nafe-Drake (1957)	*Carlson & Raskin (1984)*			*Navin et al. (1998)*	*This study*
	Vp (km s^{-1})	ρ_{nd} (g cm^{-3})	ρ_{m2} (g cm^{-3})	ρ_{m3} (g cm^{-3})	Av_ρ (g cm^{-3})	(g cm^{-3})	(g cm^{-3})
Water	1.49	-	-	-	-	1.03	1.03
Sediments	2.60	2.10	1.51	2.04	1.89	1.60	-
Layer 2A/2B	3.50/5.0	2.54	2.61	2.74	2.63	2.40/2.53	2.40/2.53
Layer 3	6.75	2.89	2.92	2.94	2.92	2.85	2.85
Mantle	8.00	3.26	3.06	3.03	3.11	3.30	3.30

Table 4.1: Initial gravity model layer densities using average *P*-wave velocities derived from the main layers of Navin *et al.* (1998)'s across-axis wide-angle seismic model. Vp - average *P*-wave velocity of each layer, ρ_{nd} - density from the Nafe & Drake (1957) relationship, and ρ_{m2} and ρ_{m3} - densities from methods 2 and 3 respectively of Carlson & Raskin (1984). The average of these three methods is shown for reference (Av_ρ). Initial density estimates for the along-axis 2-D models are shown in the right-hand column for comparison and the mantle is represented by a density of 3.30 g cm^{-3}, common to many ridge gravity studies (e.g. Kuo & Forsyth 1988; Cormier *et al.* 1995). The main difference between the two methods of Carlson & Raskin (1984) is that method 3 attempts to take into account the large-scale porosity encountered in oceanic layer 2A.

Having created a geologically reasonable crustal model its gravitational effect, including the seafloor topography, can be calculated using *grav2d*. As the program requires the calculations to be performed on a regular grid, the bathymetry data were rotated about 57°45'N/32°30'W such that the average ridge trend of 036° becomes oriented in a "north-south direction", with the data points themselves projected to a cartesian coordinate system and resampled at 0.2 km intervals in both x and y. For computational reasons the rotated grid was subdivided into two overlapping 512 by 2048 node grids (grids A and B in Figs. 4.3 and 4.4) that were mirrored on each side to avoid edge effects. *grav2d* calculates, upward continues to the sea surface and sums the gravitational attraction of each interface to give the total field predicted by the model. Table 4.2 shows the main parameters used in the MBA calculation.

	Parameter	Value
General		
	Bathymetry grid node spacing (latitude/longitude)	0.12'/0.06'
	Spreading half rate	10 mm yr^{-1}
	Resampled and rotated bathymetry:	
	number of samples in x	512
	number of samples in y	2 x 1024
	node spacing in x	0.2 km
	node spacing in y	0.2 km
MBA		
	Number of model layers	4
	Densities of layers:	
	water	1.03 g cm^{-3}
	2A	2.40 g cm^{-3}
	2B	2.53 g cm^{-3}
	3	2.85 g cm^{-3}
	mantle	3.30 g cm^{-3}
	Depth of layer interface beneath seabed:	
	2A/2B	0.5 km
	2B/3	2.5 km
	Moho	7.0 km
RMBA		
	Thermal expansion coefficient	3.4 x 10^{-5} $°C^{-1}$
	Gravitational constant	6.673 x 10^{-11} N m^2 kg^{-2}
	Plate thickness	100 km
	Asthenospheric temperature	1350 °C

Table 4.2: Main parameters used in the MBA and RMBA calculations. See Section 4.3 for details.

As Fig. 4.3 shows, a DC-shift is observed between the two resulting predicted field grids in the overlap region. As part of the calculation process the FFT algorithm removes the average seafloor depth before calculating the gravitational attraction. Thus, the average seafloor depth being different for the two grids, a DC-shift between them results. A DC-shift of 25 mGal was, therefore, applied to grid B to align the two anomaly grids (see Fig 4.3), before cutting and pasting them together along a common edge in the middle of the overlap region.

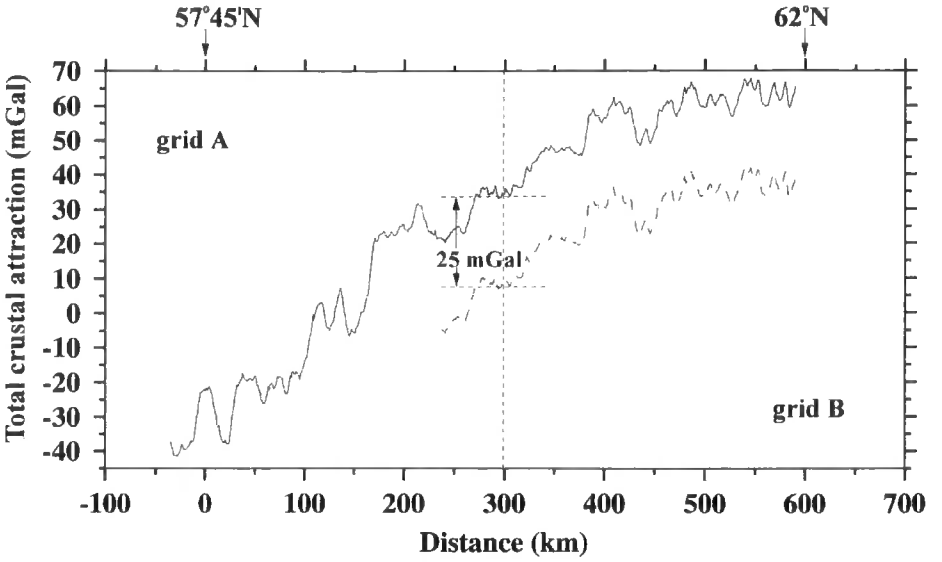

Figure 4.3: Along-ridge-axis profiles of whole crust gravitational attraction calculated by *grav2d* showing the DC-offset between grids A and B resulting from the different average seabed depths. The long-dashed line is the along-axis profile through grid B only and the solid line shows the profile through grid A as well as the shifted data from grid B. The two grids overlap along-axis between 236.6 km and 341.4 km as shown by the extent of the horizontal dotted lines, which also indicate the magnitude (25 mGal) of the DC-shift applied. Both grids were cut and paste along a common edge at 299 km along-axis (delineated by the vertical dashed line).

As approximately 70% of the total crustal attraction (Fig. 4.4c) can be attributed to the seawater-seafloor interface (Fig. 4.4b), due to the large density contrast between the water column and layer 2A, the total predicted crustal attraction, not unsurprisingly, mirrors the seafloor topography and the FAA (Fig. 4.5a). The axial rise and valley morphologies of the ridge result in total crustal attraction highs and lows respectively, with local highs associated with the more pronounced AVRs superimposed. The MBA is calculated by subtracting the calculated total crustal attraction from the FAA (Fig. 4.5). As part of this process the total crustal attraction grid was down-sampled to 0.25 km by 1 km, to match the sampling interval used for the FAA before direct subtraction. Fig. 4.5(c) shows the resultant MBA grid whose main features are:

(1) A gradual decrease in on-axis magnitude from 45 mGal at 57°25'N in the south to -10 mGal near 62°N to the north, together with an along-axis gradient of 0.095 mGal km^{-1} with peak-to-trough amplitudes of 1-10 mGal. The general northwards decrease in MBA supports the suggestion that the crust thickens and/or upper mantle density decreases towards Iceland, which may reflect ridge-hotspot interaction processes (see Section 4.4.1).

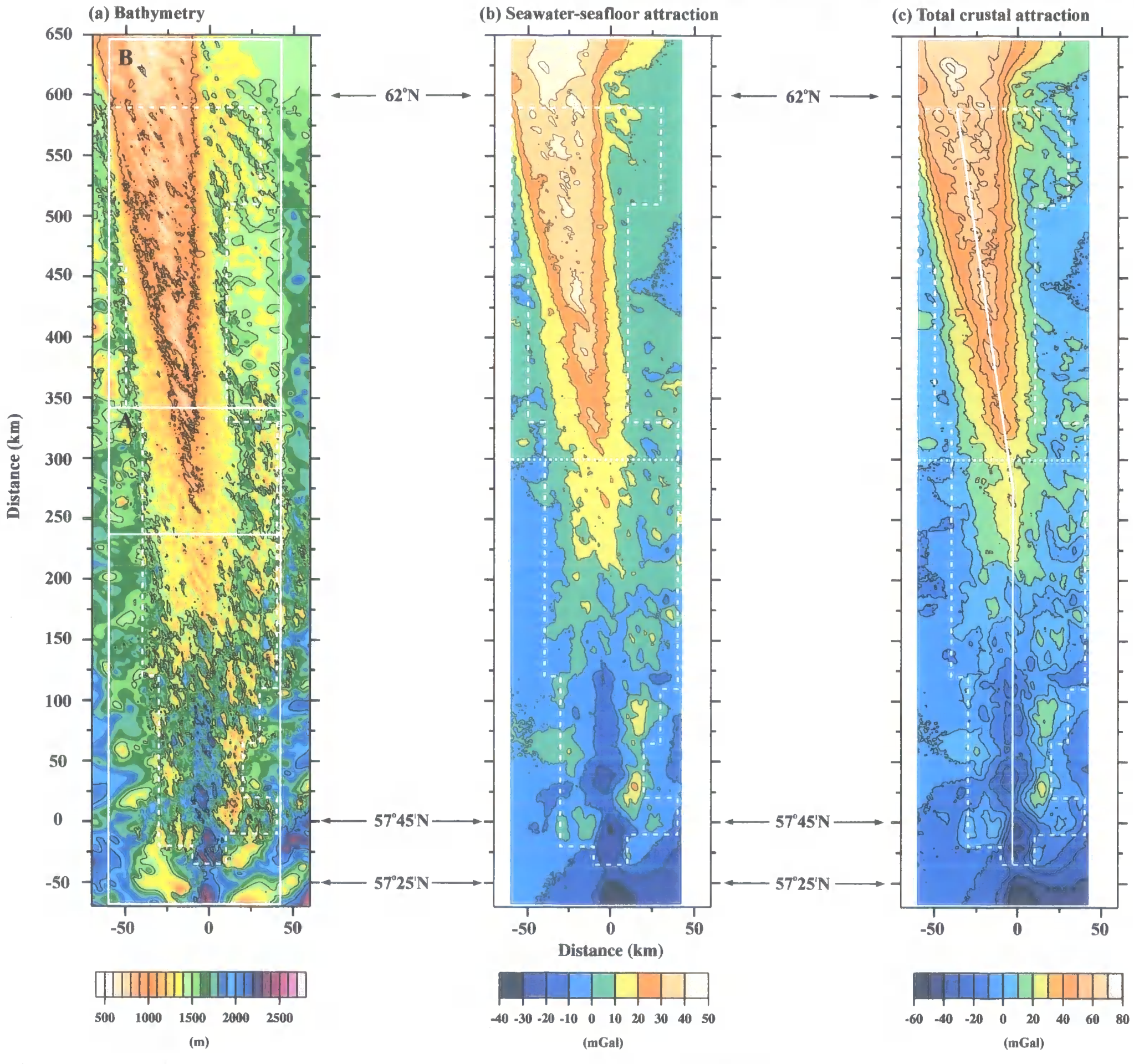

Figure 4.4: Stages of the MBA calculation - input to and output from *grav2d*. (a) The bathymetry data was rotated to align the overall trend of the ridge (036°) in the "N-S" direction, projected to cartesian coordinates and re-gridded at a spacing of 0.2 km in both x and y. Two 512 by 2048 overlapping grids (solid line), labelled A and B, were input separately to the program. Contours are plotted every 500 m. (b) Output of *grav2d* for the seawater-seafloor interface. Contours are plotted every 10 mGal. (c) Total predicted crustal attraction output from *grav2d*, consisting of the summed effect of all modelled density layer interfaces. The solid line marks the location of the along-axis profile shown Fig.4.3. Contours are plotted every 10 mGal. For both (b) and (c) grid B has been DC-shifted along the dotted line to minimise the mismatch in the overlap region (see Section 4.2.2). In all cases the dashed outline shows the approximate extent of the ship data.

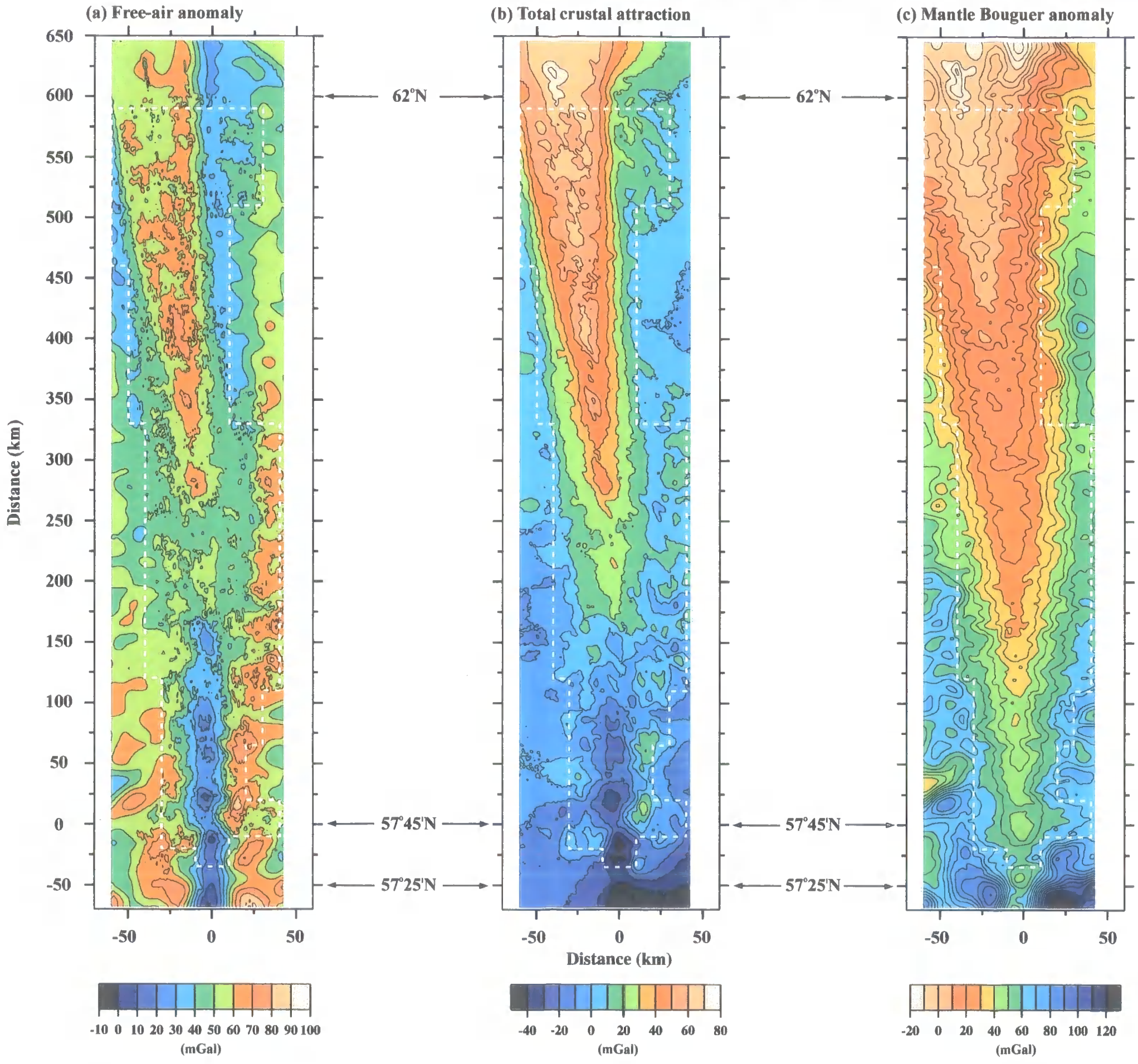

Figure 4.5: Stages of the MBA calculation - subtracting the total crustal attraction. (a) FAA projected into a cartesian coordinate system. (b) Total crustal attraction calculated for a simple crustal model draped beneath the seafloor by *grav2d*. (c) MBA calculated by subtracting the total crustal attraction from the FAA. The anomalies no longer mirror the bathymetry but instead reflect variations in crustal thickness and/or density and/or mantle density from the model. Contours are plotted every 10 mGal in (a) and (b) and every 5 mGal in (c). The dashed line indicates the extent of the ship data in all cases.

(2) A number of AVRs are associated with "bull's eye" pattern relative lows of the order of ~ 5 mGal, similar to those observed elsewhere on the MAR (Kuo & Forsyth 1988; Lin *et al.* 1990; Tolstoy *et al.* 1993; Detrick *et al.* 1995), although the latter have much larger amplitudes. These AVR-scale anomalies are investigated in detail in Section 4.4.2 but possible explanations include thicker crust, lower mid-crustal densities associated with the presence of partial melt, and/or lower upper mantle densities beneath AVR centres. The local anomaly highs over the inter-AVR basins suggest the presence of thinner crust (Searle *et al.* 1994a).

However, the MBA still contains the gravitational effects of passive upwelling at the ridge axis. Calculation of the RMBA, which attempts to remove this effect, will be described in the next section.

4.3 Calculating the RMBA

4.3.1 Theory

The result of the MBA calculation has highlighted the differences between the real crustal and upper mantle structure of the Reykjanes Ridge and the simple model which forms the basis of the calculation. However, the calculation has neglected the lateral density variations associated with the spreading and cooling of newly created lithosphere at the ridge axis. Forsyth & Wilson (1984) solved the 3-D equations for heat conduction and material transport for a ridge-transform-ridge system (Fig. 4.6a) and define as its basis a mantle flow pattern with flow in the vertical direction in a triangular region, whose width is governed by the spreading-rate, beneath each ridge segment and horizontal flow in the plate spreading direction outside of this region.

A steady-state solution is reached by calculating the effects of advection and conduction separately. In the advection step, see Fig. 4.6(b), temperatures are translated from one grid point to another, along the prescribed flow lines, by a distance dictated by the spreading rate and the time step modelled. Following this step the "model" cools conductively for the same time period as in the advection part. Conductive cooling is described by the heat flow equation (4.4), where $T = T(x,y,z,t)$ is a function of three-dimensional position and time, and κ is the thermal diffusivity.

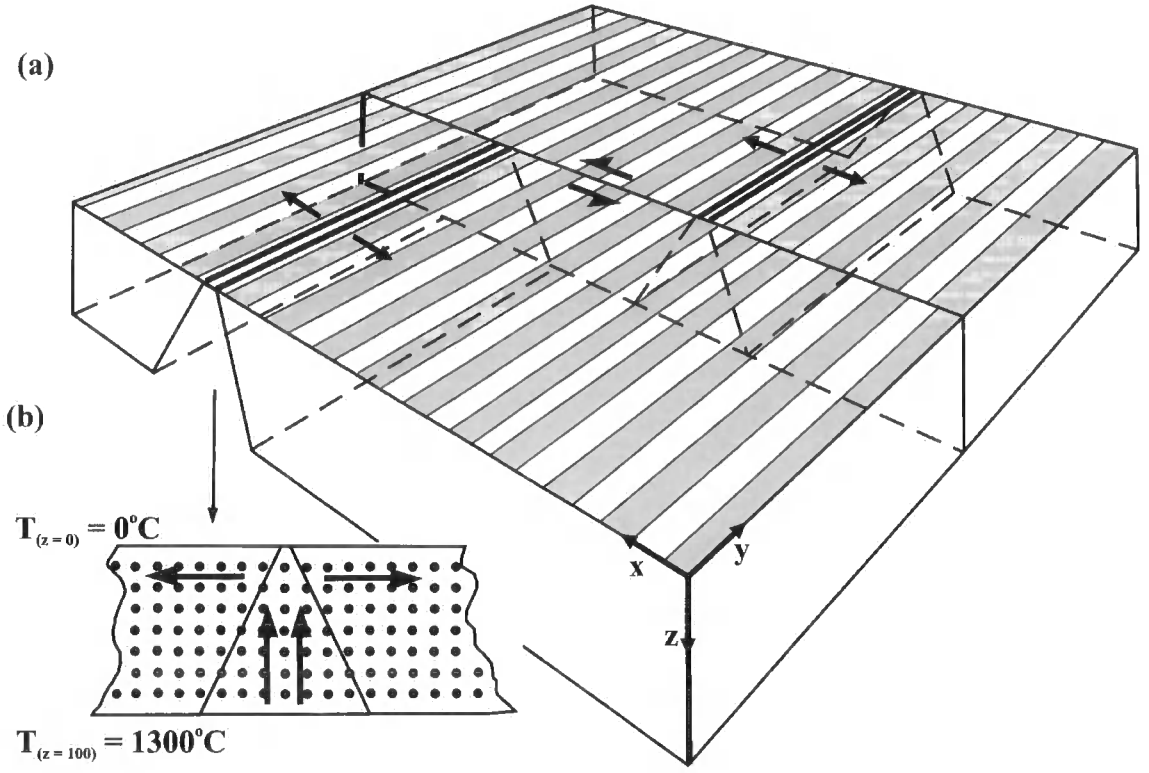

Figure 4.6: Ridge-transform-ridge system geometry used to calculate the gravitational effects of passive upwelling (after Forsyth & Wilson 1984). (a) Flow is in the vertical direction in a triangular region beneath each ridge segment and in a horizontal direction, perpendicular to the ridge, outside. (b) Diagramatic representation of the advection step of the calculation showing boundary conditions: T = 0°C at z = 0 km and T = 1300°C at z = 100 km, the top and bottom of the lithospheric plate respectively. The temperature at each point in the 3-D grid defining the ridge-transform-ridge system and depth is translated according to this flow pattern.

$$\nabla^2 T = \frac{1}{\kappa}\frac{\partial T}{\partial t} \qquad (4.4)$$

The solution must satisfy the boundary conditions $T_{(z=0)} = 0°C$ and $T_{(z=100)} = 1300°C$, temperatures defined at the top and bottom of the plate respectively, as well as the temperature distribution after advection at the start of the conduction time step. The solution, T, to the conduction step is separated into a steady-state part, T_s, and a transient component, T_t, so that $T = T_s + T_t$. The steady-state solution corresponds to a linear temperature gradient in the absence of a heat source, i.e. the "model" is simply allowed to cool via conduction. The transient state, given by subtracting the steady-state solution from the last step of the advection stage, is solved using Fourier transforms. A steady-state solution to the whole system is approached through alternating advection and conduction steps with decreasing time intervals.

4.3.2 Method

A series of fortran programs - *rtrflow*, *upwsor*, *intreg*, *intreg1* and *pratt* written by Forsyth & Wilson (1984) - calculate the flow pattern in the asthenosphere, the flow induced thermal variations, the corresponding density variations and the upward-continued thermally induced gravity anomalies respectively for a ridge-transform-ridge system. As the programs require that the ridges and transforms lie exactly on grid points running "north-south", the bathymetry was rotated so that this time the average AVR trend (006°) lay in a "north-south" direction (Fig. 4.7) as opposed to the ridge trend as is the case for the MBA calculation. The change in ridge-trend near 59°N (Fleischer 1974), ~225 km along-axis in the cartesian coordinates of Fig. 4.7, and possible thermal effects of large non-transform discontinuities were taken into account when subdividing the ridge into smaller segments along individual AVRs as identified from the bathymetry data compilation.

A ridge-transform-ridge system was traced over the en-echelon AVR pattern and transcribed into a 1024 by 1024 grid system with a 1 km node spacing. The size of the grid was chosen to effectively remove the FFT periodicity edge-effects from the study area. Fig. 4.8 shows a horizontal slice at 6 km depth through the calculated thermal anomaly and the total gravitational effect of passive upwelling of the ridge system. The long-wavelength thermal and gravity anomalies, as would be expected, follow the overall ridge trend and increase in amplitude from approximately -20 mGal at the ridge axis to 0 mGal 50 km off-axis.

The thermal anomaly and the MBA were then back-rotated to geographic coordinates and the thermal anomaly subtracted from the MBA to obtain the RMBA (Fig 4.9). Comparison of the MBA with the thermal anomaly calculation shows that the latter corresponds to the long-wavelength trend of the MBA and that removal from the MBA leaves the RMBA with a peak-to-peak amplitude that suggests that 40% of the MBA is related to the effects of passive upwelling. It follows that a siginificant part of the MBA, and therefore the RMBA, reflects crustal thickness/density variations from the crustal model (see Fig. 4.2), although another possible source of the anomaly is upper mantle density variation due to buoyant upwelling.

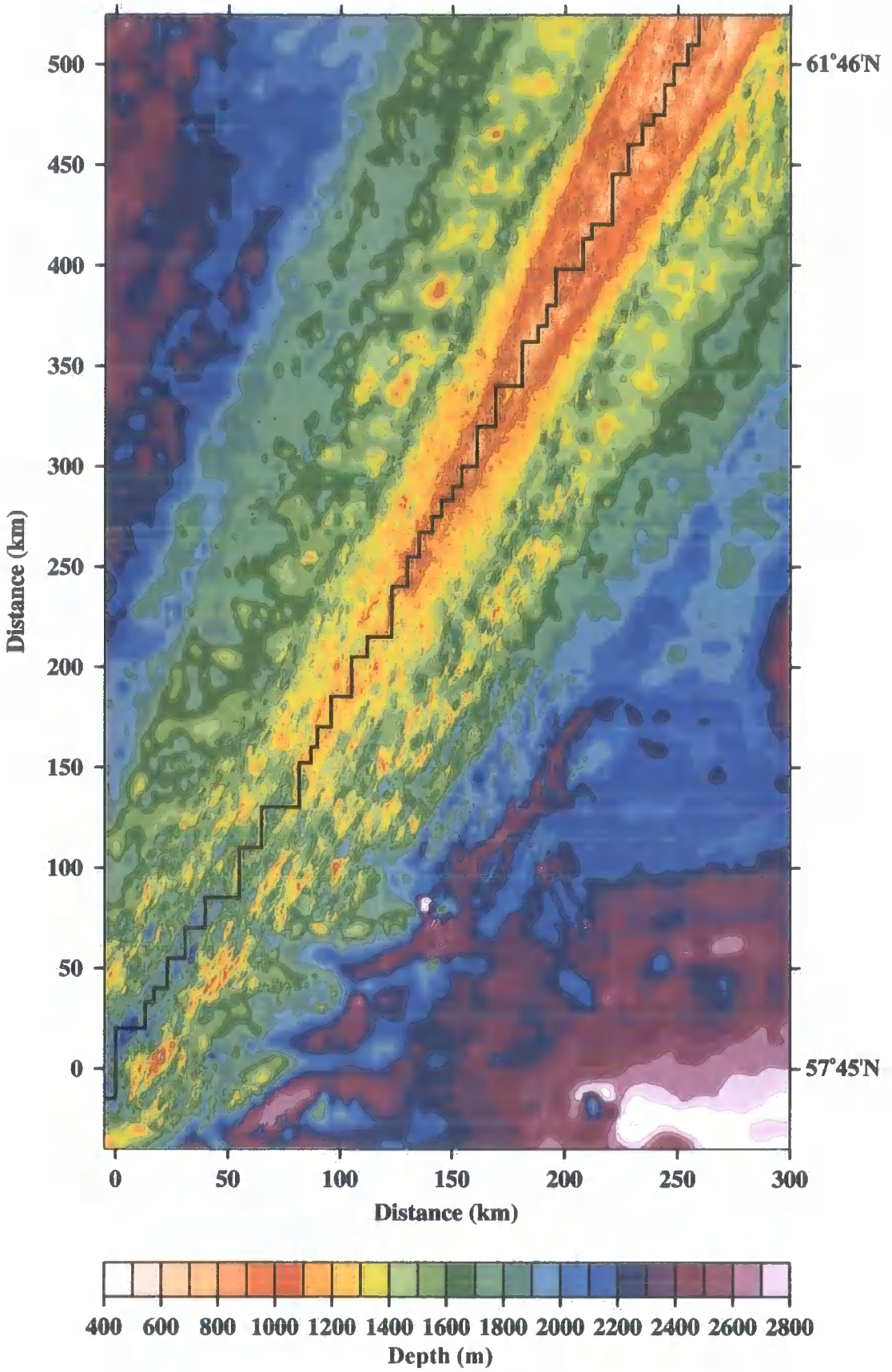

Figure 4.7: Bathymetry data rotated to align AVRs in a "N-S" direction and projected to cartesian coordinates. Solid black line shows the AVR-discontinuity-AVR system picked for the thermal calculation. Contours plotted every 500 m. Note the grid is substantially patched to both sides to avoid edge effects.

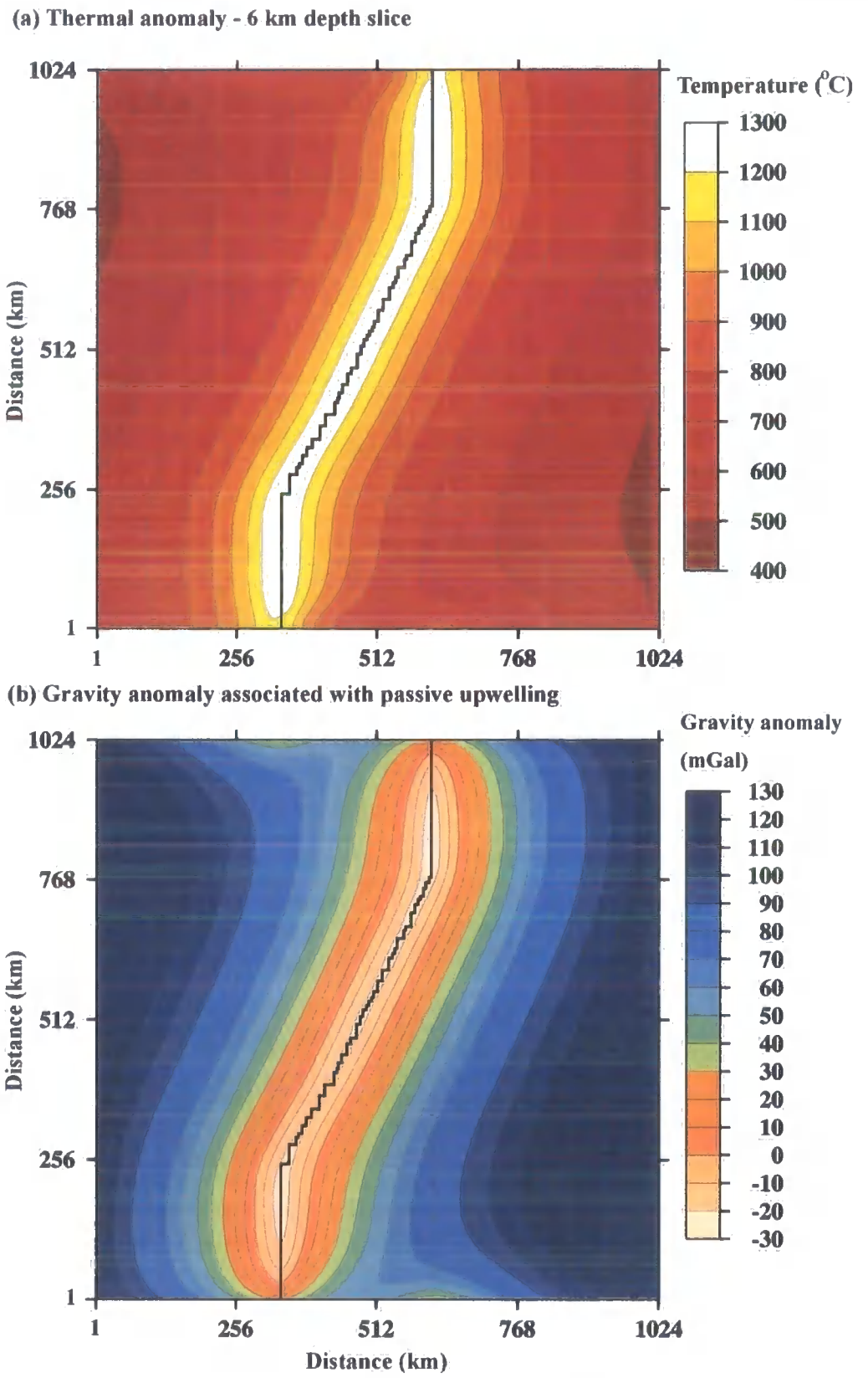

Figure 4.8: Examples of output from the thermal calculation programs. (a) A horizontal slice at 6 km depth through the thermal anomaly, showing that it follows the overall ridge trend as expected and that temperature decreases away from the ridge axis. (b) Total gravity anomaly associated with passive upwelling at the ridge axis. Again, the anomaly follows the overall ridge trend and decreases off-axis. In both cases the solid black line shows the AVR-discontinuity-AVR pattern which forms the basis of the calculation.

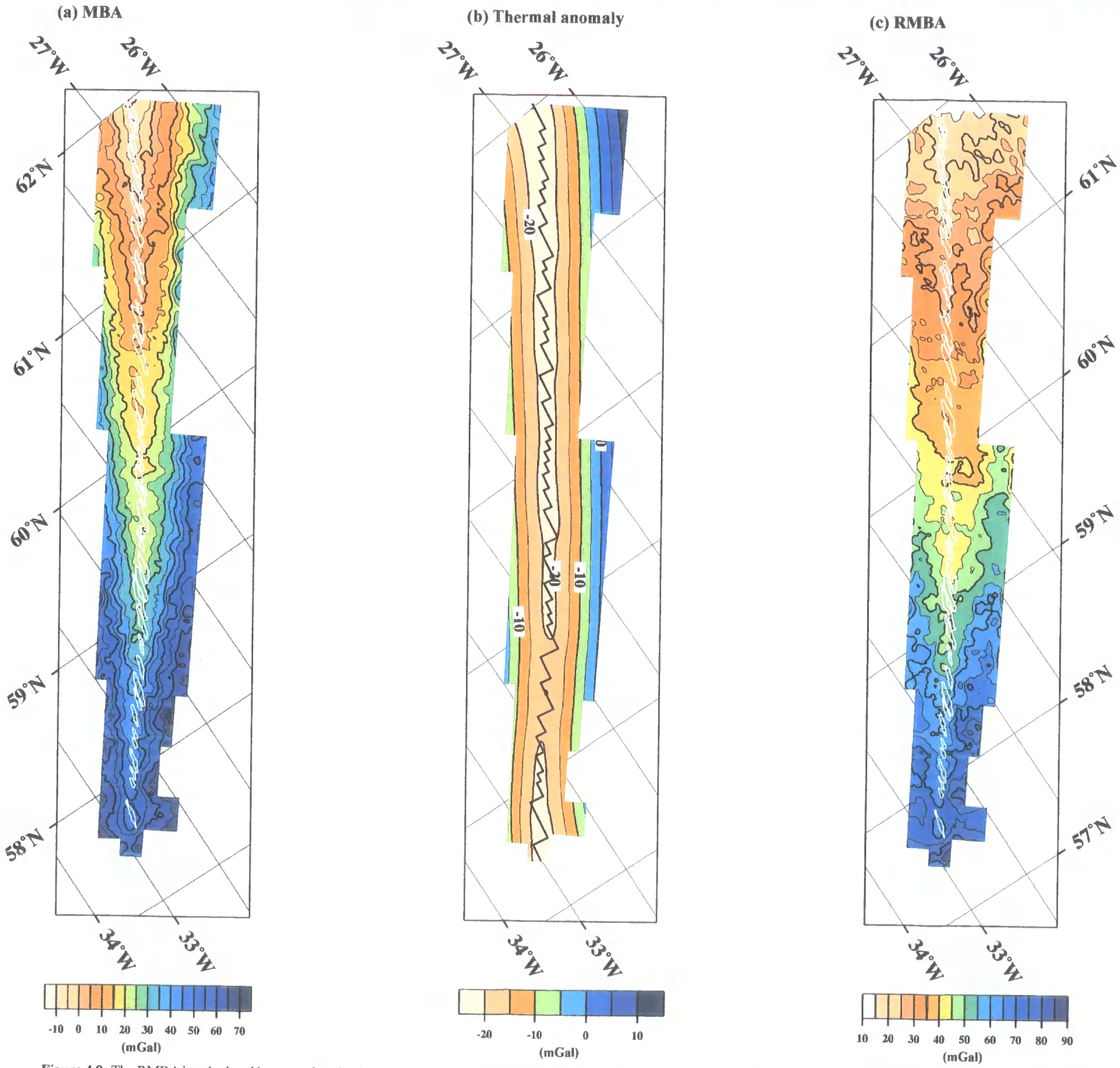

Figure 4.9: The RMBA is calculated by removing the thermal effects of passive upwelling at the ridge from the MBA. (a) MBA, back-rotated to geographic coordinates, highlighting deviations in crustal thickness, density and/or mantle density from the initial model. (b) Gravitational effect of passive upwelling at the ridge axis with AVR-discontinuity-AVR system superimposed in black. (c) RMBA calculated by subtracting the thermal effects from the MBA, thus, anomalies in the RMBA cannot be attributed to passive upwelling. AVR outlines are superimposed in white. Contours are plotted every 5mGal in all cases.

4.4 Results and models

The RMBA, calculated by subtracting the thermal anomaly from the MBA (Fig. 4.9), still shows a decrease in anomaly magnitude towards Iceland and the "bull's eye" lows associated with individual AVRs, confirming that the MBA variations are not simply related to the thermal effects of simple passive upwelling but are due to either variations in crust and/or mantle density or crustal thickness. Along-axis profiles taken from the bathymetry, FAA, MBA, thermal anomaly and RMBA grids (Fig. 4.10) show the various stages of the RMBA calculation and the two RMBA wavelengths that are observed. The long-wavelength trend is an almost linear decrease in magnitude towards Iceland, from ~80 mGal at 57°45'N to ~10 mGal near 62°N. Shorter-wavelength anomalies are superimposed on the Iceland trend and correlate with AVR positions, with relative RMBA lows of up to -6 mGal associated with AVR centres. It is hypothesised that the long-wavelength trend reflects crustal thickness and/or upper mantle density variations associated with the proximity of the Iceland hotspot and that short-wavelength anomalies reflect variations in the crustal structure of individual AVRs.

In Section 4.4.1 the influence of the Iceland hotspot on the along-axis structure of the ridge will be examined, and in Section 4.4.2 the crustal structure of individual AVRs will be investigated, establishing whether a correlation can be made between crustal structure and relative AVR age (see Sections 3.2 and 3.3).

4.4.1 Long- and intermediate-wavelength features

Before investigating any short-wavelength (~10 km) gravity anomalies, in relation to the hypothesised crustal structure signature related to the tectonomagmatic effects associated with individual AVRs, an investigation of the longer-wavelength anomaly associated with the proximity of the Reykjanes Ridge to the Iceland hotspot was undertaken. Using constraints placed on crustal layer thickness and velocity, and hence density structure, by the interpretation of wide-angle seismic data acquired along the entire ridge length (see Section 1.5.4), gravity modelling may be used to place bounds on the variation in larger-scale crustal features over this length scale.

The along-axis FAA was modelled instead of the RMBA, which has the effect of seafloor depth variations removed, to highlight the importance of the decreasing seafloor depth towards Iceland. The results of modelling the RMBA along-axis would be equally valid and would not differ significantly from the modelling results presented in this section. Thus, an approximately 650 km long profile, with a sample interval of

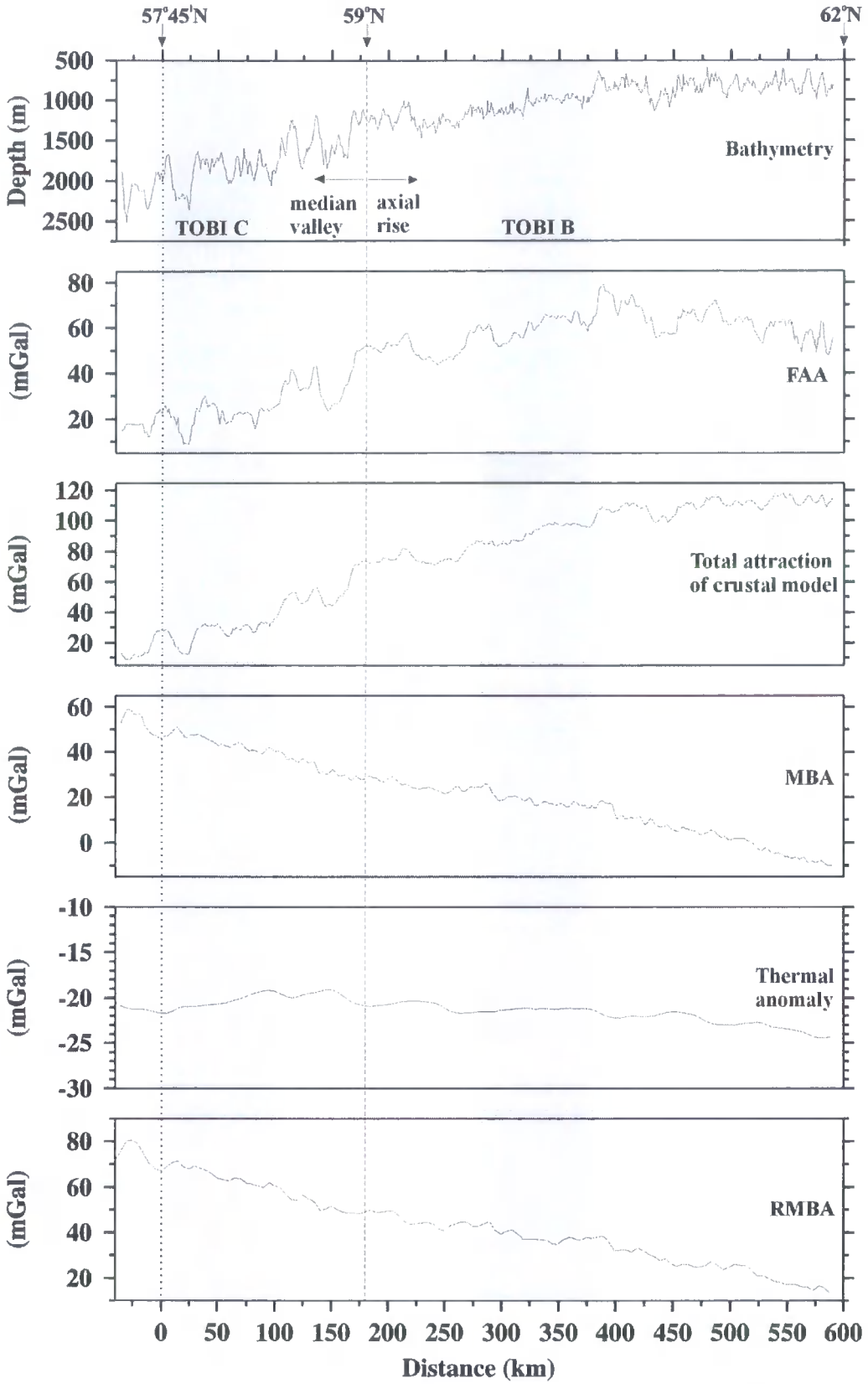

Figure 4.10: Along-ridge-axis profiles showing the various stages of the RMBA calculation. The FAA mirrors the bathymetry. However, from ~400 km, the average FAA decreases whereas the depth and the calculated total crustal attraction remains approximately constant. Subtracting the predicted crustal attraction from the FAA, therefore, results in a long-wavelength decrease in MBA towards Iceland. Short-wavelength relative MBA and RMBA highs and lows are associated with discontinuities and AVRs respectively (e.g. 57°45'N AVR at 0 km along-axis). Note that the MBA has been DC-shifted to match the MBA of Searle *et al.* (1998).

5 km, was extracted from the FAA compilation described in Section 2.5.6. The choice of sample interval was constrained by the finite number of data points accepted by the modelling program. Initial estimates of model layer density were obtained from the along-axis gravity model of Navin *et al.* (1998). A three-layer (water, crust, and mantle) approach was adopted for the along-axis modelling of the FAA since only the long-wavelength anomaly is of interest in this section. The along-axis variation in layer 2A results in only short-wavelength (<10 km) anomalies (Weir *et al.* 2001) and the increase in layer 2B thickness towards Iceland (Section 1.5.4) can be incorporated into an 'average' crustal model and, hence, these are not included specifically. Two-dimensional (2-D) gravity modelling in all cases was undertaken using the program *gravmag* (British Geological Survey - Pedley *et al.* 1993). Model boundaries were extended to 1000 km either side and to 50 km depth to avoid edge effects.

Modelling was constrained using zero-age crustal layer thickness determinations (± 1.0 km in all cases) of 7.5 km, 8.0 km and 10.0 km obtained from seismic models at 57°45'N, 59°30'N and 61°40'N respectively (Navin *et al.* 1998; Bunch & Kennet 1980; Smallwood *et al.* 1995 respectively and see Fig. 1.14). There are a number of potential causes of variation of the observed FAA (apart from variation in the seabed topography which contributes significantly to the observed field): a) crustal thickness variation; b) density variation in the crust; c) density variation in the upper mantle; and d) a combination of any of the aforementioned causes. However, only variations in crustal thickness (Fig. 4.11b), upper mantle density (Fig. 4.11c) and a combination of crustal thickness and upper mantle densities (Fig. 4.11d) were modelled, as seismic observations suggest that they are the most likely long-wavelength effects of the Iceland hotspot on the along-axis crustal structure of the ridge.

Modelling shows (Fig. 4.11b) that a simple increase in crustal thickness of ~4.5 km, from 7.0 km at 57°45'N to ~11.5 km at 62°N, can account for the observed gravity anomaly. However, the model does not fit the crustal thickness determination of Bunch & Kennet (1980) at 59°30'N and probably overestimates the crustal thickness further north (Weir *et al.* 2001). A constant thickness crust of 7.1 km, with a decrease in upper mantle density from 3.30 g cm^{-3} at 57°45'N to 3.14 g cm^{-3} near 62°N (Fig. 4.11c), can also reproduce the observed anomaly. A constant thickness crust model, however, can not be made to fit the seismic observations of Weir *et al.* (2001) both in terms of overall crustal thickness and upper mantle density, 11.0 km and 3.23 g cm^{-3} respectively at 62°40'N. Clearly, a combination of crustal thickness and upper mantle density variations is required.

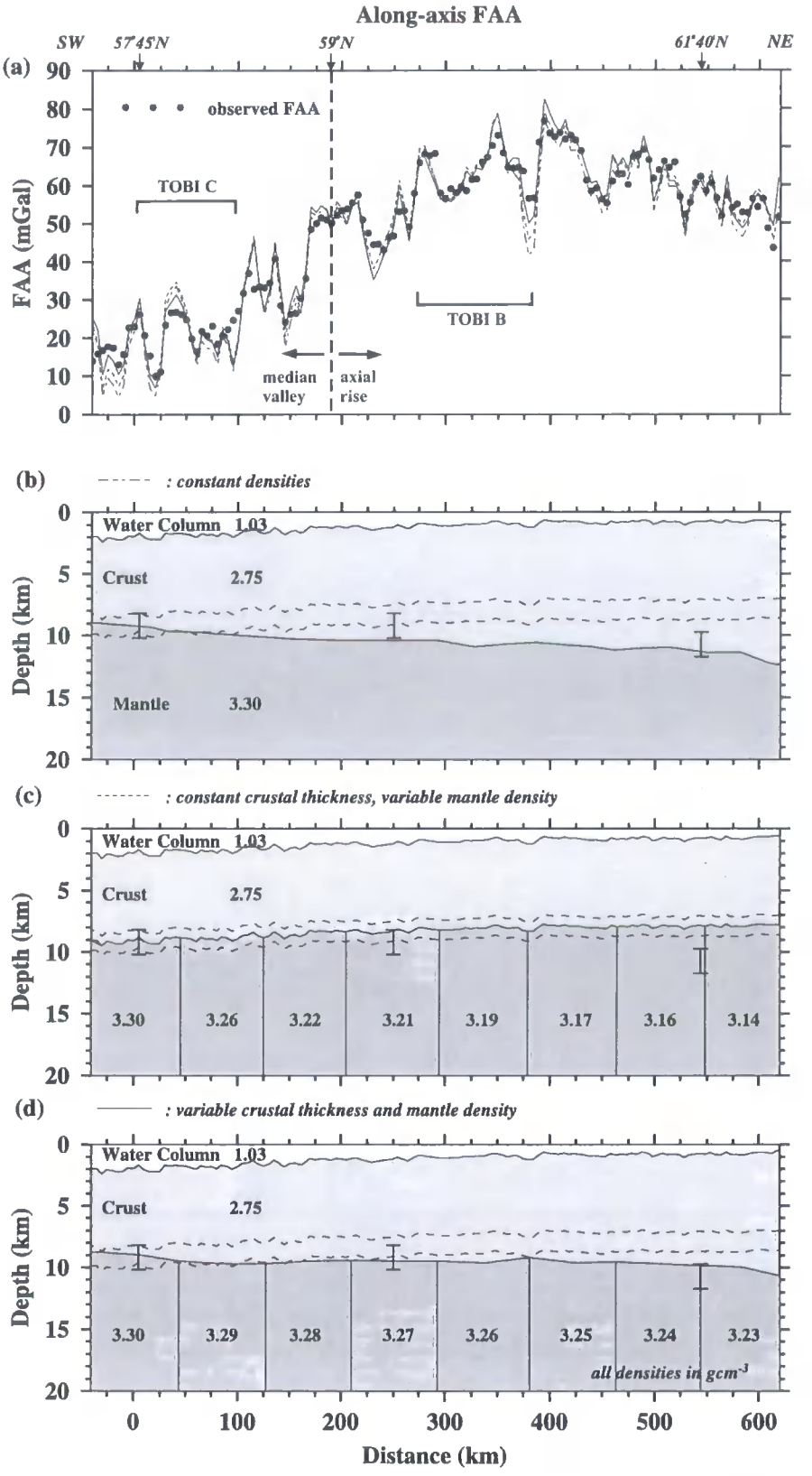

Figure 4.11: Effect of the Iceland plume on the Reykjanes Ridge from gravity modelling. (a) Calculated (dashed) and observed (dots) free-air gravity anomalies along-axis from 57°30'N to 62°12'N. (b) Constant density model showing how the crust would have to reach a thickness of ~12 km at 62°N to match the observed anomalies in the absence of any mantle density variation. (c) Model showing mantle densities required to match the observed anomalies assuming no crustal thickening. Mantle densities decrease to 3.19 g cm^{-3} at 62°N. (d) Model that fits all available seismic crustal thickness and mantle density determinations, consisting of variable crustal thickness and mantle density, with an increase in crustal thickness and a gradual decrease in mantle density towards Iceland from ~7 km and 3.30 g cm^{-3} at 57°45'N to ~10 km and 3.23 g cm^{-3} at 62°N. Error bars show the seismic crustal thickness determinations of various authors (see text). Dashed lines within the models show "normal" oceanic crustal thickness of 7.1 ± 0.8 km (White *et al.* 1992).

The model presented in Fig. 4.11(d) provides the best-fit to the available crustal thickness and upper mantle density determinations. Crustal thickness and mantle density range from 7.5 km and 3.30 g cm^{-3} at 57°30'N to ~10.5 km and 3.23 g cm^{-3} at 62°N, comparable to the 3.23 g cm^{-3} density of Weir *et al.* (2001)'*s* wide-angle seismic based model near 62°40'N. Normal oceanic crustal thickness of 7.1 ± 0.8 km (dashed lines in Figs. 4.11(b-d), White *et al.* 1992) is reached near 59°N suggesting that, unlike TOBI area B, TOBI area C is not directly influenced by the Iceland hotspot.

The gravity modelling presented in this section, therefore, supports the inference that the change in ridge morphology at 59°N, from a median valley to a rise, marks the most southerly extent of the hotspot influence. Note that the short-wavelength (~10 km) calculated free-air anomalies are not adequately modelled (within seismic constraints), indicating that smaller-scale along-axis variations in crustal thickness, and probably density, are also required to produce a better fit to the observed anomalies (see Section 4.4.2).

The along-axis anomaly pattern can be divided into three regimes (Fig 4.12a), based on along-axis changes in bathymetric slope and RMBA amplitude and gradient. This segmentation becomes clearer if the long-wavelength effect of the Iceland hotspot is removed from the RMBA, leaving intermediate-wavelength features associated with the pulsing of the hotspot and short-wavelength features associated with the crustal structure beneath individual AVRs and inter-AVR basins (Fig. 4.12b). Regime I, extending from 57°25'N to 58°50'N, shows a rapid decrease in axial depth with the RMBA varying from ~5 mGal to -6 mGal relative to the background level. The greatest relative RMBA low of the whole ridge occurs over the 57°45'N AVR. Between 58°50'N and 60°50'N, in regime II, the decrease in axial depth is less rapid and anomalies vary from ~5 mGal to -3 mGal. North of 60°50'N, which marks the start of regime III, the rate of change in axial depth levels out with only short-wavelength variations present. The anomalies are relatively subdued in this region, with variations of 3 mGal to -3 mGal about the regional trend. Based on the intermediate-wavelength fluctuations of the along-axis RMBA and bathymetry it is hypothesised that the pulse head is presently located between 58°50'N and 59°30'N resulting in a greater melt supply, a thicker crust and/or lower density crust/upper-mantle leading to the RMBA low. Regime I is as yet unaffected by the pulse, whereas the region north of 59°30'N is gradually readjusting to the passage of the hotspot pulse.

Lee & Searle (2000) observe a similar along-ridge-axis segmentation of the magnetization, the only difference being that they position the start of the second regime

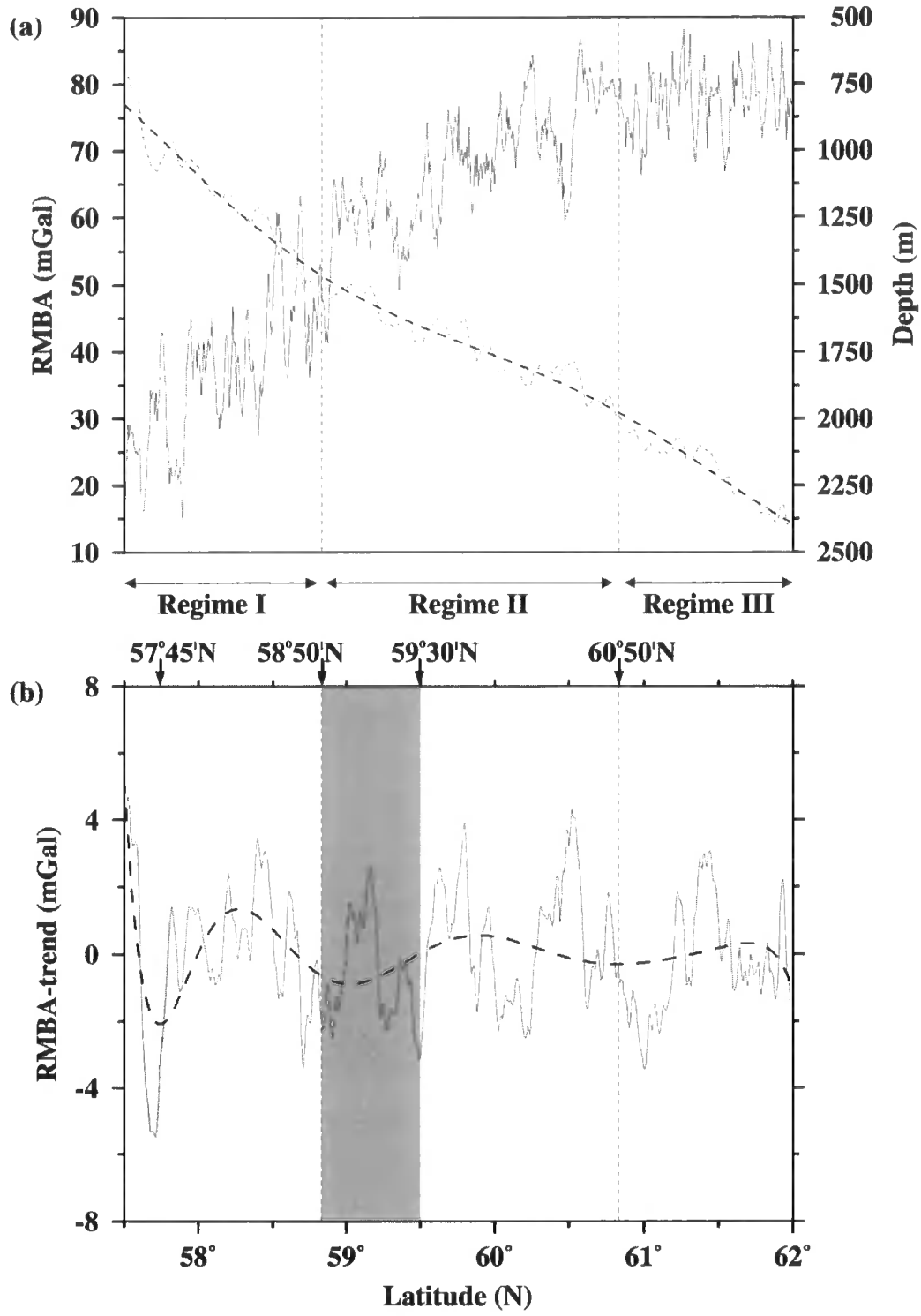

Figure 4.12: Analysis of various wavelengths in the along-axis RMBA and bathymetry. (a) Along-axis bathymetry (solid line) with RMBA (short dashed line) and RMBA trend (long dashed line) superimposed. The changes in bathymetry and RMBA slope define three hypothesised regimes (vertical dashed lines). (b) RMBA with the long-wavelength trend of (a) removed. The dashed line highlights the intermediate-wavelength of the RMBA and the low around 59°N (dark grey shading) is postulated to be associated with the hotspot pulse location. Note the pronounced RMBA low associated with the 57°45'N AVR (light grey shading).

at 59°10'N. Their results suggest that the hotspot head is now at 59°30'N, where the highest magnetization in regime II is observed, and that the overall low magnetization of regime II is due to the hotspot front raising mantle temperatures, increasing melt production and creating a reservoir in the crust or shallow mantle where mixing inhibits fractionation thereby reducing the Fe content of the melt extruded into the shallow crust. Regime II is, therefore, described as being the most magmatically active section, whereas regime I, a region not yet affected by the hotspot pulse, only shows intermittent magmatism and regime III, is readjusting after the passage of the pulse (see Section 5.4.1).

The results of modelling presented in this study support Lee & Searle (2000)'s interpretation, although uncertainty exists in the location of the transition from regime I to II but as the transition is expected to be gradual its exact position is not fundamental. The hotspot head is probably located around 59°30'N leading to an increase in melt supply which may result in either thicker crust and/or a lower density region in the crust and/or mantle. The calculated RMBA low around this region supports this interpretation. It is hypothesised that the region behind the passing hotspot head gradually readjusts and the linearly increasing RMBA of regime II points to crustal and/or mantle densities returning to normal. Intermediate-wavelength variations in RMBA decrease north of 60°50'N leaving only short-wavelength anomalies associated with AVR-scale features.

4.4.2 Short-wavelength features

Having constrained the likely extent of the hotspot influence on the ridge, sources of shorter-wavelength anomalies will be investigated in the following sections and the potential impact of tectonomagmatic cycles on the crustal structure of AVRs will be assessed. In addition, the hotspot influenced TOBI area B will be compared to the hotspot-free TOBI area C.

4.4.2.1 TOBI area C

Figure 4.13 shows along-axis profiles of the bathymetry and RMBA over the region covered by TOBI area C. From 57°30'N to 58°30'N a number of 2-5 mGal RMBA highs, relative to the linear along-axis trend, coincide with second and third order discontinuities as identified by intermediate-wavelength minima in the bathymetry profile. The observed segmentation over this region is similar to that reported by Appelgate & Shor (1994), with third order discontinuities at 57°36'N, 58°12'N, 58°24'N,

and a second order discontinuity at 57°51'N (Searle *et al.* 1994a). Relative RMBA lows are observed over most AVRs, suggesting the presence of thicker crust and/or lower densities beneath AVRs.

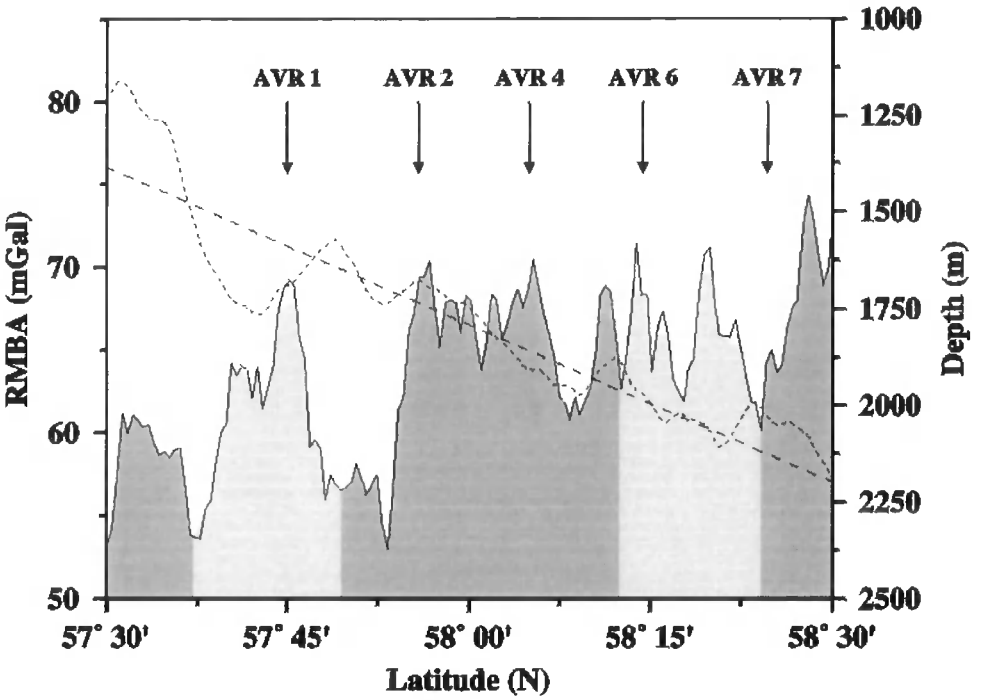

Figure 4.13: Along-axis profiles of bathymetry and RMBA data for TOBI area C. The bathymetry (solid line) shows short-wavelength variations associated with individual AVRs (annotated arrows) and intermediate-wavelength variations associated with segment discontinuities (segment boundary locations are from Appelgate & Shor (1994) and are shaded in grey. See text for details). The RMBA profile (dotted line) is superimposed together with its long-wavelength trend (dashed line). Note how bathymetry highs are generally associated with relative RMBA lows.

The dashed line in Figure 4.13 shows the long-wavelength, linear trend profile, calculated by a least-squares fit to the RMBA using the *grdtrend* program that is part of the GMT package (Wessel & Smith 1995). This long-wavelength trend was removed from the RMBA to highlight AVR relative variations in the RMBA (Fig. 4.14). A broad RMBA low of ~2 mGal, appears to follow the ridge-trend with mainly AVR-trending lows of up to -6 mGal associated with a number of AVRs superimposed. This suggests that magma delivery takes place along the ridge trend and that AVRs, created along a spreading-orthogonal direction, tap into this broad ridge-trending upwelling (Peirce & Navin 2002).

A number of small "bull's eye" lows are visible along the ridge axis. A -6 mGal low is associated with AVR 1 at 57°45'N. Further north AVR 2, centred on 58°05'N, has no distinct RMBA low, instead a -1 mGal low is visible to the south-west of the AVR. The next "bull's eye" low, of -4 mGal, occurs over AVR 4, near 58°10'N. Anomalies then

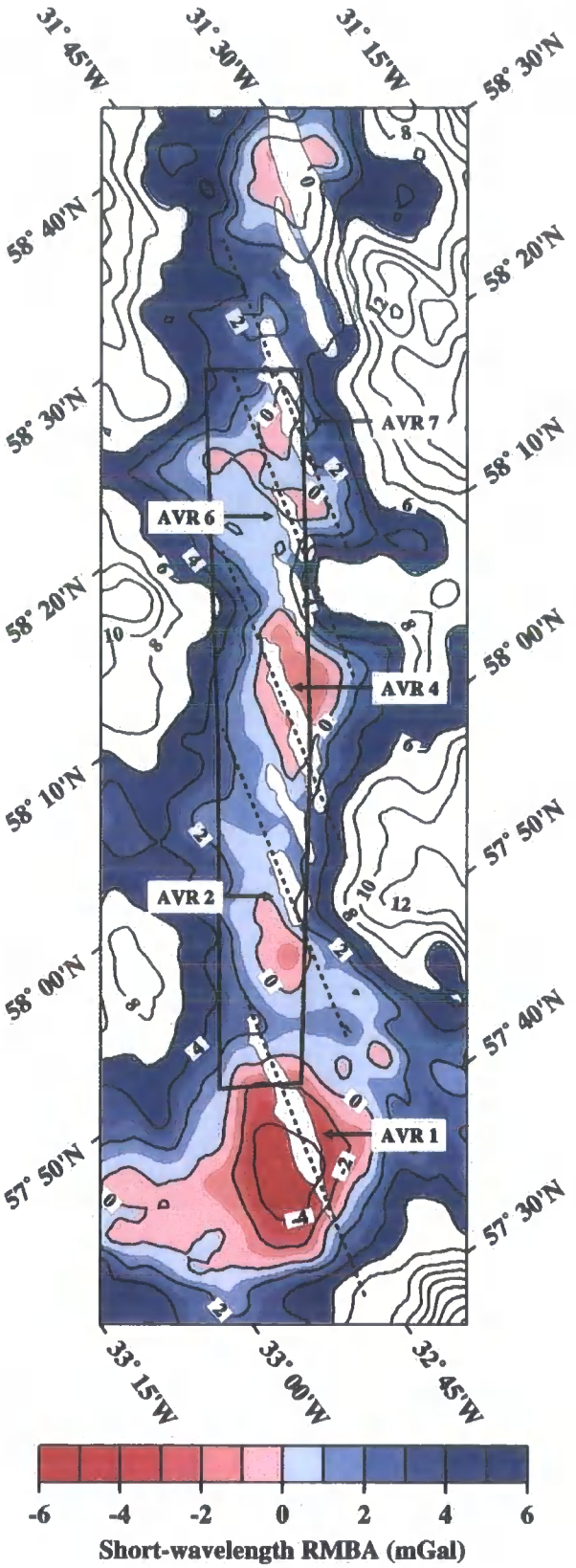

Figure 4.14: Short-wavelength RMBA for TOBI area C. Short-wavelength features have been highlighted by removing the long-wavelength planar trend from the RMBA (see text for details). A number of small "bull's eye" RMBA lows are associated with individual AVRs (outlined in white and annotated with arrows). The black box shows the outline of TOBI area C. Dashed black lines through AVRs show profiles extracted for modelling. Note that the colour scale has been chosen to highlight the on-axis anomalies.

generally increase in amplitude, culminating with a small -3 mGal low over AVR 7 at 58°24'N near the northern edge of TOBI coverage. Table 4.3, compares the relative age of AVRs (see Section 3.2) with their length and associated RMBA amplitude. A correlation between relative AVR age, length and RMBA can be made, with more mature AVRs being longer and having a more pronounced RMBA low. This relationship suggests that more mature AVRs have thicker crust than younger AVRs. This hypothesis will be tested by modelling, the results of which are discussed in the following sections.

Off-axis traces of RMBA lows over AVRs 1, 2, 4 and 6 are asymmetric, suggesting that thicker crust is locally present off-axis to the west of 57°45'N, 57°55'N and 58°15'N and to the east near 58°10'N. These observations are probably related to asymmetry in the crustal accretion process itself. This conclusion is supported by the spreading rate variations calculated by Owens (1991), from approximately 57°45'N to 58°05'N, and investigated further in Section 5.4.2.3.

Relative age	AVR No.	Length (km)	RMBA (mGal)
young-adolescent	6	11	-1
adolescent	7	20	-3
adolescent-mature	2	10	-1 (off-axis)
mature	4	35	-4
mature	1	30	-6

Table 4.3: Correlation between relative age, length and RMBA peak-to-trough amplitude measured over the length of the AVR for selected AVRs of TOBI area C. Older AVRs generally appear to be longer and have a more pronounced RMBA low.

A relative RMBA high of ~2 mGal at 57°55'N, over a 600 m deep non-transform offset, suggests that this area has a reduced melt supply (Searle *et al.* 1994a). The next prominent RMBA high, 2 mGal in amplitude, occurs near 58°15'N just north of AVR 6. RMBA amplitude and AVR length generally increase away from these two discontinuities, reaching -4 mGal and 35 km respectively for AVR 4, suggesting that an increase in crustal thickness or melt supply (and hence lower densities) exists near 58°05'N.

It is, therefore, hypothesised that the aforementioned discontinuities in bathymetry and RMBA mark the ends of a segment that includes 5 AVRs and spans ~70 km along-axis. Under this hypothesis AVR creation is initially focussed at the centre of the

segment (e.g. AVR 4) and gradually propagates towards the segment ends, explaining the pattern of progressively younger AVRs away from the segment centre.

If this hypothesis is correct, the crustal structure of each of the AVRs in this region should reflect the influence of tectonomagmatic cycles. In the next sections, this theory will be tested by modelling the RMBA along each AVR.

4.4.2.1.1 AVR 1

Gravity modelling was based on the RMBA so that the source of most variability in the gravity anomaly, i.e. the seafloor topography, is effectively removed and the smaller amplitude anomalies revealed. For each AVR a 40 km along-axis profile was extracted from the short-wavelength RMBA (see Fig. 4.14) and modelled using *gravmag* (British Geological Survey - Pedley *et al.* 1993). Each model extends from -1000 km to 1000 km laterally, to 20 km depth and has a 10000 km half-strike length in the third dimension to avoid edge effects and to give the models a 2.5-D aspect. Although the crustal structure of an AVR is unlikely to be 2-D or even 2.5-D, the 2.5-D assumption in the modelling may be reasonably valid as the RMBA strips off the water layer, effectively removing the bulk of the in and out of plane variability. A 4-layer model (Fig. 4.15), based on the wide-angle seismic work of Navin *et al.* (1998) and consisting of oceanic layers 2A, 2B, 3 and the upper mantle, was used as an initial model for all AVRs. Note that the water column has not been included in this model, as its effects are accurately predictable and, thus, removed in the RMBA calculation. Peirce & Navin (2002) explain the details of the validity of this approach. A ~100 m thin melt lens, identified by the seismic modelling of Navin *et al.* (1998), has been included in the AVR 1 gravity models for reasons of completeness although it does not give rise to a significant gravity anomaly within the ±1 mGal error in the data (Navin *et al.* 1998).

Crustal structure models for this AVR (Fig. 4.15) are based on the results of Peirce & Navin (2002) and are shown for comparison with the models of the other AVRs presented as part of this study. The seismically-derived initial model (Fig. 4.15b) fits the RMBA, within the ±1 mGal error, in overall amplitude but does not match it peak-for-peak. Varying the crustal thickness (Fig. 4.15c), within seismic constraints, improves the general fit as does including low- density regions in the mid-crust (Fig. 4.15d). The best-fit, within the ±1 mGal error bound, to the RMBA is achieved when low-density regions in layer 3 are combined with small variations in crustal thickness (Fig. 4.15e).

Peirce & Navin (2002) interpret the low-density region in layer 3 as containing a high percentage of partial melt, with the lowest density block representing the region of

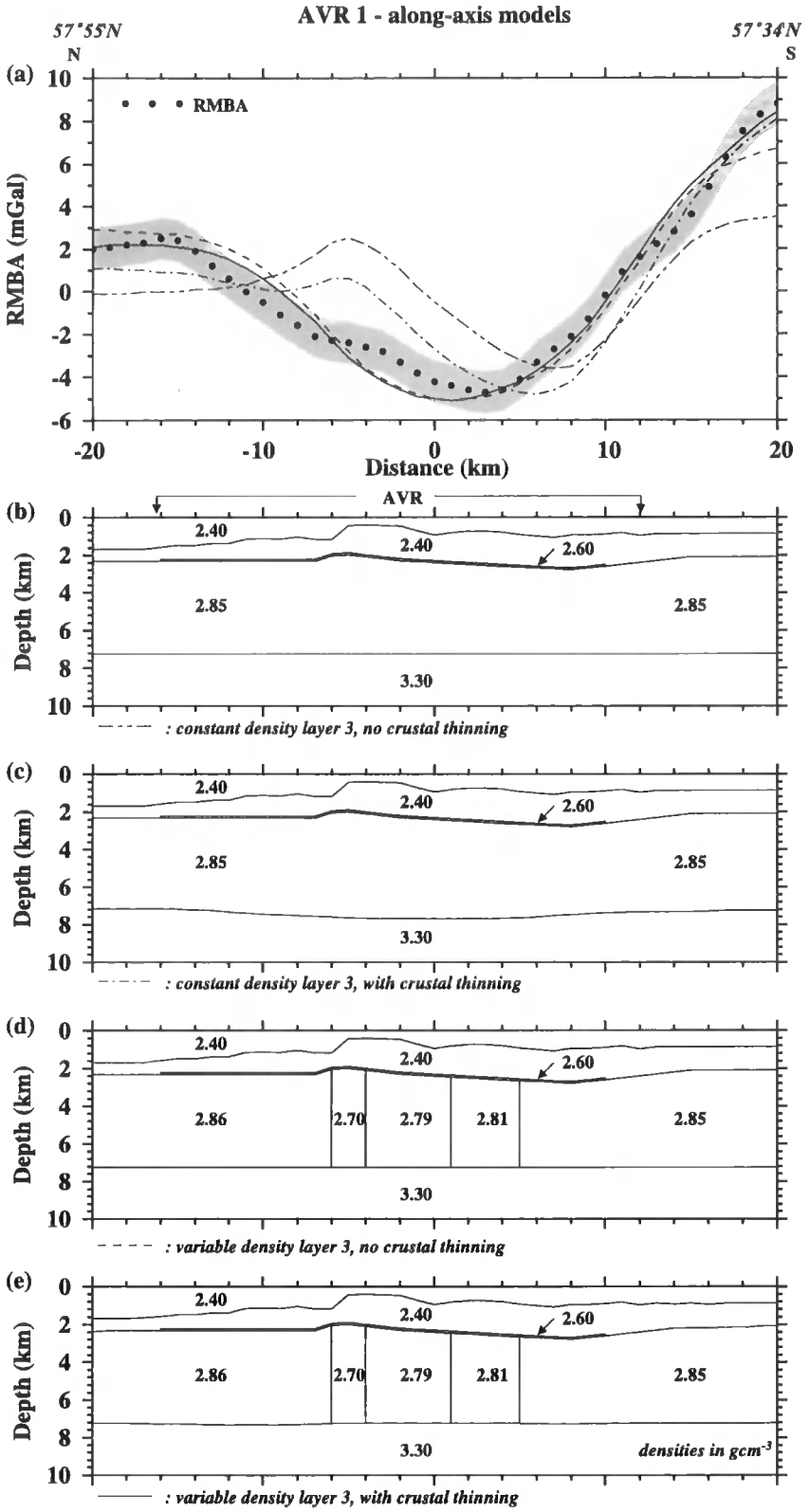

Figure 4.15: Along-axis RMBA profile for AVR 1 sampled from the short-wavelength RMBA plot of Fig. 4.14. The RMBA is shown by dots, with error bounds (grey shaded region) and calculated anomalies (see annotation for details) for each of the models shown in (b)-(e) superimposed. The RMBA has had the gravitational effects of the water/seabed interface removed, hence models only show layers 2A, 2B, 3 and the upper mantle. Each model extends from -1000 km to 1000 km laterally, to 20 km depth and has a 10000 km half-strike length in the third dimension to avoid edge effects and to give the models a 2.5-D aspect. The lateral extent of the AVR is highlighted. (b)-(e) explore the contributions to the RMBA of variations in crustal thickness, variations in mid-crustal densities, and combinations of crustal thickness and mid-crustal density variations. A crustal model that includes a low-density region towards the centre of the AVR and crustal thinning towards AVR tips results in the best fit to the RMBA. Note the presence of a thin melt lens with a density of 2.60 g cm^{-3}, which is a requirement of the seismic models of Navin *et al.* (1998) but does not significantly contribute to the gravity anomaly (Navin *et al.* 1998).

most recent melt influx. Its is, therefore, hypothesised that AVR 1 is undergoing rejuvenation with a fresh injection of melt recently reaching the mid-crust and most probably resulting in fresh eruptions and sheet lava flows overprinting the old seafloor (see Section 3.2).

4.4.2.1.2 AVR 2

The along-axis RMBA of this AVR has no distinct low associated with the segment centre, instead small fluctuations of ~1mGal on a ~5 km length-scale occur around a 1 mGal background average. A simple crustal structure with constant densities and no crustal thinning (Fig. 4.16b) produces a match to the background RMBA and crustal thinning of ~200 m (Fig. 4.16c) results in a better fit to the longer-wavelength of the RMBA. A mid-crustal density distribution such as that modelled for AVR 1 (Fig. 4.16d) produces a large misfit (~5 mGal) to the RMBA. The best-fit to the RMBA is achieved with small variations in layer 2 thickness (200-400 m) and no crustal thinning (Fig. 4.16e). A -1 mGal RMBA low, slightly off-axis to the south-west of this AVR (see Fig. 4.14), may indicate continued growth/rejuvenation of this AVR via off-axis melt migration, or that a new influx of melt to the crust is leading to the creation of a new AVR.

4.4.2.1.3 AVR 4

The along-axis RMBA of this AVR has longer-wavelength fluctuations (>10 km) similar to that of AVR 1 but the anomaly amplitude only reaches a relative -4 mGal low at the segment centre. Small variations in layer 2 thickness, in a crustal structure with no mid-crustal density variations and no crustal thinning (Fig. 4.17b), match the shorter-wavelength features of the RMBA only. Combining variations in layer 2 thickness with crustal thinning of ~400 m towards the segment ends (Fig. 4.17c) improves the overall fit to the RMBA. Including the mid-crustal densities of AVR 1 into the model (Fig. 4.17d) results in a 3 mGal misfit. However, reducing the low-density anomaly in the mid-crustal region beneath the segment centre to 0.01-0.03 g cm^{-3} (Fig. 4.17e) produces an acceptable fit to the RMBA. This low-density anomaly may indicate the presence of 5-15% retained melt, assuming a density contrast of 0.2 g cm^{-3} between basaltic melt and gabbro (Hooft & Detrick 1993). A crustal model with an increase in total crustal thickness beneath the AVR-centre or the presence of a small amount of partial melt in the mid-crust is consistent with the TOBI data interpretation of a relatively *mature* age. It is possible that most of the melt has had time to accrete to the crust, resulting in a

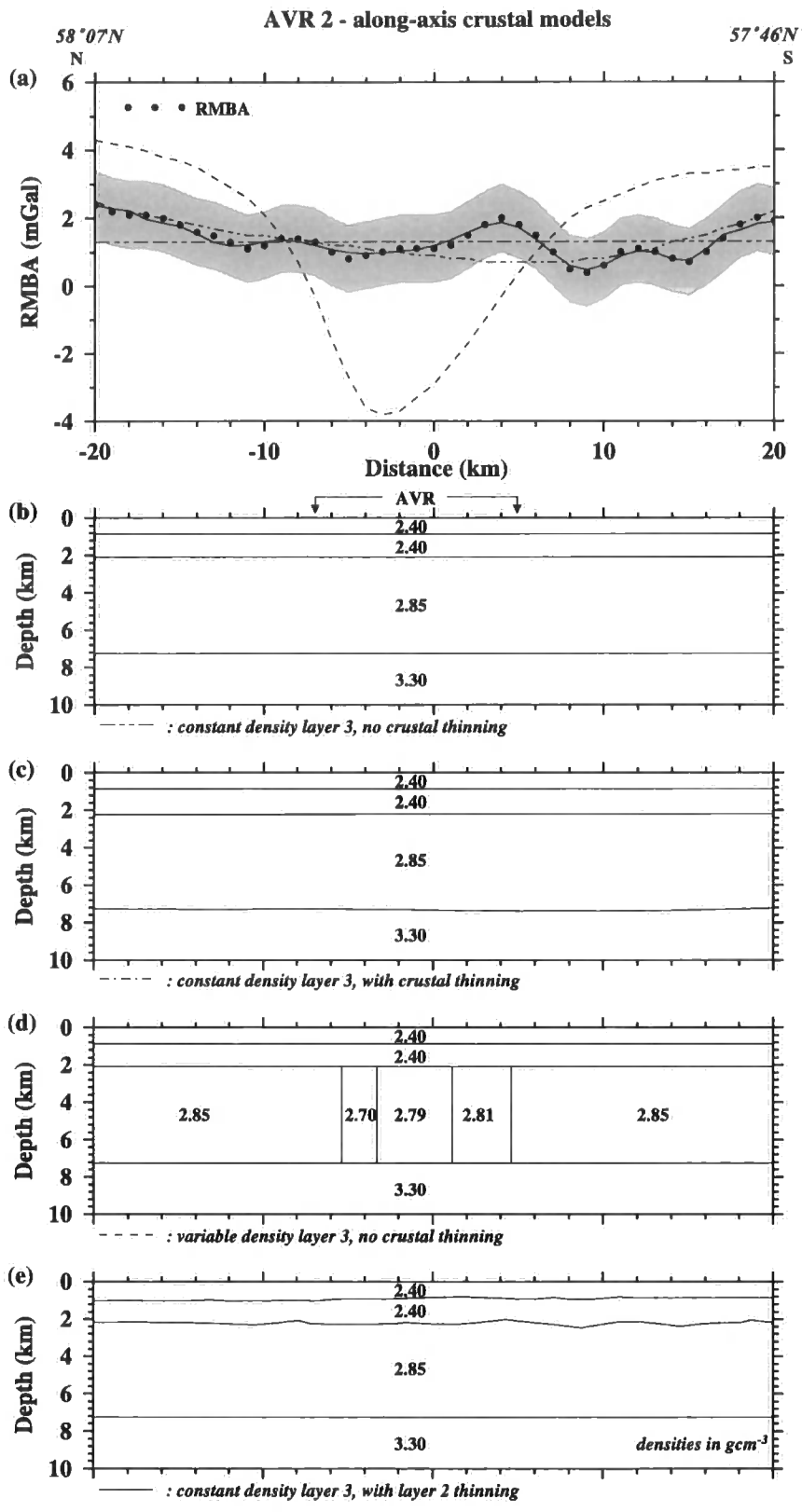

Figure 4.16: Along-axis RMBA profile for AVR 2 sampled from the short-wavelength RMBA plot of Fig. 4.14. See Fig. 4.15 for plotting and model parameters. (b)-(e) explore the contributions to the RMBA of variations in crustal thickness, variations in mid-crustal densities, and combinations of crustal thickness and mid-crustal density variations. The RMBA can be satisfactorily matched by models comprising constant density layers with little to no crustal thinning towards the AVR tips. Variations in layer 2 thickness account for the shorter-wavelength features of the RMBA.

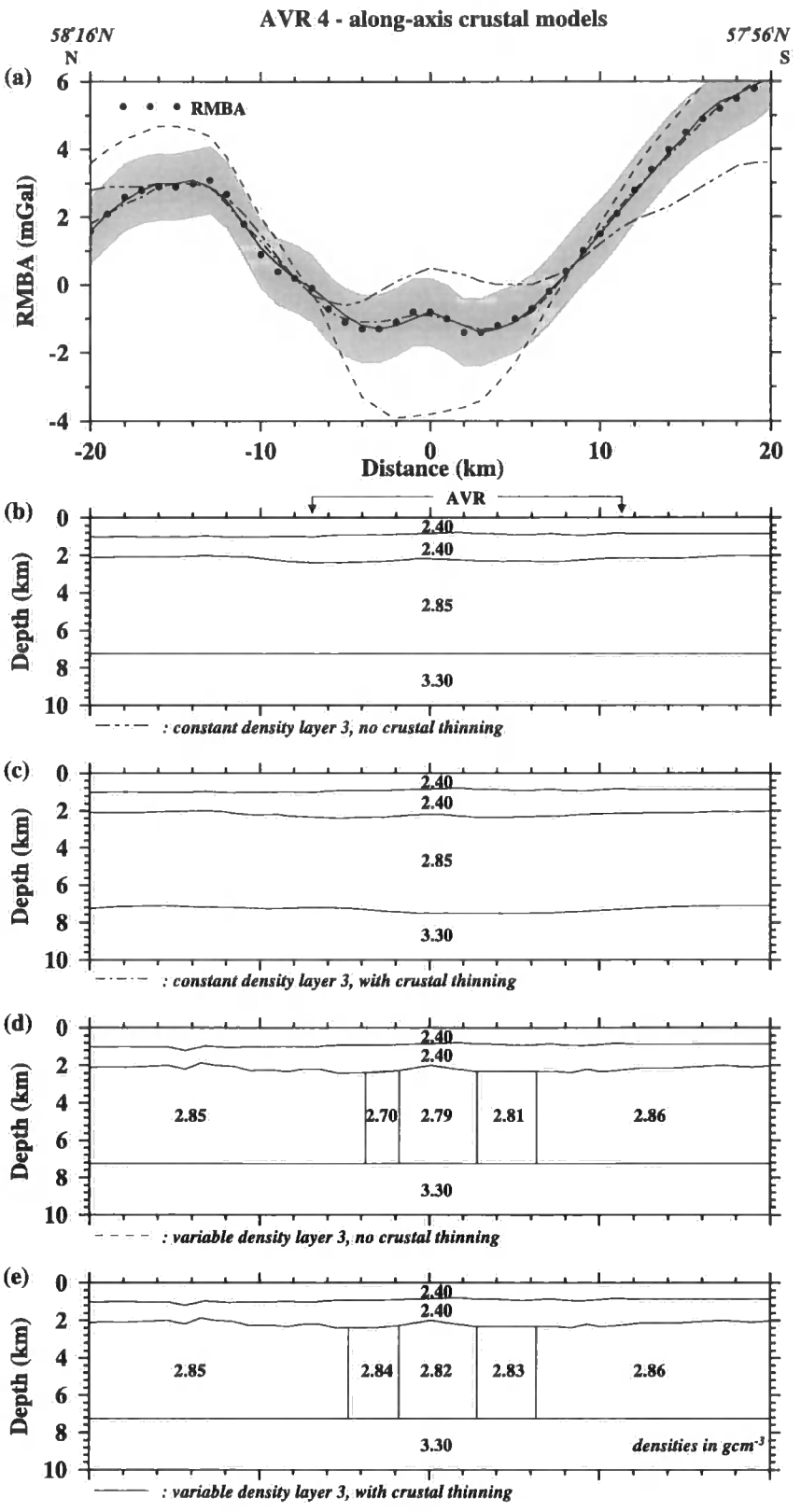

Figure 4.17: Along-axis RMBA profile for AVR 4 sampled from the short-wavelength RMBA plot of Fig. 4.14. See Fig. 4.15 for plotting and model parameters. (b)-(e) explore the contributions to the RMBA of variations in crustal thickness, variations in mid-crustal densities, and combinations of crustal thickness and mid-crustal density variations. Models with constant density layers and crustal thinning towards AVR tips, or with a low-density region in the mid-crust beneath the centre of the AVR produce a reasonable fit to the RMBA.

slightly thicker crust beneath the centre of the AVR and leaving only a small amount of partial melt in the mid-crust.

4.4.2.1.4 AVR 6

This spreading segment is characterised by a -1 mGal RMBA low at its centre. Models with variations in layer 2 thickness of up to 500 m (Fig. 4.18b), crustal thinning of ~1 km to the south and of ~500 m to the north of the segment centre (Fig. 4.18c), or an upper crustal structure with a 0.03-0.04 g cm^{-3} density anomaly (15-20% partial melt) in layer 3 beneath the segment-centre (Fig. 4.18d) all produce an acceptable fit to the RMBA. Density anomalies in the mid-crust similar to those modelled for AVR 1 (Fig. 4.18e) produce a 5 mGal misfit (Fig. 4.18c).

A crustal model with more partial melt in the mid-crust than AVR 4 is consistent with the TOBI data interpretation that suggests this AVR is *young-adolescent.* According to the tectonomagmatic theory it is hypothesised that melt has only recently arrived in the mid-crust, relative to a more *mature* AVR, and less melt has, therefore, been involved in the crustal accretion process, leaving a larger amount of melt in layer 3.

4.4.2.1.5 AVR 7

The along-AVR-axis RMBA has short-wavelength fluctuations of ~5 km and only reaches a -3 mGal low over the segment centre as opposed to the -6 mGal low of AVR 1. The along-axis crustal structure of this AVR can be modelled in several ways that all produce acceptable fits to the observed RMBA: a thicker (~500 m) layer 2 beneath the segment centre (Fig. 4.19b); crustal thinning of ~1 km towards the ends of the profile, with smaller variations in layer 2 thickness (Fig. 4.19c); or more subdued variations in crustal and layer 2 thickness with a 0.01-0.02 g cm^{-3} density anomaly, equivalent to 5-10% retained melt, in the mid-crust beneath the segment centre (Fig. 4.19e). Fig. 4.19(d) shows that mid-crustal densities as low as that modelled for AVR 1 would produce a significant misfit to the RMBA.

A model with a smaller amount of partial melt in the crust than the corresponding model for AVR 6 is consistent with its interpreted *adolescent* age.

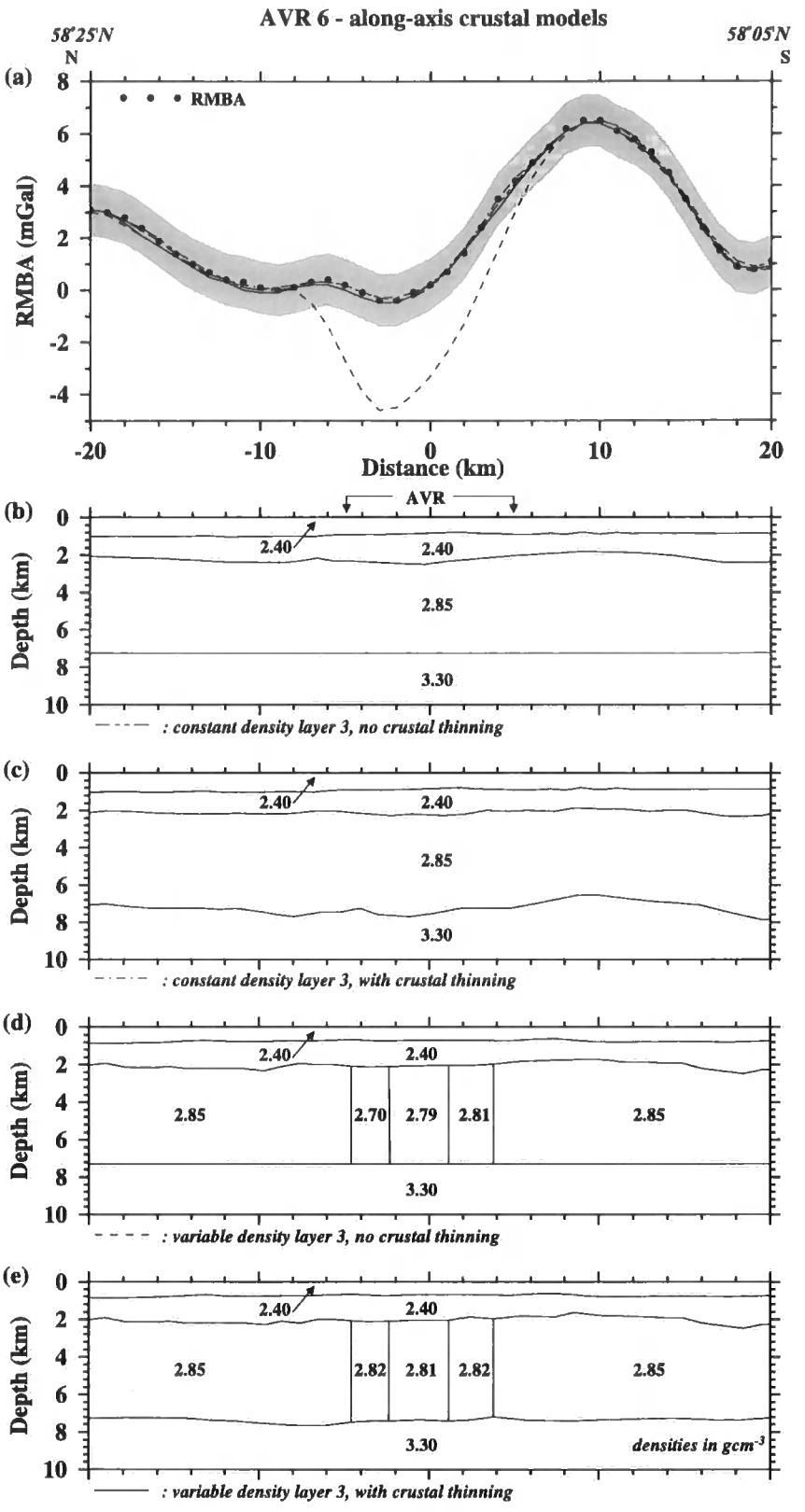

Figure 4.18: Along-axis RMBA profile for AVR 6 sampled from the short-wavelength RMBA plot of Fig. 4.14. See Fig. 4.15 for plotting and model parameters. (b)-(e) explore the contributions to the RMBA of variations in crustal thickness, variations in mid-crustal densities, and combinations of crustal thickness and mid-crustal density variations. The RMBA can be matched by variations in layer 2 thickness alone, variations in crustal thickness, or by a low-density region in the mid-crust together with crustal thinning towards the AVR tips.

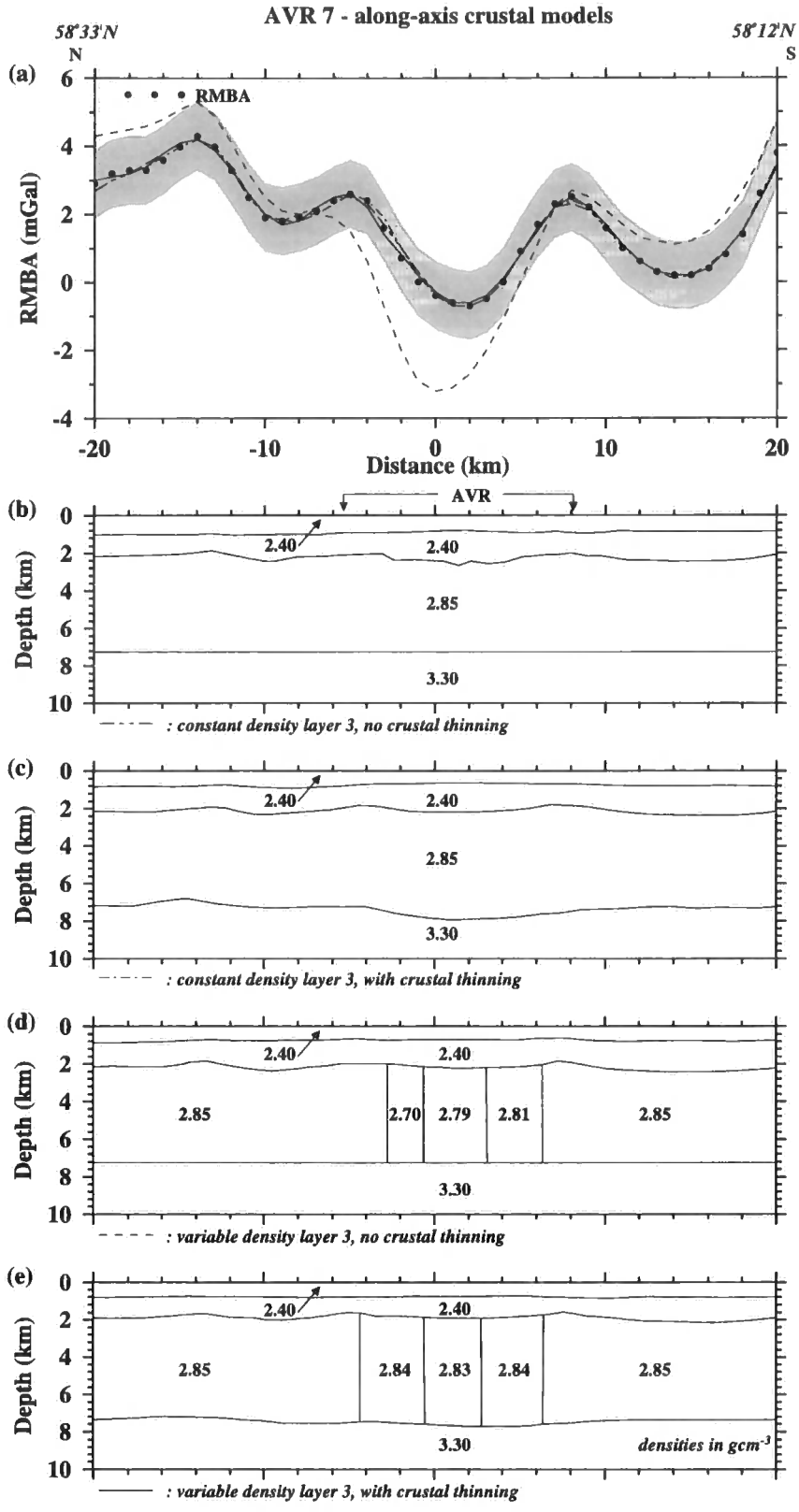

Figure 4.19: Along-axis RMBA profile for AVR 7 sampled from the short-wavelength RMBA plot of Fig. 4.14. See Fig. 4.15 for plotting and model parameters. (b)-(e) explore the contributions to the RMBA of variations in crustal thickness, variations in mid-crustal densities, and combinations of crustal thickness and mid-crustal density variations. Models with constant density layers and crustal thinning towards the AVR tips, or with a low-density region in the mid-crust and more subdued crustal thinning towards the AVR tips produce a satisfactory match to the RMBA.

4.4.2.1.6 Layer 2A and 2B density variations

The along-AVR-axis models discussed in the previous sections all have layers 2A and 2B with densities of 2.40 g cm^{-3}, in common with the model for the 57°45'N-centred AVR of Navin *et al.* (1998), as little layer 2A and 2B density variations are expected for near zero-age crust. However, in this section the effect of density variations in layers 2A and 2B are investigated (Fig. 4.20) to provide constrains on the resolvability of density variations and to test the assumption that the observed RMBA lows do not have an origin in layer 2 alone.

The best-fitting model for the upper crustal structure of AVR 1 (Fig. 4.20b), which is the only model that is constrained by seismic data, provides the starting point for this investigation. An increase in layer 2B density to 2.53 g cm^{-3}, a density generally ascribed to off-axis layer 2B (Navin *et al.* 1998), results in a misfit to the observed RMBA, especially at the northern end of the AVR (Fig. 4.20c). In fact, if layer 2B density is 2.53 g cm^{-3} its thickness would have to be halved to produce an acceptable fit to the RMBA which would be incompatible with the seismic data. Introducing a gradational change in layer 2B density (Fig. 4.20d), from 2.40 g cm^{-3} at the AVR centre to 2.53 g cm^{-3} at the AVR extremities, slightly improves the fit to the observed RMBA at the northern end of the AVR but does not provide a reasonable fit (within the ±1 mGal error bounds) to the whole profile. As for the previous model, significant variations in layer 2B thickness, which would not fit the seismic constraints, would be required to produce an acceptable fit to the RMBA. Combining gradational changes in densities of layers 2A and 2B (Fig. 4.20e) from 2.40 g cm^{-3} at the AVR centre to 2.45 g cm^{-3} and 2.53 g cm^{-3} at the AVR extremities respectively, results in a good fit to the observed RMBA at the northern end of the AVR. However, the fit for the rest of the profile is not within the error bounds.

The layer 2A and 2B density variation sensitivity modelling discussed in this section precludes large variations in density without having to significantly alter the seismically constrained layer thicknessess as well. However, subtle layer 2A and 2B density variations of ~0.05 g cm^{-3} are not precluded from the models but these cannot account for the AVR-centred RMBA low on their own.

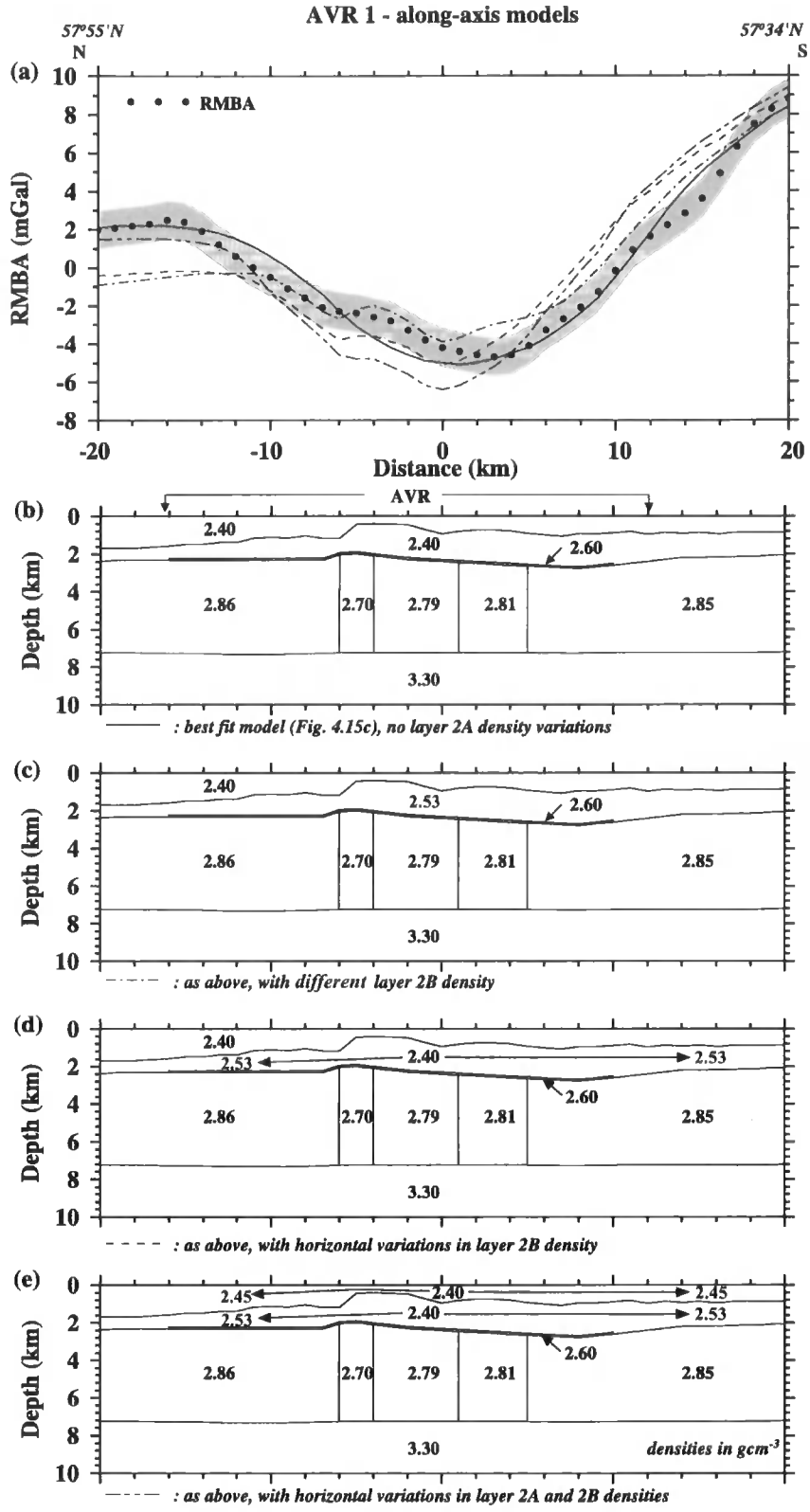

Figure 4.20: Effect of variation in layer 2A and 2B density. (a) Observed (dots) and calculated (see annotatation) gravity anomalies with error bounds superimposed (grey shading). (b) Best-fitting model of the crust for AVR 1 (see Fig. 4.15e). (c) Layer 2B density is changed to 2.53 g cm^{-3}, typical of off-axis layer 2B density, resulting in a misfit to the RMBA. (d) A gradational change in layer 2B density, from 2.40 g cm^{-3} to 2.53 g cm^{-3}, is introduced. The fit to the RMBA is improved from (c) but is still not within the error bounds. (e) Layer 2A density variations are added to the model shown in (d), resulting in a misfit to the RMBA.

4.4.2.1.7 Upper mantle contributions

The RMBA profiles presented in the previous sections have been modelled assuming that the observed anomalies result from variations in crustal thickness and/or density. However, another possible source for the RMBA lows are mantle density variations due to melt retention, thermal expansion, and compositional changes caused by the extraction of partial melt (although compositional density reductions in the mantle are unlikely to contribute significantly to the observed gravity anomaly - Magde *et al.* 1995). Although the 2-D modelling presented here can not differentiate between the different possible sources of low density in the upper mantle it can help constrain possible models for mantle plumbing, i.e. how the melt ascends from the source region in the mantle to the crust.

To investigate possible models of mantle plumbing the crustal model of AVR 4 shown in Fig. 4.17c was used. The upper mantle was extended to 80 km depth and a region of lower densities was incorporated beneath the centre of the AVR, to investigate different conduit geometries and melt retention models. Density anomalies were converted to percentages of retained melt assuming a density contrast of 0.5 g cm^{-3} between basaltic melt and hot peridotite (Sparks *et al.* 1993). Modelling shows that a mantle model with a ~10 km wide conduit extending to a depth of 80 km, with more than 4-8% retained melt, results in a significant misfit to the gravity anomaly (Fig 4.21a-b). Reducing the amount of retained partial melt in the conduit to ~0.5% results in an acceptable fit to the RMBA. If instead of extending the conduit to 80 km depth the region of partial melt only extends to 20 km depth, then up to ~1% partial melt can be retained in the mantle and still produce a good fit. A thinner conduit, 2 km in width, which extends to a depth of 80 km, and contains up to 3% retained melt, also produces a good fit to the RMBA.

The gravity modelling discussed in this section precludes the presence of more than 4-8% partial melt in a ~10 km wide conduit extending from the crust to ~80 km depth in the mantle. However, modelling in this section does not support or preclude retained melt fractions less than 4% in a region of upwelling several kilometres across. The MT data of Heinson *et al.* (2000) preclude the presence of partial melt in the upper mantle down to at least ~50 km depth beneath AVR 1. The RMBA lows observed over individual AVRs are, therefore, best explained by a combination of lower crustal densities and/or an increase in crustal thickness. Small amounts of partial melt in a

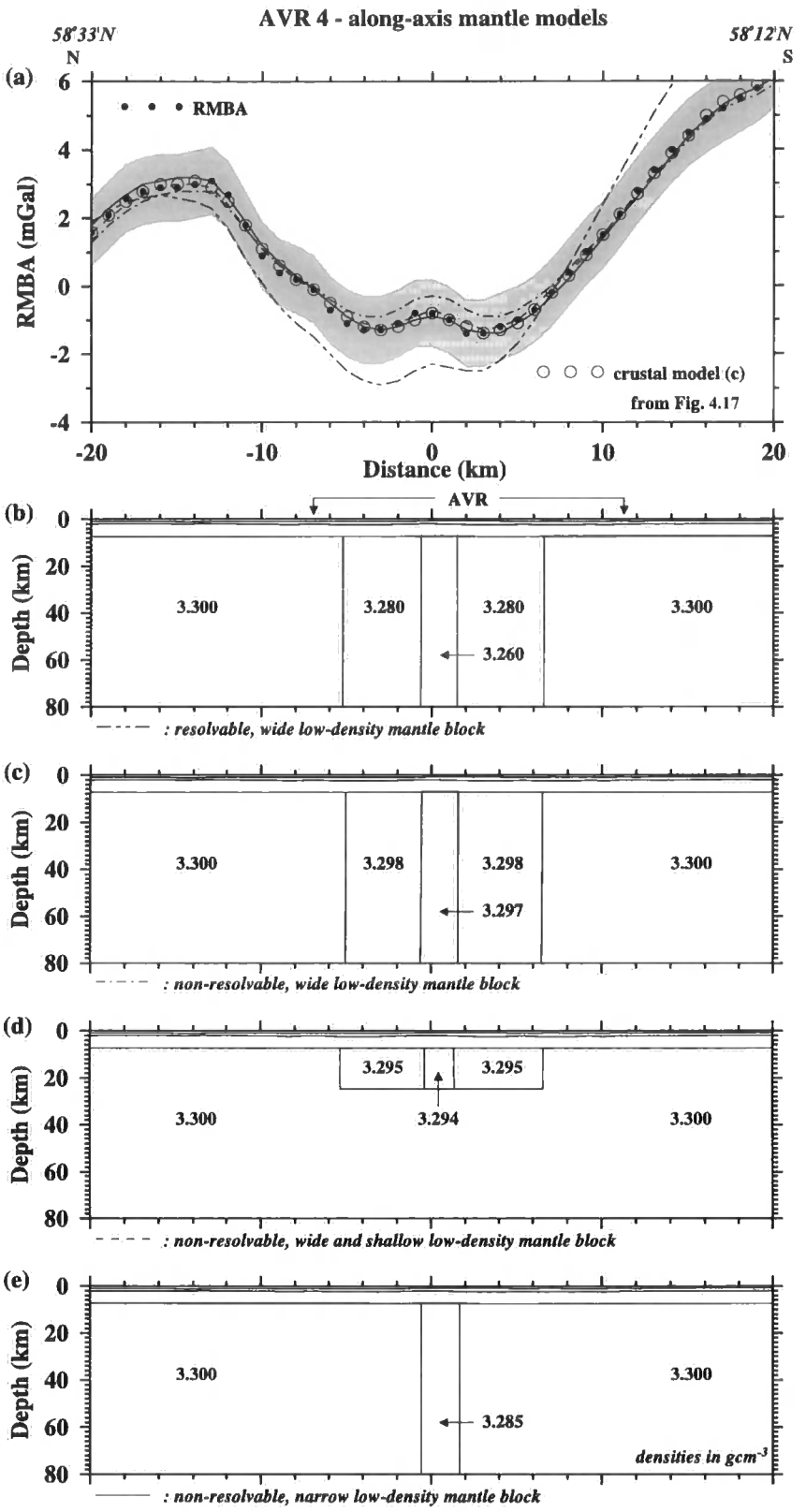

Figure 4.21: Investigation of mantle density variations on the along-axis RMBA of AVR 4. (a) Observed short-wavelength RMBA (dots) and calculated gravity anomaly (circles) for the crustal structure shown in Fig. 4.17(c), and calculated anomalies (see annotation for format) for each of the models shown in (b)-(e). The lateral extent of the AVR is highlighted. Models (b)-(e) combine the crustal structure of Fig. 4.17(c) with various models of upper mantle plumbing.

broad region of mantle upwelling are also consistent with the gravity data but are inconsequential on their own.

The modelling presented in this section, which precludes the presence of a substantial amount of melt in an upper mantle conduit, corroborates the conclusions for highly episodic melt influx to the crust in this area (MacGregor *et al.* 1998; Heinson *et al.* 2000; Navin *et al.* 1998; Peirce & Navin 2002). Similar observations have been reported for two segments of the EPR (Magde *et al.* 1995) suggesting that melt injection into the crust is episodic at all spreading rates.

4.4.2.1.8 Summary of TOBI area C

Calculation of the RMBA reveals short-wavelength, AVR-centred lows superimposed on a broad ridge-trending low. Along-AVR-axis gravity modelling shows that a number of these RMBA lows can be explained by up to a 1 km thickening of the crust and/or by the presence of low-density regions in the mid-crust (see Table 4.4). Models of the crustal structure of the AVRs, showing crustal thickening beneath older AVRs and the presence of partial melt beneath younger AVRs, are consistent with the stage of the AVRs in the tectonomagmatic cycle (see Section 3.2). Younger AVRs are undergoing magmatic activity and, thus, are likely to have more melt in the mid-crust than *mature* AVRs, which have reached full crustal thickness and are at the end of their magmatic phase.

Relative age	AVR No.	Length (km)	RMBA (mGal)	Crustal structure	
				crustal thickening (m)	partial melt
young-adolescent	6	11	-1	< 1000	< 20%
adolescent	7	20	-3	< 1000	< 10%
adolescent-mature	2	10	-1 (off-axis)	-	-
mature	4	35	-4	< 400	< 15%
mature	1	30	-6	< 500	< 40%

Table 4.4: Correlation between relative age, length, RMBA peak-to-trough amplitude (see Table 4.3) and inferred crustal structure for selected AVRs of TOBI area C. The RMBA lows can be modelled by crustal thickening and/or the presence of partial melt in the mid-crust (grey shading shows the preferred model, chosen on the basis of the relative age of AVRs). Note that the extent of thickening and the amount of partial melt shown are maximum values and that AVRs 1 and 2 appear to be anomalous. See text for details.

AVR 1 is anomalous in that previous studies indicate it is underlain by partial melt in the mid-crust (Navin *et al.* 1998), whereas its long length and *mature* age suggest it

should be reaching the end of its magmatic phase with little partial melt left in the mid-crust. If the hypothesis that tectonomagmatic cycles effect the crustal structure of AVRs is correct, then a possible explanation for the apparent age of AVR 1 and the presence of partial melt in the mid-crust, is that this AVR is undergoing rejuvenation with a recent influx of melt to the crust. AVR 2, at ~10 km in length, is unusually short for its apparent age (*adolescent-mature*). However, an RMBA low off-axis to the west of this AVR could indicate that its growth is continuing via off-axis melt migration or that the growth of a new AVR has diverted melt flux from it, resulting in its short length

The gravity models presented in this section support the theory that tectonomagmatic cycles influence the crustal structure of individual AVRs. In addition, a ridge-trending RMBA low is observed, suggesting that upwelling occurs along this direction but that melt migrates to fill spreading-normal fissures that are orientated oblique to the ridge direction, thus, forming AVRs (Peirce & Navin 2002). AVRs appear to age and lengthen away from the second order discontinuity near 58°N, suggesting that AVR growth is initially focussed at the centre of the upwelling and that crustal production gradually extends to the segment extremities.

In the following section a the same approach is used to model gravity anomalies associated with selected AVRs in TOBI area B.

4.4.2.2 TOBI area B

The ridge axis of TOBI area B is characterised by a number of RMBA highs and lows relative to the long-wavelength trend (Fig. 4.22). Comparing along-axis RMBA and bathymetry profiles shows that the majority of RMBA highs are associated with bathymetry lows and that RMBA lows are generally present over bathymetry highs corresponding to AVRs. This pattern is similar to the pattern observed for TOBI area C and suggests that the most prominent bathymetry lows at 59°51'N, 59°58'N and 60°18'N are third order discontinuities. However, the along-axis RMBA gradient of -0.0625 mGal km^{-1} is lower here than for TOBI area C (-0.1696 mGal km^{-1}) and the along-axis RMBA variations are more subdued here than in the hotspot-free part of the ridge. These observations suggests that elevated temperatures, due to the proximity of the hotspot, facilitate the along-axis redistribution of melt (Bell & Buck 1992) and result in a RMBA pattern more akin to faster-spreading ridges (Lin *et al.* 1992).

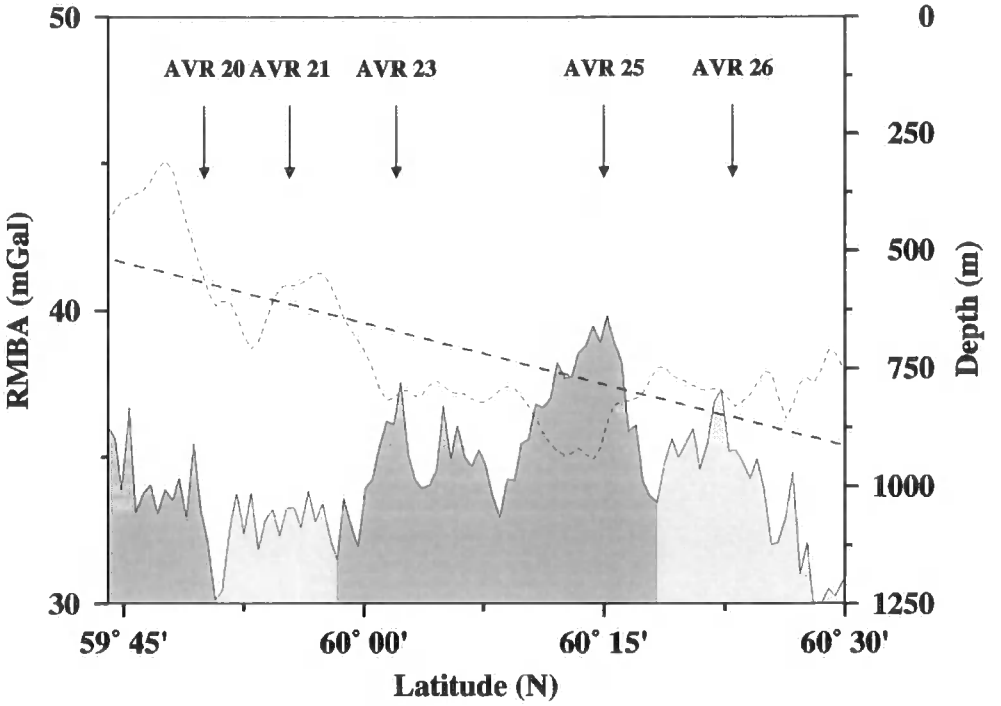

Figure 4.22: Along-axis profiles of bathymetry and RMBA data for TOBI area B. The bathymetry (solid line) shows short-wavelength variations associated with individual AVRs (annotated arrows) and intermediate-wavelength variations associated with segment discontinuities (segment boundaries from Appelgate & Shor (1994) are shaded in grey. See text for details). The RMBA profile (dotted line) is superimposed together with its long-wavelength trend (dashed line). Note how bathymetry highs are generally associated with relative RMBA lows.

The dashed line in Fig. 4.22 shows the long-wavelength, linear trend profile, calculated as described in Section 4.4.2.1. Removal of this long-wavelength trend reveals an RMBA low (Fig. 4.23) following the ridge trend that is much broader than in TOBI area C, which suggests that the crust is thicker across a wider area across-axis or that the low-density region, associated with upwelling at the ridge axis, is wider in TOBI area B than TOBI area C with only a few "bull's eye" lows superimposed over a number of AVRs.

The "bull's eye" lows are superimposed on the broad low, with the most prominent lows visible over AVR 20 at 59°50'N, AVR 21 near 59°50'N, AVR 23 centred on 60°05'N, with amplitudes of -6 mGal, -5 mGal and -3 mGal respectively. Combining the relative AVR age interpretations of Section 3.3 with the gravity observations shows that although more mature AVRs are generally longer, as in TOBI area C, there is no correlation between RMBA amplitude and AVR age (see Table 4.5).

These observations are consistent with a model where along-axis redistribution of melt "smoothes out" the along-axis crustal structure, resulting in subdued along-axis gravity anomalies (Bell & Buck 1997).

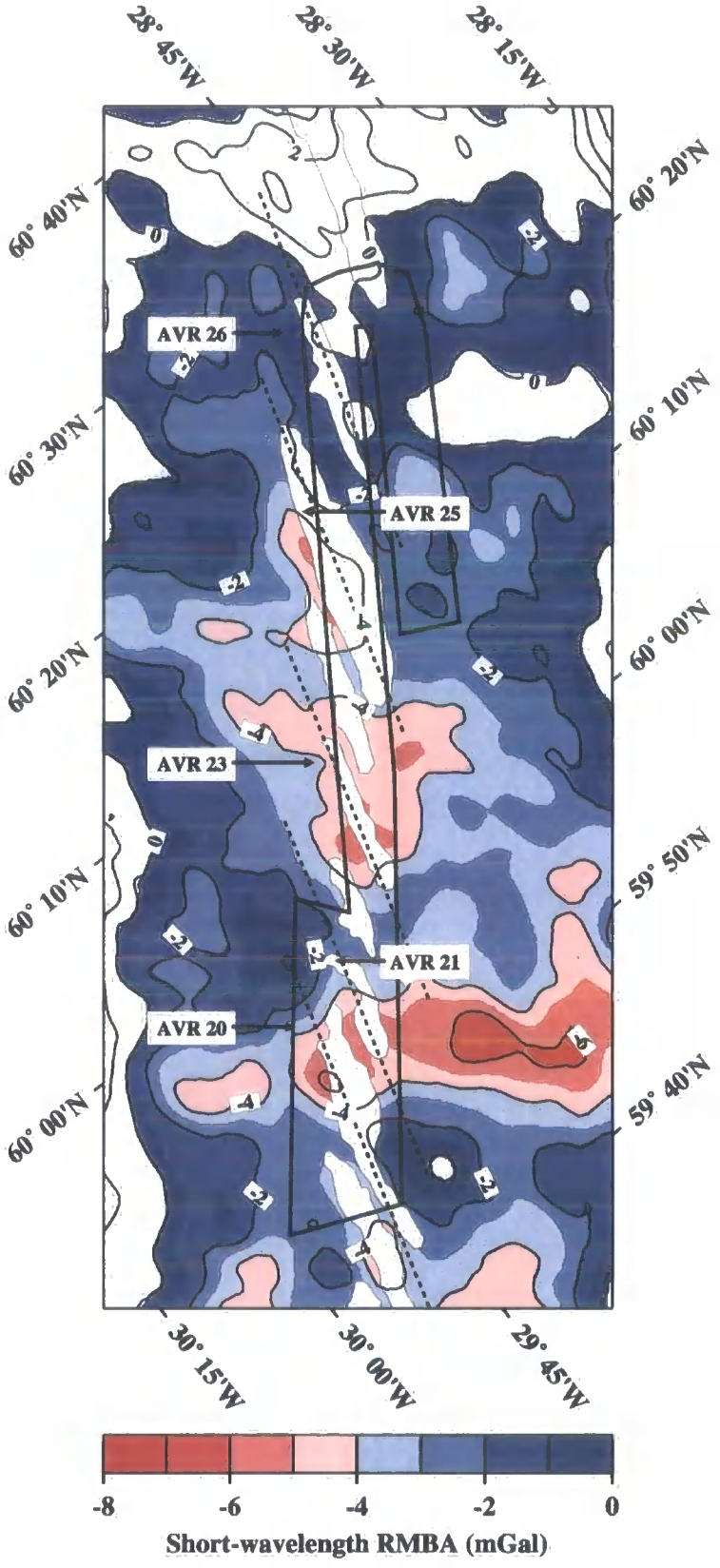

Figure 4.23: Short-wavelength RMBA for TOBI area B. Short-wavelength features have been highlighted by removing the long-wavelength planar trend from the RMBA (see text for details). A number of small "bull's eye" RMBA lows are associated with individual AVRs (outlined in white and annotated with arrows). The black box shows the outline of TOBI area B. Dashed black lines through AVRs show profiles extracted for modelling. Note that the colour scale has been chosen to highlight the on-axis anomalies.

In addition, the short-wavelength RMBA amplitudes in TOBI area B are generally higher than the amplitudes in area C, suggesting thicker crust relative to the crustal model and/or that the crust and mantle in area B are hotter than further south resulting in a constant DC-shift in the RMBA.

Relative age	AVR No.	Length (km)	RMBA (mGal)
adolescent-mature	23	12	-3
adolescent-mature	21	13	-5
adolescent-mature	26	20	-1
mature	20	28	-6
mature	25	32	-3

Table 4.5: Correlation between relative age, length and RMBA peak-to-trough amplitude for selected AVRs of TOBI area B. Older AVRs generally appear to be longer but there is no correlation with RMBA amplitude. AVR 26 is unusual in that it only has a -1 mGal anomaly (see Section 4.4.2.2.6).

Furthermore, asymmetry in the RMBA is not as obvious here as for TOBI area C, suggesting that asymmetric spreading is more difficult to maintain in the presence of higher thermal regimes (Macdonald 1977).

4.4.2.2.1 AVR 20

The along-axis RMBA reaches a -6 mGal low at the centre of this AVR (Fig 4.24a). A fit to the RMBA for this AVR can be obtained with models that feature layer 2 thickness increase of up to 800 m beneath the AVR (Fig. 4.24b), or more subdued layer 2 thickness variation with a 400-600 m thickening of the crust beneath the AVR (Fig. 4.24c). Alternatively, small crustal density variations (0.02-0.03 g cm^{-3}) equivalent to 10-15% retained partial melt (Fig. 4.24d), or a combination of a 0.01-0.02 g cm^{-3} low-density anomaly (5-10% partial melt) region with a ~400 m increase in crustal thickness beneath the AVR centre (Fig. 4.24e) can also produce an acceptable fit to the RMBA.

A model of the crust that includes crustal thickening beneath the AVR or the presence of a small amount of partial melt in the mid-crust is consistent with the TOBI interpretation of a *mature* age for this AVR.

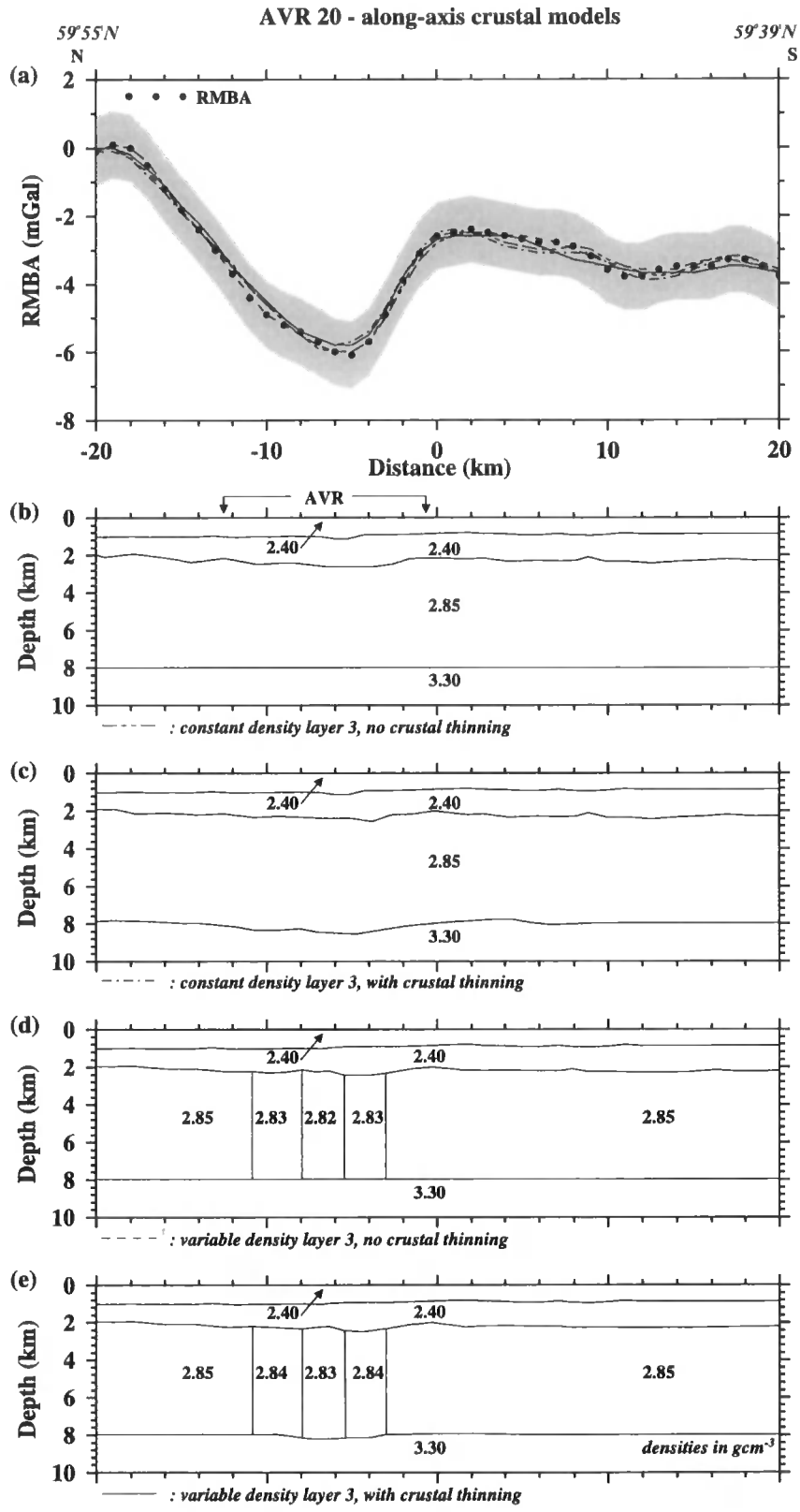

Figure 4.24: Along-axis RMBA profile for AVR 20 sampled from the short-wavelength RMBA plot of Fig. 4.23. The RMBA is shown by dots, with error bounds (grey shaded region) and calculated anomalies (see annotation for details) for each of the models shown in (b)-(e) superimposed. The RMBA has had the gravitational effects of the seawater/seabed interface removed, hence models only show layers 2A, 2B, 3 and the upper mantle. Each model extends from -1000 km to 1000 km laterally, to 20 km depth and has a 10000 km half-strike length in the third dimension to avoid edge effects and to give the models a 2.5-D aspect. The lateral extent of the AVR is highlighted. (b)-(e) explore the contributions to the RMBA of variations in crustal thickness, variations in mid-crustal densities, and combinations of crustal thickness and mid-crustal density variations (see text for details).

4.4.2.2.2 AVR 21

A ~5 mGal RMBA low is associated with this AVR (Fig. 4.25a). Models that produce an acceptable fit to the RMBA for this AVR include layer 2 thickness variations (Fig. 4.25b) and smaller layer 2 thickness variations with ~800 m crustal thickening beneath the AVR (Fig. 4.25c). Mid-crustal density variations of 0.01-0.03 g cm^{-3}, equivalent to 5-15% partial melt, in a region 12 km wide beneath the AVR (Fig. 4.25d), or variations of 0.01-0.02 g cm^{-3}, or 5-10% partial melt, combined with ~200 m crustal thickening (Fig. 4.25e) also produce an acceptable fit to the gravity anomaly.

Models showing a small amount of crustal thickening beneath the AVR and/or the presence of a small amount of partial melt are consistent with this AVR's *adolescent-mature* age interpretation.

4.4.2.2.3 AVR 23

The -3 mGal RMBA low over the centre of this AVR (Fig. 4.26a) can be modelled by layer 2 thickness variations of 100-200 m (Fig. 4.26b), crustal thickening of 400-600 m beneath the AVR (Fig. 4.26c), a 10 km wide, 0.01-0.03 g cm^{-3}, low-density region (Fig. 4.26d) corresponding to 5-15% partial melt, or a 0.01-0.02 g cm^{-3} density anomaly (5-10% partial melt) combined with a 400 m increase in crustal thickness beneath the AVR (Fig. 4.26e).

The last model, combining small amounts of partial melt with crustal thickening, is most consistent with the AVR's relative *adolescent-mature* age.

4.4.2.2.4 AVR 25

This AVR is associated with a -3 mGal RMBA low (Fig. 4.27a). Modelling shows that a reasonable fit to the RMBA can be obtained with crustal models that include layer 2 thickness variations (Fig. 4.27b), or more subtle layer 2 thickness variations with a 400-600 m increase in crustal thickness beneath the AVR (Fig. 4.27c). Alternatively, mid-crustal density variations can also produce an acceptable fit to the gravity anomaly. A ~10 km wide, 0.01-0.02 g cm^{-3} density anomaly, suggesting the presence of 5-10% retained partial melt, beneath the AVR (Fig. 4.27d), or a 0.005-0.01 g cm^{-3} density low (2.5-5% partial melt) with 200-400 m crustal thickening beneath the AVR (Fig. 4.27e) are valid models.

As for the previous AVR, the model that combines small amounts of partial melt with crustal thickening is most consistent with the *mature* age of this AVR.

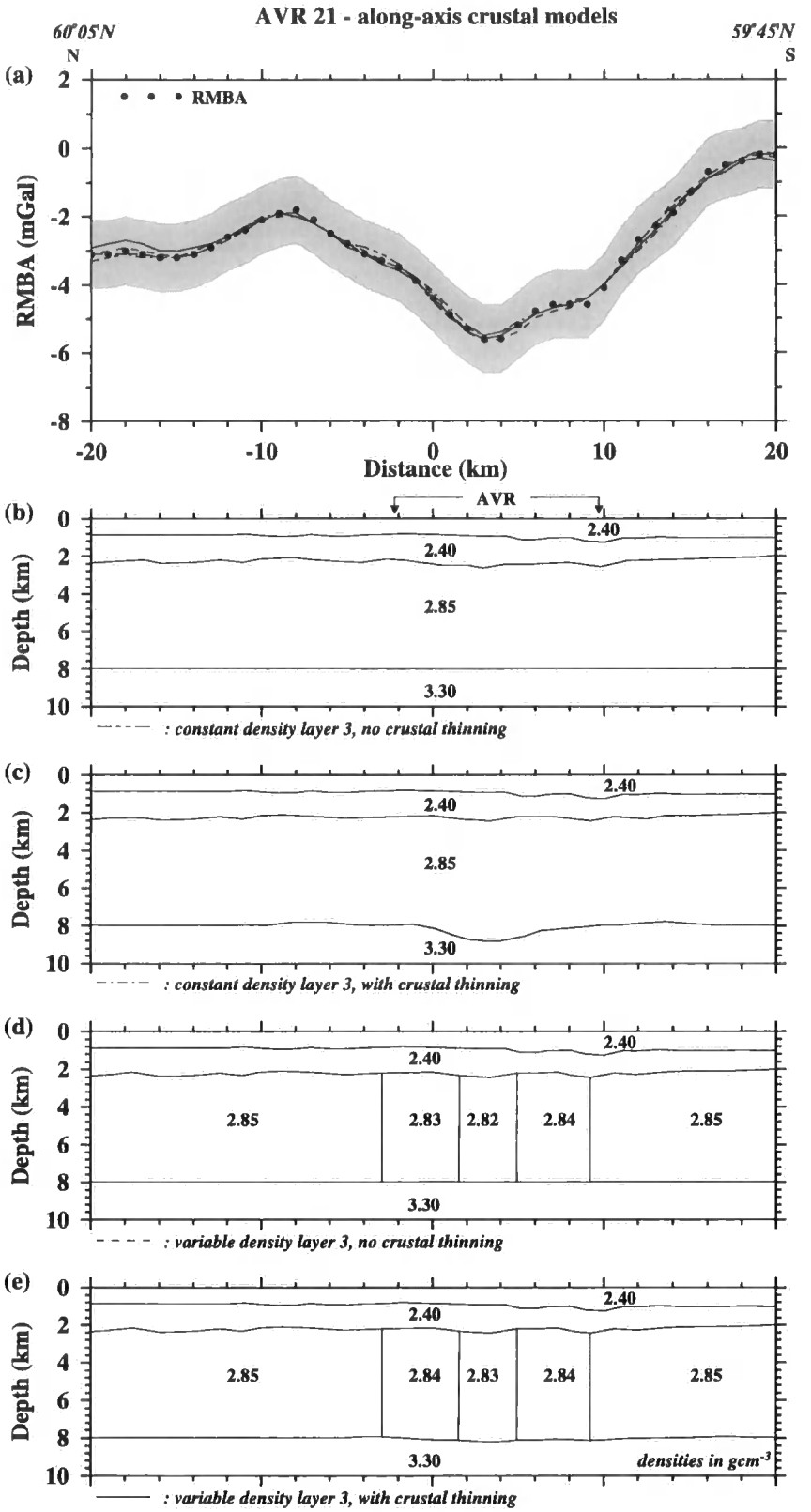

Figure 4.25: Along-axis RMBA profile for AVR 21 sampled from the short-wavelength RMBA plot of Fig. 4.23. See Fig. 4.24 for plotting and model parameters. (b)-(e) explore the contributions to the RMBA of variations in crustal thickness, variations in mid-crustal densities and combinations of crustal thickness and mid-crustal density variations (see text for details).

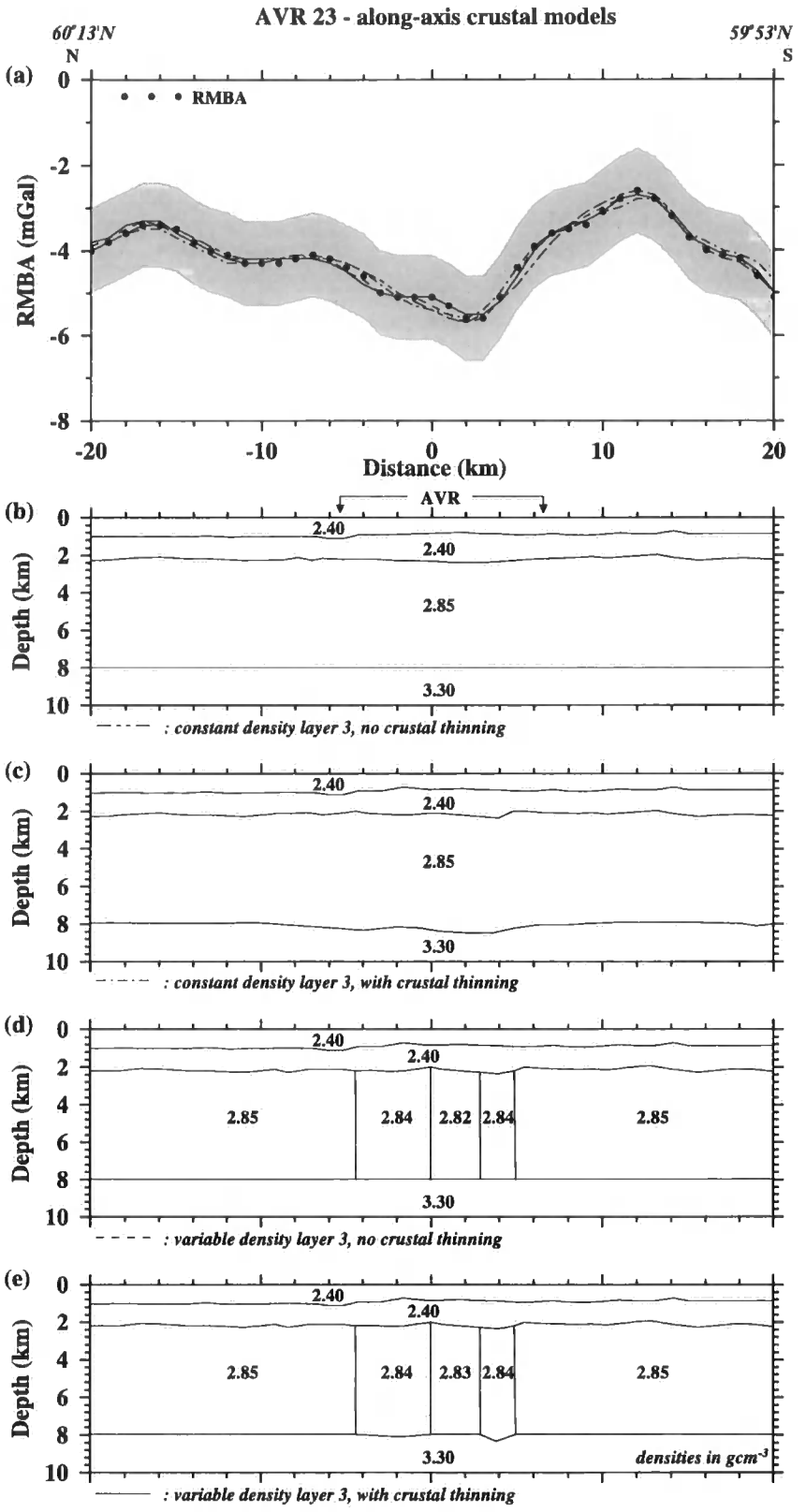

Figure 4.26: Along-axis RMBA profile for AVR 23 sampled from the short-wavelength RMBA plot of Fig. 4.23. See Fig. 4.24 for plotting and model parameters. (b)-(e) explore the contributions to the RMBA of variations in crustal thickness, variations in mid-crustal densities and combinations of crustal thickness and mid-crustal density variations (see text for details).

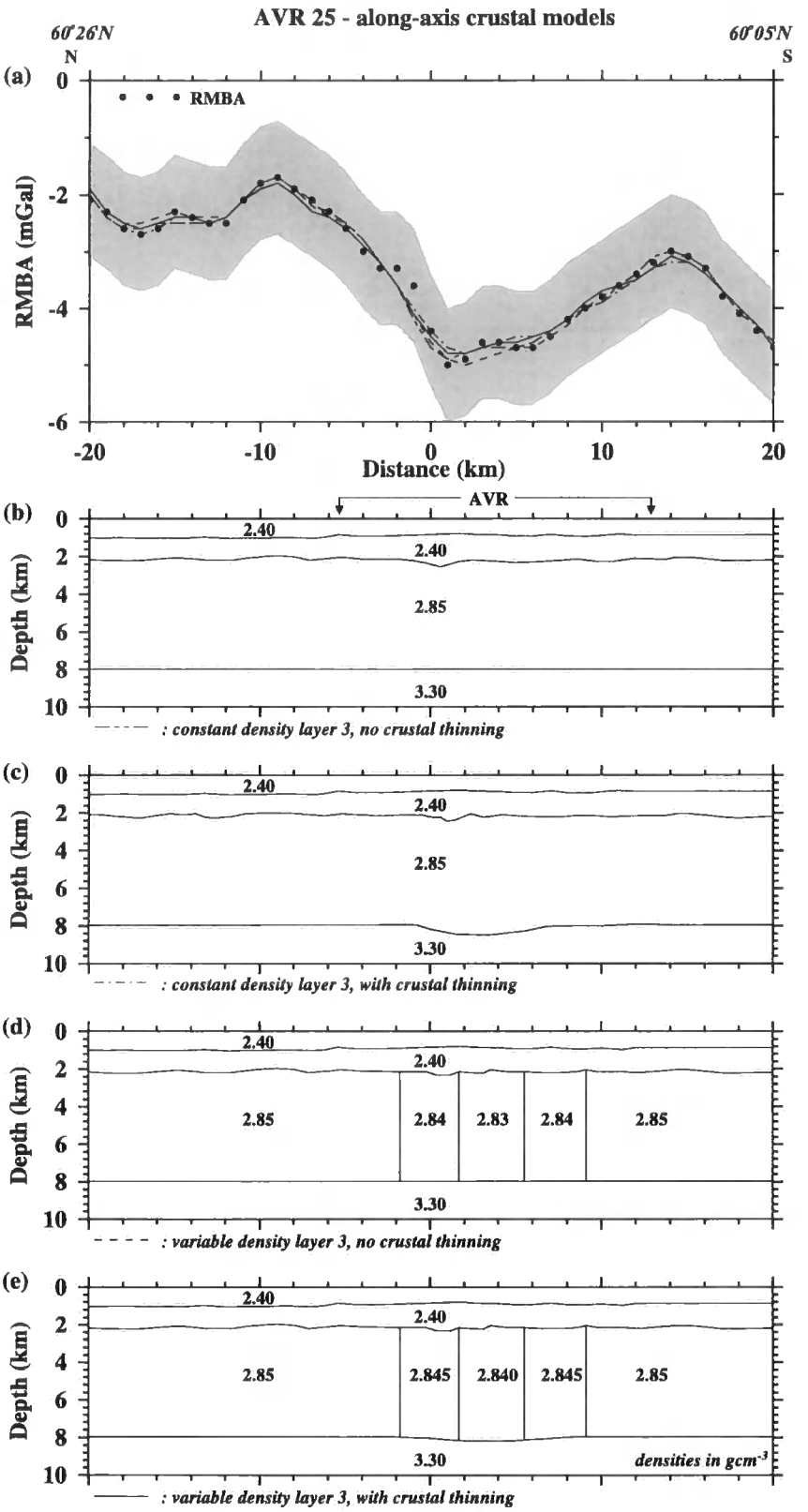

Figure 4.27: Along-axis RMBA profile for AVR 25 sampled from the short-wavelength RMBA plot of Fig. 4.23. See Fig. 4.24 for plotting and model parameters. (b)-(e) explore the contributions to the RMBA of variations in crustal thickness, variations in mid-crustal densities and combinations of crustal thickness and mid-crustal density variations (see text for details).

4.4.2.2.5 AVR 26

This AVR has no distinct RMBA low, instead ~1 mGal variations in RMBA amplitude are observed with a ~5 km wavelength (Fig. 4.28a). Short-wavelength fluctuations in layer 2 thickness (Fig. 4.28b) or smaller amplitude fluctuations with a 400 m increase in crustal thickness beneath the AVR (Fig. 4.28c) produce an acceptable fit to the RMBA. A 8 km wide, 0.02-0.03 g cm^{-3} low-density anomaly (Fig. 4.28d), equivalent to 5-15% retained melt, or a 0.01-0.02 g cm^{-3} anomaly (5-10% partial melt) with ~200 m crustal thickening beneath the AVR (Fig. 4.28e) also produce acceptable fits to the RMBA.

As for the previous AVR, the model that combined small amounts of partial melt with crustal thickening is most consistent with the *adolescent-mature* age of this AVR.

4.4.2.2.6 Resolution of models

In this section, tests to investigate the amount of partial melt in the crust and the extent of crustal thickening that are resolvable by the gravity data are discussed.

Densities in a region in the mid-crust beneath AVR 20 (see Section 4.4.2.2.1) were gradually changed to provide a series of calculated gravity anomaly profiles for 0% to 20% of partial melt content in the mid-crust, in 5% increments (Fig. 4.29a). Comparing the fit of these curves to the observed RMBA shows that greater than 5% partial melt content in the mid-crust, within a ~10 km wide region, is resolvable within the ± 1 mGal RMBA error bounds.

Similar sets of gravity anomaly curves were calculated for the crustal thickness resolution test. Crustal thickness beneath the centre of AVR 20 was increased in 0.3 km increments until it resulted in a significant misfit to the RMBA. The calculated curves cover a total increase in crustal thickness of 1.2 km from the original thickness of ~8 km. Fig. 4.29(b) shows these curves together with the observed RMBA. Thickness variations greater than 0.3 km are shown to be resolvable by the gravity data.

The resolution tests presented here are applicable to all of the modelled AVRs and show that variations in partial melt in the mid-crust of 5% and crustal thickness variations of 0.3 km can be resolved.

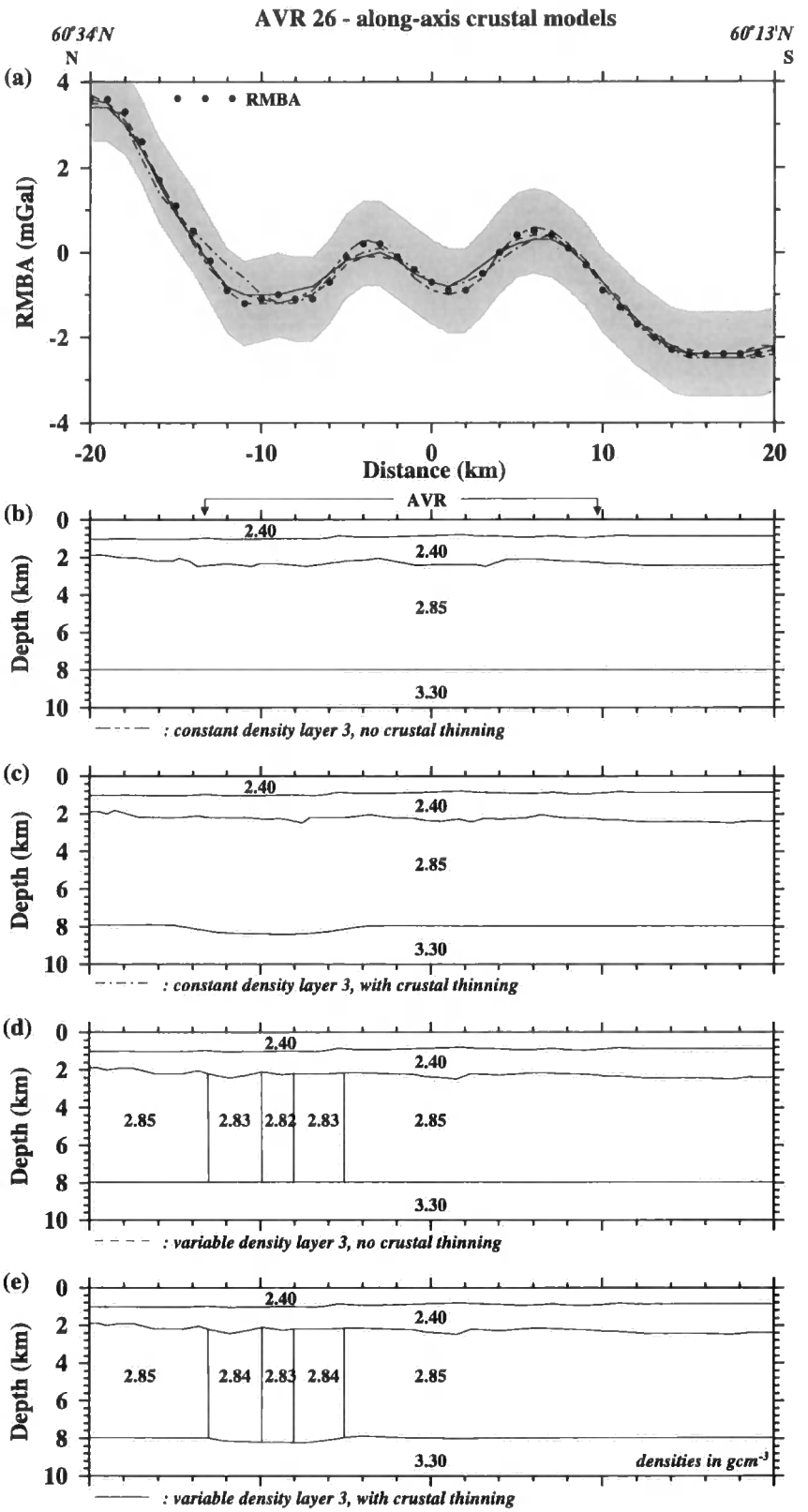

Figure 4.28: Along-axis RMBA profile for AVR 26 sampled from the short-wavelength RMBA plot of Fig. 4.23. See Fig. 4.24 for plotting and model parameters. (b)-(e) explore the contributions to the RMBA of variations in crustal thickness, variations in mid-crustal densities, and combinations of crustal thickness and mid-crustal density variations (see text for details).

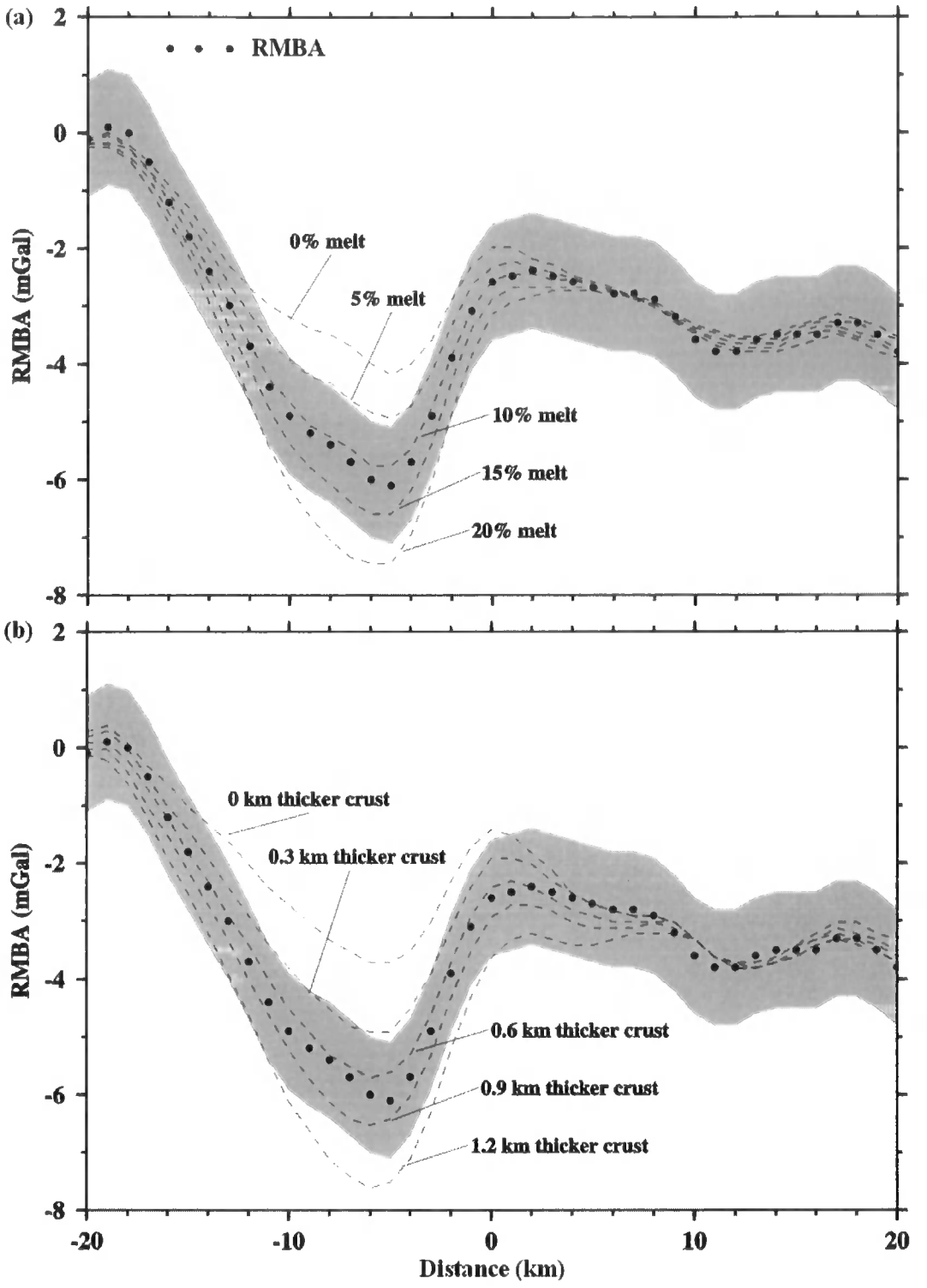

Figure 4.29: Resolution tests for gravity models. (a) Tests for amount of partial melt resolvable in the mid-crust. Dashed lines show calculated gravitational attraction of models with different amounts of partial melt (see annotation) in the mid-crust of AVR 20. Comparison of these curves to the observed RMBA (dots) and its error bounds (grey shading) shows that > 5% retained partial melt can be resolved. (b) Tests for crustal thickness variation resolution. Dashed lines show calculated gravitational attraction of models with variations in crustal thickness (see annotation) of AVR 20. Comparison of these curves to the observed RMBA (dots) and its error bounds (grey shading) shows that > 0.3 km total crustal thickness variations can be resolved.

4.4.2.2.7 Summary of TOBI area B

Removal of the long-wavelength planar trend from the RMBA leaves small gravity anomalies associated with individual AVRs. The absence of significant variation in the short-wavelength RMBA for AVRs of different relative ages suggests that along-axis redistribution of melt in the crust may be a significant active process in this hotspot influenced part of the ridge.

Along-AVR-axis gravity models are consistent with the TOBI-based relative AVR age interpretations. Older AVRs are generally longer, have less melt in the mid-crust and a thicker crust than younger AVRs (see Table 4.6). Unlike TOBI area C, no asymmetry in the RMBA, relative to the ridge axis, is observed suggesting that the thermal regime influences the degree of asymmetry that can be maintained at the ridge.

Relative age	AVR No.	Length (km)	RMBA (mGal)	Crustal structure	
				crustal thickening (m)	partial melt
adolescent-mature	23	12	-3	< 600	< 15%
adolescent-mature	21	13	-5	< 800	< 15%
adolescent-mature	26	20	-1	< 400	< 15%
mature	20	28	-6	< 600	< 15%
mature	25	32	-3	< 600	< 10%

Table 4.6: Correlation between relative age, length, RMBA peak-to-trough amplitude (see Table 4.5) and inferred crustal structure for selected AVRs of TOBI area B. The RMBA lows can be modelled by crustal thickening and/or the presence of partial melt in the mid-crust (grey shading shows the preferred model, chosen on the basis of the relative age of AVRs - no shading indicates that there is no preferred model and that both crustal thickening and partial melt are likely to be present). The long length of AVR 26, relative to the other *adolescent-mature* AVRs, and its low RMBA amplitude, suggest that it is at the very end of its *adolescent* phase. Note that the extent of thickening and the amount of partial melt shown are maximum values. See text for details.

Evidence for segmentation is similar to that observed for TOBI area C but is more subdued because of the hotter thermal regime associated with the proximity of the Iceland hotspot.

4.5 Summary

In this chapter the gravity field has been reduced by removing the 3-D effect of the seawater-seafloor interface. The gravitational effects of a simple crustal model, based on wide-angle seismic models, have also been removed. The data have been further corrected by removing thermal effects due to passive upwelling at the ridge-axis. Before investigating tectonomagmatic effects on the crustal structure of individual AVRs, the long-wavelength effect of the Iceland hotspot on the crustal structure of the ridge was examined.

The along-axis FAA was forward modelled in 2-D, revealing an along-axis increase in crustal thickness from 7.5 km to 10.5 km and a decrease in mantle densities from 3.30 to 3.23 g cm^{-3} between 57°30'N and 62°N. In addition, modelling confirms that "normal" oceanic crustal thickness of 7.1 ± 0.8 km is achieved south of 59°N and that TOBI area C, unlike TOBI area B, lies outside of the region of hotspot influence.

Along-AVR-axis gravity modelling has shown that a number of these RMBA lows can be explained by a 200-800 m thickening of the crust and/or by the presence of low-density regions in the mid-crust. Interpretation of TOBI images indicates that these AVRs are at various stages of an evolutionary lifecycle and a correlation between AVR age and crustal structure is established for TOBI area C, with longer, more mature AVRs having a thicker crust and/or lower-density region in the mid-crust. In addition, asymmetry in the across-axis RMBA pattern observed over a number of AVRs suggests that at these locations the crust is preferentially accreted to one side of the ridge. The AVRs of TOBI area B appear to have the same correlation between relative age and length. However in this region, the RMBA amplitude, and hence the inferred crustal structure, shows little variation from AVR to AVR suggesting that along-axis redistribution of melt subdues variations in gravity anomalies.

In the next chapter the magnetic data is used to provide constraints on the timing of accretionary processes and on any local spreading rate variations that may be attributed to episodic cycles of tectonic and magmatic activity. In addition, the suggestion of asymmetry in accretion presented in this chapter will be investigated further.

Chapter 5

Magnetic data inversion

5.1 Introduction

Pillow basalts and sheeted dykes, extruded at the ridge axis, cool rapidly through conduction and hydrothermal circulation as seawater percolates through the upper crust. As the temperature falls below the Curie point (T_c), titanomagnetite (T_c = ~210°C) in the extrusive layer and magnetite (T_c = ~580°C) in the intrusive part of the upper crust (the principal carriers of natural remnant magnetization (NRM)) become magnetized in the direction of the present-day magnetic field. The highest magnetization occurs in the pillow basalts forming layer 2A (Fig. 5.1), although layers 2B and 3 contribute to some extent to the anomaly observed at the sea surface (Smith & Banerjee 1986; Gee & Kent 1994).

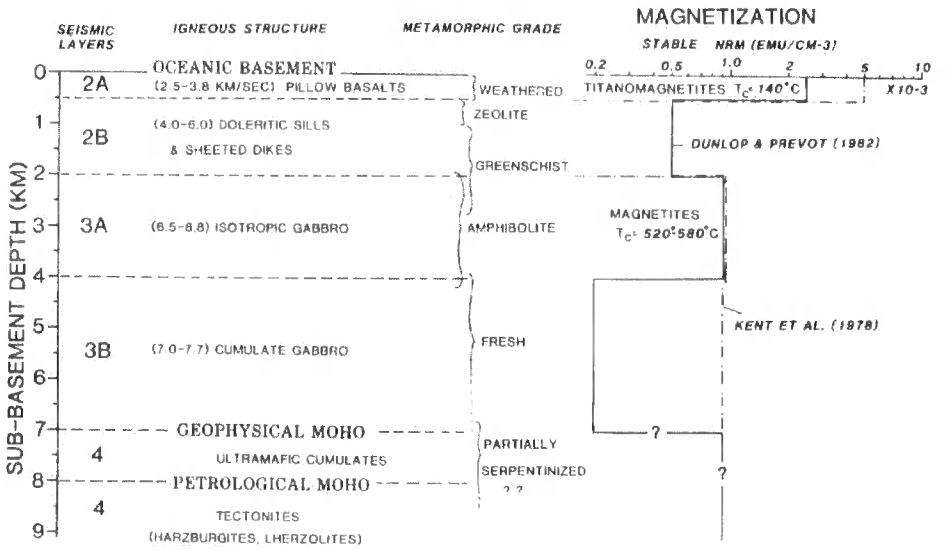

Figure 5.1: Variation in magnetization intensity with depth from Vogt (1986). The average seismic structure of the oceanic crust, with inferred igneous structure and metamorphic grade, is shown on the left-hand side. The corresponding magnetization models of Kent *et al.* (1978) (dash-dot), based on drill samples, and Dunlop & Prevot (1982) (solid line) are shown on the right-hand side. T_c is the Curie temperature and 1×10^{-3} emu cm^{-3} is equivalent to 1 A m^{-1}.

Magnetization intensities depend on the strength of the Earth's field and rock susceptibility, and vary from ~10 A m^{-1} for layer 2A to ~1 A m^{-1} for layers 2B and 3

based on measurements on drill samples (Kent *et al.* 1978; Dunlop & Prevot 1982; Vogt 1986).

Magnetic anomalies observed at the sea surface represent the integrated effect of an area of size H^2, where H is the height from the observation plane to the seafloor (Vogt 1986). This averaging effect explains the lack of direct correlation between calculated magnetization intensities and intensity values obtained from core samples. Variations in height of the observation plane to the magnetic layer also attenuate the magnetic anomalies observed at the sea surface proportionally to $e^{-H/\lambda}$, where λ is the wavelength of the anomaly.

A decrease in magnetization intensity with age (Fig. 5.2), attributed to low-temperature oxidation of titanomagnetite, has been observed at all sampled ridges (e.g. Johnson & Hall 1978; Talwani *et al.* 1971; Lowrie 1977; Johnson & Atwater 1977; Macdonald 1977) with a factor of five reduction in the NRM over the first 0.5 Myr (Johnson *et al.* 1996).

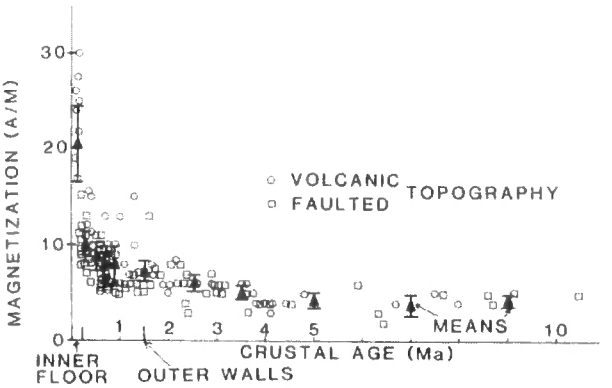

Figure 5.2: Decrease in magnetization intensity with age computed from deep-tow measurements in the FAMOUS area, located near 37°N on the Mid-Atlantic Ridge. From Macdonald (1977).

Analysis of variations in magnetization intensity across- and along-axis may, therefore, provide a useful constraint on the timing of crustal accretionary processes and provide further information on the asymmetry in spreading that has been suggested from the TOBI interpretation and gravity modelling. In this chapter, the magnetization intensities will be primarily used to groundtruth the relative age of AVRs as determined by TOBI image interpretation (see Sections 3.2 and 3.3) and to calculate local spreading

rates of individual AVRs to determine whether a correlation exists between relative AVR age and local spreading rate.

A 3-D inversion procedure that takes into account topographic effects, developed by Macdonald *et al.* (1980) using the Fourier technique of Parker & Huestis (1974), is used to calculate the magnetization intensity for the survey area. Sections 5.2 and 5.3 describe the 3-D inversion theory and method respectively. The results of the inversion, together with both long- and short-wavelength observations, including spreading rate calculations, are presented in Section 5.4.

5.2 Inversion theory

In Parker & Huestis (1974)'s inversion method the magnetic anomalies at the sea surface are assumed to originate from a constant thickness magnetic layer, with an upper surface constrained by the seafloor topography. Crustal magnetization, assumed to be uniform with depth, is oriented parallel to an axial geocentric dipole model of the Earth's field (reversals are described by negative intensities) and intensity variations are constrained to lie in the spreading direction.

The inversion procedure relies on a Fourier representation of the magnetic anomalies that was first described for the forward problem by Parker (1973) and is similar to the gravity procedure described in Section 4.2.1. Given a simple model of the crust, where h_o is the thickness of the magnetic layer, $h(x)$ describes the seafloor topography normal to the ridge axis and $M(x)$ is the magnetization intensity distribution, the Fourier transform of the magnetic anomaly, A, measured everywhere above the magnetic layer at a height z_o is given by equation 5.1.

$$F[A] = \frac{\mu_o}{2}\exp(-|k|z_o)[1-\exp(-|k|h_o)]V(k)\sum_{n=0}^{\infty}\frac{|k|^n}{n!}F[M(x)h(x)^n] \qquad (5.1)$$

where $V[k] = \hat{B}_o \cdot (\hat{z} + i\hat{x}k/|k|)\hat{M}_o \cdot (\hat{z} + i\hat{x}k/|k|)$ (5.2)

and $\hat{M}_o$ and $\hat{B}_o$ are constant unit vectors in the magnetization and ambient field directions respectively. An inverse procedure, where a magnetization intensity distribution can be found that reproduces the magnetic anomaly at the sea surface, can be formulated by rearranging equation 5.1, resulting in equation 5.3.

$$F[M] = \frac{F[A]\exp(|k|z_o)}{(\frac{\mu_o}{2})[1-\exp(-|k|h_o)]V(k)} - \sum_{n=1}^{\infty}\frac{|k|^n}{n!}F[Mh^n] \qquad (5.3)$$

An initial solution, usually $M=0$, is substituted into the right-hand side of equation 5.3 and a new magnetization intensity distribution is computed by inverting the transform. This new M is used on the right-hand side of equation 5.3 again and the procedure is repeated until M converges. The exponential terms in equation 5.3 amplify high and low wave numbers (Carbotte & MacDonald, 1992; Schouten & McCamy 1972) and a band-pass filter is, therefore, applied after every iteration to avoid introducing artefacts into the solution. In addition, the magnetization intensity distribution is non-unique as a solution can be found for any choice of $\hat{M}_o, \hat{B}_o$ and h_o. A distribution, which produces no external field for the given bathymetry, can thus always be found. This distribution is called the annihilator. It is, therefore, usual practice to add a scaled annihilator to the inversion solution such that approximately equal positive and negative magnetizations occur across a reversal. At mid-ocean ridges this reversal is normally the Brunhes/Matuyama reversal. This inversion procedure was extended into 3-D in a program called *inv3d* (Macdonald *et al.* 1980) by allowing the magnetization of the magnetic layer to vary in both horizontal directions.

5.3 Method

To facilitate the inversion process for the Reykjanes Ridge, bathymetry and magnetic data compilations described in Section 2.3 and 2.6 respectively, were converted to Cartesian coordinates, rotated about 57°45'N/32°30'W to align the x-axis with the direction of spreading, and re-gridded at a node interval of 0.5 km by 0.5 km on a 2048 by 2048 grid (Fig. 5.3). Gridding parameters were chosen to isolate the study area from possible edge effects and to comply with the file input requirements of the inversion program, *inv3d*. The main parameters used in the inversion procedure are shown in Table 5.1, with source layer thickness and filtering parameters being the most important factors.

inv3d calculates a possible magnetization solution for the given source layer thickness, taking into account the seafloor topography and skeweness in the magnetic field caused by the latitude of the survey area and the orientation of the ridge. The thickness of the magnetized layer, which is assumed in this study to be layer 2A in common with most other studies (Talwani *et al.* 1971; Carbotte & Macdonald 1992; Gee & Kent 1994; Hooft *et al.* 1996; Schouten *et al.* 1999; Bazin *et al.* 2001; Fujiwara *et al.* 2003), was taken to be 0.5 km based on seismic refraction surveys located

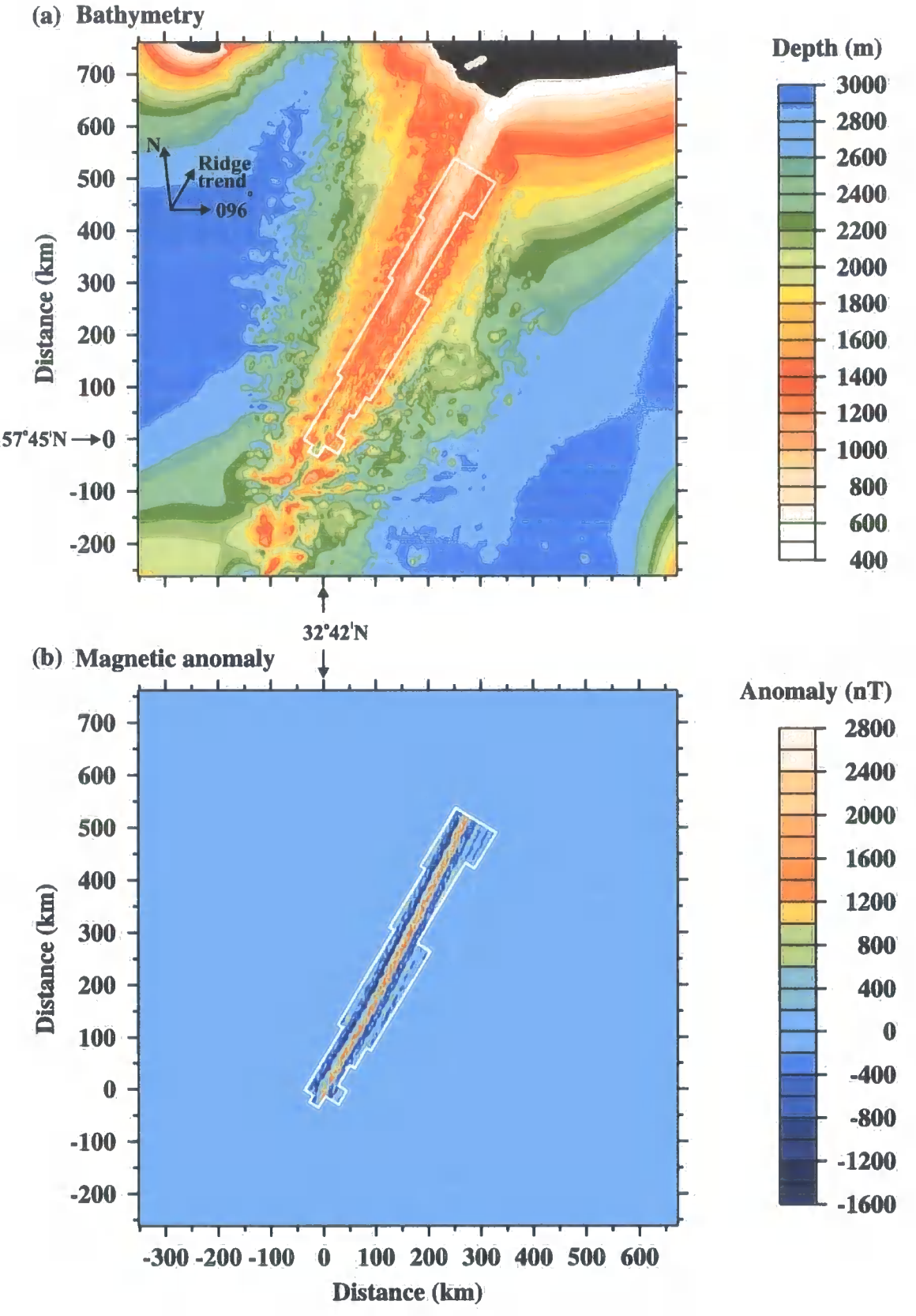

Figure 5.3: Input grids to the magnetic inversion program, *inv3d*. (a) Bathymetry grid used by *inv3d* to remove topographic effects from the calculated magnetization intensities. (b) Magnetic anomaly grid used by *inv3d* along with the bathymetry to invert for the magnetization intensity distribution. The area outside of the study area (outlined in white) has been set to 0 A m^{-1}, as spurious data points outside of the study area were found to effect the inverted magnetization intensities within the study area. Both grids contain 2048 by 2048 nodes spaced at 0.5 km interval and have been rotated to align the spreading direction (096°) along the x-direction and projected to cartesian coordinates (as required by *inv3d*).

throughout the study area (Navin *et al.* 1998; Bunch & Kennet 1980; Smallwood *et al.* 1995; Weir *et al.* 2001) and to be compatible with the results of Lee & Searle (2000).

Inversion Parameter	**Description**	**Value**
ZOBS	Depth of observation plane	0.0 km
NNX	Number of data points in x-direction (must be 2^N)	2048
NNY	Number of data points in y-direction (must be 2^N)	2048
WLONG	Low-pass filter limit	300.0 km
WSMALL	Hi-pass filter limit	3.0 km
THICK	Thickness of magnetized layer	0.5 km
RLAT/RLON	Latitude/Longitude	57.5/-32.5
YR	Decimal year	1998.4
SLIN	Strike of y-axis (assuming x-axis is along spreading direction)	354.0
INBOARD	Ramp bathymetry border at high x and y?	True
IANNI	Calculate annihilator?	True
NTERMS	Number of terms in series expansion	4
NITRS	Number of iterations	8

Table 5.1: Main parameters used in the 3-D magnetic anomaly inversion program, *inv3d* (Macdonald *et al.* 1980).

Parker & Huestis (1974) investigated the effects of varying the source layer thickness on the magnetization intensity and showed that magnetization intensity is almost inversely proportional to layer thickness. Hence, the observed magnetic anomalies can either be explained by a thin source layer with a high magnetization intensity or a thicker layer with a lower magnetization intensity (Fig 5.4). This non-uniqueness in the solution is common to all potential field problems and models can only be constrained by considering additional information, usually from seismic refraction surveys.

Lee & Searle (2000) showed that, near 63°N on the Reykjanes Ridge, only 50% of the on-axis magnetization solution could be explained solely by layer 2A thickness variations as determined from seismic refraction data (Fig. 5.5). A significant component of the solution must, therefore, originate from local magnetization intensity variations due to relative age differences of the extrusive layer.

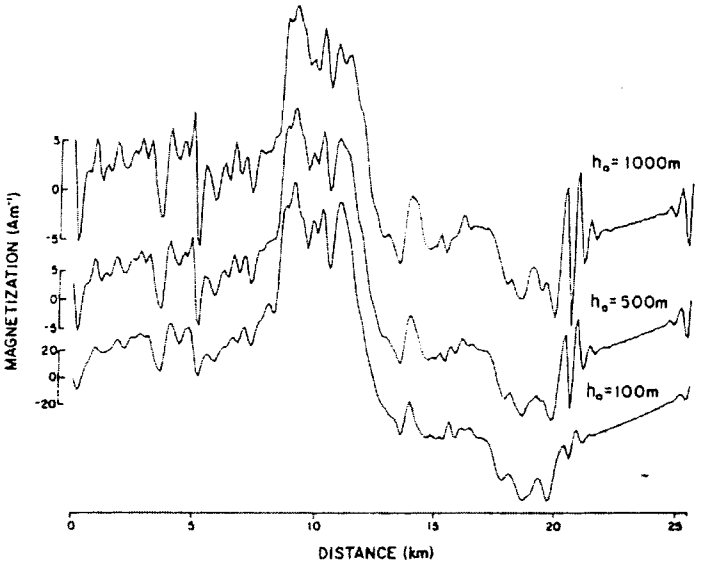

Figure 5.4: Effect of layer 2A thickness variation on the magnetization solution. Magnetic anomaly profiles across the EPR (near 51°N) were inverted using the 2-D method described in Section 5.2 with different magnetic source layer thicknesses, h_0 = 100 m, 500m and 1000 m. The figure shows the calculated magnetization intensity distributions for different layer thicknesses. Variations in crustal thickness only change the absolute intensity (note different scale used for each curve) and not the actual magnetization intensity distribution (from Parker & Huestis 1974).

The short-wavelength filter cut-off was set to 3 km as the inversion will not resolve wavelengths shorter than the depth to the seafloor (Lee & Searle 2000) and the maximum seafloor depth in the study area is ~3 km. The long-wavelength filter cut-off, chosen to avoid spatial aliasing due to the assumed periodicity of the data that is inherent to any FFT method, was set to 300 km - the maximum width of the study area - and consistent with the value chosen by Lee & Searle (2000). The borders of the bathymetry grid were ramped to avoid ringing artefacts caused by sharp discontinuities at the edges and the number of terms in the series expansion and the number of iterations were chosen to ensure convergence of the solution (Macdonald *et al.* 1980). The output of the inversion is shown in Fig. 5.6a. *inv3d* was also set to calculate the annihilator function (Fig. 5.6b), which was scaled and added to the magnetization solution to obtain equal amplitudes around the Brunhes/Matuyama reversal (Fig. 5.7). Forward modelling of the magnetization solution reproduces the observed magnetic anomalies to within 1.9 nT r.m.s. (Fig. 5.8), giving an indication of the accuracy of the solution.

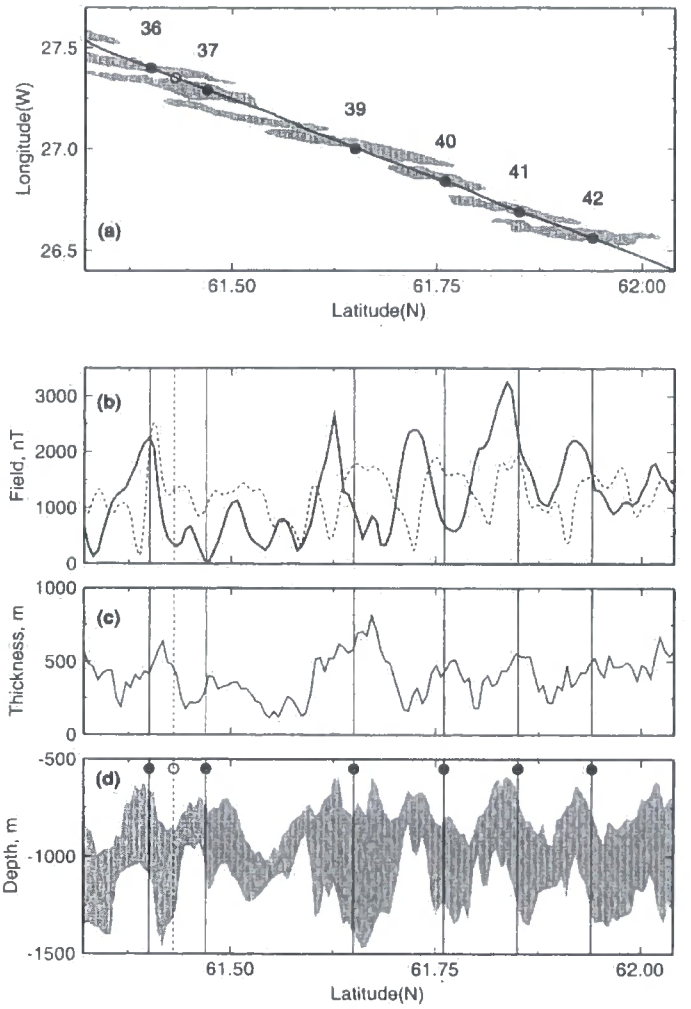

Figure 5.5: Three-dimensional forward calculation of magnetic anomalies along seismic line CAM71 (Smallwood & White 1998) taking the seismically-derived layer 2A thickness as the entire magnetic source layer. (a) Location of CAM71 (solid line) in relation to AVRs (shaded areas). (b) Comparison between the observed (solid line) and the modelled (dashed line) field at the sea surface, assuming a constant magnetization of 19 A m^{-1} of the source layer. (c) Seismically-determined layer 2A thickness variation. Layer 2A is generally thicker beneath the midpoints of AVRs. (d) The upper and lower boundaries of the magnetic source layer. From Lee & Searle (2000).

5.4 Results

The highest intensities in the calculated magnetization distribution (Fig. 5.9) occur along the ridge axis and range from 30 A m^{-1} to 75 A m^{-1}. This central anomaly magnetic high (CAMH), superimposed on the normal polarity Brunhes anomaly, marks the loci of the most recent extrusive activity. As reported by Lee & Searle (2000), the CAMH is not continuous along-axis on a small-scale (<10 km), instead discrete highs and lows in intensity are associated with AVR-scale features. The intensity decreases to ~10 A m^{-1} by 10 Ma (10 km off-axis at a half-spreading rate of 10 mm yr^{-1}), as a result

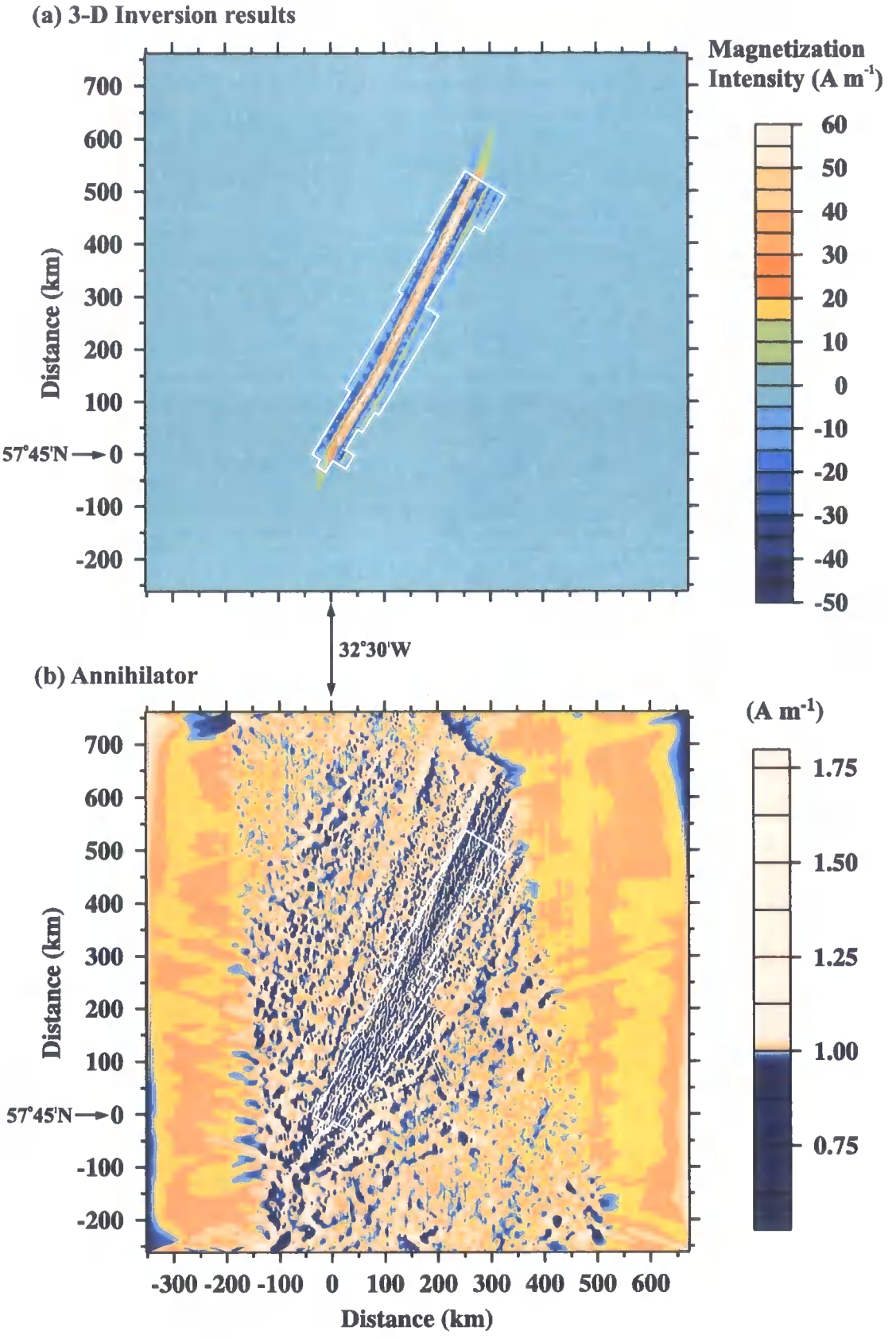

Figure 5.6: Output data from *inv3d*. (a) Magnetization intensities. Even at this scale the ride-parallel lineations and the axial high are visible (see Fig. 5.9 for a detailed view). (b) Calculated annihilator. A scaled annihilator is usually applied to the magnetization intensity solution to obtain approximately equal amplitudes across the Brunhes/Matuyama reversal (see Fig. 5.7). Note how, as expected (Parker & Huestis 1974), the annihilator appears to mirror the bathymetry.

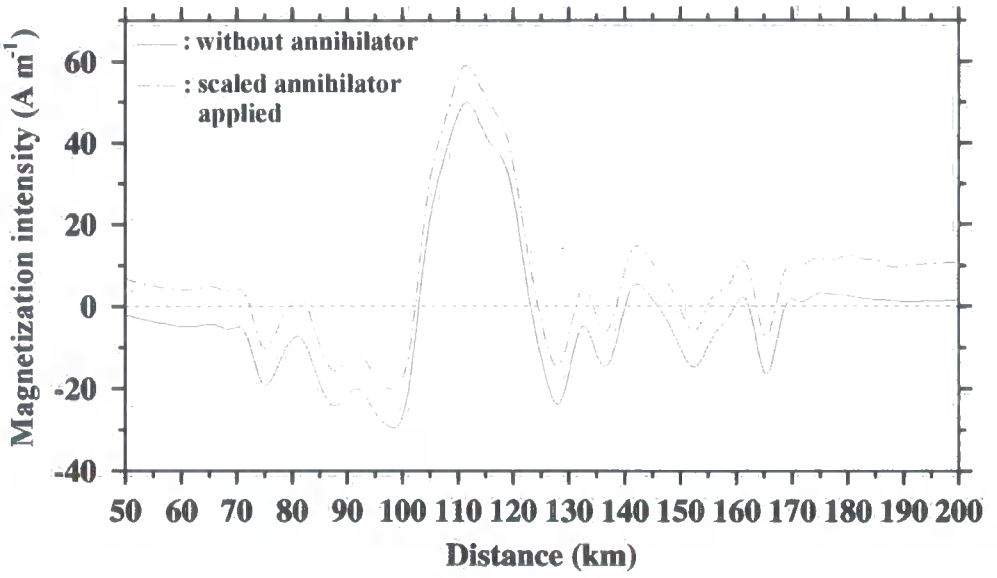

Figure 5.7: Effect of applying the annihilator function to the magnetization intensity. A profile was extracted across the study area, at y = 200 km, from the magnetization intensity shown in Fig. 5.6a before (solid lines) and after the scaled annihilator was applied (dashed line). The apparent effect is that of a DC-shift, although short-wavelength effects are observed (see 165-200 km offset).

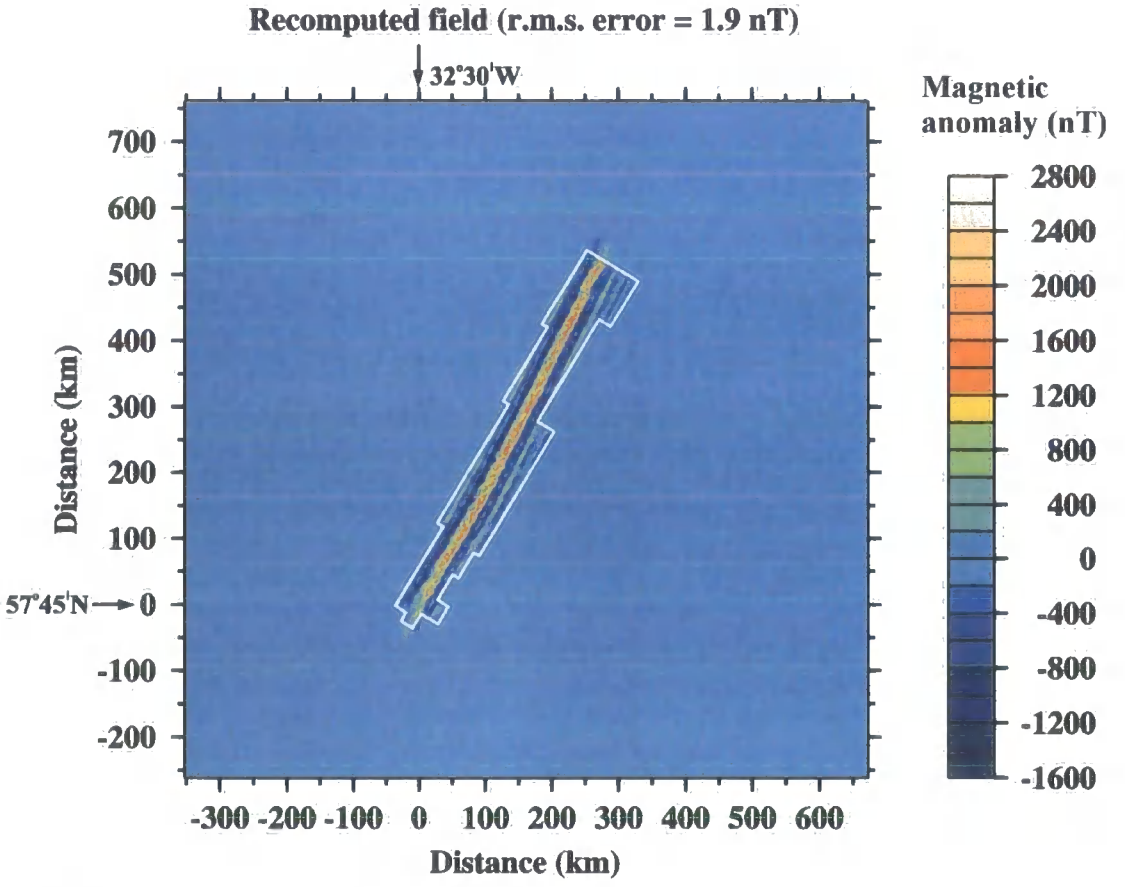

Figure 5.8: Three-dimensional forward calculation of magnetic anomaly from the magnetization intensity solution shown in Fig. 5.6(a). The r.m.s error between the recomputed and the observed anomaly (Fig. 5.3b) is 1.9 nT. The magnetization intensity solution can, thus, explain 99.95% of the variance in the magnetic anomaly.

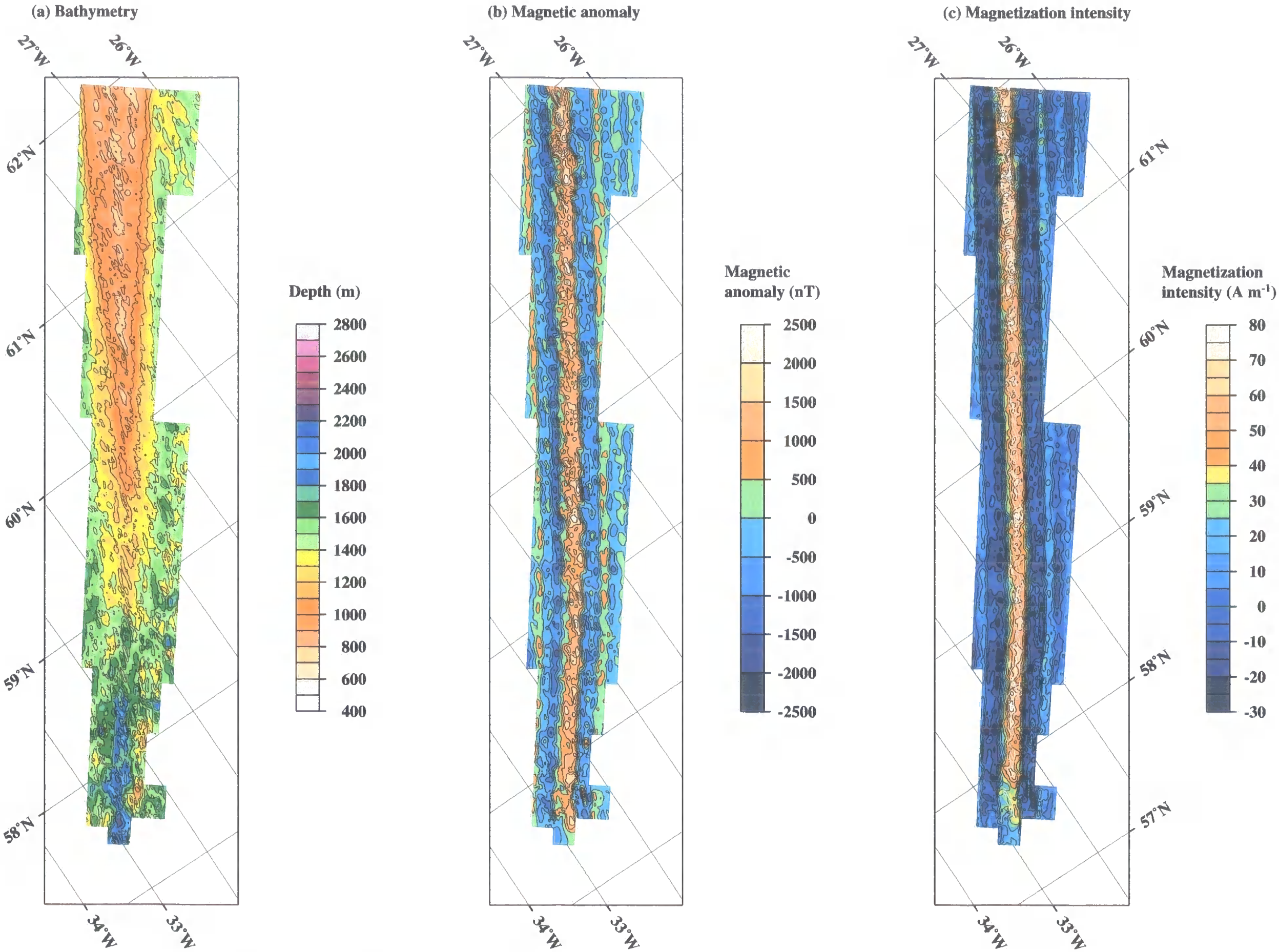

Figure 5.9: Comparison of the bathymetry, magnetic anomaly and magnetization intensity solution data for the study area. (a) Bathymetry grid with contours plotted at every 200 m intervals. See Section 2.3 for a detailed description. (b) Magnetic anomaly data with contours plotted every 10 nT intervals. See Section 2.6. (c) Magnetization intensity solution obtained by inversion of the magnetic anomaly with topographic effects removed. Magnetization intensities follow the ridge trend as expected from a local minimum of 25 A m^{-1} at 57°45'N to a high of 75 A m^{-1} near 61°50'N, a reasonable fit to the magnetization intensity range of 42 A m^{-1} to 78 A m^{-1} expected from an empirical relationship between FeO* content obtained from dredge samples and NRM (Lee & Searle 2000) . A central anomaly magnetic high (CAMH) is visible and follows the ridge axis. On a short-wavelength scale, however, the CAMH is discontinuous with local highs associated with individual AVRs (outlined in white). Contours are plotted every 10 A m^{-1} intervals. See text for details.

of low-temperature oxidation of the titanomagnetite present in the extrusive layer (Johnson & Hall 1978) or possibly due to pervasive faulting and fracturing with age which destroys magnetic domains (Tivey *et al.* 2003).

5.4.1 Long-wavelength features

Along-axis variations in the magnetization intensity (Fig. 5.10), extracted from the magnetization solution of Fig. 5.9, show the three distinct domains reported by Lee & Searle (2000). From 57°45'N to 59°10'N the magnetization intensities are highly variable and fluctuate from a minimum of 25 A m^{-1} to a high of 75 A m^{-1}. From 59°10'N to 60°50'N the intensities average 60 A m^{-1} and show less variability. A local high of 70 A m^{-1} is observed at 59°30'N. Intensities increase to an average of 65 A m^{-1} from 60°50'N to 62°N with a local minimum of 30 A m^{-1} near 61°30'N. The smoothed regional along-axis magnetization intensities mirror the FeO and TiO_2 concentrations (the goodness-of-fit coefficient, R, is 0.7-0.8, where R = 1 denotes a perfect fit) as determined by Taylor (personal communication in Lee & Searle 2000) from dredge samples (Fig 5.11). These long-wavelength, or regional, characteristics of the magnetization intensity and Fe and Ti concentrations are also thought to relate to the pulsing of the Iceland hotspot (Lee & Searle 2000), which is thought to cause high-temperature disturbances and, hence, excess melt to travel down the ridge. This excess melt may facilitate the existence of larger magma bodies where mixing inhibits crystal fractionation of the melt which, in turn, results in lower magnetization intensity (Lee & Searle 2000). The concentration of Fe in titanomagnetite increases for differentiated magma (Sinton *et al.* 1983), thereby explaining the correlation between FeO and TiO_2 concentrations and magnetization intensity.

Regime I, south of 59°10'N, appears unaffected by the latest hotspot pulse. The low melt production that is normal for slow-spreading ridges (Lee & Searle 2000) results in the episodic formation of small magma bodies. The small size of these magma chambers prevents a substantial amount of mixing to occur, allowing a high degree of differentiation of the melt and explains the relatively high average magnetization for the region. The magnetization of regime II, between 59°10'N and 60°50'N, is lower on average than regime I and can be explained by the formation of larger magma chambers where mixing occurs sufficient to impede fractionation, resulting in the emplacement of undifferentiated lavas with low magnetization intensity. Regime II is, therefore, hypothesised to be directly effected by the hotspot pulse with excess melt helping to

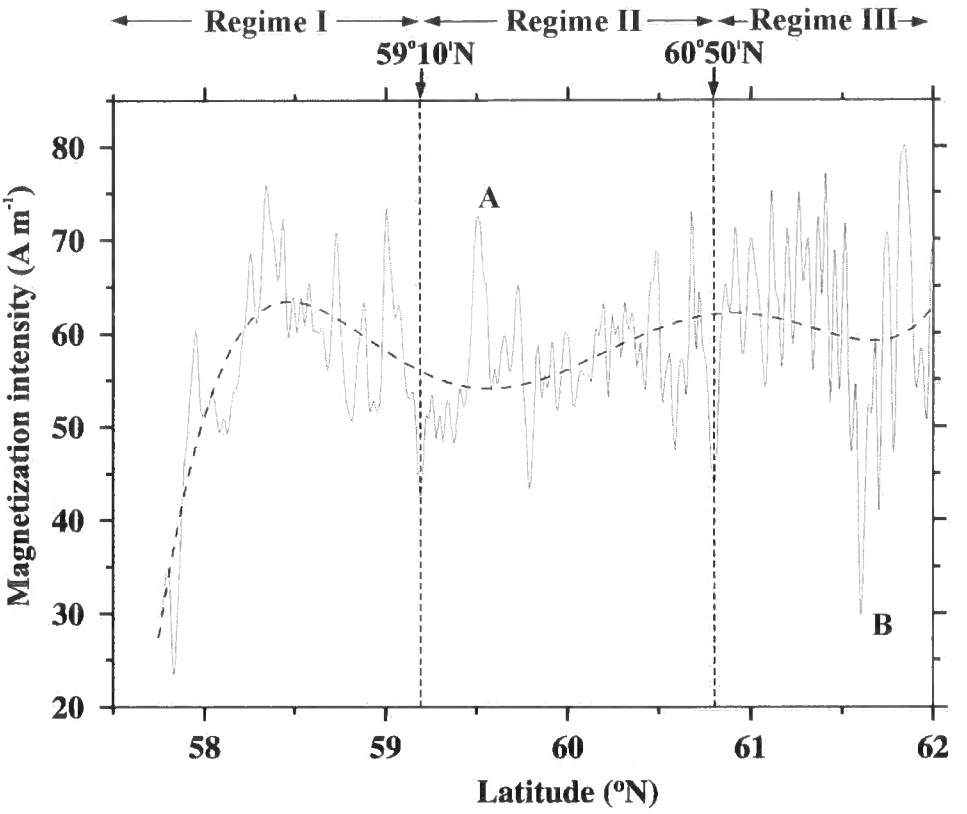

Figure 5.10: Along-axis profile through the magnetization intensity solution (solid line of Fig. 5.9). The intermediate-wavelength variations in magnetization intensity (dashed line) are used to define three different regimes (vertical dashed lines and annotation) hypothesised to relate to the influence of hotspot pulses on the generation of the extrusive layer. Letters A and B denote local magnetization intensity highs and lows at 59°30'N and 61°31'N respectively (see text for details).

create larger magma bodies. The average magnetization of regime III is slightly higher than for regime II and may indicate, and support the hypothesis of, readjustment of the crust after the passage of the hotspot pulse. The local magnetization high at 59°30'N (labelled A in Fig. 5.10) may, in fact, mark the tip of the pulse and can be explained by the existence of a small magma body as is commonly hypothesised for magnetization highs at the tip of propagating rift systems (Hey *et al.* 1986) and overlapping spreading centres (Sempere *et al.* 1984). The ~30 A m^{-1} magnetization intensity low near 61°31'N (labelled B in Fig. 5.10) is associated with a heavily faulted AVR (Lee & Searle 2000), suggesting an age/faulting dependence (see following section).

Similar conclusions have been drawn from the along-axis RMBA analysis of Section 4.4.1, although the exact location of the transition from regime I to regime II is slightly different. Analysis of the along-axis variations in the gradient of the bathymetry and RMBA data suggests that the transition from "normal" oceanic crust to hotspot effected crust occurs near 58°50'N, as opposed to 59°10'N. However, as the intermediate-wavelength variations in RMBA magnitude and magnetization intensity are relatively

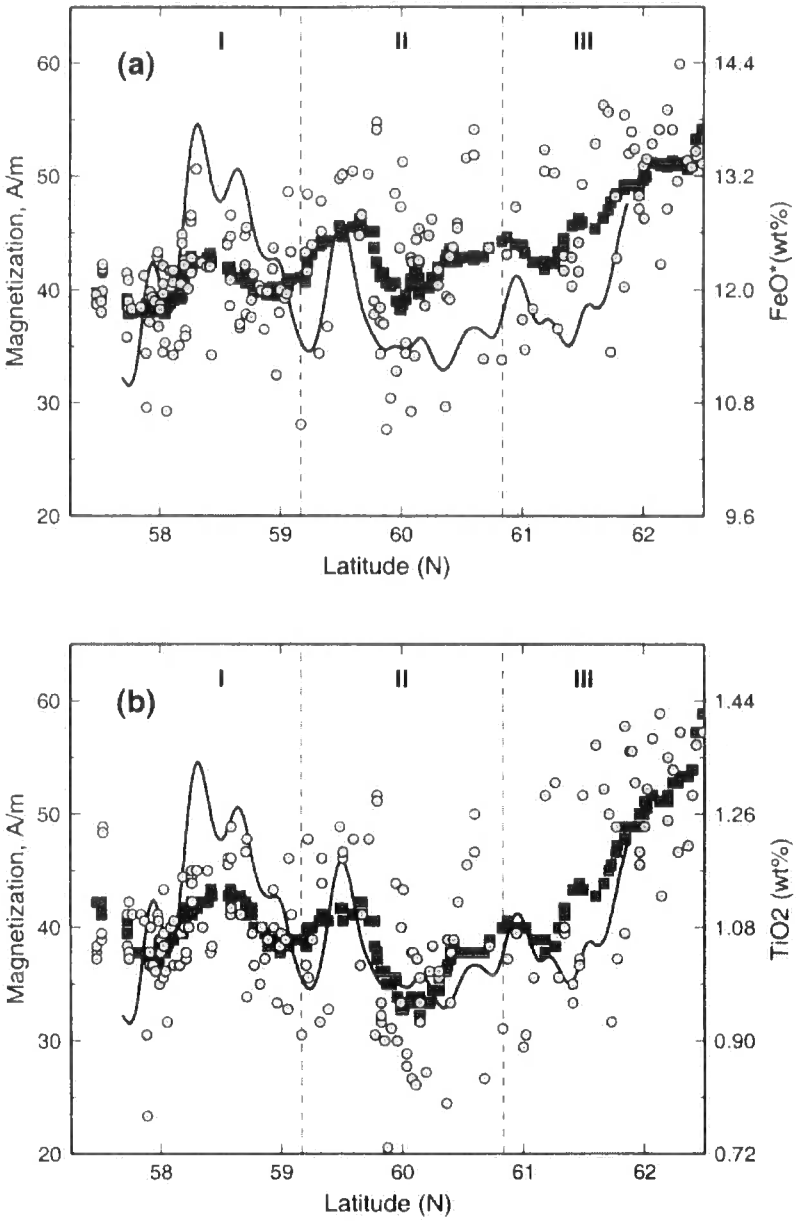

Figure 5.11: Correlation between along-axis magnetization intensity and FeO and TiO_2 concentrations (from Lee & Searle 2000 using unpublished data provided by R. Taylor). (a) Variation in FeO* (total iron as FeO in wt %) content with latitude. (b) Variation in TiO_2 content with latitude. In both cases a correlation appears to exist between the smoothed axial magnetization intensity (solid black line) and the smoothed FeO and TiO_2 content (black squares). Circles show raw concentrations. Vertical dashed lines mark the boundaries between the three regimes inferred by Lee & Searle (2000).

smooth the exact location of the transition point is difficult to define accurately.

Combining the observations near 59°N of a high abundance of seamounts, low number of fault scarps, change in median valley to axial high morphology and 5° bend in ridge axis with the along-axis crustal thickness variations modelled in Section 4.4.1 and the variations in RMBA and magnetization intensity described above, suggests that the transition most probably occurs very near 59°N. In addition, the local magnetization high at 59°30'N coincides with a local RMBA low. The latter observation, suggesting the presence of thicker crust and/or lower densities in the crust and/or mantle, supports the theory that 59°30'N marks the location of the present-day hotspot pulse. The other prominent local magnetization anomaly, a low at 61°31'N, is associated with a heavily faulted AVR and coincides with a local RMBA high. This supports the hypothesis of a relationship between AVR age, RMBA amplitude and magnetization intensity, i.e. as the AVR ages it becomes dismembered by tectonic forces, resulting in thinner crust and an RMBA high. In addition, low-temperature oxidation of titanomagnetite with age decreases the magnetization intensity.

The short-wavelength features of the magnetization intensity solution and their relationship to RMBA amplitude and AVR age are discussed in more detail in the following sections.

5.4.2 Short-wavelength features

Superimposed on the regional characteristics of the along-axis magnetization intensities described above are smaller scale anomalies (~10 km) associated with individual AVRs. The following sections discuss the magnetization intensity distribution for TOBI areas C and B respectively. In both cases, the prominent feature is a CAMH that runs along the ridge axis. It is hypothesised that a significant component of the along-axis variation in CAMH amplitude reflects relative age differences of AVRs.

5.4.2.1 TOBI area C

The AVR centred on 57°45'N, AVR 1, has the lowest, on-axis, average magnetization intensity, ~35 A m^{-1}, for the entire area (Fig. 5.12). A local magnetization intensity high of 65 A m^{-1} is associated with AVR 2, and the intensities then decrease along-axis to ~50 A m^{-1} for AVR 4. The magnetization intensity magnitude then increases gradually again to 65 A m^{-1} for AVR 6. This pattern, of a magnetization intensity high over a short AVR, decreasing to the north to an intensity low associated with a longer AVR, then increasing again in magnitude to the north to a high over a shorter AVR, can be seen, in

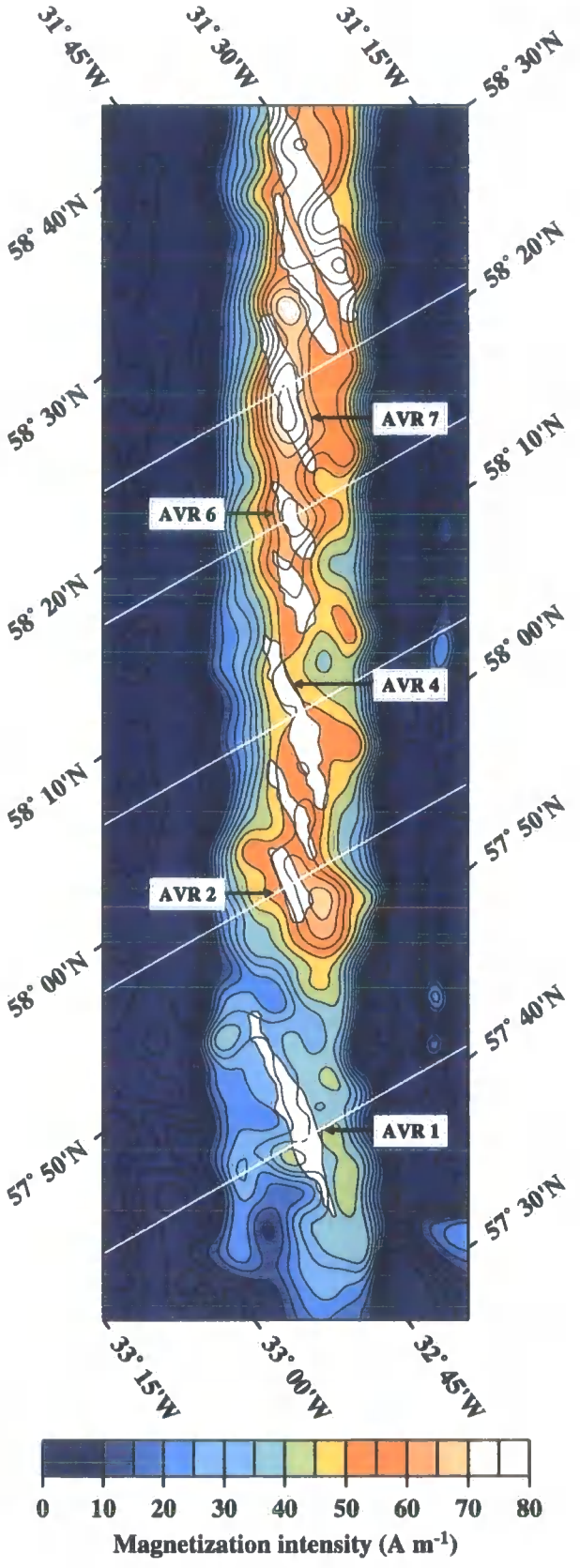

Figure 5.12: Magnetization intensity solution for TOBI area C (cf. Fig. 1.12), showing a number of highs associated with AVRs. AVR 1 is associated with a very low magnetization intensity and appears to be anomalous for this area (see text for details). AVR outlines are superimposed in white and AVRs selected for spreading rate analysis are labelled and profile lines shown in white. Note that the colour scale has been chosen to highlight on-axis features.

part, further to the north as well. Magnetization intensities decrease from 75 A m^{-1} over AVR 7 to ~60 A m^{-1} near AVR 9 located at 58°30'N.

These short-wavelength anomalies are thought to reflect local age variations of the extrusive layer (Lee & Searle 2000). As low-temperature weathering of the basalts converts titanomagnetite to titanomaghemite and results in a decay of magnetization intensities with age, the average magnetization intensity for AVR 1 is unexpected, as evidence for a magma body beneath it has been reported (Sinha *et al.* 1997, Navin *et al.* 1998). One would, therefore, expect fresh lavas to result in a higher average magnetization intensity. Lee & Searle (2000) explain this observation by saying that AVR 1 is in fact an older AVR than first thought and is undergoing recent rejuvenation through late-stage volcanism. A number of small, local magnetization intensity highs associated with small volcanic features visible in the bathymetry lend weight to this interpretation. Other explanations include the possibility that the magma body beneath AVR 1 is sufficiently large for mixing to inhibit fractionation of the melt, resulting in unusually low magnetization intensity basalts. Alternatively, it could be argued that hydrothermal activity has altered the chemical composition of the basalts and reduced the average magnetization intensity.

This age-dependant interpretation of the magnetization intensity variation suggests that, in this area within regime I, longer AVRs are older than shorter AVRs. This conclusion is corroborated by the TOBI interpretation discussed in Section 3.2 and the gravity modelling of Section 4.4.2.1, which shows that the shorter, younger AVRs associated with magnetization intensity highs, have thinner crust and/or more melt in the mid-crust than older AVRs. In addition, the spatial pattern of anomalies, with a gradual increase in magnetization intensity away to the north and south from a long central AVR to shorter AVRs, suggests that a single second order segment is ~70 km long and contains several AVRs. This hypothesis and its implications for the processes of segmentation and accretion of this ridge system are developed further in Chapter 6.

5.4.2.2 TOBI area B

In contrast to the anomalies of TOBI area C, the magnetization intensity for area B is more subdued and less variable (Fig. 5.13). A CAMH is still present and is also discontinuous on a ~10 km scale, although the intensities are generally lower, only reaching a maximum of ~60 A m^{-1}. The pattern of AVR length, however, is similar to that of area C, with the gradual shortening in length of AVRs to the north and south of the longest AVRs. The lack of variability in magnetization intensity is attributed to the

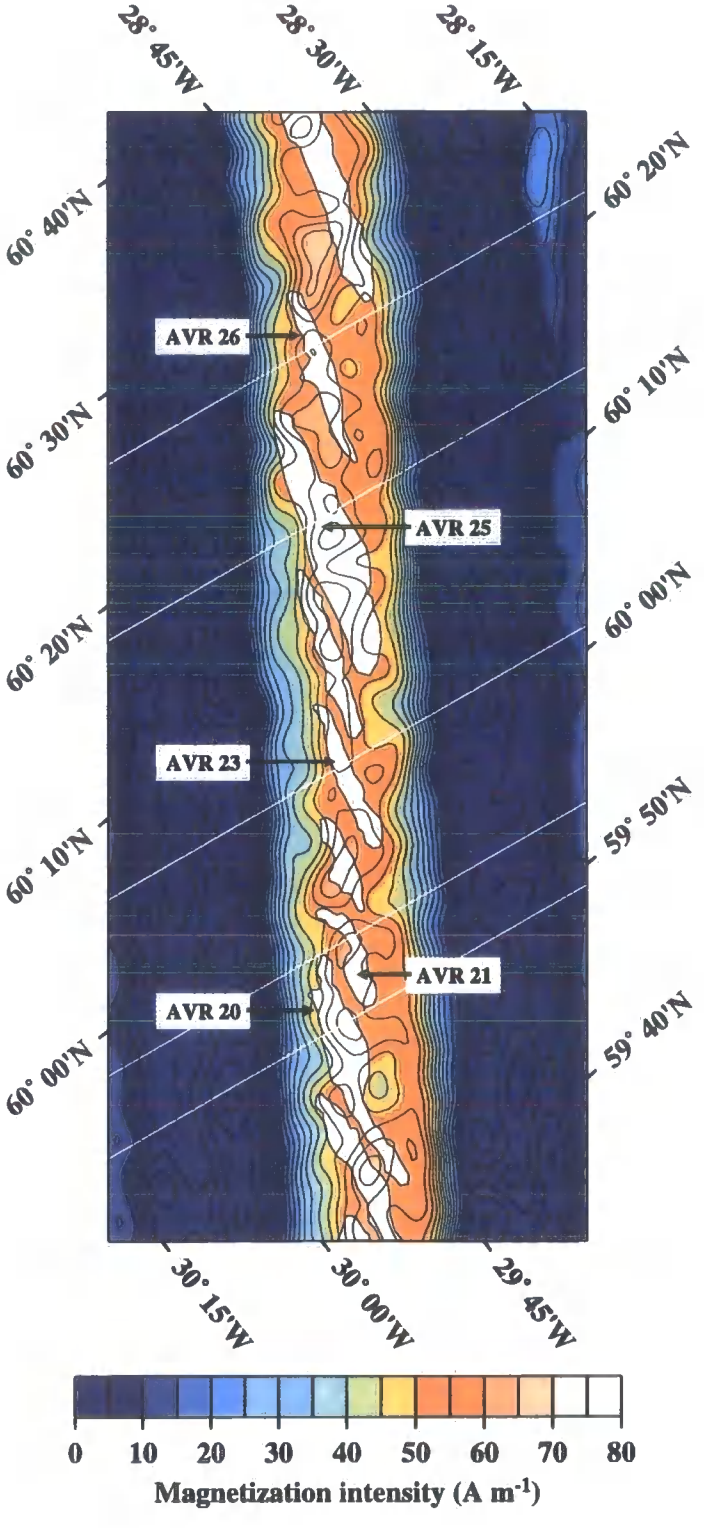

Figure 5.13: Magnetization intensity solution for TOBI area B (cf. Fig. 1.12), showing a number of highs associated with AVRs. The along-axis magnetization intensity shows less variation along-axis than observed for TOBI area C (see text for details). AVR outlines are superimposed in white and AVRs selected for spreading rate analysis are labelled and profile lines shown in white. Note that the colour scale has been chosen to highlight on-axis features.

influence of the Iceland hotspot. Area B lies well within the region of hotspot influence, as demonstrated by the presence of an axial high and the gravity modelling discussed in Section 4.4.1. It is hypothesised that the lack of along-axis variation in magnetization intensity is due to the higher thermal regime for this area that facilitates mixing and the fractionation of melt. The lack of significant variation in RMBA amplitude along-axis for this area (see Section 4.4.2.2) may also indicate that higher temperatures, associated with the presence of the hotspot, facilitate the redistribution of crustal material along-axis (Bell & Buck 1992). Therefore, it appears that although the crustal accretionary process is probably the same for TOBI areas C and B, the magnetic and gravity signature of segmentation in area B is masked, to a certain extent, by the influence of the hotspot.

5.4.2.3 Spreading rate calculations

Along-axis variations in magnetization intensity reveal information about the time of emplacement of basalts on-axis. Across-axis variations in magnetization intensity, when correlated with a reversal time scale, can provide information on spreading rate variations with time that may relate to the stage of the AVR in a tectonomagmatic cycle and to the nature of the dominant tectonic process. Tectonomagmatic cycles have been shown to have an effect on the crustal structure of AVRs (see Chapter 4) and it is, therefore, hypothesised that the intense magmatic activity associated with an AVR in the *young-adolescent* phase of the cycle may affect local spreading rates relative to an *old* AVR that is simply being dismembered by tectonic forces. This hypothesised mechanism is similar in concept the "ridge-push - slab-pull" theory of plate tectonics (e.g. Richardson 1992) but is proposed to operate at an AVR-scale over short periods of time. Using magnetization intensities for this analysis, instead of magnetic anomalies, has the advantage of having topographic effects removed by the inversion. To investigate if a correlation exists between local spreading rate and AVR age, spreading rates were calculated for profiles across AVRs labelled in Fig. 5.12 and Fig. 5.13 using the reversal scale of Cande & Kent (1995). In addition, a possible spreading rate dependence for the RMBA asymmetry discussed in Section 4.4.2.1 will be explored. The slow-spreading rate of the Reykjanes Ridge means that the Jaramillo epoch (1.03 Ma) is quite narrow and thus difficult to distinguish. Half-spreading rate calculations were, therefore, made for each AVR from zero-age to the more prominent reversal at 1.42 Ma between Jaramillo and chron 2 (1.86 Ma) and to chron 2A at 2.81 Ma. The results are shown in Figs. 5.14-5.19 and the main findings are summarised in Table 5.2.

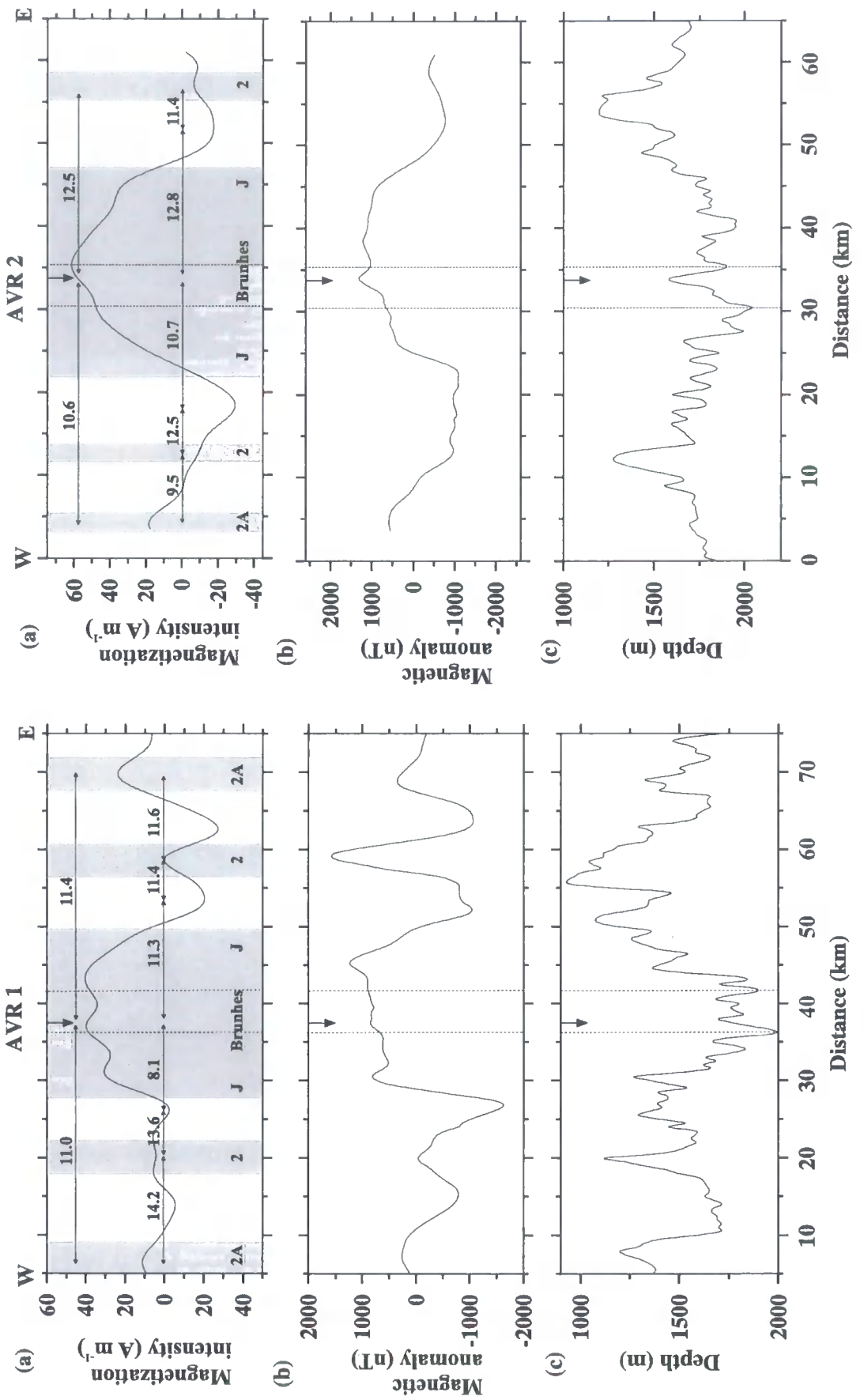

Figure 5.14: Local half-spreading rate calculations for AVRs 1 and 2. (a) Across-axis profiles taken from the magnetization intensity solution shown in Fig. 5.12. Half-spreading rates were calculated using the reversal time scale of Cande & Kent (1995) between the central high (Brunhes) to the reversal between Jaramillo (J) and chron 2 and to chron 2A. In addition, half-rates were calculated between the reversal mentioned above and chron 2 as well as between chrons 2 and 2A. All half-rates are quoted in mm yr^{-1}. (b) Across-axis magnetic anomaly profiles still showing topographic effects that were removed in the magnetization intensity by *inv3d*. (c) Across-axis bathymetry profiles. In all parts the vertical arrow and the vertical dashed lines mark the most shallow part and the horizontal extent of the AVR respectively.

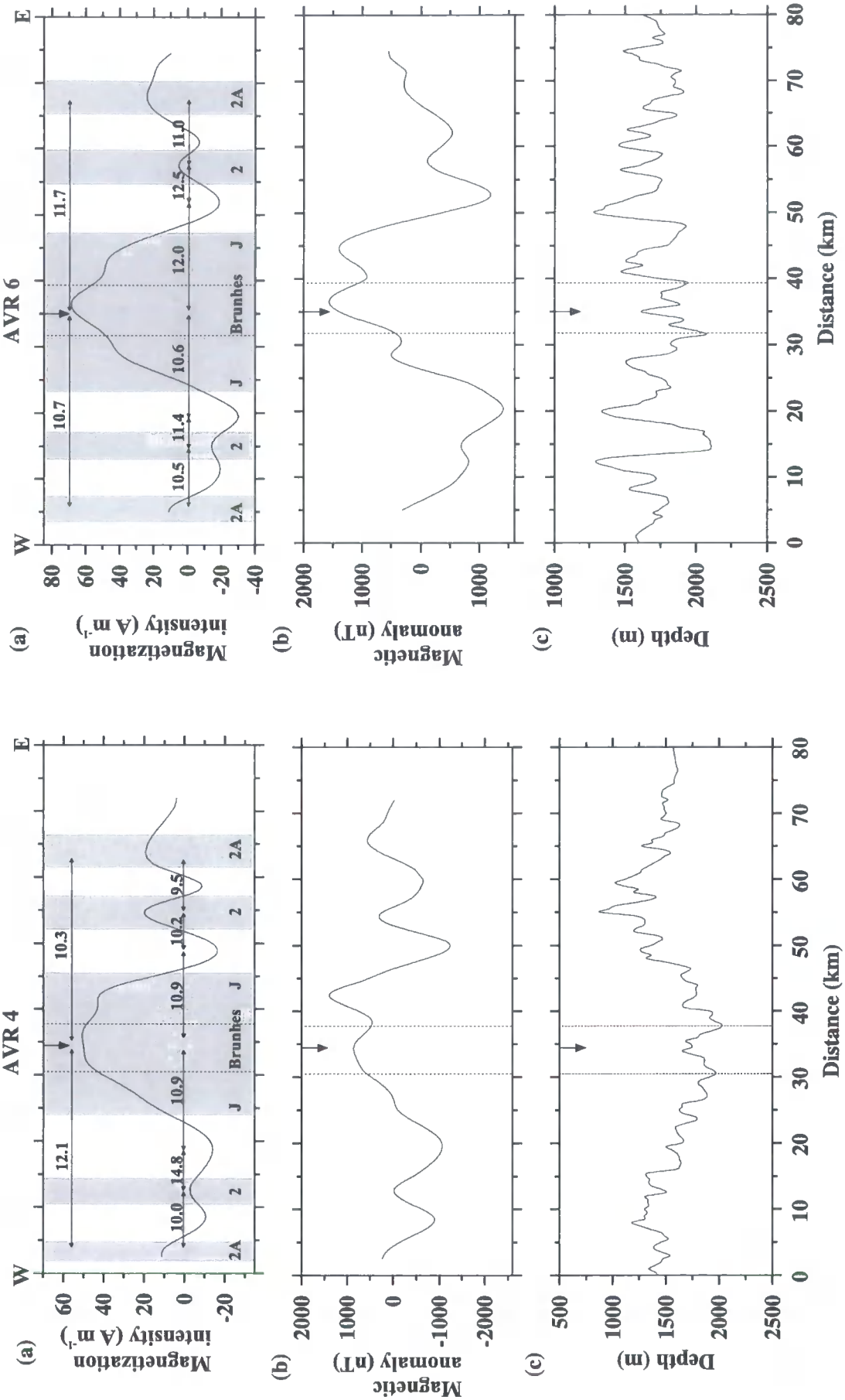

Figure 5.15: Local half-spreading rate calculations for AVRs 4 and 6. (a) Across-axis profiles taken from the magnetization intensity solution shown in Fig. 5.12. Half-spreading rates were calculated using the reversal time scale of Cande & Kent (1995) between the central high (Brunhes) to the reversal between Jaramillo (J) and chron 2 and to chron 2A. In addition, half-rates were calculated between the reversal mentioned above and chron 2 as well as between chrons 2 and 2A. All half-rates are quoted in mm yr^{-1}. (b) Across-axis magnetic anomaly profiles still showing topographic effects that were removed in the magnetization intensity by *inv3d*. (c) Across-axis bathymetry profiles. In all parts the vertical arrow and the vertical dashed lines mark the most shallow part and the horizontal extent of the AVR respectively.

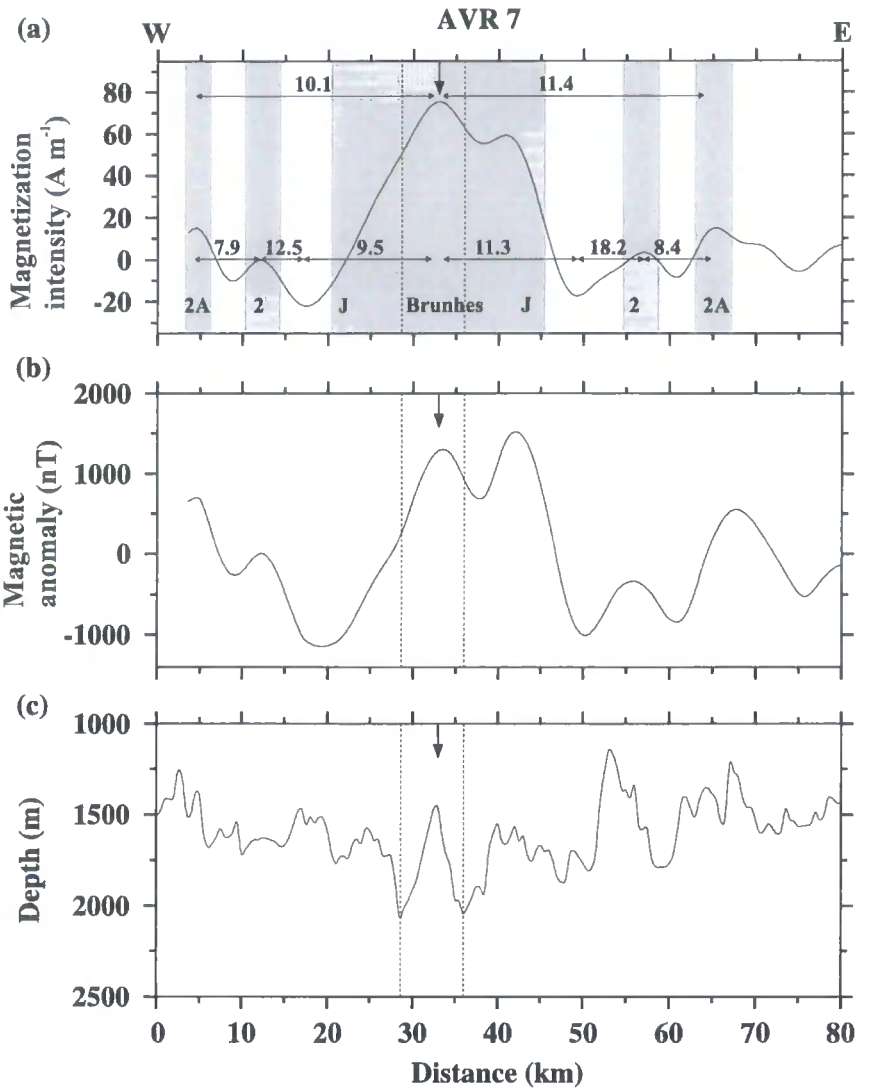

Figure 5.16: Local half-spreading rate calculations for AVR 7. (a) Across-axis profile taken from the magnetization intensity solution shown in Fig. 5.12. Half-spreading rates were calculated using the reversal time scale of Cande & Kent (1995) between the central high (Brunhes) to the reversal between Jaramillo (J) and chron 2 and to chron 2A. In addition, half-rates were calculated between the reversal mentioned above and chron 2 as well as between chrons 2 and 2A. Chrons used for spreading rate calculations are shaded in grey and annotated. All half-rates are quoted in mm yr^{-1}. (b) Across-axis magnetic anomaly profile still showing topographic effects that were removed in the magnetization intensity by *inv3d*. (c) Across-axis bathymetry profiles In all parts the vertical arrow and the vertical dashed lines mark the most shallow part and the horizontal extent of the AVR respectively.

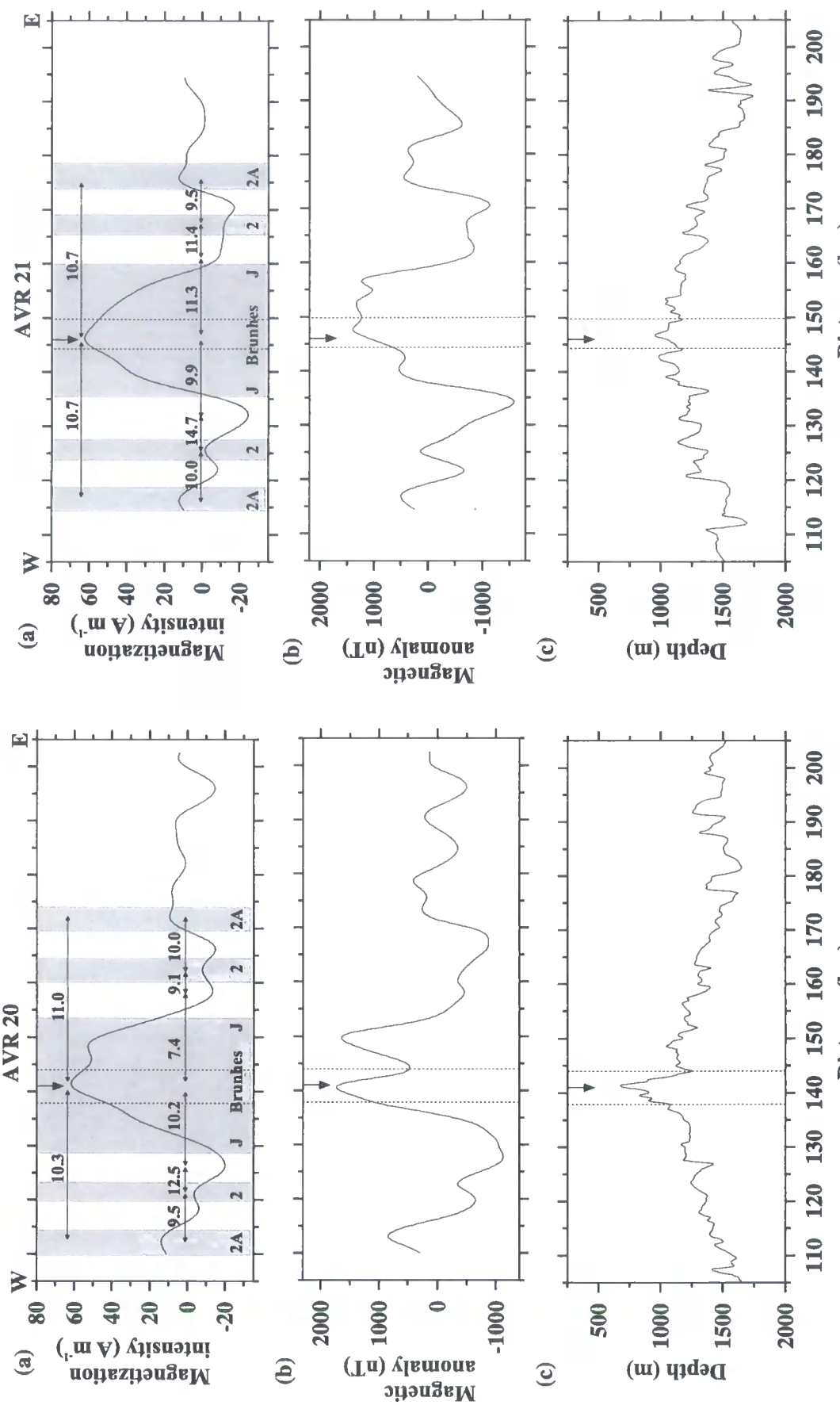

Figure 5.17: Local half-spreading rate calculations for AVRs 20 and 21. (a) Across-axis profiles taken from the magnetization intensity solution shown in Fig. 5.13. Half-spreading rates were calculated using the reversal time scale of Cande & Kent (1995) between the central high (Brunhes) to the reversal between Jaramillo (J) and chron 2 and to chron 2A. In addition, half-rates were calculated between the reversal mentioned above and chron 2 as well as between chrons 2 and 2A. All half-rates are quoted in mm yr^{-1}. Chrons used for spreading rate calculations are shaded in grey and annotated. (b) Across-axis magnetic anomaly profiles still showing topographic effects that were removed in the magnetization intensity by *inv3d*. (c) Across-axis bathymetry profiles. In all parts the vertical arrow and the vertical dashed lines mark the most shallow part and the horizontal extent of the AVR respectively.

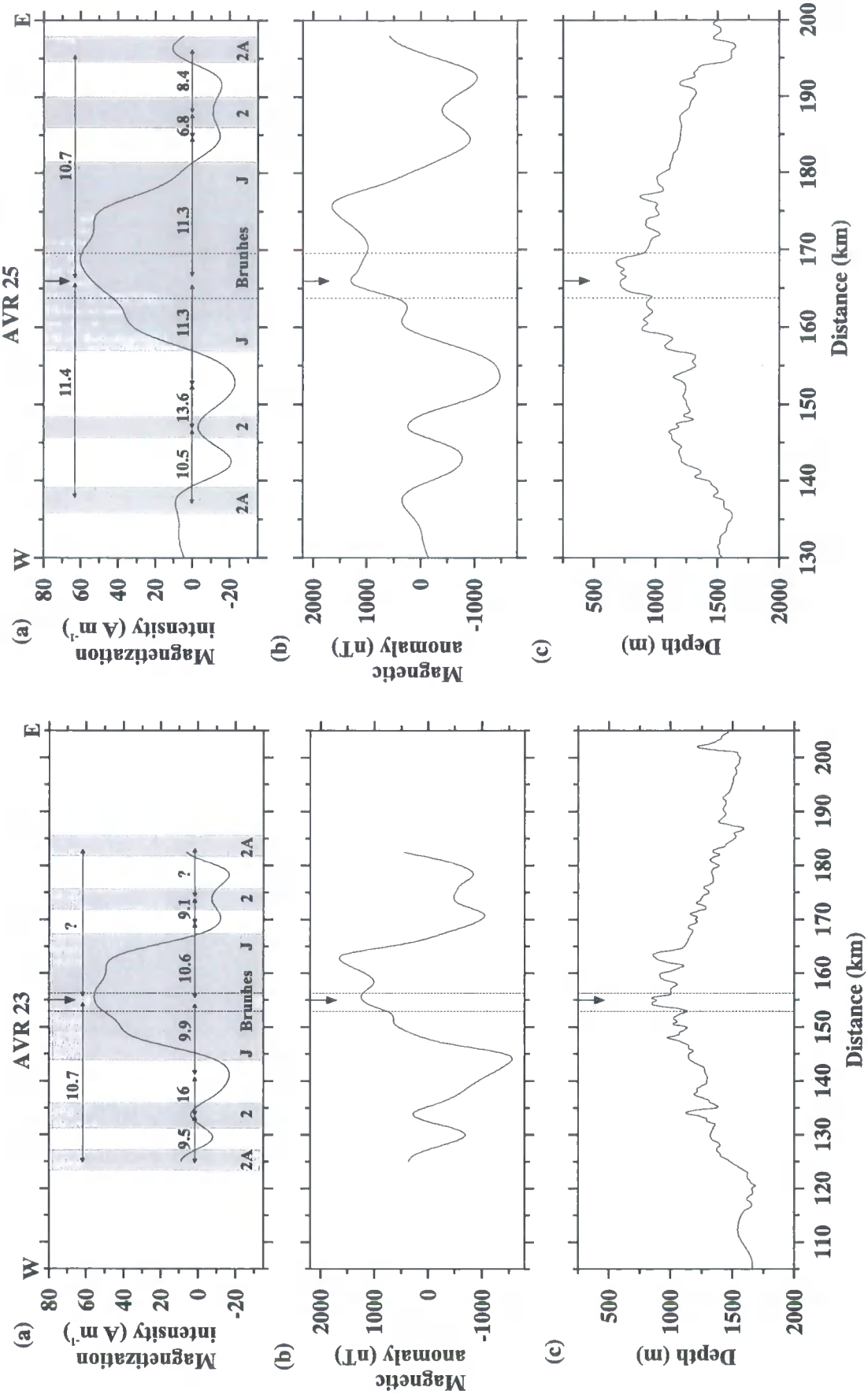

Figure 5.18: Local half-spreading rate calculations for AVRs 23 and 25. (a) Across-axis profiles taken from the magnetization intensity solution shown in Fig. 5.13. Half-spreading rates were calculated using the reversal time scale of Cande & Kent (1995) between the central high (Brunhes) to the reversal between Jaramillo (*J*) and chron 2 and to chron 2A. In addition, half-rates were calculated between the reversal mentioned above and chron 2 as well as between chrons 2 and 2A. All half-rates are quoted in mm yr^{-1}. Chrons used for spreading rate calculations are shaded in grey and annotated. (b) Across-axis magnetic anomaly profiles still showing topographic effects that were removed in the magnetization intensity by *inv3d*. (c) Across-axis bathymetry profiles. In all parts the vertical arrow and the vertical dashed lines mark the most shallow part and the horizontal extent of the AVR respectively.

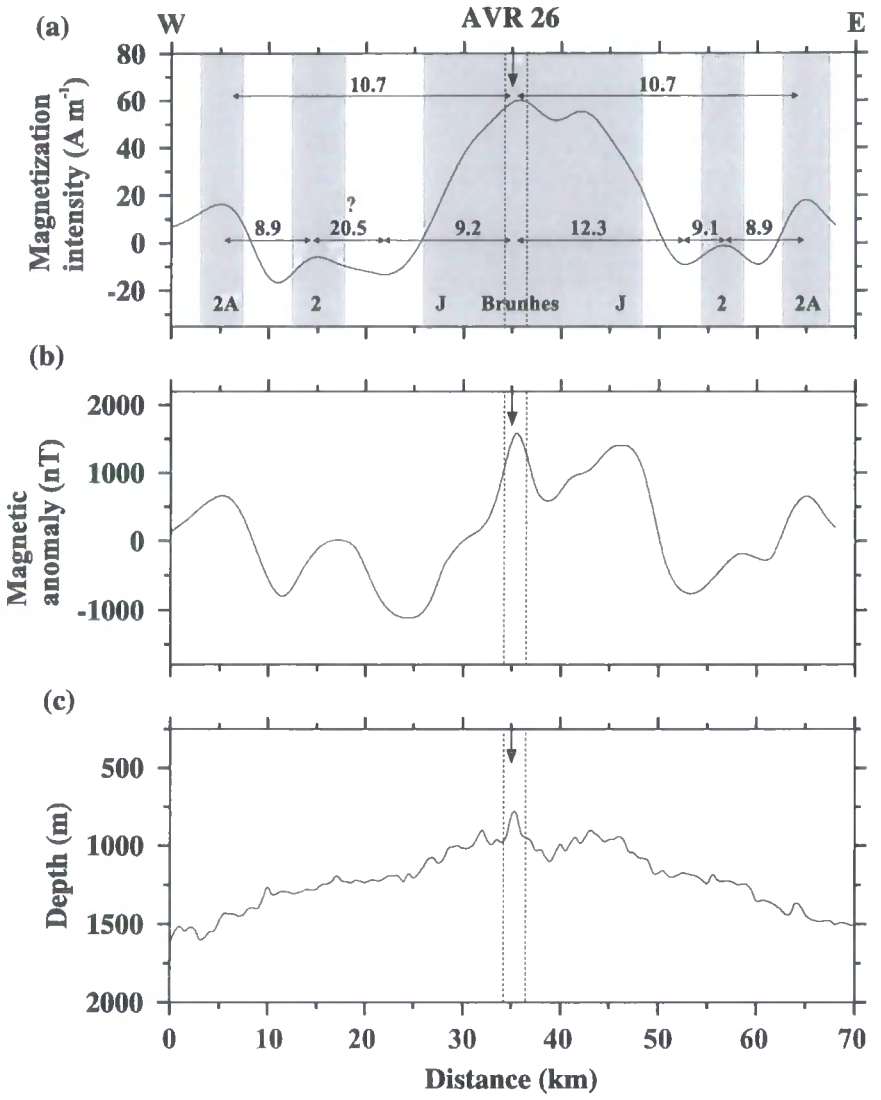

Figure 5.19: Local half-spreading rate calculations for AVR 26. (a) Across-axis profile taken from the magnetization intensity solution shown in Fig. 5.13. Half-spreading rates were calculated using the reversal time scale of Cande & Kent (1995) between the central high (Brunhes) to the reversal between Jaramillo (J) and chron 2 and to chron 2A. In addition, half-rates were calculated between the reversal mentioned above and chron 2 as well as between chrons 2 and 2A. Chrons used for spreading rate calculations are shaded in grey and annotated. All half-rates are quoted in mm yr^{-1}. (b) Across-axis magnetic anomaly profile still showing topographic effects that were removed in the magnetization intensity by *inv3d*. (c) Across-axis bathymetry profiles In all parts the vertical arrow and the vertical dashed lines mark the most shallow part and the horizontal extent of the AVR respectively.

Age	AVR	Length (km)	Mag. Intensity (A m^{-1})	Spreading rate < 1.42 Ma (± 0.7 mm yr^{-1})			Spreading rate < 2.81 Ma (± 1.0 mm yr^{-1})		
				West	East	Average	West	East	Average
Y-A	6	11	65	10.6	12.3	11.5	10.5	11.7	11.2
A	7	20	75	9.5	11.3	10.4	10.1	11.4	10.6
A-M	2	10	65	10.7	12.8	11.8	10.6	12.5	11.6
M	4	35	50	10.9	10.9	10.9	12.1	10.3	11.2
M	1	30	35	8.1	11.3	9.7	11.0	11.4	11.2

Age	AVR	Length (km)	Mag. Intensity (A m^{-1})	Spreading rate < 1.42 Ma (± 0.7 mm yr^{-1})			Spreading rate < 2.81 Ma (± 1.0 mm yr^{-1})		
				West	East	Average	West	East	Average
A-M	23	12	55	9.9	10.6	10.3	10.7	?	10.7
A-M	21	13	60	9.9	11.3	10.6	10.7	10.7	10.7
A-M	26	20	60	9.2	12.3	10.8	10.7	10.7	10.7
M	20	28	55	10.2	7.4	8.8	10.3	11.0	10.7
M	25	32	55	11.3	11.3	11.3	11.4	10.7	11.0

Table 5.2: Correlation between AVR age, length, magnetization intensity and local half-spreading rate across individual AVRs (see text for details). Longer, older AVRs are generally associated with a magnetization intensity low, whereas shorter, younger AVRs have magnetization highs, confirming the TOBI data age determinations of Sections 3.2 and 3.3. Note that before 1.42 Ma, younger AVRs have higher average spreading rates than older AVRs. However, when averaged over the last 2.81 Ma, spreading rates converge, within errors, to the average spreading rate for the ridge of 10 mm yr^{-1}. Significant asymmetric spreading rates are shaded in grey. AVR ages, obtained from the relative age interpretations of the TOBI data (see Sections 3.2 and 3.3) are abbreviated as follows: *Y-A* for *young-adolescent*, *A* for *adolescent*, *A-M* for *adolescent-mature*, *M* for *mature*.

In general, longer, older AVRs have slower spreading rates (by up to 20%) for the first 1.42 Ma than AVRs that are shorter and younger. However, spreading rates for all AVRs, averaged over 2.81 Ma, show little variation within the ± 1.0 mm yr^{-1} error bound. Under the tectonomagmatic model of crustal accretion, a possible explanation for this observation is that younger AVRs currently represent the focus of accretion, whereas older AVRs are simply being dismembered by far-field tectonic forces at the "normal" spreading rate. Older AVRs are therefore, simply rafted off-axis at the far-field spreading rate, whereas crustal genesis at younger AVRs influences the local spreading rate before returning to a "background" level. Similar non-rigid plate tectonic

behaviour on short-time scales has been reported at 37°N on the MAR (Macdonald 1977) and at ~9°N on the EPR (Carbotte & Macdonald 1992), suggesting that independent cycles of magmatic and tectonic activity occur within adjacent segments at all spreading rates.

Asymmetry is also observed for spreading rates calculated for the last 1.42 Ma, however this asymmetry disappears, within the error constraints, for spreading rates averaged over 2.81 Ma. In TOBI area C spreading appears to be faster to the east of AVRs 1, 2, 6 and 7 (see Table 5.2). Whereas, in area B asymmetric spreading is only resolvable for AVRs 20 and 26, with faster spreading to the west and east respectively. Asymmetry in the RMBA associated with the AVRs mentioned above (see Section 4.4.2), with RMBA lows present in the direction opposite to the fastest spreading direction, lends further support for the suggestion of asymmetry in accretion. This pattern suggests, assuming off-axis RMBA lows indicate the presence of thicker crust (though crustal and/or mantle density variations may be present), that differential tectonic extension "stretches" material accreting to the plate boundary more in one direction than the other. This hypothesis would be supported by evidence for asymmetric faulting, with more faulting and/or greater throw faulting to the east within TOBI area C. In fact, though "flip-flop" style faulting is observed in this area no overall asymmetry is observed and large throws would be required as the fault scarps are steep (Owens 1991). Alternatively, asymmetry in the crustal accretion process itself may occur, with dykes intruding preferentially to one side of the plate boundary (Macdonald 1977). If a recent intrusion at the ridge axis has sufficient time to cool, the crust at this location will be strong and the next intrusion may preferentially occur somewhere off-axis, along active fault-generated planes of weakness, resulting in asymmetric spreading. The episodic nature of crustal accretion at the Reykjanes Ridge (Navin *et al.* 1998; Sinha *et al.* 1997) may, therefore, sustain asymmetric spreading and the thermal control on asymmetric spreading might also explain the lower degree of asymmetry in TOBI area B, which is within the hotspot influence.

5.5 Summary

In this chapter magnetic field data for the survey area were inverted, including bathymetric effects, to obtain a magnetization intensity solution. Variations in magnetization intensity may reflect the effect of processes such as the differentiation of melt or low-temperature oxidation of titanomagnetite. Alternatively, changes may

reflect source layer thickness variations. However, Lee & Searle (2000) showed that only up to 50% of the magnetization intensity solution near 63°N could be explained solely by layer 2A thickness variations indicating that the other processes mentioned above are significant factors. Consequently, long-wavelength along-axis magnetization intensity variations were interpreted in terms of degree of fractionation of magma, with the thermal effect of the Iceland hotspot postulated to influence melt generation along-axis. Shorter-wavelength anomalies, superimposed on the regional features mentioned above, were interpreted in terms of relative age variation of the extrusive layer. Variations in magnetization intensity associated with individual AVRs, appear to agree with the relative age determinations based on TOBI data interpretations. Spreading rate calculations were made for selected AVRs showing that generally, younger AVRs appear to spread faster than older AVRs for the last 1.42 Ma. In addition, asymmetric spreading is observed for most AVRs in TOBI area C and two AVRs in TOBI area B. This asymmetric spreading can explain the observed asymmetry in the RMBA, with differential tectonic extension or asymmetry in the crustal accretion process resulting in thinning of the crust on one side of the plate boundary.

In the following chapter a model of the interplay between crustal accretion, segmentation, and tectonomagmatic cycles, within the framework of a hotspot influenced ridge, will be presented by integrating the results of this chapter with the TOBI data interpretations and gravity models discussed in Chapters 3 and 4 respectively.

Chapter 6

Discussion and suggestions for further work

6.1 Introduction

The study presented in this dissertation entailed the processing, modelling and interpretation of TOBI, gravity and magnetic data acquired during four cruises to the Reykjanes Ridge. TOBI data were interpreted in Chapter 3 to age AVRs in a relative sense and to test the hypothesis that cyclic accretion influences the seafloor morphology. Gravity data were modelled and interpreted in Chapter 4 to investigate the effects of ridge-hotspot interaction on the ridge as a whole, and of cyclic accretion on the crustal structure of individual AVRs. Inversion and analysis of magnetic data in Chapter 5 provided additional constraints on the influence of the hotspot and on the temporal variability of accretion processes.

All of the datasets can be subdivided into wavelengths of observation. Analysis of each data type has shown that long-wavelength features, discussed in Section 6.2, are generally related to the steady-state influence and proximity of the Iceland hotspot. Intermediate-wavelength features, discussed in Section 6.3, appear to be related to the pulsing of the hotspot, whereas shorter-wavelength features (Section 6.4) coincide with individual AVRs and their stage in their tectonomagmatic cycle.

Based on the results of interpretation of all the different datasets, a model for the cyclicity of crustal accretion, linking segmentation and tectonomagmatic cycles to the underlying pattern of mantle upwelling, is presented in Section 6.5. This model is compared to accretionary processes operating at different spreading rates in Section 6.6, and its implication for the temporal variability of accretion at all spreading rates is also discussed. Several suggestions for further study are made in Section 6.7. These suggestions would provide a means to test the uncertainties or ambiguities in the current model. Experiments at other ridges are also suggested to test the relevance of the model to mid-ocean ridges in general. The main conclusions drawn from the modelling and interpretation of all datasets are summarised in Section 6.8.

6.2 Long-wavelength observations

In this section all of the long-wavelength observations are integrated to present a model of the hotspot influence on the ridge (Fig. 6.1). The most obvious effect of the proximity of the hotspot on the Reykjanes Ridge is the shoaling of the ridge axis towards Iceland.

The axial depth varies from ~2500 m at 57°N to ~500 m at 63°N, with a break in slope in the bathymetry near 59°N, postulated to reflect the most southerly extent of hotspot influence on the ridge. This shoaling of the ridge is the isostatic response of the crust to an increase in crustal thickness, caused by excess melting, and an increase in upper mantle temperature towards Iceland (White *et al.* 1995; Searle *et al.* 1998). The change in axial morphology, from an axial valley to an axial high near 59°N, can also be explained by a thermally controlled isostatic compensation mechanism. The axial region becomes free to respond to the underlying buoyancy when it can no longer support significant stress induced by necking of the lithosphere under tectonic extension (Tapponnier & Franchetau 1978; Chen & Morgan 1990; Searle *et al.* 1998). The small increase in crustal and upper mantle temperature towards Iceland is sufficient to decrease the elastic thickness of the lithosphere along the ridge, resulting in a ridge axis that can support the tensional stress south of ~59°N but that cannot further north (Searle *et al.* 1998).

Gravity modelling of an along-axis profile (see Section 4.4.1), constrained by seismic refraction experiments, shows that the long-wavelength gravity anomaly towards Iceland can be attributed to an increase in crustal thickness from ~7.5 km at 57°30'N to ~10.5 km near 62°N, with "normal" crustal thickness of 7.1 ± 0.8 km (White *et al.* 1992) achieved near 59°N. In addition, a gradual decrease in upper mantle density from 3.30 g cm^{-3} at 57°30'N to 3.24 g cm^{-3} near 62°N is required to satisfy the independent seismic constraints and provide a good fit to the gravity anomaly.

The seismic refraction data compilation (see Section 1.5.4) suggests that the crustal thickening modelled from the gravity data is mainly accommodated in layers 2B and 3, with no apparent systematic variation in layer 2A thickness with latitude. This decoupling of layer 2A thickness from the thickness of layers 2B and 3 is attributed to the episodic nature of accretion at the ridge, with the rapid cooling of melt in the crust (see Section 1.4) resulting in crustal accretion occurring mainly through intrusive magmatism. This decoupling effect is also reflected in the absence of a systematic along-axis variation in seamount abundance and height, although intermediate-wavelength fluctuations (see Section 6.3) are observed. Thus, the excess melt generated

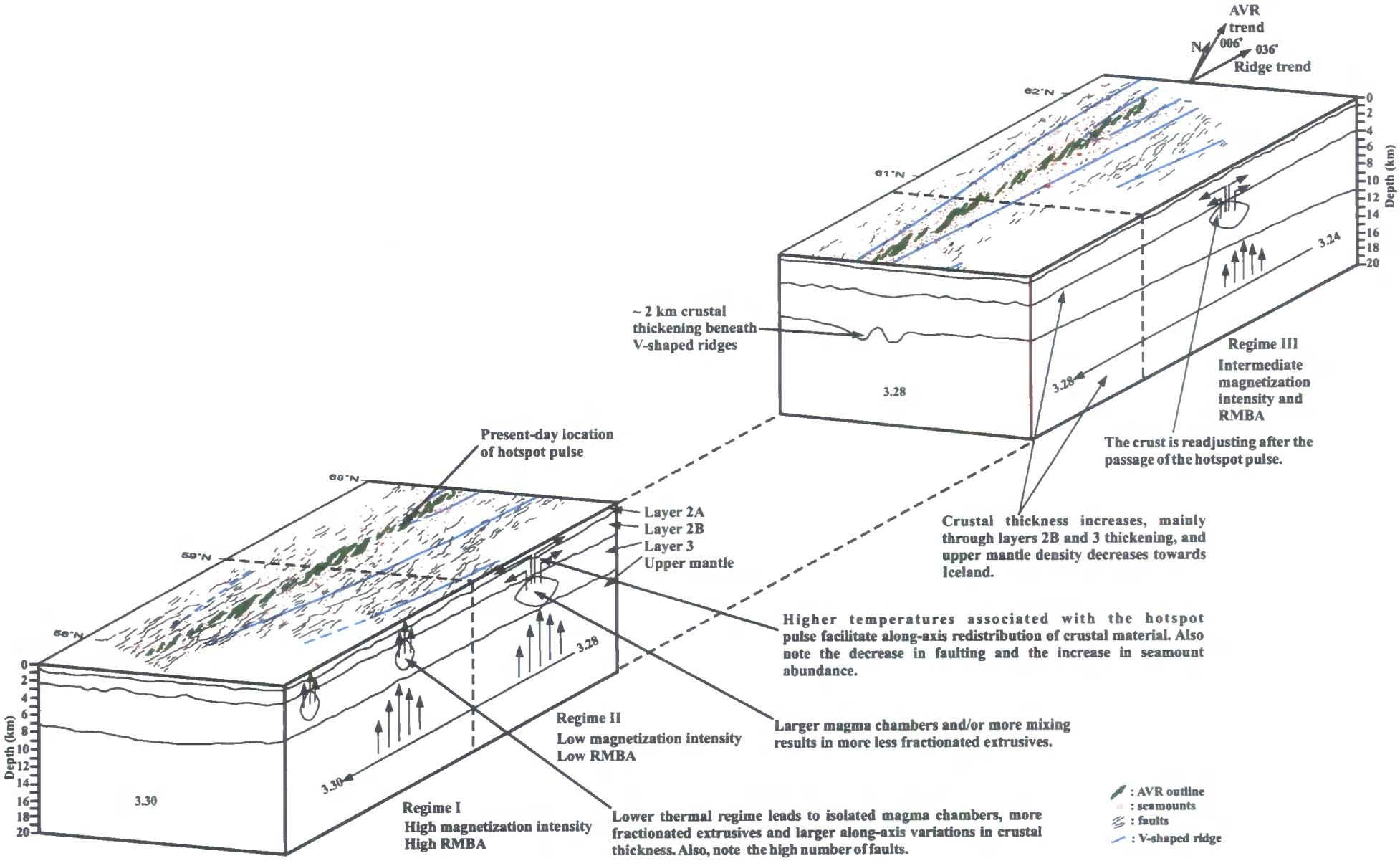

Figure 6.1: Long- and intermediate-wavelength effects of the proximity of the Iceland hotspot on the Reykjanes Ridge. Long-wavelength effects are related to the steady-state influence of the hotspot, whereas intermediate-wavelength features are related to the pulsing of the hotspot. Note that although the present day limit of the hotspot influence appears to be located near 59°N it has not always necessarily been the case. See text for more details.

by the proximity of the hotspot does not result in a greater abundance of seamounts or an increase in seamount height towards Iceland, as might be expected for a higher magma supply, magma pressure and/or volatile content.

The presence of smaller and less abundant seamounts at the MAR compared to the hotspot influenced Reykjanes Ridge (Magde & Smith 1995) confirms that the volume of available magma must be a controlling variable, but that for some reason it does not influence extrusive layer thickness along-axis towards Iceland. Further evidence for the lack of systematic layer 2A thickening towards Iceland comes from the absence of an increase in magnetization intensity with latitude, which would be expected even allowing for other possible sources of variation in the intensity (Lee & Searle 2000).

Seismic observations of uniform layer 2 thickness, regardless of total crustal thickness, have also been made for the hotspot influenced, 46-64 mm yr^{-1} intermediate-spreading Galapagos spreading centre (Sallares *et al.* 2003; Walther 2003). This suggests that, if spreading rates do indeed control the extent of layer 2 thickening at hotspot influenced ridges, excess melt associated with the presence of hotspots does not systematically effect layer 2 thickness at spreading rates of less than ~65 mm yr^{-1}.

The intersection of the V-shaped ridges with the ridge axis, along with an increase in seamount abundance and geochemical anomalies, indicates that the most southerly limit of hotspot influence occurs near 59°N. The along-axis gravity modelling presented as part of this study (see Section 4.4.1) indicates that "normal" oceanic crustal thickness is reached near 59°N providing further evidence for the extent of hotspot influence.

In the following section the intermediate-wavelength features, superimposed on the long-wavelength features discussed above, are considered in relation to hotspot pulses.

6.3 Intermediate-wavelength observations

Intermediate-wavelength observations from a variety of sources are combined in this section to investigate the effect of hotspot pulses on the Reykjanes Ridge (Fig. 6.1). V-shaped ridges, evident in bathymetry and gravity anomaly data, suggest that hotspot pulses interact with the crustal accretion process at the ridge axis (Vogt 1974).

Combined gravity and seismic data modelling (White *et al.* 1995) show that these ridges form as an isostatic response to local crustal thickening of ~2 km associated with the excess melt generated by hotspot pulses. Recent models (Ito 2001; Jones *et al.* 2002) show that instead of excess melt flowing along the ridge axis from the hotspot, thermal pulses of ~30°C spread radially away from the hotspot leading to an increase in melting

as the pulses intersect the melt source region beneath the ridge axis. Analysis of the geometry of the V-shaped ridges indicates that these pulses occur every 5 - 10 My and travel at 20 cm yr^{-1} along the ridge axis.

Hotspot pulses also appear to effect the abundance of seamounts observed along-axis, with the highest abundance of seamounts observed near 59°N, where the V-shaped ridges intersect the ridge axis. A smaller number of faults with smaller throws are also observed in this region, suggesting that the excess thermal budget associated with each pulse causes the brittle-ductile transition in the lithosphere to shallow, weakening the crust and resulting in it only being able to support smaller throw faults (Searle *et al.* 1998).

Analyses of along-axis variations in RMBA amplitude and magnetization intensity (Sections 4.4.1 and 5.4.1 respectively) show intermediate-wavelength fluctuations that may be explained by hotspot pulses. Large variations in RMBA amplitude and magnetization intensity south of ~59°N, indicate relatively large variations in crustal thickness and the presence of small magma chambers which give rise to basalts with a range of fractionation histories. These are characteristic of "normal" oceanic crust and suggest that this region is free of hotspot influence. Variations in both RMBA and magnetization intensity are more subdued between ~59°N and 60°50'N, suggesting that this region is influenced by the hotspot pulse. An increase in crustal temperature in this region may facilitate the along-axis redistribution of crustal material and/or the existence of larger magma chambers which undergo more mixing, thereby inhibiting fractionation and resulting in lower magnetization intensity extrusives. North of 60°50'N magnetization intensity variations increase slightly suggesting that the crust is readjusting after the passage of the pulse. A coincident local RMBA amplitude low and magnetization high at 59°30'N suggest that this location marks the tip of the currently propagating hotspot pulse. This RMBA low corroborates Lee & Searle (2000)'s hypothesis that a magma chamber might be present at 59°30'N, similar to ones observed at propagating rift tips.

In conclusion, the combination of multidisciplinary datasets has provided numerous constraints on the effect and extent of hotspot pulses. Analyses of V-shaped ridges, seamount and fault characteristics, and along-axis variations in RMBA and magnetization intensity suggests that the most recent hotspot pulse has reached ~59°N, with the region south of this point free of hotspot influence and the region north of 60°50'N readjusting to the passage of the pulse. In addition the RMBA and

magnetization intensity data suggest that two very different thermal regimes along the ridge axis and lead to the presence of small, independent, ephemeral magma chambers south of ~59°N, whereas between 59°N and 60°50'N magma chambers are larger and/or undergo more mixing.

Having analysed and interpreted the long- and intermediate-wavelength features, the shorter-wavelength observations are related to the phase of individual AVRs within a tectonomagmatic cycle in the next section.

6.4 Short-wavelength observations

Oblique spreading at the Reykjanes Ridge results in different trends for tectonic features and features related to the crustal accretion process itself. AVRs are oriented perpendicular to the spreading direction and faults, related to tectonic extension, generally follow the ridge trend. This location on the mid-ocean ridge system is, therefore, ideal for studying the interplay of tectonic and magmatic processes in the creation of the oceanic crust. The TOBI data interpretation undertaken as part of this study confirms the hypothesis that crustal accretion takes place through a series of tectonomagmatic cycles and establishes a correlation between AVR length and relative age - older AVRs are generally longer than younger ones. Comparison of AVRs of similar ages shows that, for example, *adolescent* AVRs incorporate features typical of more *mature* AVRs. This suggests that Parson *et al.* (1993)'s categorisation of AVRs into *young*, *adolescent*, *mature* and *old* relative ages actually reflects individual "snapshots" of a continuous AVR lifecycle.

Calculation of the RMBA for TOBI areas B and C (Figs 4.14 and 4.23) reveals a number of small "bull's eye" lows associated with individual AVRs. Gravity modelling of profiles along AVRs shows that the gravity anomaly lows can be explained by thicker crust and/or the presence of lower densities (interpreted as representing the presence of partial melt) in the mid-crust beneath AVR centres. This suggests, according to the tectonomagmatic theory of crustal accretion, that *young* AVRs are undergoing magmatic construction with RMBA lows indicating the presence of partial melt in the crust, whereas more *mature* AVRs have finished growing resulting in thicker crust at their centre resulting in a corresponding RMBA low. This theory of AVR growth also explains the correlation between relative AVR age and length; with older AVRs having simply received more injections of melt and have, therefore, been able to extend further (Figs 6.2 and 6.3).

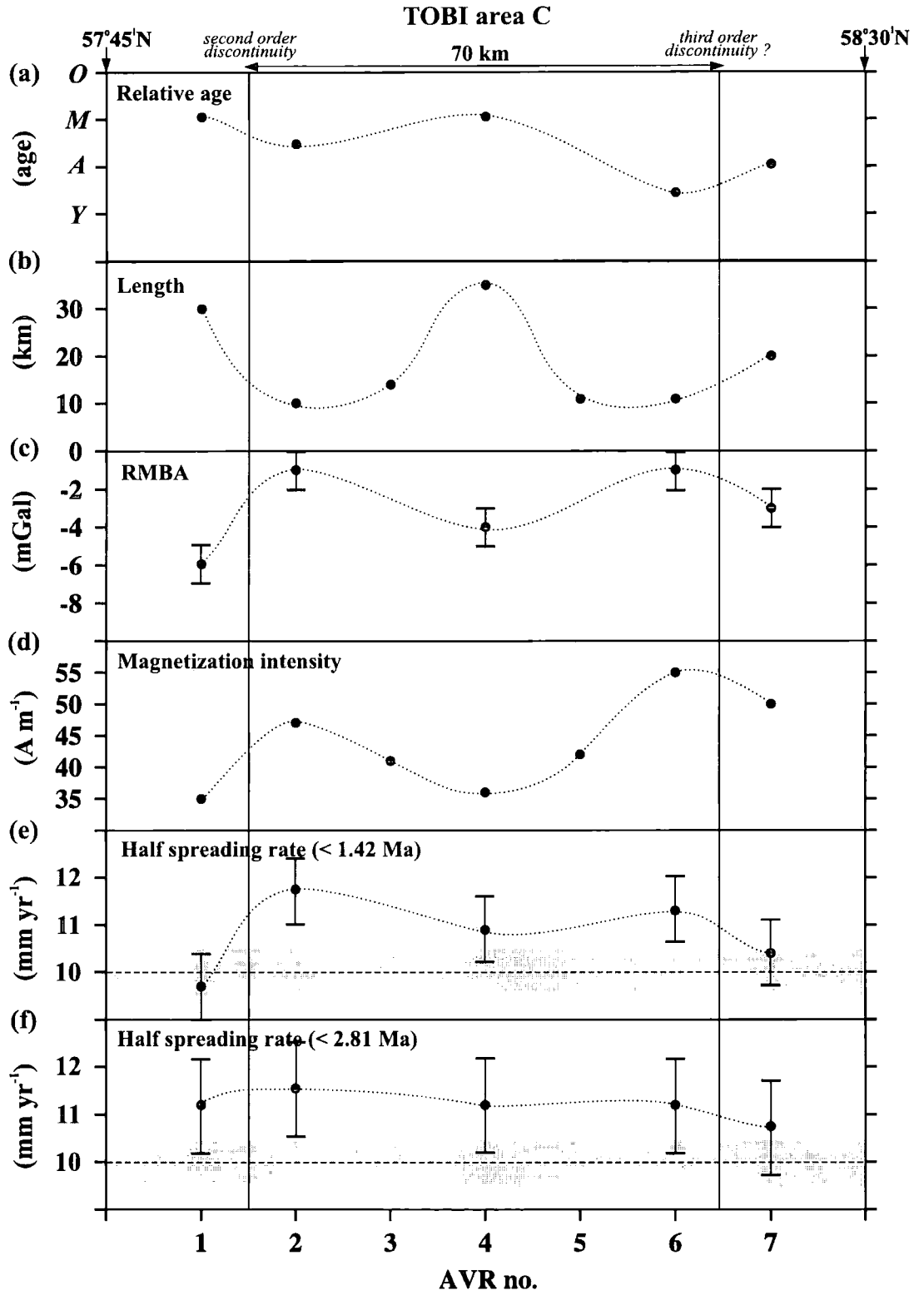

Figure 6.2: Along-axis correlation between various parameters for TOBI area C. (a) Relative ages (*Y*, *A*, *M*, *O* are *young*, *adolescent*, *mature* and *old* respectively) of the AVRs interpreted in Section 3.2. (b) Length of each AVR (Keeton *et al.* 1997). (c) RMBA low associated with each individual AVR. The error in the RMBA is ±1 mGal. (d) Magnetization intensity anomaly associated with each AVR. (e) Half spreading rate calculated across each AVR averaged over the last 1.42 Ma. Errors in spreading rate are ±0.7 mm yr^{-1}. (f) Half rate calculated for each AVR averaged over the last 2.81 Ma. Errors in spreading rate are ±1.0 mm yr^{-1}. Note that in both (e) and (f) the dashed line and the grey shading show the average half rate and its error (±0.5 mm yr^{-1}) respectively for the Reykjanes Ridge as a whole (DeMets 1990). Vertical lines across all parts show the second order discontinuity near 57°55'N and a hypothesized third order discontinuity near 58°20'N. Note the correlation between relative age, AVR length, RMBA, magnetization intensity and spreading rate for the last 1.42 Ma. Dotted lines in all parts show a hypothesized ~70 km wavelength in the observations between the discontinuities. See text for details.

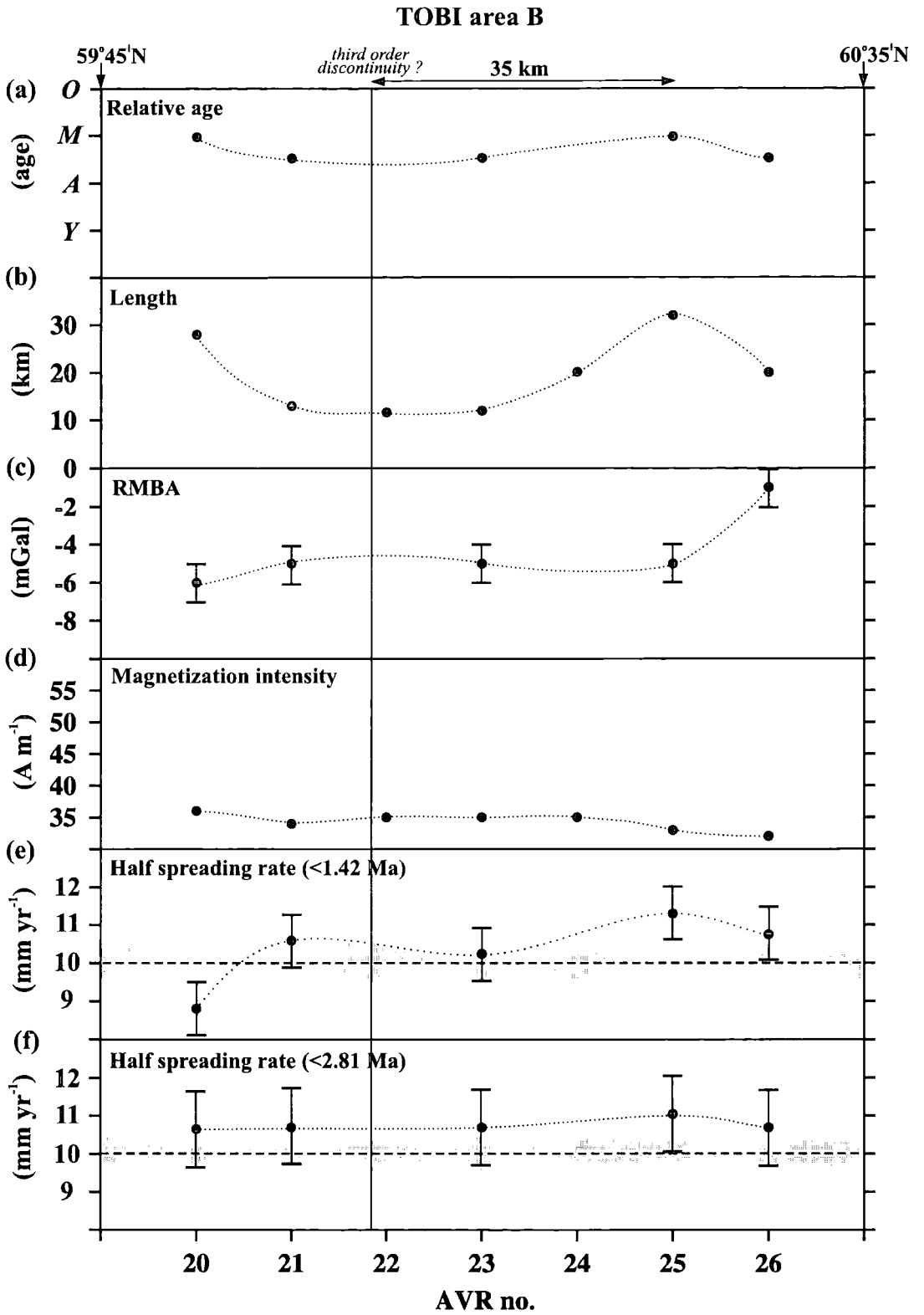

Figure 6.3: Along-axis correlation between various parameters for TOBI area B. (a) Relative ages (*Y*, *A*, *M*, *O* are *young*, *adolescent*, *mature* and *old* respectively) of the AVRs interpreted in Section 3.2. (b) Length of each AVR (Keeton *et al.* 1997). (c) RMBA low associated with each individual AVR. The error in the RMBA is ±1 mGal. (d) Magnetization intensity anomaly associated with each AVR. (e) Half spreading rate calculated across each AVR averaged over the last 1.42 Ma. Errors in spreading rate are ±0.7 mm yr^{-1}. (f) Half rate calculated for each AVR averaged over the last 2.81 Ma. Errors in spreading rate are ±0.5 mm yr^{-1}. Note that in both (e) and (f) the dashed line and the grey shading show the average half rate and its error (±1.0 mm yr^{-1}) respectively for the Reykjanes Ridge as a whole (DeMets 1990). Vertical lines across all parts show hypothesized third order discontinuity near 60°N. Note a correlation between relative age and AVR length can still be made but correlations to the RMBA, magnetization intensity and spreading rate for the last 1.42 Ma are more tenuous. Dotted lines in all parts show a hypothesised ~35 km half-wavelength in the observations between the hypothesised discontinuity and segment centre. See text for details.

However, as AVRs grow obliquely to the ridge axis the extent of AVR propagation off-axis will also be controlled by the strength of the ageing lithosphere (Searle *et al.* 1998).

In addition, the RMBA pattern over TOBI area C, with a broad, ridge-parallel low superimposed by small AVR-trending anomalies, suggests that AVRs tap into the mantle upwelling that follows the ridge trend (Peirce & Navin 2002). Further evidence for this hypothesised ridge-parallel mantle upwelling comes from melt lens-like reflection events imaged between AVRs in seismic reflection data (Topping 2002; Gill 2003 pers. comm.). Thus, it is concluded that mantle upwelling generally follows the ridge trend but migrates to fill spreading-normal fissures that are orientated oblique to the ridge direction at the Reykjanes Ridge forming individual AVRs.

The along-axis RMBA low for TOBI area B is broader than for area C, suggesting that the hotspot influence in this area results in a wider region of mantle upwelling or that the crust is thicker over a greater distance across-axis. The lack of variation in RMBA from AVR to AVR in this area suggests that along-axis redistribution of crustal material subdues the gravity signature of tectonomagmatic cycles.

Short-wavelength magnetization intensity variation, used as a proxy for relative age variations (see Section 5.4.2), corroborates the TOBI data interpretation with more *mature* AVRs associated with a smaller magnetization intensity than *young* AVRs. However, in TOBI area B, the magnetization intensity shows little variation with individual AVRs suggesting that the hotspot influence facilitates mixing in magma chambers and thereby subdues relative AVR age differences. Calculations of spreading rate variations for individual AVRs suggest that younger AVRs locally "speed up" spreading by up to 20% compared to older AVRs. It is, therefore, hypothesised that magmatic processes associated with younger AVRs, locally effect spreading rates for short periods of time as spreading rates averaged over longer periods do not show a correlation with age and are close to the "far-field" spreading rate for the ridge as a whole.

Asymmetric spreading is also observed over a number of AVRs, but especially in TOBI area C, suggesting that the higher thermal regime associated with TOBI area B inhibits, or significantly subdues, it. The asymmetry in spreading is mirrored in the short-wavelength RMBA suggesting that thinner crust is present in the direction of fastest spreading, either through differential tectonic extension or asymmetric magma injection into the crust.

All of the previously discussed short-wavelength observations are combined to present a model for the segmentation and cyclicity of crustal accretion at the Reykjanes Ridge in the following section.

6.5 Model of segmentation and cyclicity of crustal accretion

The Reykjanes Ridge is unique among mid-ocean ridges in that it is not obviously segmented. In fact, the only evidence to date for major segmentation along the whole length of the ridge is for a second order discontinuity near 57°50'N. In this section a model is proposed, developed for TOBI area C but that may apply for the entire ridge, to explain this subdued segmentation and relate it to possible patterns of mantle upwelling. In addition, it is concluded that there is an inherent relationship between the segmented mantle upwelling and tectonomagmatic cycles.

The short-wavelength RMBA modelling for TOBI area C (see previous section and Section 4.4.2) has revealed a number of gravity anomaly lows associated with individual AVRs. In addition, a spatial pattern in the anomaly is observed with a pronounced low beneath AVR 4, near 58°05'N, that decreases in amplitude in both directions along-axis towards AVRs 2 and 6 (Fig. 6.4). A coincident decrease in AVR length and relative age and an increase in magnetization intensity and local spreading rate are also observed. This pattern also appears to repeat itself north of AVR 6, with a gradual increase in the length and magnetization intensity and a decrease in the RMBA of AVRs culminating near AVR 9. AVR 1, which is relatively long and has a pronounced RMBA and magnetization intensity low, is separated from the AVRs further to the north by a second order discontinuity near 57°50'N. This discontinuity is characterised by a large offset basin, an RMBA high and magnetization intensity low that persist off-axis for ~2 Ma (Searle *et al.* 1994a). Appelgate & Shor (1994) report a large offset between AVR 1 and the AVR to the south of it that may indicate the presence of another second order discontinuity. Asymmetries in the spreading rate calculated for the last 1.42 Ma are observed over AVRs 1, 2 and 6 and mirror the asymmetry in the RMBA low patterns observed over those AVRs (see previous section and Section 5.4.2.3).

First to second order segmentation of slow-spreading ridges is usually interpreted as reflecting a segmented pattern of mantle upwelling, with the axial depth highs, gravity "bull's eye" and magnetization lows over segment centres indicating that upwelling is focussed at the segment centre. Correlations between segment lengths and MBA amplitude have also been made, with long segments associated with more pronounced

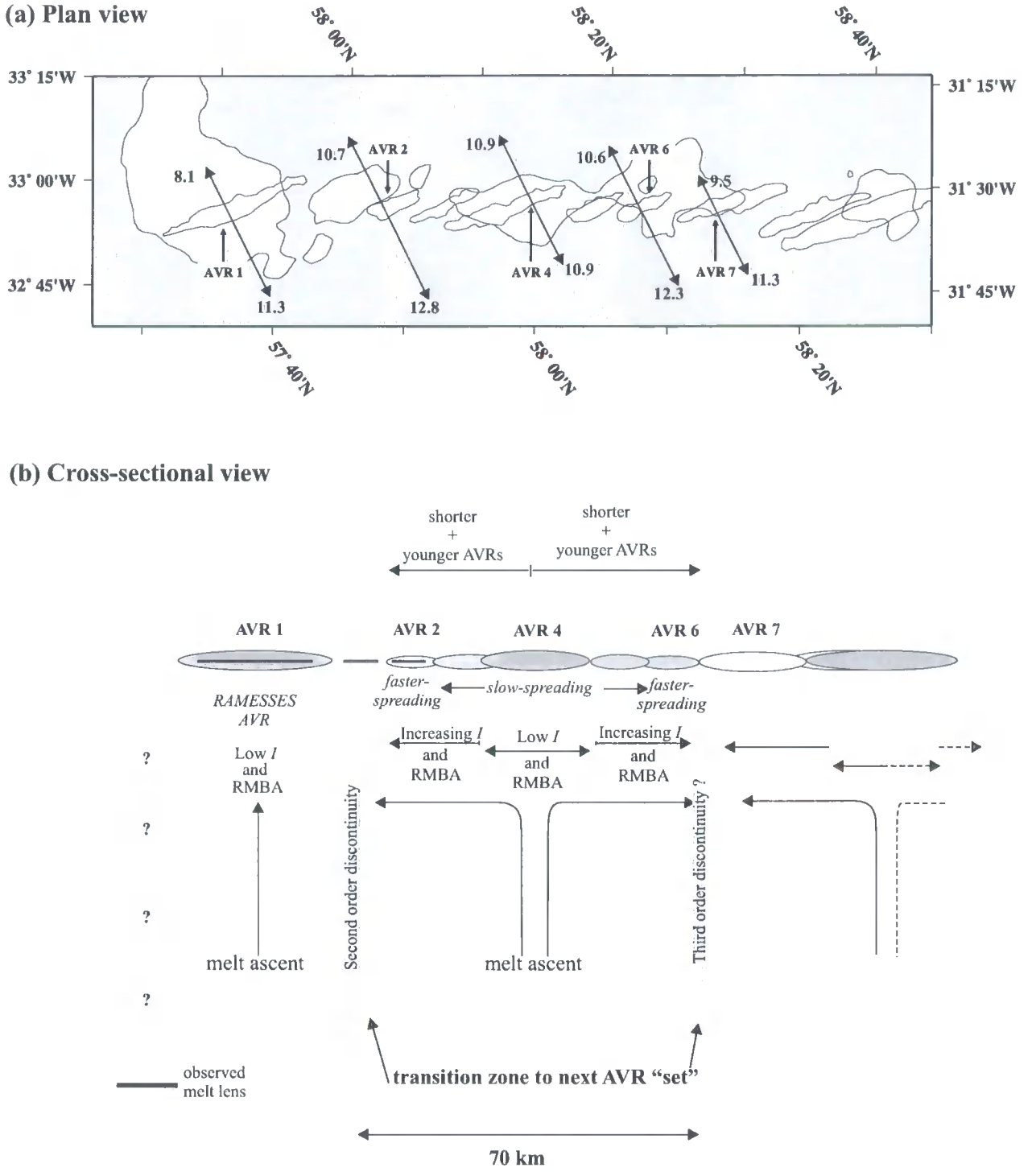

Figure 6.4: Model of segmentation and cyclicity of crustal accretion for TOBI area C. (a) Plan view of TOBI area C with AVR (white) and RMBA low (light grey) outlines superimposed. Local spreading rates for the last 1.42 Ma are annotated by arrows (all rates are half-rates and are in mm yr^{-1}). Note the correlation between asymmetric spreading and the asymmetric RMBA pattern. (b) Hypothesised pattern of mantle upwelling, with a ~70 km wavelength, which explains the observed variations in AVR length, AVR age, RMBA magnitude, magnetization intensity (*I*) and total spreading rate. A segment "cell" is hypothesised to contain ~5 AVRs. See text for details. After Peirce & Gardiner (2003).

MBA lows, indicating a direct relationship between the degree of focussing of upwelling and the length of a segment.

It is suggested, based on the evidence presented for TOBI area C (see Fig. 6.4), that segmented upwelling occurs underneath the Reykjanes Ridge with a wavelength of ~70 km. However, unlike most ridges where each ridge segment contains the equivalent of only one AVR, a segment here contains ~5 AVRs. This observation suggests that 3-D upwelling at the ridge axis follows the ridge trend, in the shape of micro-plumes triggered by Rayleigh-Taylor instabilities (Whitehead *et al.* 1984; Schouten *et al.* 1985) of the shallow (~60 km) mantle. Additional evidence for the nature of melt delivery to the crust is provided by CSEM and MT data at the 57°45'N AVR (MacGregor *et al.* 1998; Heinson *et al.* 2000) which indicate that no melt is present down to ~50 km in the upper mantle. However, the data do require the presence of partial melt between ~50-100 km depth suggesting that melt flux from the mantle to the crust is episodic. Heinson *et al.* (2000) explains the episodic nature of crustal accretion by suggesting that melt gradually accumulates in the mantle though porous flow before coalescing into diapiric upwellings when a critical level of gravitational instability is reached. The presence of melt in the mid-crust representing ~20000 years worth of crustal accretion (MacGregor 1998), in conjunction with the absence of a significant conduit extending to the region of partial melt at a depth of ~50 km in the mantle, suggests that the transport of melt to the crust must operate on a short timescale.

The following evolutionary model for crustal accretion at the Reykjanes Ridge is based on the data interpreted and modelled in this study and the observations discussed above and incorporate the results and conclusions of other studies of this section of the global ridge system. Far-field tectonic stresses result in spreading-orthogonal brittle deformation of the crust in the neovolcanic zone. As an injection of melt reaches the crust, AVRs are constructed over the fractures, initially through fissure volcanism (the *young* stage). As melt is accumulated in the mid-crust, point-source volcanism dominates, with the creation of conical and eventually flat-topped volcanoes (*adolescent* and *mature* stages respectively). As the magmatic part of the cycle wanes, tectonic forces dismember the AVRs (*mature* through to *old* stages). The first AVR forms over the centre of the upwelling in the minimum stress direction, normal to the spreading-direction. As the AVR reaches its mature stage, the crust is locally warm enough for brittle failure to propagate north and south of this AVR, resulting in the pattern of progressively younger and shorter AVRs away from the centre of the micro-plume.

Therefore, the discontinuous melt supply along-axis probably limits the length of a segment.

The inferred ~70 km wavelength of segmentation is longer than the 40 km wavelength predicted by the upper mantle Rayleigh-Taylor instability model (Fig. 1.8) of Schouten *et al.* (1985) for a ridge spreading at a total rate of 20 mm yr^{-1} (Whitehead *et al.* 1984; Schouten *et al.* 1985). In fact, the model predicts wavelengths of ~70 km for a spreading rate of 115 mm yr^{-1}. It therefore appears that the Reykjanes Ridge exhibits a wavelength of upwelling closer to fast-spreading ridges. Such a result, however, is not unexpected as the proximity of the Iceland hotspot results in numerous other features of the ridge (see Section 1.5) being more akin to fast-spreading than slow-spreading ridges. It is therefore not unreasonable to expect the presence of the hotspot to lead to an elevated thermal regime of the ridge and a longer wavelength of segmentation. In this section, this discrepancy in the wavelength of segmentation for the 20 mm yr^{-1} spreading rate of the Reykjanes Ridge is explored.

In the model of Schouten *et al.* (1985) the Rayleigh-Taylor wavelength of upwelling, λ, is proportional to spreading rate, v_e, the amount of partial melt in the upwelling layer, c, and the viscosities μ_1 and μ_2 corresponding to the region of partial melting and the surrounding asthenosphere respectively (see equation 6.1).

$$\lambda \alpha v_e^{\frac{1}{3}} \left(\frac{1}{c}\right)^{\frac{2}{3}} \left(\frac{\mu_2}{\mu_1}\right)^{\frac{2}{9}} \qquad (6.1)$$

Keeping the spreading rate and amount of partial melt constant, requires a decrease in viscosity of the partial melt layer from 10^{17} Pa s to 8.6 x 10^{15} Pa s to explain the 70 km wavelength of segmentation. Another end member to the family of possible solutions can be obtained by keeping the spreading rate and the viscosity fixed. An increase in the amount of partial melt in the upper mantle from 3% to 7% (consistent with the gravity modelling of Section 4.4.2.17) is then required to obtain a wavelength of ~70 km. It is probable that an increase in the thermal regime of the ridge will both increase the amount of partial melt present and lead to a relative decrease in upper mantle viscosity of the region of partial melt. Three orders of magnitude variations for upper mantle viscosity have been quoted for fast-spreading ridges (Crane 1985) and numerical experiments (Rabinowicz & Briais 2002) indicate that up to 32% of partial melt may be present in the upper mantle suggesting that the increase in upper mantle

partial melt content and the decrease in viscosity suggested for the Reykjanes Ridge are reasonable.

It is therefore hypothesised that the presence of the Iceland hotspot results in an increase in the amount of partial melt of 3% to 7% and a decrease in mantle viscosity of less than an order of magnitude, thereby accounting for the discrepancy between the observed intermediate-wavelength segmentation at the Reykjanes Ridge and the model of Schouten *et al.* (1985).

It is therefore possible that the spatial variations of AVR age, length, RMBA amplitude and magnetization intensity are indeed related to the pattern of mantle upwelling. Variations in local spreading rate, with younger AVRs displaying a faster total rate than older AVRs, suggest that either the rate of tectonic extension increases at the loci of recent magmatic activity to accommodate newly accreted material or that the magmatic process itself locally influences spreading rate.

The high thermal regime for this ridge inhibits the formation of first and second order discontinuities which would free individual segments to reorient normal to the spreading direction (Searle *et al.* 1994a). It is then perhaps not surprising that the only clear evidence for a second order segment occurs far from the hotspot influence near 57°50'N. The increased proximity of TOBI area B to the hotspot may also explain why the gravity and magnetic signal of segmentation is subdued in this area, but it is unlikely to affect the wavelength of mantle upwelling (Searle *et al.* 1998). It is, therefore, suggested that the pattern of mantle upwelling persists along the whole length of the ridge, from 57°50'N northwards, but that the higher thermal regime associated with the proximity of the hotspot subdues evidence for this segmentation.

In the following section the model of crustal accretion developed for the Reykjanes Ridge and discussed above is compared to other ridges to ascertain its applicability to all ridges, regardless of spreading rate.

6.6 Comparison of accretionary processes at all spreading rates

Early gravity and seismic studies of mid-ocean ridges have suggested that there is a fundamental difference between accretionary processes at slow- and fast-spreading ridges (Kuo & Forsyth 1988; Lin *et al.* 1990; Detrick *et al.* 1995; Magde *et al.* 1995). At slow-spreading rates mantle upwelling at the ridge axis is thought to be 3-D, with buoyant diapiric upwellings leading to the formation of small, isolated and ephemeral magma chambers. These, in turn, result in the large variations in along-axis crustal

structure observed at slow-spreading rates. At fast-spreading rates, however, the higher thermal regime leads to more 2-D mantle upwelling at the ridge axis. This sheet-like pattern of mantle upwelling results in steady-state magma chambers that are largely continuous along the length of a segment and in relatively little along-axis variation in crustal structure. Thus, segmentation at both slow- and fast-spreading ridges reflects the underlying pattern of mantle upwelling and the along-axis extent of individual magma bodies.

However, recent studies are starting to show the importance of temporal variability in crustal accretionary processes, through alternating phases of tectonic and magmatic activity, at all spreading rates. TOBI sidescan sonar data collected between 58°20'E and 60°20'E at the very slow-spreading (16 mm yr^{-1} total rate) Southwest Indian Ridge provides evidence for multiple magma sources along-axis and/or for the importance of lateral dyke injection (Sauter *et al.* 2002). Extensive TOBI, deep-towed camera and geochemical studies of two segments in the MARNOK area (Mid-Atlantic Ridge North of Kane) show that variations in apparent age between and within adjacent segments may be due to the episodicity of magma supply and the along-axis migration of melt respectively (Lawson 1996; Lawson *et al.* 1996). A 3-D tomography experiment over the intermediate-spreading (60 mm yr^{-1}) CoAxial segment of the Juan de Fuca Ridge shows that the along-axis velocity structure may indicate a shift from magmatic to amagmatic extension and reflect variations in magma supply along-axis (Sohn *et al.* 1997). Variations in the thickness of lava and dike units along the Hess Deep, off the fast-spreading EPR, suggest temporal fluctuations in magma supply (Karson *et al.* 2002). Samples collected along a ~25 km (370 000 yr) transect of the same area show that the high variability in magma compositions observed over short periods of time require multiple injections of melt into the crust as opposed to the simple evolution of a single, well-mixed magma reservoir (Stewart *et al.* 2002).

It therefore seems likely that accretion is 3-D at all spreading rates (Wang & Cochran 1993; Wang *et al.* 1996; Cormier *et al.* 1995), with the time frame between magma supply to the crust and the along-axis redistribution of melt the most important factors in the difference between slow- and fast-spreading ridges. Seismic evidence for the presence of melt at segment discontinuites at fast- (Detrick 2000; Kent *et al.* 2000), intermediate- (Turner *et al.* 1999; Day *et al.* 2001) and slow-spreading ridges (Topping 2002; Gill 2003 per. comm.) suggest that the along-axis migration of melt occurs at all

spreading rates with the thermal structure of the crust controlling the lateral extent to which melt can migrate.

A recent sidescan sonar study at 17°15'S on the EPR (Wright *et al.* 2002) shows a good correlation between along-axis variations in fissure density and relative ages of lava flows, with an increase in inferred relative age of lavas with fissure density. Wright *et al.* (2002) conclude that the structure of fast-spreading ridges is related to episodic cycles of magmatic and tectonic processes within second to fourth order segments, with dyke propagation along-axis a significant process within segments. Observations of lava flow morphology and tectonic features at 9°-10°N on the EPR (White *et al.* 2002) indicate that each third order segment behaves as a single volcanic system with higher effusion rates near segment centres.

The work presented in this study, therefore, provides strong evidence for the 4-D nature of crustal accretion at slow-spreading ridges and explains tectonomagmatic cycles in terms of the along-axis migration of melt. Other studies support the suggestion that magma supply to spreading ridges is 3-D and that the temporal variability of crustal accretion is a fundamental process of all mid-ocean ridges, regardless of spreading rate, with the along-axis dimension and the time frame between magma delivery episodes determining the ridge crustal structure and associated characteristics along-axis.

6.7 Suggestions for further work

The model for tectonomagmatic cycles and the temporal variability of crustal accretion presented in this chapter was developed over ~100 km of the ridge south of 59°N. Evidence from TOBI area B, further north along the ridge, suggests that the model is applicable to the whole ridge, as the Iceland hotspot merely subdues the evidence for segmentation. Thus, further work must provide additional evidence for the proposed model over a segment length, the Reykjanes Ridge as a whole and to the mid-ocean ridge system in general.

One of the main features of the model is the requirement for a single melt body with episodic fluxes of melt to the crust feeding a ~70 km long segment spanning ~5 AVRs, and that the along-axis migration of melt is the mechanism by which a single melt body feeds several AVRs. Thus, according to the proposed model, more melt would be expected beneath younger AVRs (i.e. AVRs 2 and 6 in TOBI area C) than beneath the *mature* AVR 4. Existing multi-channel seismic (MCS) data, which only covers AVR 1 and the tips of AVRs to the north and south, indicates the presence of melt beneath the

offset basin between AVRs 1 and 2 (Topping 2002; Gill 2003 pers. comm.). Extending the MCS data coverage along the ridge axis to at least AVR 6 would, therefore, allow the continuity of the axial melt to be mapped and provide further constraints on the model. Collecting deep-tow magnetic data in TOBI area C may also allow more precise determinations of spreading rates and transition widths along the segment to be made, providing further information on the relationship between magmatic accretion and local spreading rates.

The existing TOBI dataset only covers two small areas of the ridge axis. Increasing the TOBI data coverage along-axis would, therefore, allow the relative ages of AVRs to be mapped for the whole ridge and would test the applicability of the model for the Reykjanes Ridge as a whole.

Although existing studies suggest that the model presented in this chapter may be applicable at all spreading rates, further work may provide additional evidence. Two sites are proposed for further study to test the applicability of the model presented in this chapter for all spreading rates.

It is proposed that the MARNOK area, at 24°N on the MAR, may provide a good site to test the proposed model at a slow-spreading ridge that is not effected by a hotspot. TOBI, near-bottom photographic traverses and geochemical data have already been collected over two adjacent segments in this area, with the episodicity of magma supply and melt migration identified as significant factors within second order segments (Lawson *et al.* 1996). It is suggested that, in addition to the existing datasets, collecting gravity, magnetic and MCS data over the MARNOK area may provide further evidence for the episodicity of crustal accretion. The extension of the aforementioned datasets, including the additional acquisition of TOBI data, over several segments along-axis, may provide further information on the importance of the along-axis migration of melt within a segment and on the cyclicity of crustal accretion.

To test the model at the other end of the spreading rate scale it is suggested that further study on the EPR at 9°-10°N be conducted. A sidescan sonar experiment at this location (Wright *et al.* 1995) has mapped the density of fracturing and the relative age of lava flows along-axis, with the along-axis variations in the mean density of fissuring and the relative age of axial lavas coinciding with high order segment boundaries. These observations, along with systematic variations in volcanic morphology within third order segments, have led White *et al.* (2002) to propose that a third order segment at this location behaves as a single volcanic system. In addition, existing seismic data (Kent *et*

al. 2000) in this area indicates that melt is ponded at segment discontinuities suggesting that melt may migrate along-axis. A gravity study from 9°-10°N on the EPR (Wang *et al.* 1996) attributes subcrustal gravity anomalies to density variations within the mantle related to focussed mantle upwelling.

Thus, the different observations made as part of this study, including evidence for relative age variations of extrusives along-axis, inferred melt distribution, segmentation and 3-D mantle upwelling, have also been made at the EPR. However, to date, no work has linked the observations from these different studies into a comprehensive model for high order segmentation fed by an episodic melt supply. It is proposed, therefore, that in addition to combining the existing datasets over 9°-10°N at the EPR into a self-consistent model of the cyclicity of crustal accretion, the along-axis extension of existing sidescan sonar, seismic and gravity data may provide further constraints on the relationship between tectonomagmatic cycles, segmentation and 3-D mantle upwelling at all spreading rates.

6.8 Conclusions

- Interpretation of TOBI data confirms the existence of tectonomagmatic cycles based solely on morphological observations. AVRs appear to undergo a lifecycle from *young* to *adolescent* through to *mature* and *old* ages, as proposed by Parson (1993). However, this study indicates that the evolutionary lifecycle of an AVR is a continuous process and that the four stages of Parson (1993) only represent discrete "snapshots" of this lifecycle.

- Along-axis modelling of the long-wavelength gravity anomaly data suggests that influence of the Iceland hotspot results in an increase in crustal thickness from 7.5 km at 57°45'N to ~10.5 km near 62°N. A gradual decrease in upper mantle density from 3.30 g cm^{-3} to 3.24 g cm^{-3} at 62°N is also required to satisfy the seismic data constraints. This modelling also indicates that "normal" oceanic crustal thickness of 7.1 ± 0.8 km (White *et al.* 1992) is reached at ~59°N, thus marking the most southerly extent of direct hotspot influence.

- Removal of the long-wavelength trend in the RMBA and magnetization intensity solution reveals intermediate-wavelength variations that are hypothesised to reflect effects of the pulsing hotspot. South of ~59°N both the along-axis RMBA and

magnetization intensity have the greatest peak-to-trough variations. Between ~59°N and 60°50'N the variations in RMBA and magnetization intensity are more subdued, whereas north of 60°50'N magnetization intensity variations become slightly more pronounced. These observations support the hypothesis of Lee & Searle (2000), in which the region south of ~59°N is free of hotspot influence and the crustal accretionary process is typical of slow-spreading ridges with small, ephemeral, isolated magma chambers giving rise to large along-axis variations in crustal thickness and/or density as reflected in the RMBA. In addition, these magma chambers have a wide range of fractionation histories resulting in the large along-axis variations in magnetization intensity. The region between ~59°N and 60°50'N has been effected by the latest hotspot pulse, and the associated higher thermal regime results in larger magma chambers and/or more mixing in the magma reservoirs, resulting in more subdued magnetization intensity variations. The higher temperatures in this regime may also facilitate the along-axis redistribution of crustal melt, resulting in smaller along-axis variations in crustal thickness and/or density as suggested by the subdued along-axis RMBA variations. A coincident RMBA low and magnetization intensity high at 59°30'N may indicate the presence of a small magma chamber at the tip of the propagating pulse. The slight increase in magnetization intensity variations north of 60°50'N suggests that the crust is readjusting after the passage of the hotspot pulse.

- Short-wavelength variations in RMBA are associated with individual AVRs and support the morphological observations for the existence of tectonomagmatic cycles. Gravity models of individual AVRs support a model for tectonomagmatic cycles where cyclic injections of melt gradually build AVRs. Models of *young* AVRs are consistent with the presence of partial melt in the mid-crust, indicating that they are presently undergoing magmatic construction. Models of slightly older AVRs, from *young* to *adolescent* in age, are consistent with there being slightly less melt in the crust suggesting that magmatic accretion is declining. Models of *mature* AVRs are consistent with the presence of thicker crust beneath the AVR centre, suggesting that these AVRs are at the very end of the magmatic phase of the cycle, with the crust built to its maximum thickness by repeated injections of melt, and are about to be dismembered by the tectonic part of the process.

- Short-wavelength variations in magnetization intensity, which can be used as a proxy for the relative age of extrusives, confirm the relative age interpretations of the TOBI data. Older AVRs generally have a lower average magnetization intensity than younger AVRs, suggesting that basalts there have been extruded for longer and have undergone more low-temperature oxidation. An ~20% increase in total spreading rate for young AVRs over the last 1.42 Ma suggests that magmatic accretion influences local spreading rates or that the loci of crustal accretion are governed by tectonic forces. Asymmetry in spreading rates explains the asymmetric RMBA pattern, with the thinnest crust lying in the direction of fastest spreading.

- The spatial pattern of RMBA and magnetization intensity variations are used to develop a model of crustal accretion at the Reykjanes Ridge that explains tectonomagmatic cycles in terms of patterns of mantle upwelling and segmentation.

  The 20 mm yr^{-1} total spreading rate of the Reykjanes Ridge results in a ~70 km wavelength of mantle upwelling along the ridge axis. Far-field tectonic stresses result in the spreading-orthogonal brittle deformation of the crust in the neovolcanic zone, with fractures tapping initially into the centre of the upwelling melt. AVRs are constructed over these fractures, initially through fissure volcanism (the *young* stage), as melt is gradually accumulated in the mid-crust, point-source volcanism dominates, with the creation of conical and eventually flat-topped volcanoes (*adolescent* and *mature* stages respectively). As the crust warms, brittle failure propagates away from the initial point of magma injection in both directions along-axis. These new fractures tap into the melt, resulting in the creation of new AVRs and the pattern of progressively younger and shorter AVRs on either side of *mature* AVRs. As the magmatic part of the cycle wanes, tectonic forces dismember AVRs (the *old* stage). This cycle is repeated along the ridge-axis and through time, generating the oceanic crust.

- The work presented as part of this study combined with recent evidence from fast-spreading ridges (Stewart *et al.* 2002; Wright *et al.* 2002; White *et al.* 2002), suggests that crustal accretion is a cyclic process at all spreading rate, with the time frame between magmatic phases of the cycle and the thermal state of the underlying mantle accounting for the differences in morphology and segmentation between slow- and fast-spreading ridges.

References

Appelgate, B. & Shor, A.N., 1994. The northern Mid-Atlantic and Reykjanes Ridges: Spreading centre morphology between 55°50'N and 63°00'N, *J. Geophys. Res.*, **99**, 17935-17956.

Batiza, R., 1996. Magmatic segmentation of mid-ocean ridges: a review. In: *MacLeod, C.J., Tyler, P.A., Walker, C.L.* (eds.) *Tectonic, magmatic, hydrothermal and biological segmentation of mid-ocean ridges*, Geol. Soc. Spec. Pub., **118**, 103-130.

Bazin, S., Harding, A.J., Kent, G.M., Orcutt, J.A., Tong, C.H., Pye, J.W., Singh, S.C., Barton, P.J., Sinha, M.C., White, R.S., Hobbs, R.W. & Van Avendonk, H.J.A., 2001. Three-dimensional shallow crustal emplacement at the 9°03'N overlapping spreading center on the East Pacific Rise: Correlations between magnetization and tomographic images, *J. Geophys. Res.*, **106**, 16101-16117.

Bell, R.E. & Buck, W.R., 1992. Crustal control of ridge segmentation inferred from observations of the Reykjanes Ridge, *Nature*, **357**, 583-586.

Blondel, P. & Murton, B.J., 1997. Handbook of seafloor sonar imagery, *PRAXIS-Wiley & Sons*, pp. 314.

Briais, A. & Rabinowicz, M., 2002. Temporal variations of the segmentation of slow to intermediate spreading mid-ocean ridges - 1. Synoptic observations based on satellite altimetry data, *J. Geophys. Res.*, **107**, ECV 3-1 - 3-19.

Buck, W.R., Carbotte, S.M. & Mutter, C., 1997. Controls on extrusion at mid-ocean ridges, *Geology*, **25**, 935-938.

Bunch, A.W.H. & Kennett B.L.N., 1980. The crustal structure of the Reykjanes Ridge at 59°30'N, *Geophys. J. R. Astr. Soc.*, **61**, 141-166.

Cande, S.C. & Kent, D.V., 1995. Revised calibration of the geomagnetic polarity timescale for the Late Cretaceous and Cenozoic, *J. Geophys. Res.*, **100**, 6093-6095.

Cannat, M., Mevel, C., Maia, M., Deplus, C., Durand, C., Gente, P., Agrinier, P., Belarouchi, A., Dubuisson, G., Humler, E. & Reynolds J., 1995. Thin crust, ultramafic exposures, and rugged faulting at the Mid-Atlantic Ridge (22°-24°N), *Geology*, **23**, 49-52.

Carbotte, S. & Macdonald, K., 1992. East Pacific Rise 8°-10°30'N: Evolution of ridge segments and discontinuities from SeaMARC II and three-dimensional magnetic studies, *J. Geophys. Res.*, **97**, 6959-6982.

Carbotte, S., Solomon, A. & Ponce-Correa, G., 2000. Evaluation of morphological indicators of magma supply and segmentation from a seismic reflection study of the East Pacific Rise 15°30'-17°N, *J. Geophys. Res.*, **105**, 2737-2759.

Carlson, R.L. & Raskin, G.S., 1984. Density of the oceanic crust, *Nature*, **311**, 555-558.

Chen, Y. & Morgan, W.J., 1990. Rift valley/no rift valley transition at mid-ocean ridges, *J. Geophys. Res*, **95**, 17571-17581.

Christenson, G.L., Purdy, G.M. & Rhor, K.M.M., 1993. Structure of the northern symmetrical segment of the Juan de Fuca Ridge, *Marine Geophys. Res.*, **15**, 219-240.

Collier, J.S. & Singh, S.C., 1998. Poisson's ratio structure of young oceanic crust, *J. Geophys. Res*, **103**, 20981-20996.

Collier, J.S. & Sinha, M.C., 1992. Seismic mapping of a magma chamber beneath the Valu Fa Ridge, Lau Basin, *J. Geophys. Res*, **97**, 14031-14053.

Cormier, M.-H., Macdonald, K.C. & Wilson, D.S., 1995. A three-dimensional gravity analysis of the East Pacific Rise from 18° to 21°30'S, *J. Geophys. Res.*, **100**, 8063-8082.

Crane, C., 1985. The spacing of rift axis highs: dependence upon diapiric processes in the underlying asthenosphere, *Earth Planet. Sci. Lett.*, **72**, 405-414.

Day, A.J., Peirce, C. & Sinha, M.C., 2001. Three-dimensional crustal structure and magma chamber geometry at the intermediate-spreading, back-arc Valu Fa Ridge, Lau Basin - results of a wide-angle seismic tomographic inversion, *Geophys. J. Int.*, **146**, 31-52.

Dehlinger, P., 1978. Marine Gravity, *Elsevier Oceanography Series*, **22,** Elsevier Scientific Publishing Company, Amsterdam, pp. 322.

DeMets, C., Gordon, R.G., Argus, D.F. & Stein, S., 1990. Current plate motions, *Geophys. J. Int.*, **101**, 425-478.

Detrick, R.S., 2000. Portrait of a magma chamber, *Nature*, **406**, 578-579.

Detrick, R.S., Buhl, P., Vera, E.E., Mutter, J.A., Orcutt, J.A., Madsen, J. & Brocher T., 1987. Multichannel seismic imaging of a crustal magma chamber along the East Pacific Rise, *Nature*, **326**, 35-41.

Detrick, R.S., Needham, H.D. & Renard, V., 1995. Gravity anomalies and crustal thickness variations along the Mid-Atlantic Ridge between 33°N and 40°N, *J. Geophys. Res.*, **100**, 3767-3787.

Dilek, Y., Moores, E.M. & Furnes, H., 1998. Structure of modern oceanic crust and ophiolites and implications for faulting and magmatism at oceanic spreading centers, In: *Buck, W.R., Delaney, P.T., Karson, J.A. & Lagabrielle, Y.* (eds.), *Faulting and magmatism at mid-ocean*

ridges, Geophysical Monograph **106**, American Geophysical Union, Washington, D.C., 219-265.

Dunlop, D.J. & Prevot, M., 1982. Magnetic properties and opaque mineralogy of drilled submarine intrusive rocks, *Geophys. J. R. Astr. Soc.*, **89**, 9800-9990.

Ewing, J. & Ewing, M., 1959. Seismic-refraction measurements in the Atlantic Ocean Basin, in the Mediterranean Sea, on the Mid-Atlantic Ridge, and in the Norwegian Sea, *Geol. Soc. Am.*, **70**, 291-318.

Field, P.R., 1994. Crustal structure of the spreading plate boundary in Iceland and the north Atlantic from gravity data, *Ph.D. Thesis*, University of Durham (unpublished), pp. 224.

Fleischer, U., 1974. The Reykjanes Ridge: A summary of geophysical data, In: *Kristjansson* (ed.), *Geodynamics of Iceland and the North Atlantic Area*, D. Reidel, Norwell, Mass., 17-31.

Flewellen, C., Millard, N. & Rouse, I., 1993. TOBI, a vehicle for deep ocean survey, *Electronics and Communication Engineering Journal*, **April**, 85-93.

Forsyth, D.W. & Wilson, B., 1984. Three-dimensional temperature structure of a ridge-transform-ridge system, *Earth Planet. Sci. Lett.*, **70**, 355-362.

Foulger, G.R., Pritchard, M.J., Julian, B.R., Evans, J.R., Allen, R.M., Nolet, G., Morgan, W.J., Bergsson, B.H., Erlendsson, P., Jakobsdottir, S., Ragnarsson, S., Stefansson, R. & Vogfjord, K., 2001. Seismic tomography shows that upwelling beneath Iceland is confined to the upper mantle, *Geophys. J. Int.*, **146**, 504-530.

Fryer, G.J., Miller, D.J. & Berge, P.A., 1989. Seismic anisotropy and age-dependant structure of the upper oceanic crust, In: *Sinton, J.M.* (ed.), *Evolution of mid-ocean ridges*, Geophysical Monograph **57**, IUGG vol. 8, Library of Congress, AGU, Washington, 1-7.

Fujiwara, T., Lin, J., Matsumoto, T., Kelemen, P.B., Tucholke, B.E. & Casey, J.F., 2003. Crustal evolution of the Mid-Atlantic Ridge near the Fifteen-Twenty Fracture Zone in the last 5 Ma, *Geochem. Geophys. Geosyst.*, **4**(3), 1-25.

Gee, J. & Kent, D., 1994. Variation in layer 2A thickness and the origin of the central anomaly magnetic high, *Geophys. Res. Letts.*, **21**, 297-300.

Heinson, G., Constable, S. & White, A., 2000. Episodic melt transport at mid-ocean ridges inferred from magnetotelluric soundind, *Geophys. Res. Letts.*, **27**, 2317-2320.

Hess, H.H., 1962. History of the ocean basins, In: *Engel, A.E.J., James, H.L. & Leonard, B.F.* (eds.), *Petrological studies: A volume in honour of A.F. Buddington,* Geol. Soc. Am., Boulder, Colorado, U.S.A., 559-620.

Hey, R.N., Kleinrock, M.C., Miller, S.P., Atwater, T.M. & Searle, R.C., 1986. SeaBeam/Deep-Tow investigation of an active oceanic propagating rift system, *J. Geophys. Res.*, **91**, 3369-3393.

Hooft, E.E. & Detrick, R.S., 1993. The role of density in the accumulation of basaltic melt at mid-ocean ridges, *Geophys. Res. Letts.*, **20**, 423-426.

Hooft, E.E., Schouten, H. & Detrick, R.S., 1996. Constraining crustal emplacement processes from the variation in seismic layer 2A thickness at the East Pacific Rise, *Earth Planet. Sci. Lett.*, **142**, 289-309.

Houtz, R. & Ewing, J., 1976. Upper crustal structure as a function of plate age, *J. Geophys. Res*, **81**, 2490-2498.

Ito, G., 2001. Reykjanes 'V'-shaped ridges originating from a pulsing and dehydrating mantle plume, *Nature*, **411**, 681-684.

Jha, K., Parmentier, E.M. & Phipps Morgan, J., 1994. The role of mantle-depletion and melt-retention buoyancy in spreading-center segmentation, *Earth Planet. Sci. Lett.*, **125**, 221-234.

Johnson, H.P. & Atwater, T., 1977. Magnetic study of basalts from the MAR, lat. 37°N, *Geol. Soc. Am. Bull.*, **88**, 637-647.

Johnson, H.P. & Hall, J.M., 1978. A detailed rock magnetic and opaque mineralogy study of basalts from the Nazca plate, *Geophys. J. R. Astr. Soc.*, **52**, 45-64.

Johnson, H.P. & Helferty, M., 1990. The geological interpretation of sidescan sonar, *Review of Geophysics*, **28**, 357-380.

Johnson, H.P., Patten, D.V. & Sager, W.S., 1996. Age-dependent variation in the magnetization of seamounts, *J. Geophys. Res.*, **101**, 13701-13714.

Jones, S.M., White, N. & Maclennan, J., 2002. V-shaped ridges around Iceland: Implications for spatial and temporal patterns of mantle convection, *Geochem. Geophys. Geosyst.*, **3**(10), 1-23.

Karson, J.A., Tivey, M.A. & Delaney, J.R., 2002. Internal structure of uppermost oceanic crust along the Western Blanco Transform Scarp: Implications for subaxial accretion and deformation at the Juan de Fuca Ridge, *J. Geophys. Res.*, **107**, EPM 1-1 - 1-24.

Keeton, J.A., Searle, R.C., Parsons, B., White, R.S., Murton, B.J., Parson, L.M., Peirce, C. & Sinha, M.C., 1997. Bathymetry of the Reykjanes Ridge, *Marine Geophys. Res.*, **19**, 55-64.

Kent, D.V., Harding, A.J. & Orcutt, J.A., 1993. Distribution of magma beneath the East Pacific Rise between the Clipperton transform and the 9°17'N deval from forward modelling of common depth point data, *J. Geophys. Res*, **98**, 13945-13969.

Kent, D.V., Honnerez B.M., Opdyke N.D. & Fox P.J., 1978. Magnetic properties of dredged oceanic gabbros and the source of marine magnetic anomalies, *Geophys. J. Roy. Astron. Soc.*, **55**, 513-537.

Kent, G.M., Singh, S.C., Harding, A.J., Sinha, M.C., Orcutt, J.A., Barton, P.J., White, R.S., Bazin, S., Hobbs, R.W., Tong, C.H. & Pye, J.W., 2000. Evidence from three-dimensional seismic reflectivity images for enhanced melt supply beneath mid-ocean ridge discontinuities, *Nature*, **406**, 614-618.

Kuo, B.Y. & Forsyth, D.W., 1988. Gravity anomalies of the ridge-transform system in the south Atlantic between 31° and 34.5°S upwelling centres and variations in crustal thickness, *Marine Geophys. Res.*, **10**, 205-232.

Laughton, A.S., Searle, R.C. & Roberts, D.G., 1979. The Reykjanes Ridge crest and the transition between its rifted and non-rifted regions, *Tectonophysics*, **55**, 173-177.

Lawson, N.K., 1996. Crustal accretion near ridge-transform intersections: Kane fracture zone, Mid-Atlantic Ridge, *Ph.D. Thesis*, University of Durham (unpublished), pp. 459.

Lawson, K., Searle, R.C., Pearce, J.A., Browning, P. & Kempton, P., 1996. Detailed volcanic geology of the MARNOK area, Mid-Atlantic Ridge north of Kane transform, In: *MacLeod, C.J., Tyler, P.A., Walker, C.L.* (eds.) *Tectonic, magmatic, hydrothermal and biological segmentation of mid-ocean ridges*, Geol. Soc. Spec. Pub., **118**, 61-102.

Le Bas, T.P., Mason, D.C. & Millard, N.C., 1995. TOBI image processing: The state of the art, *IEEE Journal of Oceanic Engineering*, **20**, 85-93.

Lee, S.M. & Searle, R.C., 2000. Crustal magnetisation of the Reykjanes Ridge and implications for its along-axis variability and the formation of axial volcanic ridges, *J. Geophys. Res.*, **105**, 5907-5930.

Lin, J. & Phipps Morgan, J., 1992. The spreading rate dependence of three-dimensional mid-ocean ridge gravity structure, *Geophys. Res. Letts.*, **19**, 13-16.

Lin, J., Purdy, G.M., Schouten, H., Sempere, J.C. & Zervas, C., 1990. Evidence from gravity data for focused magmatic accretion along the Mid-Atlantic Ridge, *Nature*, **344**, 627-632.

Lowrie, W., 1977. Intensity and direction of magnetization in oceanic basalts, *J. Geol. Soc. Lon.*, **133**, 61-82.

Macdonald, K.C., 1977. Near-bottom magnetic anomalies, asymmetric spreading, oblique spreading and tectonics of the Mid-Atlantic Ridge near 37°N, *Geol. Soc. Am. Bull.*, **88**, 541-555.

Macdonald, K.C., 1982. Mid-ocean ridges: Fine scale tectonic, volcanic and hydrothermal processes within the plate boundary zone, *Ann. Rev. Earth planet. Sci.*, **10**, 155-190.

Macdonald, K.C., 1998. Linkages between faulting, volcanism, hydrothermal activity and segmentation on fast spreading centers, In: *Buck, W.R., Delaney, P.T., Karson, J.A. & Lagabrielle, Y.* (eds.), *Faulting and magmatism at mid-ocean ridges*, Geophysical Monograph **106**, American Geophysical Union, Washington, D.C., 27-58.

Macdonald, K.C., Fox, P.J., Perram, L.J., Eisen, M.F., Hayman, R.M., Miller, S.P., Carbotte, S.M., Cormier, M.-H. & Shor, A.N., 1988. A new view of the mid-ocean ridge from the behaviour of ridge-axis discontinuities, *Nature*, **335**, 217-225.

Macdonald, K.C., Miller, S.P., Huestis, S.P. & Spiess, F.N., 1980. Three-dimensional modeling of a magnetic reversal boundary from inversion of deep-tow measurements, *J. Geophys. Res.*, **85**, 3670-3680.

Macdonald, K.C., Scheirer, D.S. & Carbotte, S.M., 1991. Mid-ocean ridges: Discontinuities, segments and giant cracks, *Science*, **253**, 986-994.

MacGregor, L.M., Constable, S. & Sinha, M.C., 1998. The RAMESSES experiment III: Controlled-source electromagnetic sounding of the Reykjanes Ridge at 57°45'N, *Geophys. J. Int.*, **135**, 772-789.

Magde, L.S. & Smith, D.K., 1995. Seamount volcanism at the Reykjanes Ridge: Relationship to the Iceland hot spot, *J. Geophys. Res.*, **100**, 8449-8468.

Magde, L.S., Detrick, R.S. & the TERA group, 1995. Crustal and upper mantle contribution to the axial gravity anomaly at the southern East Pacific Rise, *J. Geophys. Res.*, **100**, 3747-3766.

Murton, B.J. & Parson, L.M., 1993. Segmentation, volcanism and deformation of oblique spreading centres: a qualitative study of the Reykjanes Ridge, *Tectonophysics*, **222**, 237-257.

Murton, B.J., Parson, L., Evans, J., Owens, R., Satur, N., Redbourn, L., Sauter, D., Taylor, R., Walker, C.L., Forster, J., Anderson, J., Fern, A., Jones, J., Paulson, C., Phipps, R. & Wyner, J., 1993. The PERTROS program (PETRogenesis of Oblique Spreading), RRS Charles Darwin 80 Cruise Report (unpublished), **214**, pp. 77.

Murton, B.J., Taylor, R.N. & Thirlwall, M.F., 2002. Plume-ridge interaction: A geochemical perspective from the Reykjanes Ridge, *J. Petro.*, **43**, 1987-2012.

Mutter, J.C., Carbotte, S.M., Su, W.S., Xu, L.Q., Buhl, P., Detrick, R.S., Kent, G.M., Orcutt, J.A. & Harding, A.J., 1995. Seismic images of active magma systems beneath the East Pacific Rise between 17°05' and 17°35'S, *Science*, **268**, 391-395.

Nafe, J.E. & Drake, C.L., 1957. Variation with depth in shallow and deep water marine sediment of porosity, density and the velocities of compressional and shear waves, *Geophysics*, **22**, 523-553.

Nafe, J.E. & Drake, C.L., 1962. Physical properties of marine sediments, In: *Hill, M.N. (ed.), The Sea*, **3**, Wiley, New York, 794-815.

Navin, D.A., 1996. Seismic investigation of crustal accretion at the slow spreading Mid-Atlantic Ridge – the Reykjanes Ridge at 57°45'N, *Ph.D. Thesis*, University of Durham (unpublished), pp. 309.

Navin, D.A., Peirce, C. & Sinha, M.C., 1998. The RAMESSES experiment - II. Evidence for accumulated melt beneath slow spreading ridge from wide-angle refraction and multichannel reflection seismic profiles, *Geophys. J. Int.*, **135**, 746-772.

Nicolas, A. & Boudier, F., 1995. Mapping oceanic ridge segments in Oman ophiolite, *J. Geophys. Res.*, **100**, 6179-6197.

Orcutt, J.A., Kennett, B.L.N., Dorman, L. & Prothero, W., 1975. Evidence for a low velocity zone underlying a fast spreading ridge crest, *Nature*, **256**, 475-476.

Owens, R.B., 1991. An investigation of marine anomalies from Reykjanes Ridge 58°N 32°20'W, *M.Sc. Thesis*, University of Durham (unpublished), pp. 54.

Parker, R.L., 1973. The rapid calculation of potential anomalies, *Geophys. J. R. Astr. Soc.*, **31**, 447-455.

Parker, R.L. & Huestis, S.P., 1974. The inversion of magnetic anomalies in the presence of topography, *J. Geophys. Res.*, **79**, 1587-1593.

Parmentier, E.M. & Phipps Morgan, J., 1990. Spreading rate dependance of three-dimensional structure in oceanic spreading centers, *Nature*, **348**, 325-328.

Parson, L.M., 1993. Side-scan sonar and swath bathymetry investigation of the Reykjanes Ridge, southwest of Iceland, R/V Maurice Ewing EW9008 Cruise Report (unpublished), pp. 8.

Parson, L.M., Murton, B.J., Searle, R.C., Booth, D., Evans, J., Field, P., Keeton, J., Laughton, A., McAllister, E., Millard, N., Redbourne, L., Rouse, I., Shor, A., Smith, D., Spencer, S., Summerhayes, C. & Walker, C.L., 1993. En echelon axial volcanic ridges at the Reykjanes Ridge: a life cycle of volcanism and tectonics, *Earth Planet. Sci. Lett.*, **117**, 73-87.

Pedley, R.C., Busby, J.P. & Dabek, Z.K., 1993. GRAVMAG User Manual – Interactive 2.5-D gravity and magnetic modelling, *British Geological Survey, Technical Report WK/93/26/R*, pp. 73.

Peirce, C. & Gardiner, A.B., 2003. Temporal and spatial cyclicity of accretion at slow-spreading ridges - evidence from the Reykjanes Ridge, *in preparation*.

Peirce, C. & Navin, D. A., 2002. The RAMESSES experiment - V. Crustal accretion at axial volcanic ridge segments-a gravity study at 57°45'N on the slow spreading Reykjanes Ridge, *Geophys. J. Int*, **148**, 1-19.

Peirce, C. & Sinha, M.C., 1998. RAMESSES II - Reykjanes Ridge axial melt experiment: structural synthesis from electromagnetics and seismics, RRS Discovery 235c Cruise Report (unpublished), pp. 38.

Phipps Morgan, J. & Forsyth, D.W., 1988. Three-dimensional flow and temperature perturbations due to a transform offset: effects on oceanic crustal and mantle structure, *J. Geophys. Res.*, **93**, 2955-2966.

Prince, R.A. & Forsyth, D.W., 1988. Horizontal extent of anomalously thin crust near the Vema fracture zone from the 3-D analysis of gravity anomalies, *J. Geophys. Res.*, **93**, 8051-8063.

Rabinowicz, M. & Briais, A., 2002. Temporal variations of the segmentation of slow to intermediate spreading mid-ocean ridges - 2. A three-dimensional model in terms of lithosphere accretion and convection within the partially molten mantle beneath the ridge axis, *J. Geophys. Res.*, **107**, ECV 2-1 - 2-19.

Raitt, R.W., 1963. The crustal rocks, In: *Hill, M.N.* (ed.), *The Sea*, vol. **3**, Wiley (Interscience), New York, 85-102.

Richardson, R.M., 1992. Ridge forces, absolute plate motions, and the intraplate stress field, *J. Geophys. Res.*, **97**, 11739-11748.

Rouse, I.P., 1991. TOBI: A deep-towed sonar system, In: colloquium on "civil applications of sonar systems", *Institute of Electrical Engineers*, Digest no. 1991/028, 7/1-7/5.

Sallares, V., Charvis, Ph. & Flueh, E.R., 2003. Wide-angle seismic constraints on the evolution of Galapagos Hotspot - Cocos-Nazca Spreading Center interaction, *in preparation.*

Sandwell, D.T. & Smith, W.H.F., 1997. Marine gravity anomaly from Geosat and ERS-1 satellite altimetry, *J. Geophys. Res.*, **102**, 10039-10054.

Sauter, D., Parson, L., Mendel, V., Rommevaux-Jestin, C., Gomez, O., Briais, A., Mevel, C., Tamaki, K. & the FUJI scientific team, 2002. TOBI sidescan sonar imagery of the very slow-spreading Southwest Indian Ridge: evidence for along-axis magma distribution, *Earth Planet. Sci. Lett.*, **199**, 81-95.

Schilling, J.G., 1973. Iceland mantle plume: Geochemical study of Reykjanes Ridge, *Nature*, **242**, 565-571.

Schouten, H. & McCamy, K., 1972. Filtering marine magnetic anomalies, *J. Geophys. Res.*, **77**, 7089-7099.

Schouten, H., Klitgord, K.D. & Whitehead, J.A., 1985. Segmentation of mid-ocean ridges, *Nature*, **317**, 225-229.

Schouten, H., Tivey, M.A., Fornari, D.J. & Cochran J.R., 1999. Central anomaly magnetization high: constraints on the volcanic construction and architecture of seismic layer 2A at a fast-spreading mid-ocean ridge, the EPR at 9°30'-50'N, *Earth Planet. Sci. Lett.*, **169**, 37-50.

Searle, R.C. & Laughton, A.S., 1981. Fine-scale sonar study of tectonics and volcanism on the Reykjanes Ridge, *Oceanol. Acta*, **4** (Suppl.), 5-13.

Searle, R.C., Field, P.R. & Owens, R.B., 1994a. Segmentation and a non-transform ridge offset on the Reykjanes Ridge near 58°N, *J. Geophys. Res.*, **99**, 24159-24172.

Searle, R.C., Keeton, J.A., Owens, R.B., White, R.S., Mecklenburgh, R., Parsons, B. & Lee, S.-M., 1998. The Reykjanes Ridge: Structure and tectonics of a hot-spot influenced, slow-spreading ridge, from multibeam bathymetry, gravity and magnetic investigations, *Earth Planet. Sci. Lett.*, **160**, 463-478.

Searle, R.C., Parsons, B.E. & White, R.S., 1994b. Multibeam bathymetric and potential field studies of the Reykjanes Ridge, RRS Charles Darwin 87 Cruise Report (unpublished), pp. 43.

Sempere, J.C. & Macdonald, K.C., 1987. Marine tectonics: Processes at mid-ocean ridges, *Rev. Geophys.*, **25**, 1313-1347.

Sempere, J.C., Macdonald, K.C. & Miller, S.P., 1984. Overlapping spreading centres: 3D inversion of the magnetic field at 9°03'N on the East Pacific Rise, *Geophys. J. Roy. Astron. Soc.*, **79**, 799-811.

Shaw, P.R., 1994. Age variations of oceanic crust Poisson's ratio: Inversion and porosity evolution model, *J. Geophys. Res.*, **99**, 3057-3066.

Sinha, M.C., Peirce, C. & Constable, S., 1994. An integrated geophysical investigation of the axial volcanic region of the Reykjanes Ridge at 57°45'N, RRS Charles Darwin 81 Cruise report (unpublished), pp. 39.

Sinha, M.C., Navin, D.A., MacGregor, L.M., Constable, S., Peirce, C., White, A., Heinson, G. & Inglis, M.A., 1997. Evidence for accumulated melt beneath the slow-spreading Mid-Atlantic Ridge, *Phil. Trans. R.. Soc. Lond.*, A, **355**, 233-253.

Sinha, M.C., Constable, S., Peirce, C., White, A., Heinson, G., MacGregor, L.M. & Navin, D.A., 1998. Magmatic processes at slow spreading ridges: implications of the RAMESSES experiment, Mid-Atlantic Ridge at 57°N, *Geophys. J. Int*, **135**, 731-745.

Sinton, J.M. & Detrick, R.S., 1992. Mid-ocean ridge magma chambers, *J. Geophys. Res*, **97**, 197-216.

Sinton, J.M., Wilson, D.S., Christie, D.M., Hey, R.N. & Delaney, J.R., 1983. Petrologic consequences of rift propagation on oceanic spreading ridges, *Earth Planet. Sci. Lett.*, **62**, 193-207.

Smallwood, J.R. & White, R.S., 1998. Crustal accretion at the Reykjanes Ridge, 61°-62°N, *J. Geophys. Res,* **103**, 5185-5201.

Smallwood, J.R., White, R.S. & Minshull, T.A., 1995. Sea-floor spreading in the presence of the Iceland plume - the structure of the Reykjanes Ridge at 61°40'N, *J. Geol. Soc. London*, **152**, 1023-1029.

Smith, G.M. & Banerjee, S.K., 1986. Magnetic structure of the upper kilometer of the marine crust at Deep Sea Drilling Project hole 504B, Eastern Pacific Ocean, *J. Geophys. Res,* **91**, 10337-10354.

Smith, D.K. & Cann, J.R., 1990. Hundreds of small volcanoes on the median valley floor of the Mid-Atlantic Ridge at 24°-30°N, *Nature*, **348**, 152-155.

Smith, D.K. & Cann, J.R., 1992. The role of seamount volcanism in crustal construction at the Mid-Atlantic Ridge (24°-30°N), *J. Geophys. Res,* **97**, 1645-1658.

Smith, D.K., Humphris, S.E. & Bryan W.B., 1995. A comparison of volcanic edifices at the Reykjanes Ridge and the Mid-Atlantic Ridge at 24°-30°N, *J. Geophys. Res,* **100**, 22485-22498.

Sohn, R.A., Webb, S.C., Hildebrand, J.A. & Cornuelle, B.D., 1997. Three-dimensional tomographic velocity structure of the upper crust, CoAxial segment, Juan de Fuca Ridge: Implications for on-axis evolution and hydrothermal circulation, *J. Geophys. Res,* **102**, 17679-17695.

Sparks, D.W. & Parmentier, E.M., 1993. The structure of three-dimensional convection beneath oceanic spreading centers, *Geophys. J. Int*, **112**, 81-91.

Sparks, D.W., Parmentier, E.M. & Phipps Morgan, J., 1993. Three-dimensional mantle convection beneath a segmented spreading center: Implications for along-axis variations in crustal thickness and gravity, *J. Geophys. Res.*, **98**, 21977-21995.

Stewart, M.A, Klein, E.M. & Karson, J.A., 2002. Geochemistry of dikes and lavas from the north wall of the Hess Deep Rift: Insights into the four-dimensional character of crustal construction at fast spreading mid-ocean ridges, *J. Geophys. Res.*, **107**, EPM 4-1 - 4-23.

Talwani, M., Windsich, C.C. & Langseth, M.G., 1971. Reykjanes Ridge Crest: A detailed geophysical study, *J. Geophys. Res.*, **76**, 473-517.

Tapponnier, P. & Franchetau, J., 1978. Necking of the lithosphere and the mechanics of slowly accreting plate boundaries, *J. Geophys. Res.*, **83**, 3955-3970.

Taylor, R.N., Murton, B.J. & Thirwall, M.F., 1995. Petrographic and geochemical variation along the Reykjanes Ridge, 57°N-59°N, *J. Geol. Soc. Lond.*, **152**, 1031- 1037.

Thatcher, W. & Hill, D.P., 1995. A simple model for fault-generated morphology for slow-spreading mid-ocean ridges, *J. Geophys. Res.*, **95**, 561-570.

Tivey, M.A., Schouten, H. & Kleinrock M.C., 2003. A near-bottom magnetic survey of the Mid-Atlantic Ridge axis at 26°N: Implications for the tectonic evolution of the TAG segment, *J. Geophys. Res.*, **108**, art. no. 2277, EPM 15-1 - 15-13.

Tolstoy, M., Harding, A.J. & Orcutt, J.A., 1993. Crustal thickness on the Mid-Atlantic Ridge: bull's-eye gravity anomalies and focused accretion, *Science*, **263**, 726-729.

Toomey, D.R., Solomon, S.C. & Purdy, G.M., 1994. Tomographic imaging of the shallow crustal structure of the East Pacific Rise at 9°30'N, *J. Geophys. Res*, **99**, 24135-24157.

Topping, S., 2002. RAMESSES II: Seismic reflections at the Mid-Atlantic ridge from analysis of real and synthetic data, *Ph.D. Thesis*, University of Cambridge (unpublished), pp. 196.

Turner, I.M., Peirce, C. & Sinha, M.C., 1999. Seismic imaging of the axial region of the Valu Fa Ridge, Lau Basin - the accretionary processes of an intermediate back-arc spreading ridge, *Geophys. J. Int*, **138**, 495-519.

Vera, E.E., Mutter, J.C., Buhl, P., Orcutt, J.A., Harding, A.J., Kappus, M.E., Detrick, R.S. & Brocher, T.M. 1990. The structure of 0-My to 0.2-My old oceanic crust at 9°N on the East Pacific Rise from expanded spread profiles, *J. Geophys. Res*, **95**, 15529-15556.

Vine, F.J. & Matthews, D.H., 1963. Magnetic anomalies over oceanic ridges, *Nature*, **199**, 947-949.

Vogt, P.R., 1971. Asthenospheric motion recorded by the ocean floor south of Iceland, *Earth Planet. Sci. Lett.*, **13**, 153-160.

Vogt, P.R., 1974. The Iceland phenomenon: imprints of a hot spot on the ocean crust, and implications for flow below the plates, In: *Kristjansson* (ed.), *Geodynamics of Iceland and the North Atlantic Area*, D. Reidel, Norwell, Mass., 105-126.

Vogt, P.R., 1986. Magnetic anomalies and crustal magnetization, In: *Vogt, P.R. & Tucholke, B.E.* (eds.), *The Geology of North America, Vol. M, The Western North Atlantic Region*, Geol. Soc. Am., Boulder, Colorado, U.S.A., 229-256.

Walther, C.H.E., 2003. The crustal structure of the Cocos ridge off Costa Rica, *J. Geophys. Res.*, **108**, EPM 1-1 - 1-21.

Wang, X. & Cochran, J.R., 1993. Gravity anomalies, isostasy, and mantle flow at the East Pacific Rise Crest, *J. Geophys. Res.*, **98**, 19505-19531.

Wang, X., Cochran, J.R. & Barth, G.A., 1996. Gravity anomalies, crustal thickness, and the pattern of mantle flow at the fast spreading East Pacific Rise, 9°-10°N: Evidence for three-dimensional upwelling, *J. Geophys. Res.*, **101**, 17927-17940.

Weir, N.R.W., White, R.S., Brandsdottir, B., Einarsson, P., Shimamura, H. & Shiobara, H., 2001. Crustal structure of the northern Reykjanes Ridge and Reykjanes Peninsula, southwest Iceland, *J. Geophys. Res.*, **106**, 6347-6368.

Wessel, P. & Smith, W.H.F, 1995. New version of the Generic Mapping Tool released, *EOS Trans.*, AGU, **76**(33), 329.

Wessel, P. & Watts, B., 1988. On the accuracy of marine gravity measurements, *J. Geophys. Res.*, **93**, 393-413.

White, R.S., Bown, J.W. & Smallwood, J.R., 1995. The temperature of the Iceland plume and origin of outward-propagating V-shaped ridges, *J. Geol. Soc. Lond.*, **152**, 1039- 1045.

White, R.S., McKenzie, D. & O'Nions, R.K., 1992. Oceanic crustal thickness from seismic measurements and rare earth element inversions, *J. Geophys. Res.*, **97**, 19683-19715.

White, S.M., Haymon, R.M., Fornari, D.J., Perfit, M.R. & Macdonald, K.C., 2002. Correlation between volcanic and tectonic segmentation of fast-spreading ridges: Evidence from volcanic structures and lava flow morphology on the East Pacific Rise at 9°-10°N, *J. Geophys. Res.*, **107**, EPM 7-1 - 7-20.

Whitehead, J.A., Dick, H.J.B. & Schouten, H., 1984. A mechanism for magmatic accretion under spreading centres, *Nature*, **312**, 146-148.

Wright, D.J., Haymon, R.M. & Fornari, D.J., 1995. Crustal fissuring and its relationship to magmatic and hydrothermal processes on the East Pacific Rise crest (9°12'N-54'N), *J. Geophys. Res.*, **100**, 6097-6120.

Wright, D.J., Haymon, R.M., White, S.M. & Macdonald, K.C., 2002. Crustal fissuring on the crest of the southern East Pacific Rise at 17°15'N-40'S, *J. Geophys. Res.*, **107**, EPM 5-1 - 5-14.